Stony Brook University

Thin Films for X-ray Optics

A Dissertation Presented

by

Raymond Conley

to

The Graduate School

in Partial Fulfillment of the

Requirements

for the Degree of

Doctor of Philosophy

in

Material Science & Engineering

Stony Brook University

May 2017

Stony Brook University

The Graduate School

Raymond Conley

We, the dissertation committee for the above candidate for the

Doctor of Philosophy degree, hereby recommend

acceptance of this dissertation.

Michael Dudley – Dissertation Advisor
Professor and Department Chair, Material Science & Engineering

Dilip Gersappe - Chairperson of Defense
Professor, Material Science & Engineering

Balaji Raghothomachar – Committee Member
Senior Research Scientist, Material Science & Engineering

Nathalie Bouet – External Member
Scientific Staff, Physicist, Brookhaven National Laboratory

This dissertation is accepted by the Graduate School

Charles Taber

Dean of the Graduate School

Abstract of the Dissertation

Thin Films for X-ray Optics

by

Ray Conley

Doctor of Philosophy

in

Material Science & Engineering

Stony Brook University

2017

X-ray optics are a subset of optics that are used to focus, filter, or otherwise manipulate light in the x-ray range. Visible light and x-rays propagate through space in the same manner because they are both electromagnetic radiation, but in contrast to visible light, x-rays interact very weakly with matter because the refractive index of all materials is very close to 1 at x-ray wavelengths. This weak interaction with matter has led to the global proliferation of both laboratory and accelerator based x-ray instruments that have the advantages of high penetration power, allowing the study of thick specimens, buried or hidden structures, and in-situ studies. The strong penetrating power of x-rays also means that x-ray optics need to be designed very differently from their visible-light analogues. Focusing x-rays with refraction requires an entire array of lens instead of a single element, each contributing a minute amount of focusing to the system. In contrast to their visible light counterparts, diffractive optics require a certain depth along the optical axis in order to provide sufficient phase shift. Mirrors reflect only at very shallow angles. In order to increase the angle of incidence, contribution from constructive interference within many layers needs to be collected. This requires a multilayer coating. Thin films have become a central ingredient for many x-ray optics due to the ease of which material composition and thickness can be controlled.

Chapter 1 starts with a short introduction and survey of the field of x-ray optics. This begins with an explanation of reflective multilayers. Focusing optics are presented next, including mirrors, zone plates, refractive lenses, and multilayer Laue lens (MLL). The strengths and weaknesses of each "species" of optic are briefly discussed, alongside fabrication issues and the ultimate performance for each. Practical considerations on the use of thin-films for x-ray optics fabrication span a wide array of topics including material systems selection and instrumentation design. Sputter deposition is utilized exclusively for the work included herein because this method of thin-film deposition allows a wide array of deposition parameters to be controlled. This chapter also includes a short description of two deposition systems I have designed.

Chapter 2 covers a small sampling of some of my work on reflective multilayers, and outlines two of the deposition systems I have designed and built at the Advanced Photon Source. A three-stripe double multilayer monochromator is presented as a case study in order to detail specifications, fabrication, and performance of this prolific breed of x-ray optics. The APS Rotary Deposition System was the first deposition system in the world designed specifically for multilayer Laue lens, however my advancements in MLL fabrication technology led to new generations of deposition instruments that were better suited. In order to re-purpose the APS Rotary Deposition System, a concept to upgrade the machine with a suborbital planetary is discussed. The APS Modular Deposition System (MDS) is the state of the art instrument that was designed to keep APS at the forefront of x-ray optics technology for the foreseeable future. By including flexibility in the design, the machine is ideally suited for research on all types of multilayers and thin-films for x-ray optics applications. A new method for in-situ surface metrology is presented which relies on the infrastructure provided by the MDS. The chapter concludes with discussion on several types of reflective multilayers that span a broad range of x-ray wavelengths, from soft x-rays (below 5-10 keV) to hard x-rays (above 5-10keV).

A method for fabrication of precision elliptically-figured mirrors called profile coating (conceived at the APS) is covered in Chapter 3. Profile-coating is a technique where a specially shaped mask is designed to partially obscure the sputtering source in order to produce a coating with a specially defined film thickness profile perpendicular to substrate translation. Source shape modeling and mask calculation is presented. Initially, Au was used as the filler material for profile coating, however I found that Pt offered better performance. Rh has also been used to fabricate profile-coated KB mirrors. Performance and commissioning results for the APS profile-coating deposition system (another machine designed by myself) is included.

Chapter 4 covers my work on multilayer Laue lens. Motivation and current status are presented, and the nomenclature we devised to name the various MLL types is listed. Following this, a theoretical overview is provided. Important advancements I have spearhead in this field are included, such as the introduction of metal silicides, reactive sputtering for stress reduction, marker layers, and the first ever wedged MLL fabrication. My early successes with these optics led the National Synchrotron Light Source-II to commission new laboratories which I designed explicitly for development of MLL. Several world records are highlighted, including performance of the world's first wedged MLL, and the achievement of an MLL over 100 μm thick with 15,170 layers in the stack. My efforts culminated in MLL optics that provide the highest resolution in the world of below 15 nm x 15 nm which is available for routine user operations at the Hard X-ray Nanoprobe at NSLS-II. Finally, an outlook on the future of MLL is discussed.

My optics have been deployed at facilities and beamlines spanning multiple continents. Optics specifically discussed here were used at beamlines 1BM, 2ID, 7BM, 12BM, 16ID, 26ID, 32-ID 34ID at the APS, and 3-ID at the NSLS-II.

Dedicated to

My children:

Ryan, Samantha, and Lorraine.

Table of Contents

List of Figures

List of Tables

List of Abbreviations

AA	Atomic absorption
ANL	Argonne National Laboratory
APS	Advanced Photon Source
BM	Bending magnet
BNL	Brookhaven National Laboratory
BSA	Brookhaven Science Associates
CCP	Computer controlled polishing
CRL	Compound refractive lens
DC	Direct current
DMM	Double multilayer monochromator
DOE	Department of Energy
DRIE	Deep reactive ion etching
EDM	Electrical discharge machining
EEM	Elastic emission machining
EPICS	Experimental physics and industrial control system
ESRF	European Synchrotron Radiation Facility
EUV	Extreme ultra-violet
FIB	Focused ion beam
fMLL	Flat multilayer Laue lens
FOB	Field of view
FWHM	Full width at half maximum
FZP	Fresnel zone plate
HXN	Hard X-ray Nanoprobe
ID	Insertion device
IOC	Input-output controller
KB	Kirkpatrick-Baez
LIFO	Last in, first out
LLNL	Lawrence Livermore National Laboratory
MDS	Modular Deposition System
MFC	Mass flow controller
MLL	Multilayer Laue lens
MOS	Multi-beam optical sensor
MRF	Magneto-rheological finishing
MZP	Multilayer zone plate
NA	Numerical aperture
NSLS	National Synchrotron Light Source
NSLS-II	National Synchrotron Light Source-II
PID	Proportional-integral-derivative
PLC	Programmable logic controller
PLD	Pulsed laser deposition
PTFE	Polytetrafluoroethylene
P-V	Peak-to-valley
QCM	Quartz crystal rate monitor
R&D	Research and development

RMS	Root-mean-square
RPM	Rotations per minute
SBIR	Small Business Innovative Research
SCCM	Standard cubic centimeters per minute
SEM	Scanning electron microscope
STXM	Scanning transmission x-ray microscopy
SUT	Surface under test
TM	Transmission flat
TXM	Transmission x-ray microscope
UHV	Ultra-high vacuum
UV	Ultra-violet
VCW	Vacuum chamber window
wMLL	Wedged multilayer Laue lens
XPD	X-ray power diffraction
XRR	X-ray reflectivity
ZP	Zone plate

Acknowledgments

I thank Chian Liu, Nathalie Bouet, Matt Vescovi, Jimmy Biancarosa, and Bing Shi for their assistance with some of the coatings. Simulations were provided by Hanfei Yan, Hyon Chol Kang, Jorg Maser, Albert T. Macrander, Yong Chu, Adam Kubec, and Cameron Kewish. MLL sectioning and imaging was provided by H.C.K., N.B., Nima Jahedi, and Juan Zhou. Metrology measurements were performed by Jun Qian, Lahsen Assoufid, and Jayson Chiao. Beamline measurements were performed by H.Y, H.C.K, A.T.M., G. Brian Stephenson, David Shapiro, Kramer Akli, Eric Gullikson, and Michael Storm. I also thank Christian Morawe and David Windt for years of fruitful exchanges

Work at the Argonne National Laboratory was supported by the U.S. DOE under Contract No. DE-AC02-06CH11357. Work at Brookhaven National Laboratory was supported by the Department of Energy, Office of Basic Energy Sciences under contract DE-SC00112704. The Advanced Photon Source and The National Synchrotron Light Source-II are Office of Science User Facilities operated for the U.S. Department of Energy (DOE) Office of Science by Argonne National Laboratory, and Brookhaven National Laboratory, respectively. This research used resources of the Advanced Light Source, which is a DOE Office of Science User Facility under contract no. DE-AC02-05CH11231

Selected Publications

1 C. Liu, L. Assoufid, R. Conley, A. T. Macrander, G. E. Ice and J. Z. Tischler, Profile coating and its application for Kirkpatrick-Baez mirrors. *Optical Engineering **42***, 3622-3628 (**2003)**.

2 C. Liu, R. Conley, L. Assoufid, A. T. Macrander, G. E. Ice, J. Z. Tischler and K. Zhang, Profile coatings and their applications. *Journal of Vacuum Science & Technology A: Vacuum, Surfaces, and Films **21***, 1579-1584 (**2003)**.

3 H. C. Kang, G. B. Stephenson, C. Liu, R. Conley, A. T. Macrander, J. Maser, S. Bajt and H. N. Chapman, Synchrotron x-ray study of multilayers in Laue geometry. *Proc. SPIE **5537***, 127-132 (**2004)**.

4 J. A. Libera, R. W. Gurney, S. T. Nguyen, J. T. Hupp, C. Liu, R. Conley and M. J. Bedzyk, X-ray nanoscale profiling of layer-by-layer assembled metal/organophosphonate films. *Langmuir **20***, 8022-8029 (**2004)**.

5 C. Liu, R. Conley, L. Assoufid, Z. Cai, J. Qian and A. Macrander, From flat substrate to elliptical KB mirror by profile coating. *AIP Conference Proceedings* 704 (**2004)**.

6 C. Liu, R. Conley and A. Macrander, Functional profile coatings and film stress. *Journal of Vacuum Science & Technology A: Vacuum, Surfaces, and Films **22***, 1610-1614 (**2004)**.

7 C. Liu, R. Conley, A. T. Macrander, T. Graber, C. Morawe, C. Borel and E. M. Dufresne, Small d-spacing WSi_2/Si narrow bandpass multilayers. *Proc. SPIE - Int. Soc. Opt. Eng.* 154-160 (**2004)**.

8 J. Maser, G. B. Stephenson, S. Vogt, Y. Wenbing, A. Macrander, H. C. Kang, L. Chian and R. Conley, Multilayer Laue lenses as high-resolution x-ray optics. *Proc. SPIE - Int. Soc. Opt. Eng. **5539***, 185-194 (**2004)**.

9 H. C. Kang, G. B. Stephenson, C. Liu, R. Conley, A. T. Macrander, J. Maser, S. Bajt and H. N. Chapman, High-efficiency diffractive x-ray optics from sectioned multilayers. *Applied Physics Letters **86***, 151109-151103 (**2005)**.

10 C. Liu, R. Conley, A. T. Macrander, J. Maser, H. C. Kang, M. A. Zurbuchen and G. B. Stephenson, Depth-graded multilayers for application in transmission geometry as linear zone plates. *Journal of Applied Physics **98***, 113519-113516 (**2005)**.

11 H. C. Kang, J. Maser, G. B. Stephenson, C. Liu, R. Conley, A. T. Macrander and S. Vogt, Nanometer Linear Focusing of Hard X Rays by a Multilayer Laue Lens. *Physical Review Letters **96***, 127401-127404 (**2006)**.

12 C. Liu, R. Conley and A. Macrander, Film stress studies and the multilayer Laue lens project. *Proc. SPIE - Int. Soc. Opt. Eng.* 63170J (**2006)**.

13 C. Liu, R. Conley, A. Macrander, J. Maser, H. Kang and G. Stephenson, A multilayer nanostructure for linear zone-plate applications. *Thin Solid Films **515***, 654-657 (**2006)**.

14 L. Assoufid, J. Qian, C. M. Kewish, C. Liu, R. Conley, A. T. Macrander, D. Lindley and C. Saxer, A microstitching interferometer for evaluating the surface profile of precisely figured X-ray KB mirrors. *Proc. SPIE - Int. Soc. Opt. Eng.* 670460 (**2007)**.

15 R. Conley, C. Liu, C. M. Kewish, A. T. Macrander and C. Morawe, Multilayer growth in the APS rotary deposition system. *Proc. SPIE - Int. Soc. Opt. Eng. **6705***, 670505-670507 (**2007)**.

16 R. Conley, C. Liu and A. T. Macrander in *Multilayer Deposition Control System*, Argonne National Laboratory, **2007**.

17 H. C. Kang, G. B. Stephenson, C. Liu, R. Conley, R. Khachatryan, M. Wieczorek, A. T. Macrander, H. Yan, J. Maser, J. Hiller and R. Koritala, Sectioning of multilayers to make a multilayer Laue lens. *Review of Scientific Instruments **78***, 046103 (**2007)**.

18 A. Khounsary, E. M. Dufresne, C. M. Kewish, J. Qian, L. Assoufid and R. Conley, Fabrication and evaluation of variable focus X-ray lenses. *Nuclear Instruments and Methods in Physics Research Section A: Accelerators, Spectrometers, Detectors and Associated Equipment **582***, 117-119 (**2007)**.

19 C. Liu, R. Conley, J. Qian, C. Kewish, A. Macrander, J. Maser, H. Kang, H. Yan and G. Stephenson, Bonded Multilayer Laue Lens for focusing hard X-rays. *Nuclear Instruments and Methods in Physics Research Section A: Accelerators, Spectrometers, Detectors and Associated Equipment **582***, 123-125 (**2007)**.

20 H. Yan, H. C. Kang, J. Maser, A. T. Macrander, C. M. Kewish, C. Liu, R. Conley and G. B. Stephenson, Characterization of a multilayer Laue lens with imperfections. *Nuclear Instruments & Methods in Physics Research Section a-Accelerators Spectrometers Detectors and Associated Equipment **582***, 126-128 (**2007)**.

21 R. Conley Jr, C. Liu, A. Macrander, H. Yan, H. Kang, J. Maser and G. B. Stephenson in *Zone compensated multilayer Laue lens and apparatus and method of fabricating the same*, U.S. Patent PCT/US2010/060057, **2008**.

22 R. Conley, C. Liu, J. Qian, C. M. Kewish, A. T. Macrander, H. Yan, H. C. Kang, J. Maser and G. B. Stephenson, Wedged multilayer Laue lens. *Review of Scientific Instruments **79***, 053104 (**2008)**.

23 H. C. Kang, H. Yan, R. P. Winarski, M. V. Holt, J. Maser, C. Liu, R. Conley, S. Vogt, A. T. Macrander and G. B. Stephenson, Focusing of hard x-rays to 16 nanometers with a multilayer Laue lens. *Applied Physics Letters **92***, 221114 (**2008)**.

24 C. Q. Liu, R. P. Conley, A. T. Macrander, H. C. Kang, G. B. Stephenson and J. Maser in *Method of making and structure of multilayer Laue lens for focusing hard x-rays*, U.S. Patent 7,440,546 B2, Uchicago Argonne, LLC, US, **2008**.

25 M. Wieczorek, X. Huang, J. Maj, R. Conley, J. Qian, A. Macrander, C. Christensen, J. Hodsden and R. Khachatryan in *Assessing the quality of x-ray optic surfaces of Si crystals cut by diamond-wire and rotating-blade sawing techniques*, Argonne National Laboratory (ANL), **2008**.

26 R. Conley, N. Bouet, J. Biancarosa, Q. Shen, L. Boas, J. Feraca and L. Rosenbaum, The NSLS-II multilayer laue lens deposition system. *Proc. SPIE - Int. Soc. Opt. Eng.* 74480U-74481 (**2009)**.

27 A. Macrander, K. MacArthur, J. Maj, J. Qian, D. Linnen, R. Khachatryan, M. Wieczorek, R. Conley and A. Genis, Silicon x-ray monochromator surfaces by independent oxidation and etching steps. *Bulletin of the American Physical Society **54***, (**2009)**.

28 A. T. Macrander, H. Yan, H. C. Kang, J. Maser, C. Liu, R. Conley and G. B. Stephenson in *Nanofocusing of Hard X-rays with Multilayer Laue Lenses, Vol. V* McGraw-Hill Professional, **2009**.

29 N. Bouet, R. Conley, J. Biancarosa, R. Divan and A. Macrander, WSi_2/Si Multilayer Sectioning by Reactive Ion Etching for Multilayer Laue Lens Fabrication. *Society of Photo-Optical Instrumentation Engineers (SPIE) Conference Series* 780203-780205 (**2010)**.

30 N. Jahedi, R. Conley, B. Shi, J. Qian, K. Lauer and A. Macrander, Metrology of multilayer Laue lens structures by means of scanning electron microscope imaging. *Nuclear Instruments and Methods in Physics Research Section A: Accelerators, Spectrometers, Detectors and Associated Equipment* ***616***, 89-92 (**2010)**.

31 J. M. Kim, I. H. Cho, S. Y. Lee, H. C. Kang, R. Conley, C. Liu, A. T. Macrander and D. Y. Noh, Observation of the Talbot effect using broadband hard x-ray beam. *Optics Express* ***18***, 24975-24982 (**2010)**.

32 C. Liu, B. Shi, J. Qian, R. Conley, H. Yan, M. Wieczorek, A. Macrander, J. Maser and G. Stephenson, Full Multilayer Laue Lens for Focusing Hard X-rays. *AIP Conference Proceedings* 47 (**2010)**.

33 B. Shi, C. Liu, J. Qian, W. Liu, L. Assoufid, A. Khounsary, R. Conley Jr and A. T. Macrander, Platinum Kirkpatrik-Baez mirrors for a hard x-ray microfocusing system made by profile coating. *SPIE Optical Engineering + Applications* 78020G-78026 (**2010)**.

34 H. Yan, H. C. Kang, R. Conley, C. Liu, A. T. Macrander, G. B. Stephenson and J. Maser, Multilayer Laue Lens: A Path Toward One Nanometer X-Ray Focusing. *X-Ray Optics and Instrumentation* ***2010***, 401854 (**2010)**.

35 L. Zhou, Y. Wang, H. Zhou, M. Li, R. L. Headrick, K. MacArthur, B. Shi, R. Conley and A. T. Macrander, Pressure-dependent transition from atoms to nanoparticles in magnetron sputtering: Effect on WSi_2 film roughness and stress. *Physical Review B* ***82***, 075408 (**2010)**.

36 R. Conley, N. Bouet, K. Lauer, M. Carlucci-Dayton, J. Biancarosa, L. Boas, J. Drannbauer, J. Feraca and L. Rosenbaum, Multilayer Laue Lens Growth at NSLSII. *AIP Conference Proceedings* ***1365***, 69 (**2011)**.

37 M. G. Honnicke, J. W. Keister, R. Conley, K. Kaznatcheev, P. Z. Takacs, D. S. Coburn, L. Reffi and Y. Q. Cai, Synchrotron X-ray tests of an L-shaped laterally graded multilayer mirror for the analyzer system of the ultra-high-resolution IXS spectrometer at NSLS-II. *Journal of Synchrotron Radiation* ***18***, 862-870 (**2011)**.

38 S. Y. Lee, I. H. Cho, J. M. Kim, H. F. Yan, R. Conley, C. A. Liu, A. T. Macrander, J. Maser, G. B. Stephenson, H. C. Kang and D. Y. Noh, Hard x-ray nano patterning using a sectioned multilayer. *Journal of Applied Physics* ***109***, 5 (**2011)**.

39 K. MacArthur, B. Shi, R. Conley and A. T. Macrander, Periodic variation of stress in sputter deposited Si/WSi_2 multilayers. *Applied Physics Letters* ***99***, 081905-081903 (**2011)**.

40 A. Macrander, K. MacArthur, B. Shi and R. Conley, Tension in the Initial Growth Stages of Sputter Deposited WSi_2 on Si in Multilayers. *Bulletin of the American Physical Society* ***56***, (**2011)**.

41 H. Yan, V. Rose, D. Shu, E. Lima, H. C. Kang, R. Conley, C. Liu, N. Jahedi, A. T. Macrander and G. B. Stephenson, Two dimensional hard x-ray nanofocusing with crossed multilayer Laue lenses. *Optics Express* ***19***, 15069-15076 (**2011)**.

42 V. V. Yashchuk, E. H. Anderson, S. K. Barber, N. Bouet, R. Cambie, R. Conley, W. R. McKinney, P. Z. Takacs and D. L. Voronov, Calibration of the modulation transfer function of surface profilometers with binary pseudorandom test standards: expanding the application range to Fizeau interferometers and electron microscopes. *Optical Engineering* ***50***, 093604-093612 (**2011)**.

43 V. V. Yashchuk, R. Conley, E. H. Anderson, S. K. Barber, N. Bouet, W. R. McKinney, P. Z. Takacs and D. L. Voronov, Characterization of electron microscopes with binary pseudo-random multilayer test samples. *Nuclear Instruments and Methods in Physics Research Section A: Accelerators, Spectrometers, Detectors and Associated Equipment* ***649***, 150-152 (**2011)**.

44 R. Conley, N. Bouet, J. Zhou, H. Yan, Y. Chu, K. Lauer, J. Miller, L. Chu and N. Jahedi, Advanced multilayer Laue lens fabrication at NSLS-II. *SPIE Optical Engineering + Applications* 850202-850207 (**2012)**.

45 C. Liu, R. Conley, J. Qian, C. M. Kewish, W. Liu, L. Assoufid, A. T. Macrander, G. E. Ice and J. Z. Tischler, Plastic Deformation in Profile-Coated Elliptical KB Mirrors. *ISRN Optics* p. 1-3 (**2012)**.

46 A. Rack, L. Assoufid, W. K. Lee, B. Shi, C. Liu, C. Morawe, R. Kluender, R. Conley and N. Bouet, Hard X-ray multilayer mirror round-robin on the wavefront preservation capabilities of W/B_4C coatings. *Radiation Physics and Chemistry* ***81***, 1696-1702 (**2012)**.

47 H. Wu, S. Chen, Y. Chu, R. Conley, N. Bouet, C. Chien, H. Chen, C. Lin, H. Tung and Y. Chen, Nanoresolution radiology of neurons. *J. Phys. D: Appl. Phys* ***45***, 242001 (**2012)**.

48 X. Huang, H. Yan, E. Nazaretski, R. Conley, N. Bouet, J. Zhou, K. Lauer, L. Li, D. Eom, D. Legnini, R. Harder, I. K. Robinson and Y. S. Chu, 11 nm hard X-ray focus from a large-aperture multilayer Laue lens. *Scientific Reports **3***, (**2013)**.

49 M. Idir, K. Kaznatcheev, S. Qian and R. Conley, Current status of the NSLS-II optical metrology laboratory. *Nuclear Instruments and Methods in Physics Research Section A: Accelerators, Spectrometers, Detectors and Associated Equipment **710***, 17-23 (**2013)**.

50 I.-J. Lee, N.-E. Sung, K. H. Chae and R. Conley, Characterization of zinc–tin–oxide films deposited by radio frequency magnetron sputtering at various substrate temperatures. *Thin Solid Films **548***, 385-388 (**2013)**.

51 R. Conley, B. Shi, M. Erdmann, S. Izzo, L. Assoufid, K. Goetze, T. Mooney and K. Lauer, APS deposition facility upgrades and future plans. 92070I-92076 (**2014)**.

52 M. G. Honnicke, R. Conley, C. Cusatis, E. M. Kakuno, J. Zhou, N. Bouet, J. B. Marques and F. C. Vicentin, Exotic X-ray back-diffraction: a path toward a soft inelastic X-ray scattering spectrometer. *Journal of Applied Crystallography **47***, 1658-1665 (**2014)**.

53 E. Nazaretski, X. Huang, H. Yan, K. Lauer, R. Conley, N. Bouet, J. Zhou, W. Xu, D. Eom, D. Legnini, R. Harder, C.-H. Lin, Y.-S. Chen, Y. Hwu and Y. S. Chu, Design and performance of a scanning ptychography microscope. *Review of Scientific Instruments **85***, 033707 (**2014)**.

54 B. Shi, A. T. Macrander, J. Maser, R. Conley and L. Assoufid, The effect of unequal bilayer thickness on stress in WSi_2/Si multilayers for multilayer Laue Lens structures. 920708-920705 (**2014)**.

55 H. Yan, R. Conley, N. Bouet and Y. S. Chu, Hard x-ray nanofocusing by multilayer Laue lenses. *Journal of Physics D: Applied Physics **47***, 263001 (**2014)**.

56 N. Bouet, R. Conley, R. Divan and A. Macrander in *Technique for etching monolayer and multilayer materials*, U.S. Patent 13/371,124, Brookhaven Science Associates LLC, UChicago Argonne LLC, U.S., **2015**.

57 X. Huang, R. Conley, N. Bouet, J. Zhou, A. Macrander, J. Maser, H. Yan, E. Nazaretski, K. Lauer, R. Harder, I. K. Robinson, S. Kalbfleisch and Y. S. Chu, Achieving hard X-ray nanofocusing using a wedged multilayer Laue lens. *Optics Express **23***, 12496-12507 (**2015)**.

58 M. Idir, L. Huang, N. Bouet, K. Kaznatcheev, M. Vescovi, K. Lauer, R. Conley, K. Rennie, J. Kahn, R. Nethery and L. Zhou, A one-dimensional ion beam figuring system for x-ray mirror fabrication. *Review of Scientific Instruments* ***86***, 105120 (**2015)**.

59 A. Kubec, N. Kujala, R. Conley, N. Bouet, J. Zhou, T. M. Mooney, D. Shu, J. Kirchman, K. Goetze, J. Maser and A. Macrander, Diffraction properties of multilayer Laue lenses with an aperture of 102 μm and WSi_2/Al bilayers. *Optics express* ***23***, 27990-27997 (**2015)**.

60 A. Macrander, M. Erdmann, N. Kujala, S. Stoupin, S. Marathe, X. Shi, M. Wojcik, D. Nocher, R. Conley and J. Sullivan, X-ray Optics Testing Beamline 1-BM at the Advanced Photon Source. *12th International Conference on Synchrotron Radiation Instrumentation (SRI-2015), New York, NY* 6-10 (**2015)**.

61 A. T. Macrander, A. Kubec, R. Conley, N. Bouet, J. Zhou, M. Wojcik and J. Maser, Efficiency of a multilayer-Laue-lens with a 102 μm aperture. *Applied Physics Letters* ***107***, 081904 (**2015)**.

62 E. Nazaretski, K. Lauer, S. Kalbfleisch, U. Wagner, C. Rau, Y. Chu, H. Yan, N. Bouet, J. Zhou and R. Conley, Pushing the limits: an instrument for hard X-ray imaging below 20 nm. *Journal of synchrotron radiation* ***22***, 336-341 (**2015)**.

63 D. L. Windt and R. Conley, Two-dimensional differential deposition for figure correction of thin-shell mirror substrates for x-ray astronomy. *SPIE Optical Engineering + Applications* 96031H-96012 (**2015)**.

64 R. Conley, N. Bouet, Y. S. Chu, X. Huang, H. C. Kang, A. T. Macrander, J. Maser, E. Nazaretski, G. B. Stephenson and H. Yan, Multilayer Laue Lens: A Brief History and Current Status. *Synchrotron Radiation News* ***29***, 16-20 (**2016)**.

65 H. Yan, E. Nazaretski, K. Lauer, X. Huang, U. Wagner, C. Rau, M. Yusuf, I. Robinson, S. Kalbfleisch, L. Li, N. Bouet, J. Zhou, R. Conley and Y. S. Chu, Multimodality hard-x-ray imaging of a chromosome with nanoscale spatial resolution. *Scientific Reports* ***6***, 20112 (**2016)**.

Chapter 1: Introduction and Literature Survey

1.1 Overview

Thin films have a wide variety of applications and have invaded about every segment of humanity, from anti-reflection coatings on automotive glass, wear-resistant additives on tooling, the microelectronics industry, power generation, and so on. Over the last several decades, their use in x-ray optics[1-3] has steadily increased. As thin-film technology has advanced from the simplest evaporation and cathodic sputtering[4] methods to modern plasma-processes, the performance of thin-film x-ray optics has been greatly improved, along with a similar widening of the breadth of their application. Over the last decade, the application of thin-films for x-ray optics has advanced significantly at both the Advanced Photon Source at Argonne National Laboratory and the National Synchrotron Light Source II at Brookhaven National Laboratory. Both facilities have invested heavily in thin-film based optics both in support of user science and beamline development. Originally, the infrastructure at the APS was intended for coating of single-layer films on large substrates to produce simple x-ray mirrors. As the field progressed, new equipment and expertise was added at the APS in order to produce simple multilayer mirrors for user applications. This equipment provided a natural avenue for research into new types of thick multilayer-based optics for use in transmission mode, called multilayer Laue lens (MLL). Early successes with these optics led the NSLS-II to commission new laboratories explicitly for development of MLL, with the obvious "side-effect" of allowing for production of many other types of thin-film based optics. In this dissertation, three broad types of optical elements are discussed; figured mirrors, reflective multilayers, and MLL. Deposition system instrumentation and design is presented. The majority of the dissertation covers R&D undertaken by myself (and my collaborators, to varying degrees of involvement) at National Laboratories across the country, involving x-ray facilities around the world.

1.1.1 Reflective Multilayers

All x-ray sources exhibit some polychromatic characteristics; from the Bremsstrahlung or radiation of elemental tube sources to the broad-band emission of a bending magnet beamline. For the vast majority of experimental techniques, some amount of monochromatization is desired which is obtained with a Bragg reflection from an ordered structure. The ordered structure is either a crystal or a multilayer. The energy selectivity (or bandpass) of a Bragg reflector is often roughly expressed as **1/n**, where n is the number of contributing layers in the Bragg reflector. The reflectance contribution of an individual atomic plane is defined as the ratio of the electron density contrast between the maximum of the plane itself and the minimum directly between two planes. A periodic multilayer deposited with thin film techniques behaves as a one-dimensional synthetic crystal, with **n** being limited by absorption through the stack and deposition stability. Since **n** for a crystal is based on the atomic spacing, but a multilayer is (typically) an amorphous deposition of constituent layers, the bandpass of Bragg reflection for multilayers is much greater than crystals. The x-ray flux, however, is much greater for multilayer optics than crystal optics due to the integrated reflectance of this bandwidth spread. To decrease the width of the bandpass, one may use low absorption material or a small d-spacing[5] (bilayer thickness) to increase n. The required d-spacing of a multilayer is based on the reflectance angle and energy of interest, expressed as:

$$d = N \lambda/2 \sin(\theta) \qquad \text{Eq. (1.1)}$$

Bragg's law (eq. 1.1) is shown schematically below in Figure 1.1. The thickness ratio between the two materials is known as **Γ**, and is colloquially expressed as the ratio of the thickness of the absorber layer to the total bilayer thickness. In Figure 1.1, **Γ=A/(A+B)**. In a typical specular reflectance measurement of a multilayer, Bragg peak strength is minimized for each **Nth** Bragg peak where **N=1/Γ** due to destructive interference within the multilayer. In other words, for **Γ=0.5**, the even numbered Bragg peaks are minimized. For **Γ=1/3**, every third Bragg peak is minimized.

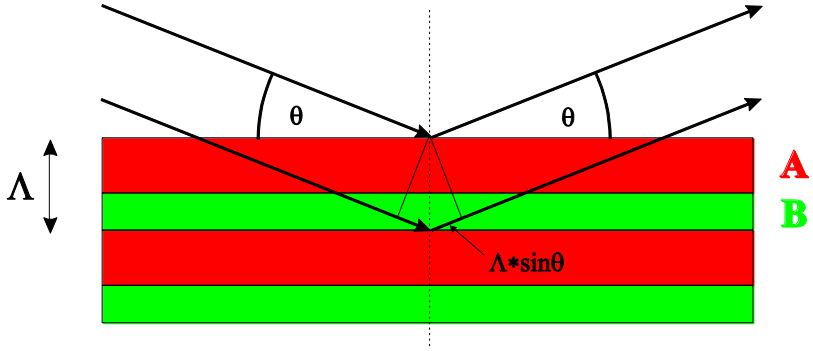

Figure 1.1: Schematic representation of Bragg reflection.

1.1.2 Nano-focusing X-ray Optics

Optical elements which can focus x-rays find application worldwide in areas such as volume-specific spectroscopy, full field microscopy, and scanning microscopy, to name a few. Focusing optics can be found at every synchrotron facility and are employed in a variety of laboratory-based x-ray systems. All focusing elements rely upon refraction, diffraction, or reflection (or a combination thereof) in order to modify the incoming radiation. The list of optical elements which can compress or focus is quite huge, however many of these hit lower limits due to either intrinsic fabrication issues or geometry, and so there are only three feasible nano-focusing (below roughly 50 nm) elements; namely, focusing mirrors, lithographically-produced zone plates, and multilayer Laue lens.

1.1.2.1 Focusing Mirrors

Focusing mirrors can be categorized into two general families; flat mirrors that are dynamically bent to fit into a desired profile, or monolithically figured mirrors with a fixed Figure. Over the years, many engineering designs have yielded successful results with dynamically bent mirrors. Significant effort has been put into the design of bender apparatus which can accurately bend mirrors possessing a trapezoidal shape into an ellipsoid. Bender design runs the gamut in complexity, from a thumb-screw pusher to a piezo actuated multi-point force application system. Further analytical work done at the ESRF found a more precise elliptical figure can be bent into a substrate which is not exactly trapezoidal, but contains a slight deviation from an ideal trapezoid[6]. The shape precision with this design requires that the silicon substrate is cut with a wire EDM, for example

While, in principle, a mirror with a three dimensional figure should focus as well as any other mirror, the fabrication issues intrinsic with development of the required geometries currently occludes use of such optics for the most demanding focusing needs. An alternative to a single surface for focusing in both the horizontal and vertical dimension is to create a small bonding joint between two precisely figured mirror surfaces, called colloquially a Montel optic. Such types of optics are widely employed in laboratory x-ray sources as collimating mirrors. While there have been major efforts aimed at producing around 100 nm spot sizes[7], joint imperfections become the dominating factor in obtaining higher performance. The present state of the art in nano-focusing mirror systems rely upon a two (or more) element scenario called the Kirkpatrick-Baez (KB) geometry[8], where one mirror upstream focuses in one direction, and the downstream mirror focuses in the other direction. Employment of this geometry is independent on the type of mirrors used. Mirror system performance is universally limited by mirror figure error, mechanical stability, alignment, and demagnification or numerical aperture. Mirror figures approaching 0.05 μrad RMS are on the horizon, and stable bending systems are widely available. Perhaps the most illustrative example of KB mirror nano-focusing performance comes from a joint effort between Osaka University and SPRing-8. Utilizing their 1 kilometer beamline, a two-element monolithic mirror system that was fabricated using EEM and coated with a laterally-graded multilayer for increased demagnification, and two (one horizontal, one vertical) adaptive-mirror phase correcting mirrors (giving, in total, four reflective elements) a focus of 7x8nm was recently disclosed[9]. While this is a momentous demonstration, the prospects for deploying such a setup for real scientific use is daunting.

1.1.2.1.1 Mirror Figuring Techniques

Focusing mirrors utilizing a pre-figured substrate have been fabricated using a wide array of methods. Mirror figuring is done with one of two basic approaches; either additive, or subtractive processes.

1.1.2.1.2 Subtractive Methods

For some applications, the spherical figure that is intrinsically produced with a basic over-arm polisher is adequate. Other methods that have been employed for figured optics include magneto-rheological finishing (MRF), computer-controlled polishing (CCP), elastic-emission machining (EEM), and plasma-assisted chemical etching, to name a few.

1.1.2.1.3 Additive Methods

Additive methods using thin-film techniques can also be employed for mirror figure modification. Two thin-film techniques available for surface figure modification are differential deposition[10] and profile coating[11-14]. Differential deposition methods (described in more detail later for fabrication of laterally-graded multilayers) require the engineered alteration of either a deposition flux density, or substrate dwell time. Original methods focused on altering sputtering power, however sputtering power versus flux density can be highly non-linear, and so current methods involve dwell time modification via velocity raster scanning.

1.1.2.1.4 Profile Coating

Profile coating is a method where the sputter source power is kept constant, while the substrate, or mirror surface, is passed over a precisely contoured mask at a uniform velocity to

achieve a desired profile along the direction normal to substrate motion. The shape of the profiled mask depends on the desired profile and the thickness distribution directly above the gun at the substrate level. This flux density distribution is then convoluted with the desired thickness profile to produce a mask contour. The flux density distribution of a ring source can be defined mathematically, and this is discussed in more detail in Chapter 3. Figure 1.2 shows an example of a mask designed for uniform coating in part (a) as well as an elliptical coating mask with a pair of mirrors mounted for coating in (b).

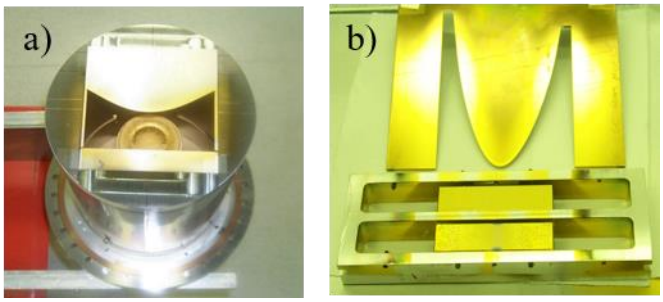

Figure 1.2: Profile-coating masks for uniform and elliptical figuring. The uniform-coating mask in part (a) partially obscures a 75mm Au target. The mask in part (b) is cut to produce an elliptical figure on a flat substrate. Two mirrors mounted for coating are also shown.

Extensive production of profile coatings with the ideal source model produced occasionally unpredictable profiles, and it was found that deviations in the ideal profile were the cause. This instability was found to be caused by dimensional tolerance errors in the targets, cathode magnetic field fluctuations, and imperfect mask-to-cathode alignment. To account for all of these variations at once, a new method for experimentally measuring the real flux density distribution was developed where a stationary substrate is placed at the mirror plane, sputtered onto, and measured via ellipsometry. The results of this method attest to its efficacy.

1.1.2.2 Lithographically Produced Zone Plates

Lithographically-produced zone plates (ZP) have a prolific footprint at synchrotron facilities (and indeed laboratory based systems) around the world. ZP operate by diffracting the incoming radiation around circularly symmetric zones that are properly placed such that the path length through each "space" in a ZP is an integer multiple of $\lambda/2$[15]. The focus size of a ZP is proportional to the width of the outermost zone, and the optimum thickness for a ZP with the highest optical efficiency scales with x-ray energy[16]. ZP are produced[17] via lithographic methods by patterning a photoresist with an electron-beam lithography instrument, and then electroplating a dense material (usually gold) into the troughs. Since lithography is used, ZP usually do not suffer from zone placement errors and can be written to an arbitrary size. These optics have been widely successful in focusing x-rays; in particular, soft x-rays[18] (generally accepted as radiation below 5-10keV, characterized as readily absorbed in air) and have been demonstrated to produce a spatial resolution of about 10nm at 707 eV[19]. A comprehensive review on the historical development of ZPs and their technical applications was published by Burkhard[20]. Because ZP resolution is roughly equal to the outermost zone width of the structure, and the thickness of the electroplated material should be sufficient to impart either complete absorption or π phase shift,

high aspect ratios are required for hard x-ray wavelengths. State of the art ZPs for hard x-rays have zone widths of approximately 20 nm, and aspect ratios around 20 or 30[21-23] which is still far below the optimum for hard x-ray wavelengths. Alternative approaches to overcome fabrication difficulties have been explored[18,24,25] with some successes. In order to side-step the difficulties imposed by lithographically based fabrication methods an alternative approach using multilayer deposition was first reported[26] in 1988 and has been explored by several groups[27-31]. With these approaches, a sputtered-sliced ZP or circular multilayer zone plate (MZP) is produced by depositing a multilayer on a rotating metal or glass wire. After coating, the multilayer-coated wire is sliced and polished to a ZP structure with an optimum section thickness for a targeted energy range. Because the wires have a significantly larger diameter than the ideal circular ZP structure innermost zone, the MZP is a partial zone-plate structure. These optics have been demonstrated to be effective in focusing extremely high energy x-rays up to 100 keV[30]. Although early attempts had limited success in realizing nanoscale x-ray focusing due to imperfections in the multilayer, more recent work has shown significantly enhanced focusing properties. Koyama et. al.[31] resolved a 50-nm test pattern structure at 20 keV using a circular MZP comprised of $Si/MoSi_2$ layers with an outermost zone of 40.4 nm width, and a 32 μm zone-plate thickness. This optic had an aspect-ratio of 792, and produced an efficiency of 27%. Döring et. al.[32] fabricated a MZP by growing W/Si multilayers on a rotating wire of a 0.9 μm diameter using a pulsed laser deposition (PLD) method, and then sectioning it using a focused-ion-beam (FIB) technique. This process generated a miniaturized circular MZP of 1.6 μm diameter and 54 zones with widths from 5 nm to 8.6 nm, resulting in a focal length of 50 μm at 7.9 keV. The same work described the wave-field reconstruction of a sub-5 nm focus from the measured far-field diffraction pattern, using a phase-retrieval method. Using atomic layer deposition (ALD) and FIB milling, Mayer et. al. fabricated circular MZPs that attained over 15% efficiency at 8 keV and an imaging resolution of 60 nm at 1.5 keV[33]. Other approaches to work around the requirement for high aspect-ratios were explored such as operation of ZP structures in reflection mode[34,35] however performance demonstrations comparable to what is currently achieved with standard ZP optics have not yet been reported.

1.1.2.3 Multilayer Laue Lens

Multilayer Laue lens, first described by Maser, et. al. in 1992 as a "Volume Zone Plate", [38-42] (MLL) are a relatively new class of nano-focusing x-ray optic, fabricated with a thin-film growth technique where thousands of individual layers are deposited on a substrate according to the Fresnel zone plate equation and sectioned. When this section is illuminated by a plane wave of x-rays, the x-rays will focus to a line[43]. If a pair of MLLs are used in a crossed geometry[44] a point focus can be obtained. MLL overcomes two major difficulties encountered in the conventional lithography fabrication of zone plates (ZP): small zone width and high aspect ratio, which limits the resolution and efficiency that ZP can achieve. As thin-film deposition techniques can easily produce atomically-thin layers, and the stack can be sectioned to an arbitrary thickness by several methods[45,46], MLL fabrication is not limited by these two factors, but other challenges such as layer placement error, and film growth issues such as film stress[47], sectioning damage and interfacial roughness arise. To date, MLL have been demonstrated to produce a 11nm line focus, and a 13x13 nm point focus.

1.1.2.4 Refractive Optics

Two common types of refractive optics are kinoform lens and compound refractive lens (CRL). Both lens behave in the same fashion to refract x-rays, however the fabrication methods have led to different delineations between the two lens. Kinoform lens are defined as optics where a lithographically patterned (thus one-dimensional) optical structure is fabricated out of a material that acts as a refractor. Conventional kinoform lens designs hit a theoretical[36] limit in the tens of nanometers range, while experimental verification has yielded only modest focal performance[37]. Multiple element arrays are straightforward to produce due to the nature of modern lithography. Compound Refractive Lenses are another type of focusing (or, collimating) optic that find use worldwide at synchrotron facilities. CRLs are usually formed by stamping a parabolic (or some other figure, such as elliptical) into beryllium plates, or by extruding lithium into the desired form. These low-z materials are used in order to exploit their comparatively high refractive index while minimizing overall absorption. The benefit of CRLs lies in the fact that they can be compounded; that is, a single lens may have little effect, but four, or eight, or perhaps 100 elements, when combined, can provide high gain, and as they are transmission optics, mechanical stability requirements are minimized. Depending on the stamping design, CRLs can be produced which focus in both directions, or collimate in one and focus in the other, and so on. The main limitations intrinsic to CRLs are surface figure and roughness, which causes scattering; and thus, loss of flux.

1.2 Literature Survey

1.2.1 Reflective Multilayers

1.2.1.1 Multilayer Materials Introduction

The material system selection process for application towards a specific optical design needs to take into account the intrinsic material deposition performance, desired energy, reflectance or bandwidth requirements, and possible environmental exposure hardships for the optic. Elemental absorption edges and intrinsic roughness are often examined first. The two most common material systems in use for synchrotron applications[48] are W/B_4C and Mo/Si. It is well known that W/B_4C exhibits good performance up to ~79.5 keV; this is right at the absorption edge for W. A multilayer which must operate just above this energy may find slightly higher performance if Pt is used as a substitute for W. However, B_4C also exhibits high intrinsic compressive stress, so that layers grown above ~6 nm may begin to fail due to delamination or "worm-tracking". When deposited on precisely figured substrate blanks, or bendable mirrors, this high stress may cause figure deformation leading to sub-optimal focusing performance if not taken into account. For large d-spacing multilayers[49], or lower energy multilayers, Mo/Si is often employed. While this material system can often be grown with extremely thick d-spacings and total overall growth thicknesses, Mo and Si mix chemically at the interface and create a molybdenum-silicide interdiffusion layer. This interdiffusion layer will artificially reduce the intended d-spacing, which also must be taken into account if a specific d-spacing is required. Interdiffusion will also widen the bandpass of a given multilayer, all else being equal.

1.2.1.2 Sputtering Rate Decay Correction

Sputtering is utilized as the deposition method of choice due to the wide range of film properties obtainable, stable deposition rates, thickness gradient capabilities, and homogeneous films. Unfortunately, this also means that since sputtering is a consumptive process the deposition rate necessarily falls with time as target material is used. X-ray multilayer optics require layer thickness precision higher than is measurable with commercially available in-situ growth monitors[50], so the sputtering environment must instead be kept as stable as possible, and sputtering rate drift should be accounted for and corrected. As the film is grown onto the substrate, material removal from the target during multilayer deposition results in an erosion ring centered on the area of the target where the magnetic field are tangent to the target surface. The sputtering rate slowly decays as the target is eroded, and this rate must be compensated for as film growth proceeds. This appears to be the single weakness of the sputtering technique when used for very thick depositions. Larger cathodes will reduce the amount of erosion correction required, but will not eliminate it entirely. For thin multilayers, time-based erosion decay is used. When using a uniform coating mask with a 15-mm central gap, 3-in-diameter sputtering guns, and typical sputtering parameters, a rate decay of 0.03% per 100 seconds of sputtering time for Si and 0.045% per 100 seconds for WSi_2 was found to be sufficient. These values were obtained by fitting the reflectivity of uniform d-spacing multilayers grown with no sputtering rate correction (see Figure 1.3). The rate decay correction is achieved by progressively slowing down the substrate linear or angular velocity (depending on which deposition system is used) at the start of each new layer. For thick multilayers, a more complex non-linear rate decay is used because the rate of decay slows down as the target erosion ring slowly sinks deeper into the target, and then speeds up as more material is removed from the side walls of the erosion ring. Again, the correction is generally not necessary when using large cathodes for reflective multilayer deposition where the total film growth is small, but with small cathodes or for MLL deposition, this correction is necessary. The latest technique for erosion correction is an iterative refinement of growth rate based on marker layers which are inserted in the growth. More details on this technique are described below. The use of sputtering guns designed for more target utilization may allow for thicker growths and relaxed sputtering rate decays, however more complicated designs involving (for example) dynamic magnetic fields may compromise growth rate repeatability.

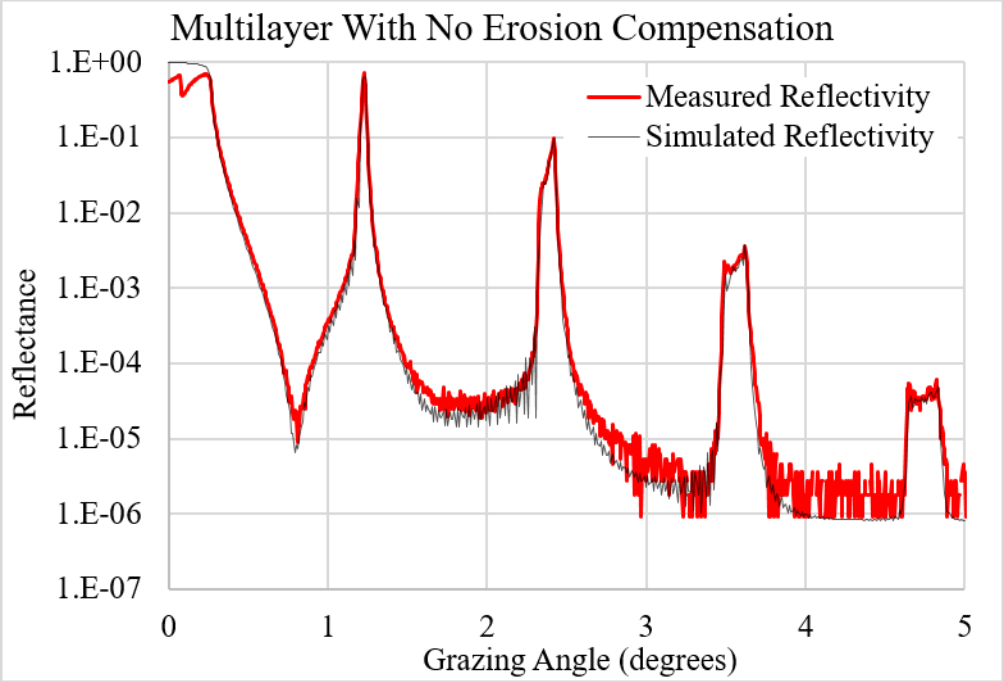

Figure 1.3: Reflectivity measurement at 8 keV for growth rate decay determination. 400 bilayers, WSi_2 = 7.1 Å to 7.2 Å, Si = 29.4 Å to 31 Å

1.2.1.3 Periodic Narrow Bandpass Multilayer

By using the erosion rates as described above, a uniform d-spacing multilayer with 400 periods of alternating 7.2-Å WSi_2 layers and 30.8-Å Si layers was grown on a Si substrate with a surface roughness of about 0.5 Å. Reflectivity measurements with the APS reflectometer show this multilayer to have a first-order reflectivity of 70.6% with a bandpass of 1.34%, and a second-order reflectivity of 39% with a bandpass of 0.28% (see Figure 1.4). Some minor broadening at the base of each Bragg peak in the experimental reflectivity data, which becomes more obvious for higher-order reflections, is a characteristic of the lab source and is not an error within the structure.

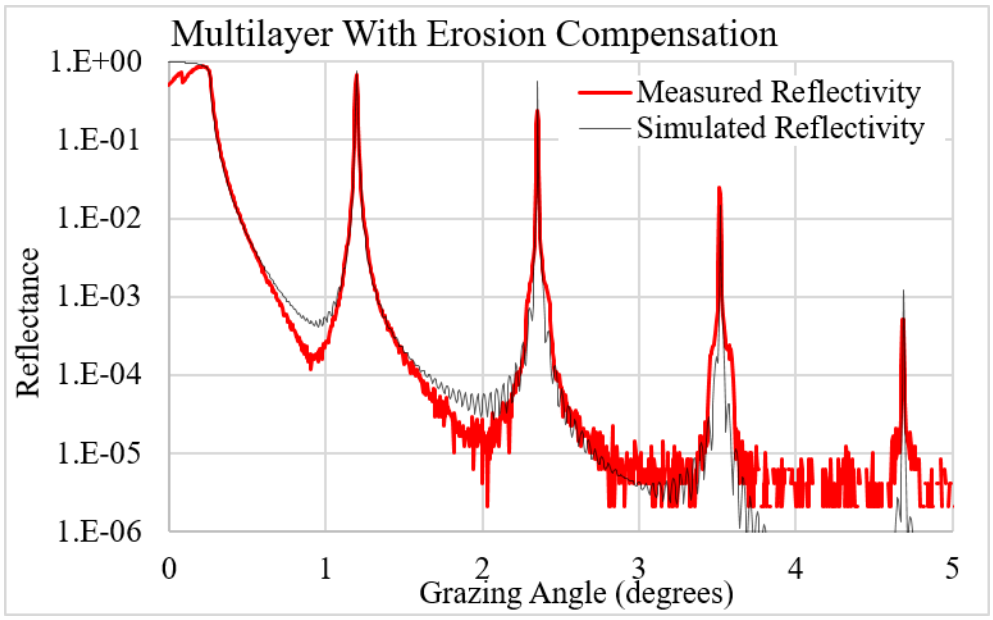

Figure 1.4: Reflectivity measurement at 8 keV after growth rate decay compensation. 400 bilayers, WSi_2 = 7.2 Å, Si = 30.8 Å, 1st order R = 70.6 %, BW = 1.34

1.2.1.4 Depth-Graded Wide Bandpass Multilayer

The angular bandwidth of a periodic multilayer structure is (usually) several orders of magnitude larger than that of a crystal monochromator. However, for applications requiring significantly higher bandwidth, such as collimating or focusing optics, or in situations where resolution can be sacrificed to obtain higher integrated photon flux, aperiodic multilayers are particularly well suited. A depth-varying bilayer thickness profile may be obtained from a desired reflectivity function by first approximating the layer thicknesses and then optimizing the thicknesses using numerical algorithms. In the present case, an approximate analytical formula for the bilayer reflectivity as a function of depth is inverted to give a set of recurrent expressions that yield a sequence of bilayer thicknesses beginning at the upper surface. The bilayer thickness gradient is a monotonic function of depth and is assumed to be sufficiently large such that the reflection condition for each given wavelength or incident angle is satisfied within a region that is narrow compared to the thickness of the multilayer stack. These conditions restrict the number of bilayers in the sequence and therefore the achievable reflectivity from a given pair of materials. The layer sequence is then iteratively refined using a least-squares fitting routine (and later a genetic evolution algorithm), allowing the bilayer thicknesses to vary until the average difference between the designed and calculated reflectivity is below a threshold value.

As an example, a depth-graded WSi_2/Si multilayer was designed to have a flat-topped reflectivity of 10% over an angular range of approximately 8 mrad. The resulting depth-graded sequence of 77 bilayers ranging from 22 Å to 55 Å as shown in Figure 1.5 (with the thickest layers at the surface) was deposited on a Si wafer. Reflectivity measurements with the APS reflectometer (1.54 Å) revealed a quite constant reflectivity of 9.5% and a bandpass of 42.6%, which agrees well with the reflectivity calculated for this structure (see Figure 1.6).

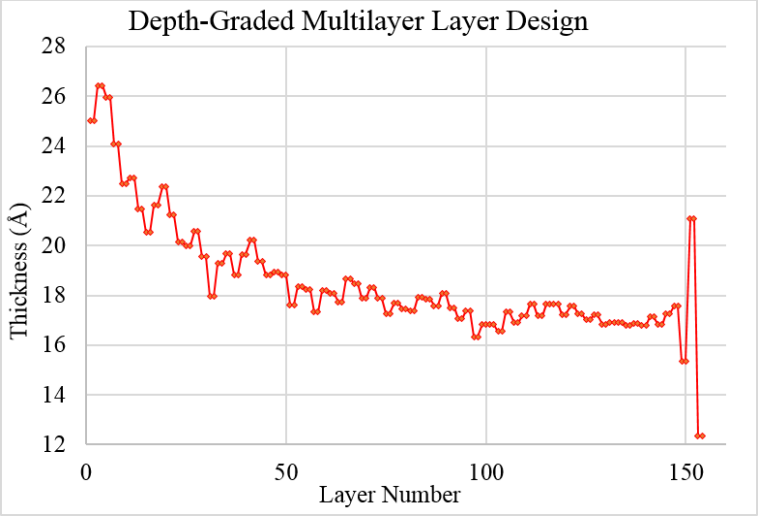

Figure 1.5: Depth-graded multilayer structure. Layer 1, Si, is grown first. Note that Γ=0.5 for all 77 bilayers.

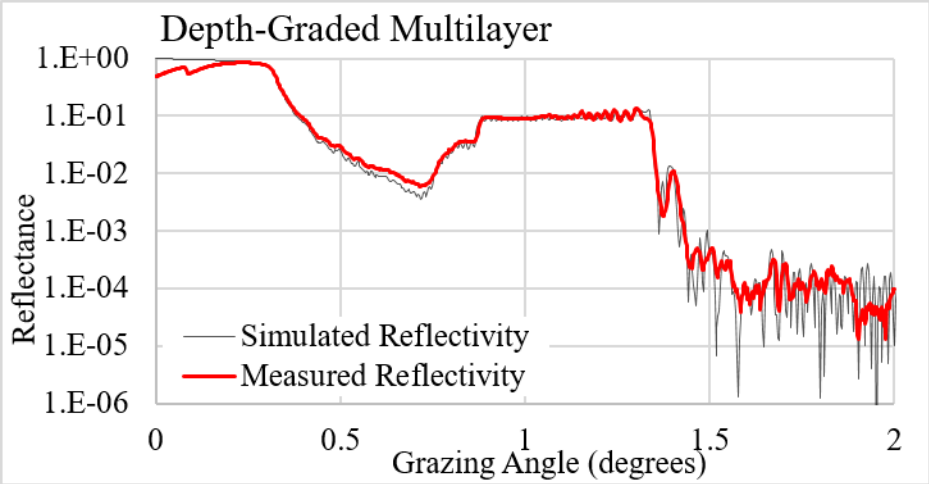

Figure 1.6: Depth-graded multilayer reflectivity.Flat spectral response of 10% has a bandwidth of 42.6%.

1.2.2 Profile coating with Au

Many microfocusing mirrors, starting out as either a flat, a sphere, or a cylinder, were profile coated at the APS with Cr/Au. Focusing spot sizes below 1 μm are standard[11,12,14]. Focal performance below 100 nm has been documented[51] with Au profile coated mirrors, with simulations suggesting diffraction limits below 50 nm[52].

Figuring of a flat substrate into an elliptical shape for a typical beamline application may require 7 or more μm of film deposition at the edges. High-purity Au is used because an exceptionally high deposition rate is achievable along with a tendency to maintain low roughness when deposited at low pressures. After two or three corrections, mirrors with exceptionally low figure errors were routinely produced, as seen in Figure 1.7, below.

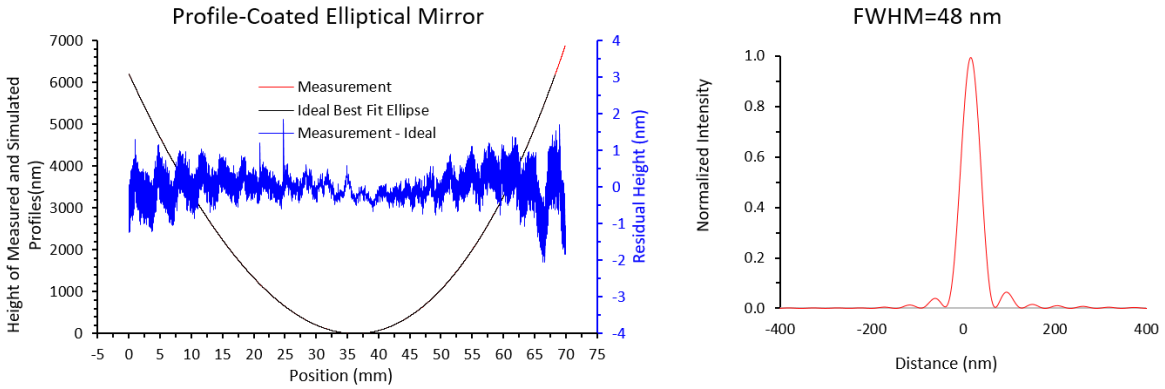

Figure 1.7: Au-profiled KB mirror surface measurement and focal simulation.

Initial x-ray testing with Au profile-coated mirrors was undertaken at sector 34-ID at the APS. Mirror focal performance was 0.4 μm^2 as measured with a knife-edge test, and this focal performance method continues to be a standard technique for profile-coated KB systems. The smallest focal size measurement with an au profile-coated mirror of 70 nm x 95 nm was performed with a horizontal profile-coated mirror and a vertically-focusing deterministically polished mirror (produced by an outside vendor).

1.2.3 Multilayer Laue Lens

In the late 1980's zone plates offered the highest x-ray resolution, primarily used as imaging lenses in microscopes. For a TXM, one zone plate is used to focus the radiation to the sample, and the sample is imaged by a detector in the far field while the sample is held in the focal plane. For a STXM, an extra condenser zone plate is used. It was widely accepted that intensity in these microscopes suffered due to the limited aspect ratios possible with fabrication methods available at the time. Several efforts[27-30] throughout the late 1980's to early 2000's worked on a MZP, which is produced by deposition of thin films on a rotating wire and are discussed above in the overview section of this chapter. This was a promising way to achieve arbitrary aspect ratios and extremely small outermost zones since the deposited wire and multilayer combination can be sectioned to any width and illuminated in cross section. All of these MZP attempts were met with some modest success[27,30]. This limited success was due mostly to fabrication issues. First, deposition techniques replicate the underlying substrate, which in all cases is an imperfectly round wire. Second, deposition on a wire necessarily means that film growth is normal to the wire surface over a small region, and becomes increasingly grazing incidence as the film grows on the outer tangents. This produces a roughening effect in the film which leads to unsatisfactorily rough interfaces.

In 1992, Maser and Schmahl[53] published theoretical work on a coupled wave description of diffraction through "volume zone plates". At the time, diffraction by a zone plate was explained by kinematic diffraction theory which assumes that the lens is optically thin. This was appropriate because zone plate aspect ratios were very small, and the lens appeared homogenous throughout the depth. The primary contribution of this work is description of local diffraction efficiency through a volume that is either "off Bragg" or "on Bragg" and this lays the groundwork for consideration of the first MLLs.

Multilayer deposition of a linear FZP structure on a flat substrate rather than on a cylindrical wire was attempted using helicon plasma sputtering as early as 1995 [54,55]. Ag/Al and Ti/Al linear FZPs with, respectively, about 190 nm- and 73 nm-outermost zone widths were deposited first, and then vertically sectioned. The polished slice then was glued to a germanium crystal. This duo of multilayer FZP and crystal operates in reflection mode as a combined monochromator and focusing optic.

In 2004, the Advanced Photon Source recognized that MLL may be an attractive replacement for nano-focusing optics in beamlines worldwide. A well organized effort was launched at the lab, beginning with a study on the effects of dynamical diffraction within thick multilayer structures. Two periodic multilayer structures were produced, one by Liu and Conley, et. al.[39,56] consisting of W/Si, and another by LLNL consisting of Mo/Si. The W/Si multilayer was produced in the APS large deposition system (described below) with a period of 29 nm and thickness of 6 μm. The Mo/Si multilayer had a period of 7 nm and a total thickness of 14 μm. These were, to our knowledge, the thickest multilayers produced to date. After deposition, the samples were sectioned using conventional TEM polishing techniques into several μm thick wedges and their transmission properties were examined at 12BM at the APS. These structures exhibited clear properties of Laue transmission where there transmitted beam intensity versus angle is symmetric around zero. The same team also extended the standard double-beam dynamical diffraction theory for crystals to the case of transmission multilayers and found that the reflectivity (or transmission coefficient) curves observed versus section thickness were well matched to the Pendellosung fringes. Since synchrotron experimentation with these periodic structures matched with theory, Maser, Kang[56], and others[57-59] developed a theoretical basis for nano-focusing optics based on dynamical diffraction with sectioned thin films. This work clearly describes the limitations of lithographically produced zone plates; namely, spatial resolution and efficiency, and how a depth-graded multilayer can overcome both. The most significant contribution of this manuscript is description of how tilting of the structure can increase efficiency by invoking dynamical diffraction for higher efficiency in the outermost zones.

Other theoretical research was devoted to detailing the effects of structural imperfections on the focusing performance of MLLs[60], focusing by high orders[61], and guiding the optimization of the MLL parameters for scanning x-ray microscopy[62].

1.2.3.1 The First MLL

A preliminary MLL was produced using the APS Large Deposition System by R. Conley and C. Liu using the W/Si material system[63]. However, Kang found that it was difficult to section[45] and also was susceptible to intermixing[64], inadequate adhesion, and accumulated film stress. Following the earliest attempt at APS with W/Si, a new structure was deposited with WSi_2/Si, a material system described elsewhere[5] for narrow bandpass reflective multilayers. In order to deposit this structure, an extensive re-write of the control system for the deposition apparatus was completed by Conley[65] in order to bypass the memory limitations found in the SX6 stepper indexer. This new control system was the first at APS to implement real-time scripting and parameter logging. Following successful sectioning by Kang, SEM images were taken but found to be difficult to analyze. Conley wrote a binary approximation algorithm in order to extract inverse d-spacing profiles of SEM images in order to provide feedback for subsequent growth. These images first appear in 2006[42]. Utilizing SEM analyses as feedback is successfully

demonstrated by Kang, et. al.[43] in 2006, where a focus of 30nm is measured at 19.5 keV with 44% efficiency. Two years later, the same group achieved a 16 nm line focus with 31% efficiency at 19.5 keV using an MLL with 5-nm wide outermost zone and a 13.3 μm lens aperture[41]. More recently, Koyama et. al. achieved 13 nm line focus using MLLs [66], Ruhlandt et. al. demonstrated the feasibility of producing a sub-10 nm x-ray focusing using an MLL with a ultra-short focal length of 15 μm at 13.8 keV [67]. Nonmetal-silicide systems, such as ZrO_2/Ti [68,69] and Al_2O_3/Ta_2O_5 [70], are being explored by the PLD method for soft x-ray applications.

The total aperture of MLL quickly hit a limit at around 13 μm when using the standard deposition processes. MLL much thicker than this were found by Kang to be difficult to section with film stress[63] as the expected culprit. Liu and Conley[71] designed an apparatus to bond two MLL halves together in UHV using a bakeout lamp and deposition of AuSn alloy as a bonding agent, however the propensity for the material to flow during melting resulted in unreliable bond widths.

1.2.3.2 MLL Sectioning

MLL sectioning, first reported by Kang[45], borrowed heavily from the TEM community by using manual polishing techniques and optical microscopy for section width determination. Film stress and mechanical properties made the procedure more difficult as MLL aperture gradually increased. Furthermore, the process was time consuming and labor intensive. An alternative technique, first proposed by Conley, utilized reactive ion etching (RIE) with multiple reactive gases, such as CH_4 and Cl, to etch the multilayer into "plateaus". When the etching process reaches the substrate, the procedure is complete. This technique was thought to produce higher quality MLL sections since no mechanical stress due to polishing and handling are imparted on the structure. Initial successes by Divan led to significant advancement by Bouet, who first reports successful etching[46] in 2010. Two patents have been filed by BSA Associates for this work. Unfortunately, the technique of RIE is necessarily always behind the latest MLL growth, so it was found that a final step using focused ion beam (FIB) milling produces the best sections.

1.2.4 Equipment

While work herein was performed on a multitude of deposition systems, it is worthwhile to describe two machines, in particular, due to their unique capabilities.

1.2.4.1 Rotary Deposition System

The success of the MLL project led APS to invest in the fabrication of a new deposition system intended specifically for MLL fabrication. The rotary deposition system[72], a custom system made by Denton Vacuum, Inc., is based around a 762 mm dia., 330 mm tall chamber with two 75 mm dia. circular magnetrons mounted horizontally and sputtering towards the center of the chamber as shown in Figure 1.8. Two horizontally-opposed magnetrons are mounted sideways so that flakes from accumulated film growth fall down and away from the target, minimizing the possibility of disrupting the sputtering process. The sputtering guns are encapsulated by an aluminum fixture upon which is mounted a figured mask for obtaining either film uniformity or some film thickness profile in the vertical direction (Figure 1.8). The aluminum fixture is then lined with aluminum foil to reduce flaking from the accumulated film,

as the thin aluminum foil flexes slightly with the accumulating film. It was found through experience that thicker growth buildup without flaking from the foil is achieved if the dull, rough side of foil is facing the cathode. A base pressure of ~$5x10^{-9}$ Torr vacuum is typically reached via a CTI-10 cryogenic pump, with the lowest observed pressure being $2.9x10^{-9}$ Torr. Process gas pressure is monitored with an MKS Instruments 627B Baratron gauge, and two methods for pressure control can be selected. Downstream control can be achieved by use of the VAT variable position gate valve. In contrast the more standard practice of using a vendor-supplied hardware PID system for process gas pressure control, the gas pressure value is used as the input variable in a software PID loop running on the system control computer. The gate valve is an infinite-position servo drive type, allowing for fast process gas pressure changes, if necessary. Upstream gas control can be achieved by setting the VAT gate valve to a fixed throttle set-point, controlling the flow output from the MFC into the chamber using the same software PID loop. Sputtering voltage, current, and process gas flow are monitored to provide an indication of target oxidation, outgassing, flaking events, or other fault events during sputtering. Substrates of various thicknesses are mounted in a vertical orientation on one of six facets available on a 200 mm dia. central drum and rotated back and forth in front of each gun for layer growth. The substrate-to-target distance is variable but typically fixed to ~70 mm, with a 15 mm wide sputtering flux shaped aperture discussed in more detail below. No electrical bias is applied, nor is active heating or cooling presently applied to the substrates; however, the substrate temperature rises slightly above room temperature due to the presence of the plasma and energetic ion bombardment.

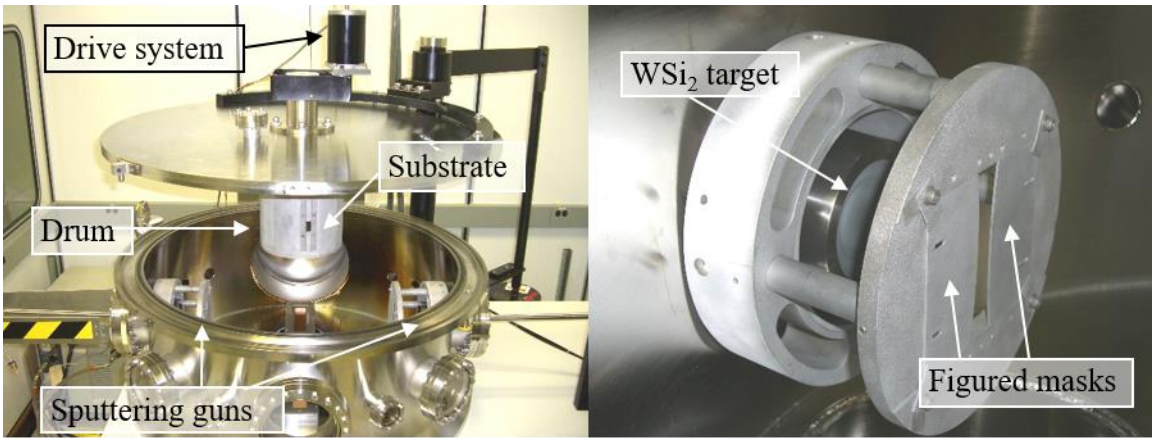

Figure 1.8: APS rotary deposition system and mask-holder and target with foil removed

A single layer of film is grown by first igniting the plasma long enough for the sputtering to stabilize while the substrate is sufficiently outside the deposition region. Fresh targets are "burned-in" by sputtering onto a blank plate or aluminum foil for 20 minutes. After exposing the system to atmosphere, 30 to 60 seconds may be required in order to sputter away the surface oxidation on a given target material or allow the sputtering flux and associated plasma region to remove water that has adsorbed on the surfaces within the chamber. The process gas flow volume per unit time that is injected within the chamber in order to maintain a constant process gas pressure will drop momentarily as these contaminants are freed from the component surfaces and contribute their partial pressure to the total system pressure. Once the contaminants are removed, the process gas flow volume will return to a steady-state. Seven seconds of initial start-

up time is typically used for layers grown after the first, although for thicker growths in other machines discussed later, this pre-on time has been reduced to 4 seconds. Once the plasma has stabilized, a single layer is grown by rotating the substrate past the aperture, exposing it to sputtering flux. Custom software controls design each loop over the sputtering gun to deposit as close as possible to 10 Å of film growth, or 5 Å per pass. The individual layer thickness requirement is then divided by the closest number of calculated loops to meet this thickness, and the drum angular velocity is adjusted as needed. As the required thickness changes, additional passes over the appropriate sputtering gun and drum velocity adjustments are handled automatically.

The thickness of a deposited layer is a function of drum angular velocity and number of passes over the sputtering gun; for uniform layer thicknesses, the drum velocity must be controlled precisely. The deposition system substrate drum rotation is performed by a Parker-Compumotor stepper motor and microstepping indexer. The microstepping indexer has an active-dampening electronic circuit to reduce stepper-motor oscillation. In order to avoid high-frequency oscillations in the drum velocity about its steady state value, the stepper motor is coupled to the drum rotary feedthrough by a zero-backlash nylon-impregnated timing belt from 2SPI with internal fiberglass tensile members and matching pulley system. The growth of uniform and lateral-graded multilayers is achieved through the application of profile-coating, described previously.

MLL deposited in this machine and the APS linear system with 728 layers of WSi_2/Si were characterized both at wavelength and via electron microscopy by Yan[73], et. al., who also developed a theoretical understanding of the impact of imperfections within the lens. Follow-on experimentation demonstrated a 16 nm line focus[41] at 19.5 keV using an improved lens, grown by Conley, with 1653 layers. This is the first MLL to require SEM metrology of more than one aperture, and the difficulties of accurate layer placement determination with an SEM lead to an investigation by Jahedi[74], et. al. Around the same time, Conley[38] described and experimentally verified a method to produce a wedged MLL, where each layer is tilted to the Bragg condition for both higher ultimate resolution and efficiency. This is the fabrication method that NSLS-II expects to eventually employ for the Hard X-ray Nanoprobe (HXN) beamline which is expected to see first light in 2014.

1.2.4.2 BNL MLL Linear Deposition System

In 2009, Conley reports on a new machine designed specifically for MLL deposition at Brookhaven National Laboratory. This linear deposition system[75] is comprised of five sub-chambers totaling 7 m long with four cryogenic pumps (Figure 1.9). Substrates are loaded in a vertical orientation on a linear-translation stage (referred to as the car) that moves one-dimensionally within the vacuum system, riding on a stationary base and rail assembly. An analysis chamber in the middle of the machine contains multiple ports intended for certain types of in-situ measurement and an ion-milling system. The ion milling system is a radio-frequency inductively-coupled plasma system commercially available from Kauffman and Robinson, Inc. however with a custom two-element vertically oriented strip optic to provide a pencil beam in the horizontal direction with good vertical uniformity. Adjacent to the analysis chamber is a large normal-incidence port with a laser-based curvature measurement system capable of deducing film stress[76] by direct substrate radius-of-curvature measurement. In order to surpass

current multilayer growth thickness limits, a procedure for automatic growth without breaking vacuum or perturbing the plasma with accumulated film flaking has been developed in which eight main magnetrons are used sequentially to grow each successive layer in the stack. This method proportionally reduces the total film growth per cathode by the number of available cathodes while at the same time providing a similar reduction in growth rate decay due to target erosion. This multi-cathode design also provides reduced magnetron thermal loading, and potentially the ability to grow a thicker multilayer before film accumulation on the shrouding starts flaking, which disrupts the growth. Four magnetron sources are mounted horizontally in-line on each door of the two gun chambers (Figure 1.9). For the fabrication of full MLLs where both halves of the structure are grown during a single deposition run, a ninth magnetron located in the landing chamber is intended for growth of a central zone compensation layer, which is described elsewhere[77]. The magnetrons use 75 mm dia., 6.25 mm thick targets with stationary magnets and direct-gas injection. Two 1 kW DC supplies with pulsing (Advanced Energy 1K coupled with SPARC-LE pulsing units) can energize any of the 9 cathodes through a custom RF power relay bank. A new high-stability power supply with fast arc detection and quenching from MSI-PE called the ION1500 has been implemented and used for all multilayer growth over the last couple years.

An advanced control system[78] was designed utilizing the platform-independent Python language and Nokia's user interface framework Qt. The system incorporates a text-based scripting language, threshold alarms, real-time feedback and control, a fully customizable user interface, mathematical functions, and a system console allowing for maximum operator control. All of the distributed subsystems have been successfully integrated, including the servo drive, laser-based curvature measurement system (MOS), heaters, gauges, and system interlock PLC.

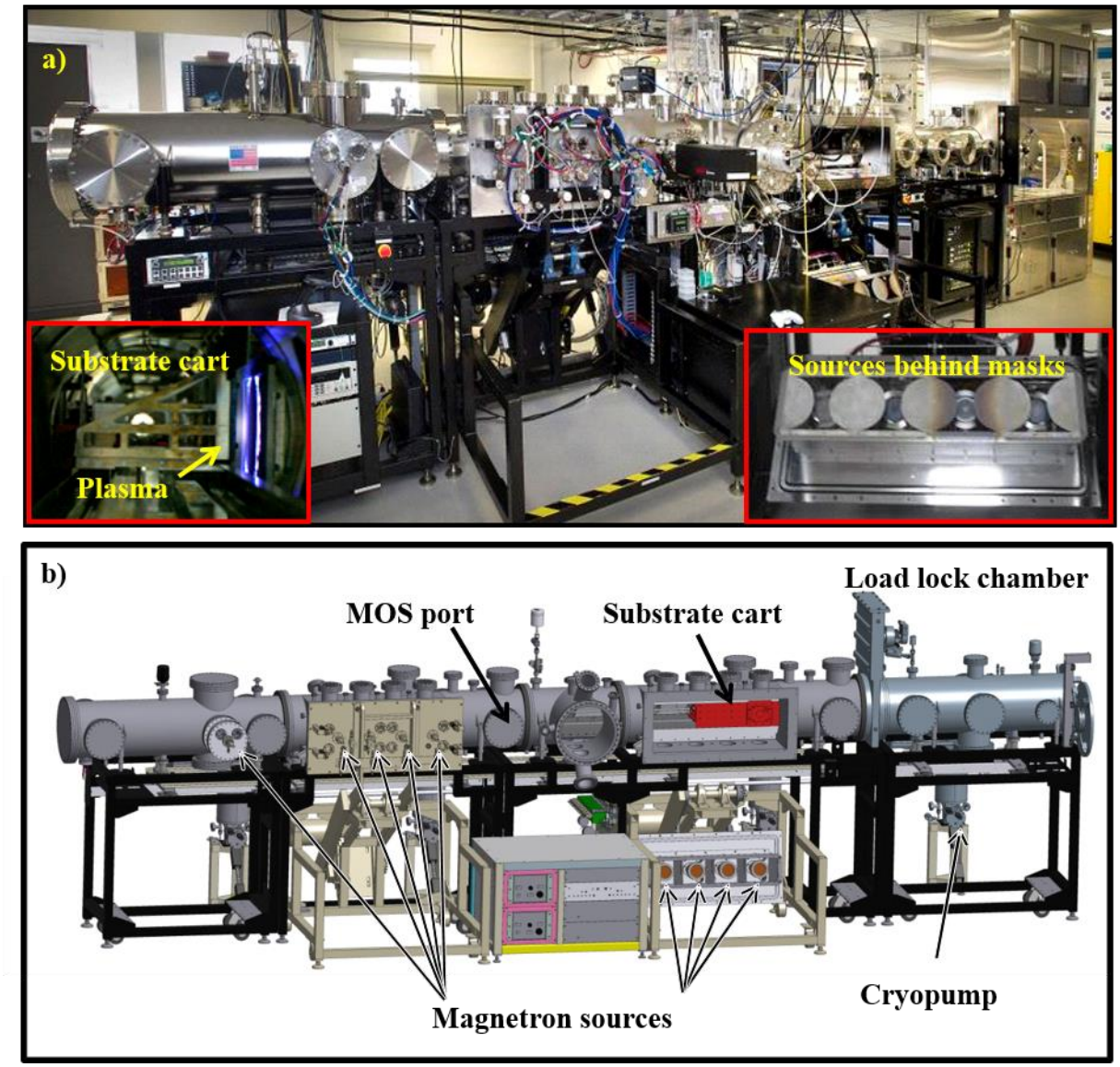

Figure 1.9: Multilayer deposition system. The red and blue cooling lines lead to the horizontally-oriented cathodes.

The mask assembly for each gun chamber (again, both chamber segments accommodate four cathodes each) is electrical-discharge machined out of a single sheet-metal plate and is attached to a mask frame in the shape of an "L" for rigidity. This mask and mask frame assembly is then positioned in front of the cathodes 2-10 mm away from the substrates by four poles that protrude through a flexible vacuum feed-through on gun door corners. These poles are attached to mechanical adjustment fixtures, which provide a small amount of travel to allow the entire mask to be both rotated and translated along all three axes. This freedom will allow the mask assembly to be aligned parallel to the direction of substrate travel, enabling all 8 guns to contribute properly to steeply-graded multilayer growth.

1.2.4.2.1 Linear Drive System and Base Assembly

The entire machine is based around a single apparatus; the linear substrate translation assembly. A one-piece, precision ground 440-series stainless-steel base plate of about 4.5 meters in length is supported outside the vacuum chamber walls through guide pins which attach to the steel chamber support frame via flexible bellows and rubber vibration dampers. This design allows the entire motion platform to maintain alignment and position without being subjected to vacuum chamber instability during numerous pump-down cycles and deposition runs. In order to further minimize straightness of trajectory errors in the linear drive system, the base rail contains multiple water lines (Figure 1.10) for temperature regulation that pass through the chamber walls. Water for this regulation circuit is supplied by a chiller with a temperature regulation specification of 0.01° C. Fixed to this base plate are two sets of recirculating ball guides with a full-length stationary linear motor magnet channel which is shielded by a high magnetic-permeability sheet metal, Mu-metal, to attenuate the magnetic field generated by both the permanent magnet track and the coils located on the transport. Since the use of an in-vacuum linear motor for a sputtering system (where the cathodes themselves are highly sensitive to external magnetic fields), a study[79] of total film thickness and uniformity difference was conducted. This study found that there is no discernable change in film growth when the stationary magnetic field from the linear motor is properly shielded from the magnetrons. A 20MHz optical encoder strip which provides a resolution of 50nm after interpolation is fixed to the baseplate behind a physical deposition shield. All metal-metal contact points are lubricated with Castrol Braycote 601EF, which is a PTFE dispersion in a perfluorinated polyether. The vapor pressure of this lubricant is specified by the manufacturer to be $4x10^{-13}$ Torr at 20°C. Braycote is used exclusively in place of more conventional vacuum greases for the various chamber o-rings as well. The drive system typical operating speed range is from 250 μm/sec to 230 mm/sec, with a maximum acceleration of at least 127 mm/sec^2. However, lower speeds and higher speeds are possible but as yet remain unused. More importantly, the substrate stage linear velocity at any speed and position over the entire travel length of ~4.3 meters was originally specified to have a maximum velocity deviation of less than 0.01%. As this is an x-ray multilayer deposition system where absolute layer deposition thickness precision (and thus flux dwell time) is the goal, uniform velocity is more important than positioning accuracy. Commissioning tests with a Renishaw RLE20 laser interferometer have shown that the linear motion velocity instability was held to within 0.0025% at velocities of up to 4mm/sec after proper motion controller tuning. Higher velocities could not be tested with the interferometer due to the limited bandwidth of the particular type of laser interferometer used. It was not practical to test the drive system while under vacuum, so it is also possible that some of the noise in this measurement was due to air turbulence within the cleanroom and chamber. This direct-drive linear motor allows for variable linear motion of hundreds of thousands of cycles per deposition, with the capability to program the motion system where any position must maintain an arbitrary velocity (within the maximum allowable acceleration limits) to allow for large area laterally-graded multilayer fabrication utilizing differential deposition, described below.

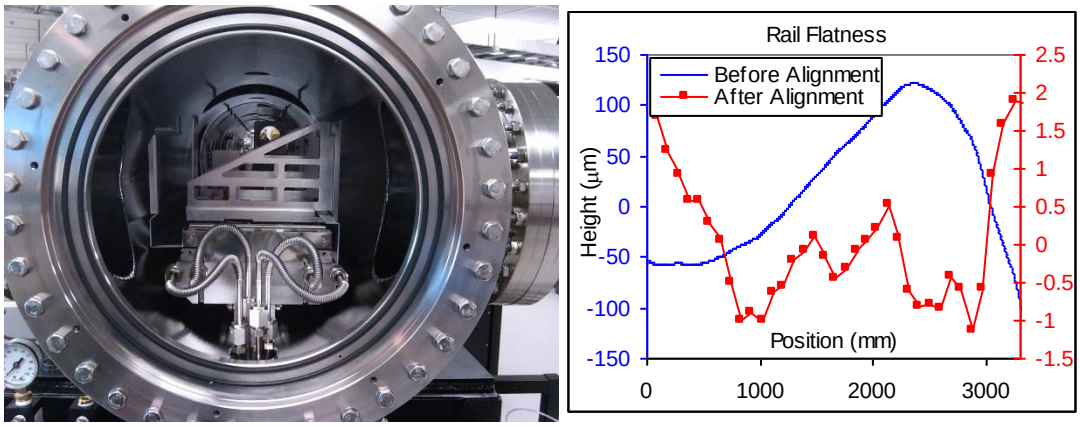

Figure 1.10: Side-view of the rail and transport. The rail water-lines and translator are seen on left. Rail vertical displacement before/after alignment is on the right.

A central design specification associated with the technique planned for wedged MLL growth with minimum layer thicknesses of approximately 1 nm (and focal lengths of as little as 1mm) is that the vertical trajectory path of the substrate must be kept to within 10 μm throughout the entire MLL deposition. This requirement places unprecedented demands on the translation system. The rail was aligned after installation in the vacuum chamber using a UDT Instruments V3700Q vacuum-compatible electronic autocollimator with a resolution of 0.01 arc-sec. By integrating slope error into height error, the rail was tuned after about 10 iterations by minor adjustments of the external support jacks to within +/- 1.5 μm of total vertical height variation over 3.5 meters as shown in Figure 1.10. Real testing of substrate vertical displacement drift during deposition must await x-ray focusing measurements with wedged MLLs.

Chapter 2: Reflective (Bragg Diffracting) Multilayers

2.1 Motivation and current status

The goals of the following two chapters are general in scope and topic, whereas the thesis work in this chapter is based on the ultimate requirements for beamlines at both the APS and NSLS-II, as well as perceived interest from the x-ray optics community-at-large. The expertise and facilities developed within the DOE national laboratory system for thin-film optics have garnered requests from multiple facilities wishing to utilize our optics at their beamlines. The topics presented here are based on what the community have requested. As such, one significant instrumentation task lie in bringing the laboratory facilities up to state-of-the-art standards and beyond through new equipment that can meet new challenges. The instrumentation outlined here, in part, is intended to explore most or all of the grand challenges for thin-film based x-ray optics that were identified in a report[80] by the community.

Reflective multilayers have been developed in the NSLS-II MLL Deposition System, however the design of that instrument and some initial results were presented in the introduction of this dissertation as background work. Therefore, further details on that particular equipment will be kept to a minimum throughout the rest of this chapter.

Reflective multilayer technology is currently limited by both intrinsic material properties as well as deposition system mechanics. The basic principles and background information were presented in Chapter 1 of this dissertation. The APS has a long history of producing thin-film coatings for a diverse set of applications. While coatings for user science experiments are very common, the majority of the applications are x-ray optics related. Some of these have very loose requirements such as single-layer metallization coatings on bendable KB mirrors, while others, such as specialized multilayers or profile-coatings are increasingly complex. Since 2006, the APS has had three deposition systems, each used for different purposes. All three employ fixed magnetron sputtering cathodes; two of these systems translate the substrate linearly with the third using radial substrate translation. The three machines have limitations or reliability issues which have been addressed with two replacement linear deposition systems and a proposed upgrade for the rotary deposition system.

The original “Small Deposition System” employed two upwards-facing cathodes and was used primarily for profile-coated[12] KB mirrors. Recently, a new dual-cathode linear machine was designed and constructed in-house as a replacement for this aging and failing system. The main purpose for this machine is profile-coating of flat, spherical, or cylindrical substrates with an elliptical figure for x-ray focusing. This work is described in the chapter on profile coating. The machine is also capable of depositing a limited subset of multilayer coatings; an example is discussed in more detail below.

The APS also has a rotary deposition system, where the cathodes point inwards or skyward and sputter towards a central rotating drum. This machine was the first machine built specifically for multilayer Laue lens (MLL) development[81]. Plans for an upgrade to the rotary deposition system will install a planetary within the chamber for substrate rotation. Linear cathodes that face upwards will then deposit through a chimney onto the substrates for intrinsically uniform multilayer coatings on substrates up to roughly 150 mm. The substrate

rotator has very low wobble tolerance, and must run in-vacuum with 100% duty cycle at 200 RPM. These requirements produced an interesting design which is detailed as a topic in this chapter.

The existing "Large Deposition System" is the oldest of the three and was originally designed for metallization coatings of large (up to 1.5 meter) synchrotron mirrors. All four cathodes sputter in the upwards geometry, with the substrates hanging from a trolley facing downwards. The APS, as well as the planned APS Upgrade, require high-performance multilayer coatings, multilayer Laue lens, as well as mirror figure correction capabilities. In order to meet these future needs well into the future, a new Modular Deposition System (MDS) was designed. The goals, motivations, performance requirements, and hardware are described as one topic in this chapter. The MDS, which is currently in the commissioning and calibration phase, will accommodate mirrors up to 1.5 meters long that translate on a precision stage across multiple chamber sections housing a variety of deposition sources, ion mills, or metrology instruments.

Periodic multilayers for various applications have been developed with the older APS equipment for a number of years[5,49,82]. The machines mainly use small cathodes, which requires layer-by-layer compensation. This is an extra step in the deposition process that is unnecessary with larger sources, but is well understood[65,72]. Tailored bandpass multilayers can be readily produced for an engineered bandwidth. Modern equipment, such as the BNL deposition system, the small system at APS, and the MDS utilize precision substrate translation mechanisms in order to maintain a well-defined substrate velocity profile over the deposition flux. This allows these machines to deposit lateral gradients in d-spacing by adjusting the velocity of the substrate while over the flux. At the time of this writing, however, no results from these particular instruments have been published. The fabrication process and performance of the first laterally-graded multilayer produced with this equipment are documented within this chapter. Lastly, new multilayer material systems for various applications and x-ray energies that have been explored with this collection of equipment are surveyed.

2.2 Experimental Topics

2.2.1 Three-stripe double multilayer monochromator for 2-ID-D.

A new three-stripe double multilayer monochromator (DMM) for 2-ID was designed and fabricated using the new small deposition system. Information about the substrates, multilayer coating, and performance are discussed here, while technical details about the deposition system can be found in more detail in Chapter 3. The main purpose of the DMM is to provide monochromatization of the beam with high intensity and larger bandwidth than a crystal. Three different multilayer stripes are used such that each stripe is optimized for a particular wavelength. In short, the incident beam diffracts through both multilayers; the energy that passes through is a function of angle and of the stripe that has been selected. When the angle is changed, one mirror also translates along the beam so that the second reflection occurs from a constant offset distance. By using two multilayers, energy can be changed without changing beam position. This is a standard technique. When a different energy is required, both optics are translated laterally to select the proper multilayer stripe. Because the incident beam is rather small (roughly 1 mm) and in order to keep costs to a minimum, the substrates and related stages and chambers should be kept as small as possible. For this reason, each stripe is limited to

roughly 10 mm in width. Table 2.1 provides the important parameters for each stripe, and a schematic of the substrates is shown in Figure 2.1.

Energy Range	Material System	D-spacing	M-silicide Thickness	# Bilayers
>20keV	WSi2/Si	21 Å	8.4 Å	250
<20keV	MoSi2/Si	25 Å	10.0 Å	250
<20keV	MoSi2/Si	33.5 Å	11.7 Å	140

Table 2.1: Parameters for the three-stripe double multilayer monochromator.

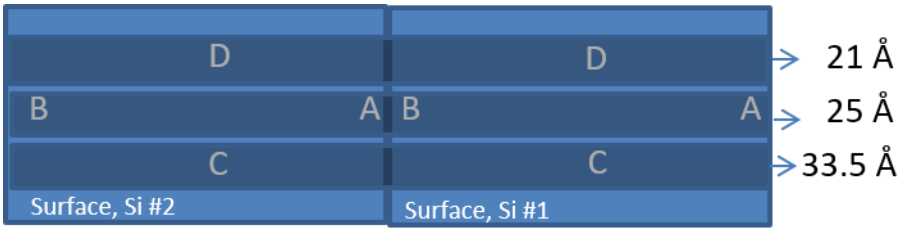

Figure 2.1: Schematic of DMM substrate pair. The alphabetic demarkations on the substrate schematic is used later to denote scan orientations.

First, substrate specifications and their impact on multilayer performance deserves some mention. The two main parameters that most effect the resulting optic are substrate roughness and figure error. In order to diffract sufficiently, multilayer interface roughness needs to be kept sufficiently low. Since multilayers tend to replicate substrate features, this implies that the substrate roughness also needs to be kept low, otherwise replication of high spatial frequency roughness within the multilayer stack will result in increased roughness. More details can be found in the literature[83]. The second metric, figure error, refers more to low frequency figure error and typically does not affect total diffraction efficiency. Rather, figure imperfections tend to impart features in the beam which lead to artifacts during imaging or blurring, in the case of focusing optics. Measurements of both surface parameters are shown separately.

Two super-polished silicon substrates with dimensions of 100 mm x 50 mm x 35 mm were used for the DMM pair. Prior to coating, the substrates were measured in the optical metrology laboratory for surface figure and finish information. A Micro-XAM Michelson Interferometer fitted with a 5x objective yielding a field of view of 2.44 mm x 2.44 mm was used to measure six random spots on both substrates. The results of these measurements yielded an average roughness of 0.095 nm and 0.091 nm RMS for both substrates. Surface roughness profiles are shown below in Figure 2.2.

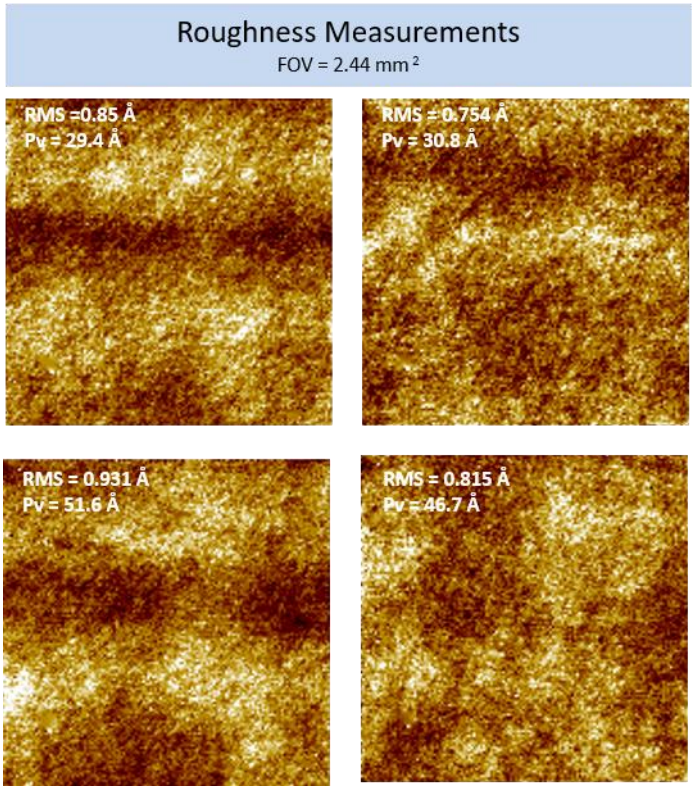

Figure 2.2: Examples of the substrate surface roughness profiles. Measurements were taken with a roughness microscope interferometer. Roughness values below 0.1nm are sufficient for multilayer use.

Among other equipment, two interferometers are available in the metrology lab for large surface figure measurement. Both were used to measure the mirror blanks. The first interferometer is an older 150 mm aperture Fizeau WYKO 6000 interferometer. The second is 100 mm aperture short coherence laser interferometer called a FizCam 2000 by 4D Technology. This instrument will eventually be outfitted onto the MDS instrument described later. The measurements had tilt and piston removed, but no higher terms. Both measurements indicate that the radius of curvature of the substrates is well above 20 km. As seen in Figure 2.3 below, the measurement results are generally similar in scale, however the WYKO measurement suggests the mirrors are slightly concave, while the FizCam measurements indicate that the mirrors are slightly convex. Discrepancies at this level of precision are common; an introduction to the challenges of equipment found in a state of the art synchrotron metrology laboratory can be found in the literature[84]. The upper range of measured height error found with this set of substrates is about 8 nm RMS and 50 nm P-V.

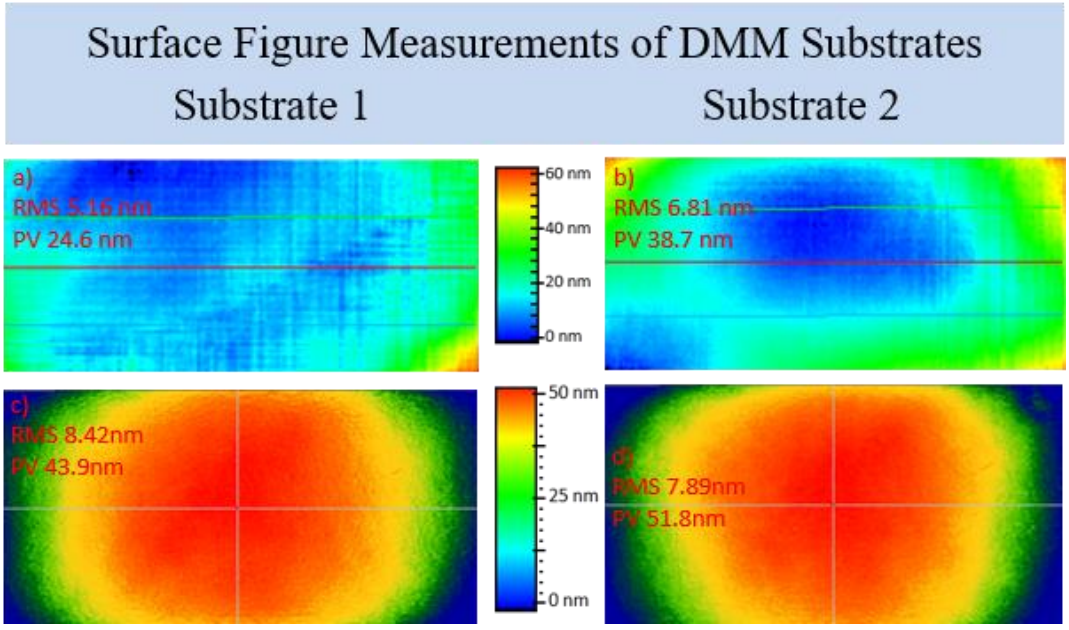

Figure 2.3: Surface figure measurements of two 100 x 50 mm multilayer substrates. Measurements were performed with two different interferometers. A WYKO 6000 was used to measure substrate 1 in part (a) and substrate 2 in part (b). Measurements taken with a FizCAM 2000 of substrate 1 is shown in part (c) and substrate 2 is shown in part (d). The results are similar in magnitude.

With the substrates characterized, the next step in the fabrication procedure is to calibrate the deposition system. Calibration involves, in part, extensive x-ray reflectivity measurements of trial multilayers. General background information can be found in Chapter 1, however two subjects that warrant detail here are how to determine individual layer thicknesses within a bilayer pair and the equipment used to perform x-ray reflectivity measurements.

X-ray diffraction is widely used in order to understand the structure and composition of multilayers. Although data fitting can yield a wide range of information including (but not limited to) interfacial roughness, density, optical contrast, and individual layer thickness, confidence in the results of such details is often subjective and reliant on accurate knowledge of the optical properties of the structure. When a multilayer (comprised of two or more materials) is fabricated, it is critical to extract the individual layer thicknesses, not just the bilayer pair thickness. Unfortunately, the bilayer pair thickness (or d-spacing) is the only information that is essentially independent of a-priori knowledge of material properties. A simple way to extract the individual layer widths from the total thickness of the pair of materials is to deposit two different multilayers, whereby with the pair the thickness of one (and only one) material has been doubled. Measuring the d-spacing of this matched set and subtracting one from the other yields difference between the pair, which can then be used to determine the thickness of each material assuming there is no chemical intermixing at the interface.

The reflectivity of the multilayers presented here were measured using either a tube x-ray source or beamline 1-BM at the APS. Details on the beamline can be found elsewhere[85]. Lab-based x-ray measurements were done using 1.54 Å wavelength radiation from a Cu anode tube

operating at 1.2 kW. The source size at the copper target is 0.4 mm wide by 12 mm tall, which provides a 42 µm wide source as used at the 6° takeoff angle. Two slits are mounted downstream of the source, the first at 140 mm and the second at 300 mm, set to 100 µm wide by 6 mm tall, and 120 µm wide by 6 mm tall, respectively. The radiation is monochromatized by a 3 mm-thick U-shaped <111> Ge monochromator located 410 mm downstream of the source, mounted inside a motorized adjustable enclosure. A computer-controlled filter box consisting of 4 sets of Al foil of varying thicknesses for beam attenuation is located at 800 mm downstream. Directly after the filter box is another slit set at 120 µm wide by 2 mm tall. During alignment, this slit is intentionally widened to measure the peaks of both Cu $K\alpha_1$ and Cu $K\alpha_2$ and then set into position to eliminate the Cu $K\alpha_2$ radiation. The sample under measurement is downstream of this third slit, mounted on a diffractometer with a motorized X-Y-Z stage. Upon this stage is a sample tilt stage mounted on large spring-loaded balls so the axis of tilt can be centered with respect to the sample. Mounted to the detector axis are two anti-scatter slits at 1300 mm and 1360 mm downstream from the source, respectively. The diffractometer has decoupled detector (2θ) and sample (θ) axes to measure specular reflectance while varying the grazing angle of incidence. The reflected X-rays were detected with a scintillation detector which has been electronically windowed to reject higher order reflected X-rays from the monochromator.

Initial calibration runs include optimizing deposition masking for uniformity and acquiring accurate deposition rate information with the calculation method and x-ray reflectometer described above. For the rate calibrations, fewer bilayer pairs are deposited on a small substrate to save time and material. In order to obtain matched coatings on both substrates, they are coated side by side. Once the deposition rate is calibrated accurately, coatings that span the full length of both optics are performed on small witness samples. These are measured and fit[86] in order to quantify, and then, compensate for the drift in d-spacing from target erosion. In order to sequentially deposit three different stripes on the same substrate pair, a slit mask is placed directly in front of the substrate with a 10 mm wide opening for the coating. Spacers are used to raise or lower the optic to the proper elevation for each stripe. The slit mask is seen in Figure 2.4, below.

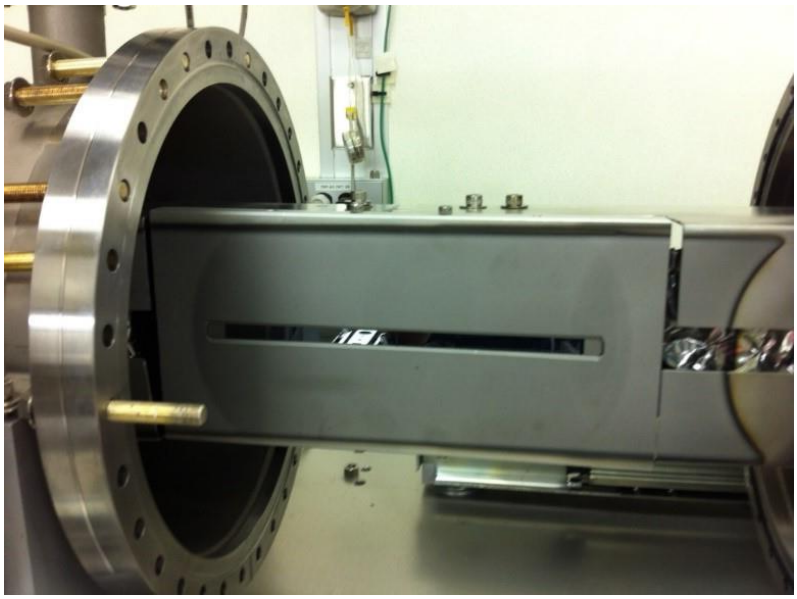

Figure 2.4: Photograph of the coated substrates behind 10mm wide slit. Residual shadowing of the uniform masks can be seen on the right-hand flux shield.

With all parameters calibrated, a full-scale trial coating was done on a super-polished Si substrate. The purpose of this trial run was to ascertain the effect on film uniformity due to the 10 mm wide shadow mask. Due to beam divergence and various growth-related effects the film thickness gradually decreases upon approach of the slit walls. This film thickness change was mapped at 1BM with a series of reflectance measurements on this witness sample at 8 keV using 0.25 mm steps along the “A” to “D” direction as depicted in Figure 2.1 above. Individual reflectance measurements were taken along the “A” to “B” axis according to Figure 2.1. As seen in the reflectance measurements in Figure 2.5 there is a significant variation in d-spacing for a large portion of the substrate surface.

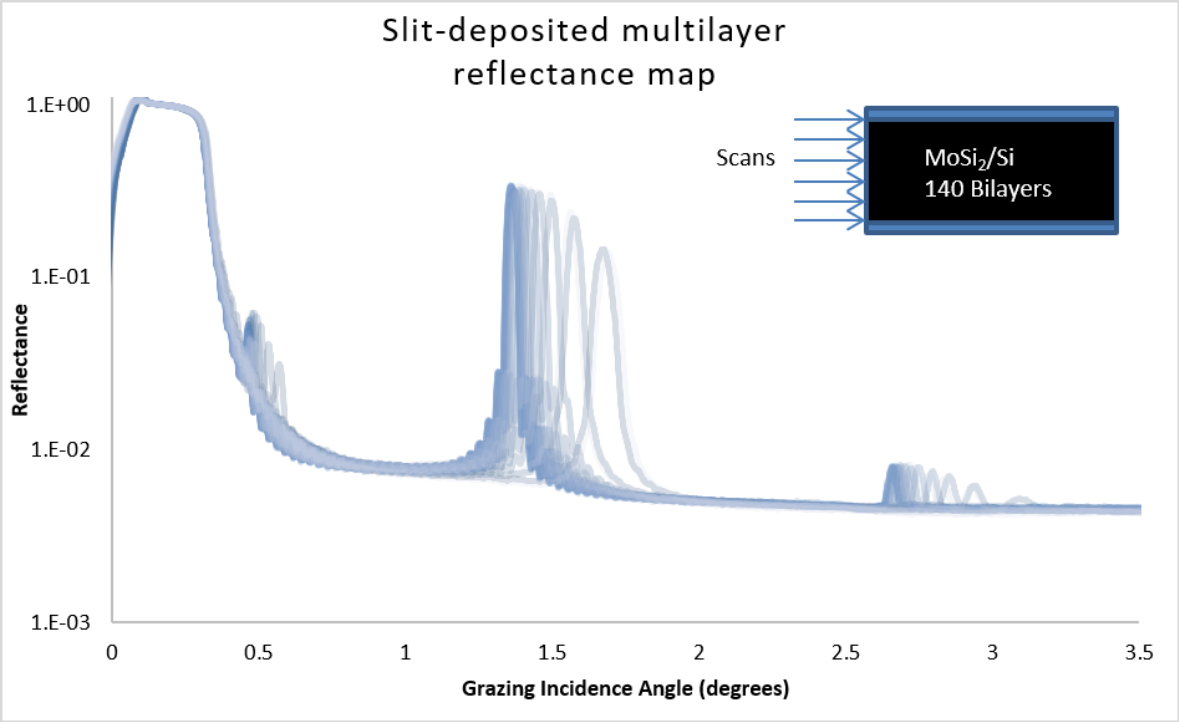

Figure 2.5: Reflectance measurements at 8 keV taken at 1BM. The inset schematic illustrates measurement orientation. Small peaks around 0.5° are from harmonic contamination.

The d-spacing exhibits significant reductions in thickness near the slit edges as would be expected. As seen in Figure 2.6 below, reflectance values across more than 5 mm are quite uniform, between 30 and 35%. The uniform region of the multilayer where the d-spacing stays within +/-0.5% is approximately 3 mm wide. This is shown in the bottom graph within Figure 2.6. The incident beam intensity to determine absolute reflectivity for these sets of measurements was only roughly estimated by averaging the intensity measured at between theta = 0.15 and 0.17 deg.

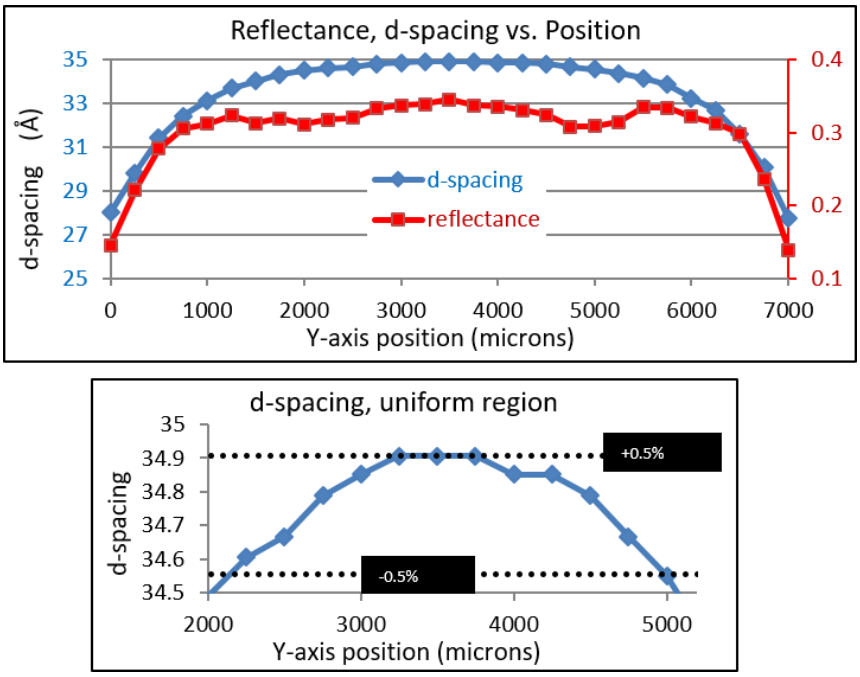

Figure 2.6: 10 mm wide stripe, reflectance and d-spacing uniformity. Data is from 1BM measurement in Figure 2.4, plotted as a function of position along the 10 mm width of the multilayer. The uniform region of the multilayer is 3 mm wide.

Although the stationary masks positioned in front of the sources produce a uniform coating on an unobstructed surface, the addition of the slit clearly degraded uniformity over the entire 10 mm width. In the future, the stationary masking should be modified to compensate for this. In any case, the incident beam is significantly smaller than 3 mm so the multilayer will reflect the entire beam. All three multilayer stripes were deposited on the substrates, seen in Figure 2.7.

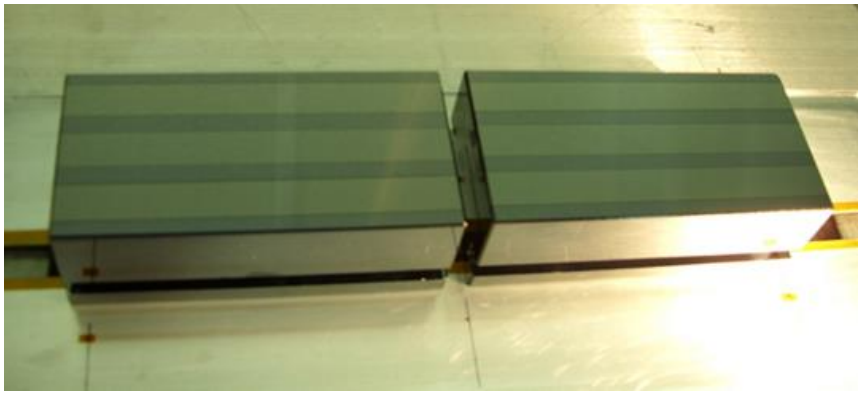

Figure 2.7: Final, coated DMM pair.

After coating, one stripe each was measured with the laboratory x-ray source described previously and simulated. The results are seen in Figure 2.8. Multilayer d-spacing was quite close to the requirements; the largest deviation was with the 33.5 Å stripe. This stripe was off by 0.05 nm in d-spacing, or 1.5%.

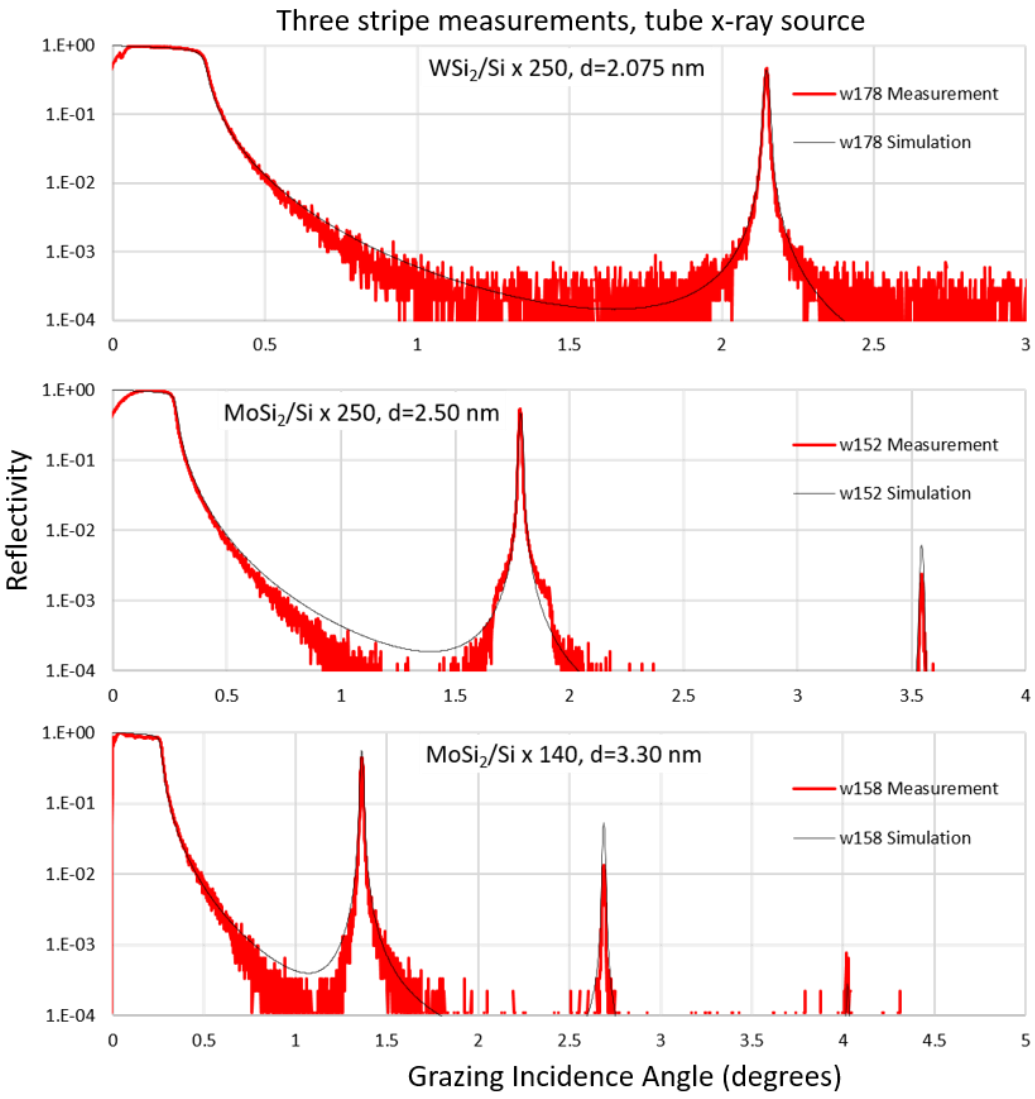

Figure 2.8: Laboratory x-ray measurements of the three multilayer stripes. The broad shoulders on 1st Bragg peak are artifacts from the lab x-ray instrument.

Finally, a series of measurements were performed at 1BM. Here, reflectance of the 33.5 Å stripe at 18 keV is shown in Figure 2.9. Significant Kiessig fringe oscillation suggests very high long-range order through the stack.

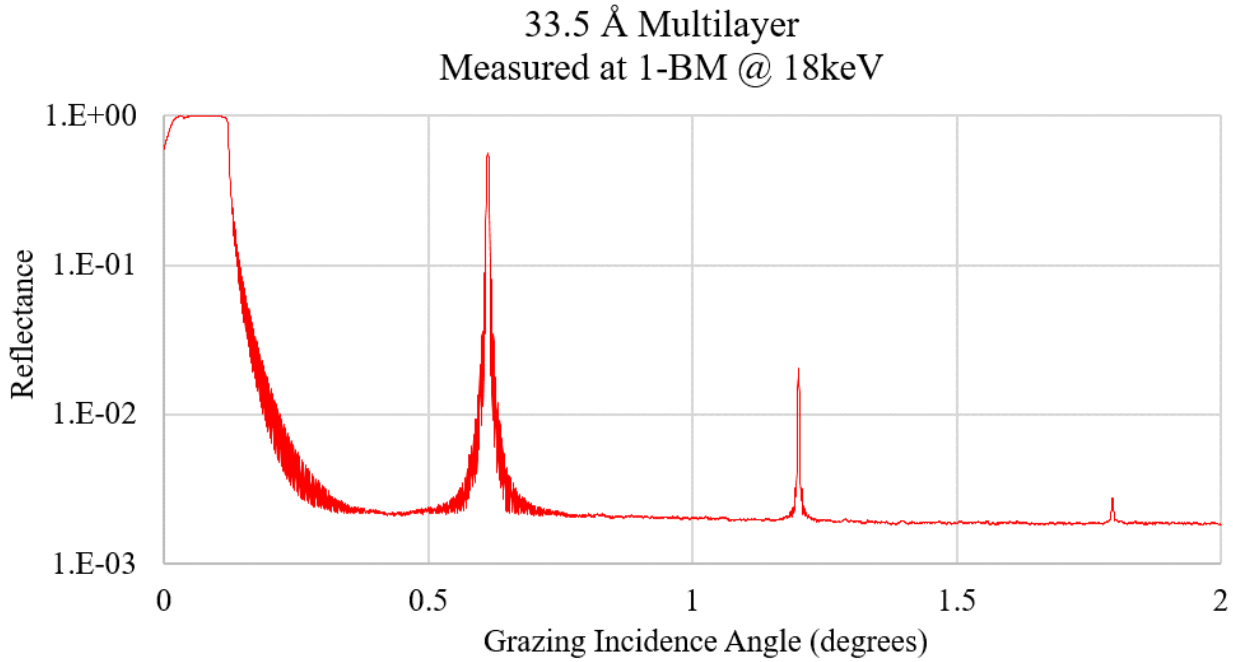

Figure 2.9: Measurement at APS beamline 1-BM of the 33.5 Å multilayer stripe. 1st order peak detail illustrates good thickness uniformity through the multilayer stack.

Lastly, Table 2.2 summarizes efficiency of all three stripes at specified energies. Due to the slight d-spacing non-uniformity caused by deposition through the slit, it would be expected that efficiency should drop as the incident beam size becomes wider. This is the case with the short d-spacing (21 Å) WSi_2/Si stripe. With a 0.5 mm wide slit, efficiency is 60%. When the slit is opened to 2 mm, efficiency drops to 37.4%. However, the same behavior is not seen with the other two stripes. This behavior is likely just a function of the multilayer bandwidth. As the bandwidth for the optic narrows, so does the tolerance for d-spacing variation.

Energy	D-spacing	2mm wide slit	0.5mm wide slit
22keV	21 Å	0.374	0.6
18keV	25 Å	0.778	0.784
18keV	33.5 Å	0.807	0.802

Table 2.2: 1BM Efficiency measurements of three stripes at two slit widths.

2.2.2 APS Rotary Deposition System upgrade design

The rotary deposition system was fabricated by Denton Vacuum, Inc. to APS specifications and design. The express intent for this machine is to address the challenges encountered in the growth of MLL optics, which are introduced in Chapter 1 and discussed in Chapter 4. The 330 mm tall, 762 mm diameter chamber is seen in Figure 2.10. Four sources are located inside the machine. Two are 150 mm long planar cathodes that sputter skyward. These were added to the machine much later, and will be used with the upgrade discussed here. The original two used for MLL deposition are horizontal, sputtering towards the center of the chamber. The horizontal geometry was chosen so that flakes from accumulated film growth fall down and away from the target, minimizing the possibility of disrupting the sputtering process.

Figure 2.10: Rotary Deposition System. The drum chamber rests on the controls cabinet.

Substrates are mounted in a vertical orientation shown in Figure 2.11(a) on one of 6 arms available on central drum and rotated back and forth in front of each gun for layer growth. The sputtering guns are surrounded by an aluminum fixture, as shown in Figure 2.11 (b), upon which is mounted a figured mask for obtaining either film uniformity or some film thickness profile along the vertical axis. The aluminum fixture is then lined with aluminum foil in an effort to minimize flaking from the accumulated film. A base pressure of ~5×10^{-9} Torr vacuum is achieved with a CTI-10 cryogenic pump. Process gas pressure is monitored with an MKS Instruments Baratron gauge. Process gas pressure can be controlled with either the variable position gate valve to throttle pumping from the cryogenic pump in downstream mode, or with a mass flow controller in upstream mode. The substrate to target distance is variable within

geometric constraints of the chamber and source neck. No electrical bias is applied, nor is active heating or cooling presently applied to the substrates.

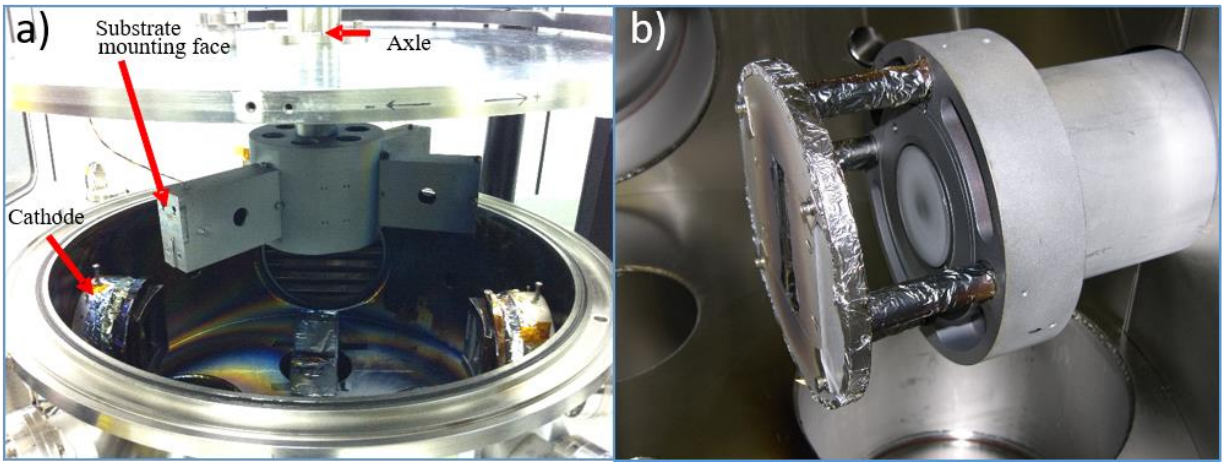

Figure 2.11: Horizontally-opposed guns and sample drum. The substrate mounting face is seen in (a). The round cathode with its aluminum foil cover removed is seen in (b).

A key parameter that guided the original design of this machine is that MLL substrates are physically small; wafer slices that are large enough to comfortable handle without requiring special tools or tweezers is the only requirement. Arbitrarily, MLL substrate dimensions were standardized to roughly 12.5 x 25 mm x several mm thick. Coatings were usually done in batches of six. This means that the hardware required to mount and translate the substrates could be extremely simple but with very high reliability. The few moving parts in a rotary geometry are attractive for long deposition cycle times required for MLL. While this design is appropriate for multilayer devices with a small footprint such as MLL, fabrication of larger optics with this geometry is difficult because film uniformity is only controllable along the vertical axis using figured masks. As the targets erode, the uniformity degrades as well. Also, because the flat substrates rotate along an arc, the target to substrate distance varies tangentially along the substrate. This generates a film thickness gradient along the axis of rotation. This limits the usefulness of this machine to only very small optics. A large proportion of multilayers, both for soft or hard x-rays, are laterally uniform and can be produced on 140 mm dia. or smaller substrates. In order to meet a large number of these needs for the user community and greatly expand the usefulness of this machine, two hardware upgrades to this machine would be required.

The first upgrade discussed is to the substrate translator and uses the planar cathodes. A technique for producing highly uniform film deposition which is commonly used in many industries is to rotate the substrates at a relatively high speed while they slowly raster scan across the deposition source aperture. By sputtering upwards through a chimney instead of horizontally and adding a “planetary” substrate rotation to the main axis, the rotary deposition system will be able to accommodate up to three 150 mm diameter (or smaller) substrates in a single deposition cycle. A robust design for this upgrade is presented here. The second upgrade adds multiple process gases and is more straightforward.

Several core principles and requirements drive the design. The upward facing planar cathodes are used, and substrates are mounted facing down. The substrates rotate in-plane. Rotating the substrate at a high speed relative to its source scanning speed can be used to produce uniform coatings without much regard for shaping the source. Also, the ability to precisely control both velocities and positions of both rotation axes will allow for programmable gradients, especially with radial symmetry. This secondary axis will be used to rotate the substrate at a high speed (about 200 RPM)

For this modification, the top cover of the vacuum chamber will be removed and modified to accept the new flanges and mounting hardware. The existing rotation feedthrough and drive motor are not used. The concept, shown in Figures 2.12 and 2.13, utilizes a main rotating platen upon which the substrate sub-axes are mounted for substrate rotation. The main rotation platen is mounted to a circular crossed roller bearing assembly and is driven externally by a servo drive (not shown). A nested ferro-fluidic feed-through allows the main shaft to contain a secondary inner shaft. The secondary shaft connects to a rotary drive system at the bottom of the assembly, in the vacuum chamber. The rotary drive is driven on the atmosphere side by a second servo drive. For the substrate motion during deposition, smooth velocity is critical to maintain high film uniformity. Transferring radial motion in a smooth manner is surprisingly complex. The rotary drive system uses a rotary roller pinion[87] gear system that allows the rotary motion to transfer to the smaller substrate planetary assemblies without the cogging action commonly found with conventional gear drives.

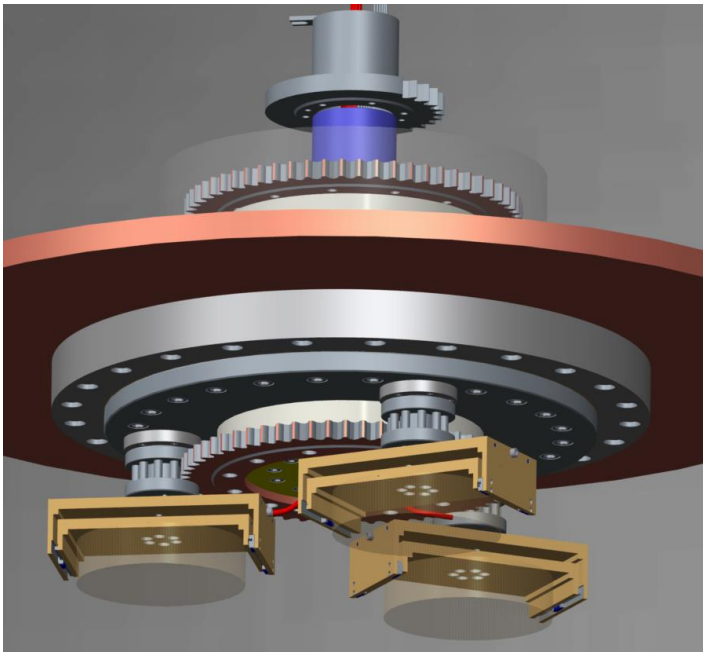

Figure 2.12: Rendering of the drive. Evident are the robust rotational bearings, three substrate platens, and the roller pinion gear drives.

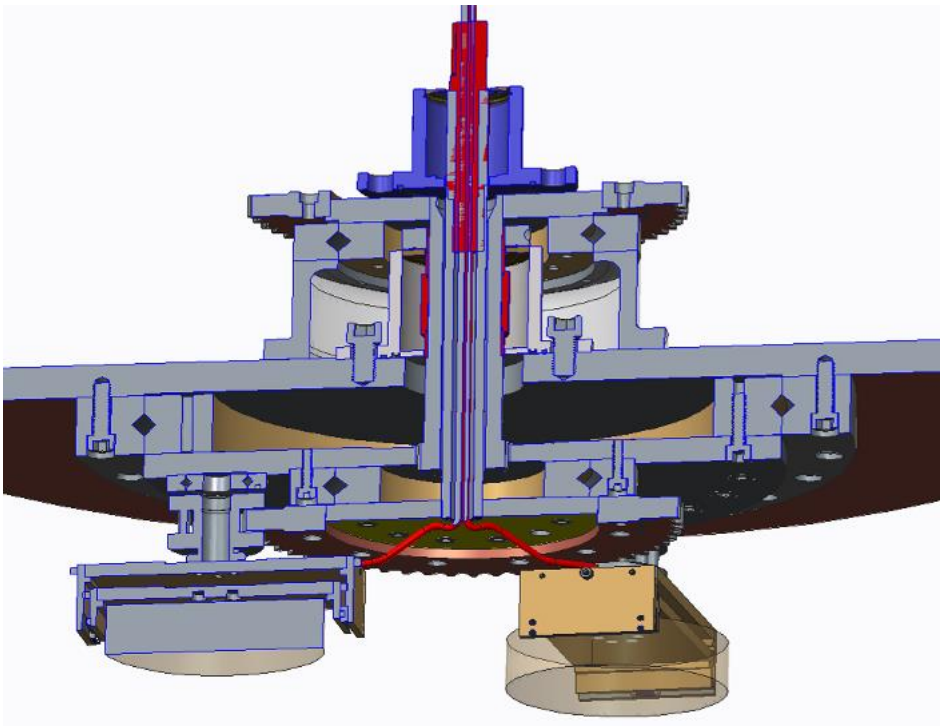

Figure 2.13: Cutaway of the internal planetary design for the APS rotary deposition system. The base above where the nested ferro-fluidic feedthrough is mounted to is the outer rotation axis. The substrate motor will be mounted to this surface. Roller bearing guides are used for all axes of rotation.

One critical specification to consider is the variability in film thickness caused by the change in substrate to target distance when the substrates are rotated in-plane. The real effect on film thickness of change in substrate to target distance is complex, but can be roughly estimated as:

$$\frac{f_1}{f_2} = \frac{{D_1}^2}{{D_2}^2} \qquad \text{(Eq. 2.1)}$$

Where the ratio of the film thicknesses $\mathbf{f_{1,2}}$ is proportional to the ratio of squares of the source distances $\mathbf{D_{1,2}}$. For reflective multilayers, the practical lower limit on optical bandwidth due to absorption and material related issues is around 0.1%. A rather stringent rule of thumb is to hold d-spacing precision within the multilayer to 10% of the bandwidth. This sets the allowable variation in film thickness that can be tolerated as 0.01%. With a typical lower limit for source to substrate distance of 70 mm, the design should attempt to keep the tolerance of the substrate plane variation to below 3.5 μm in the vertical axis. Because of this rather tight tolerance goal, the planetary design here has to employ highly rigid mechanical hardware throughout. As can be seen in the design, roller bearing and heavy duty recirculating guides are used for all rotating surfaces.

The second upgrade to the machine would add a process gas mixing system. Accumulated stress from a multilayer coating can distort the shape of optical elements which leads to blurring, focal expansion, artifacts, and wavefront distortion. One way to reduce film

stress is to use reactive sputtering. Instrumentation for reactive deposition to reduce stress have been employed in both of the new APS deposition systems as well as the BNL deposition system. On the other end of the frequency spectrum, the performance of small d-spacing multilayers for (especially) soft x-rays has been limited by material interfacial imperfections. It is possible that reflective multilayers for soft x-ray can benefit from new reactive sputtering techniques for reduced interfacial widths.

Reactive sputtering is a widely used technique, however it is worth mentioning that there are few, if any, other applications besides x-ray multilayer optics that have tighter requirements on deposition system stability, repeatability, and accuracy. It is worth noting to the machine designer that even fractional degree temperature variations in the laboratory[75] can have a noticeable impact on deposition rate due to instrumentation vulnerability. In order to allow the gas to mix and equalize thoroughly before injection into this machine, the easiest way to implement this system would be to add one new MFC for each desired gas species. The output from each species-specific MFC would blend into common plumbing, and the pressure in this gas mixing cavity would be measured. This pressure would be held to a constant value by altering the flow of each species-specific MFC to contribute their required partial contribution of particular gas species to the mix. This mixed gas can then be distributed into the chamber by the existing MFC.

2.2.3 Design new Multilayer Deposition System for the Advanced Photon Source

A new "Modular Deposition System" has been designed and constructed to replace the existing 20-year old large deposition system. The equipment consists of a 4.7 meter long linear substrate translator which is housed inside a vacuum chamber. This substrate translator uses a state of the art direct-drive in-vacuum servo system with velocity stability better than 99.9975%. An absolute optical encoder provides 5nm resolution over the entire length of travel. Encoder error is published as 5 μm/m. The machine model, shown in Figure 2.14, is 6.9 meters long including the load/lock chamber and can accommodate mirrors up to 1.5 meters in length. The design revolves around modularity and adaptability; where sources, metrology, or other instrumentation are easily changed or upgraded to adapt to future needs. The goals for the machine are not only to produce a wide variety of multilayer and other thin-film based x-ray optics, but also to allow the APS to initiate an ion-beam figuring (IBF) based mirror surface correction capability. Provisions for a dynamically-actuated aperture will be used to explore methods for 3-D multilayer deposition intended to enable the use of new optical geometries and allow for higher efficiency and mirror figure correction[88]. The core of this deposition system, the in-vacuum direct drive substrate translator, can be used both for in-situ stitching interferometry measurements of a mirror as well as for ion-beam figuring without separate processing cycles. Machine capabilities will come online in phases. Multilayer deposition will be the first priority for the machine, while the other features related to metrology, figuring, and the dynamic aperture will be brought online later as they are developed.

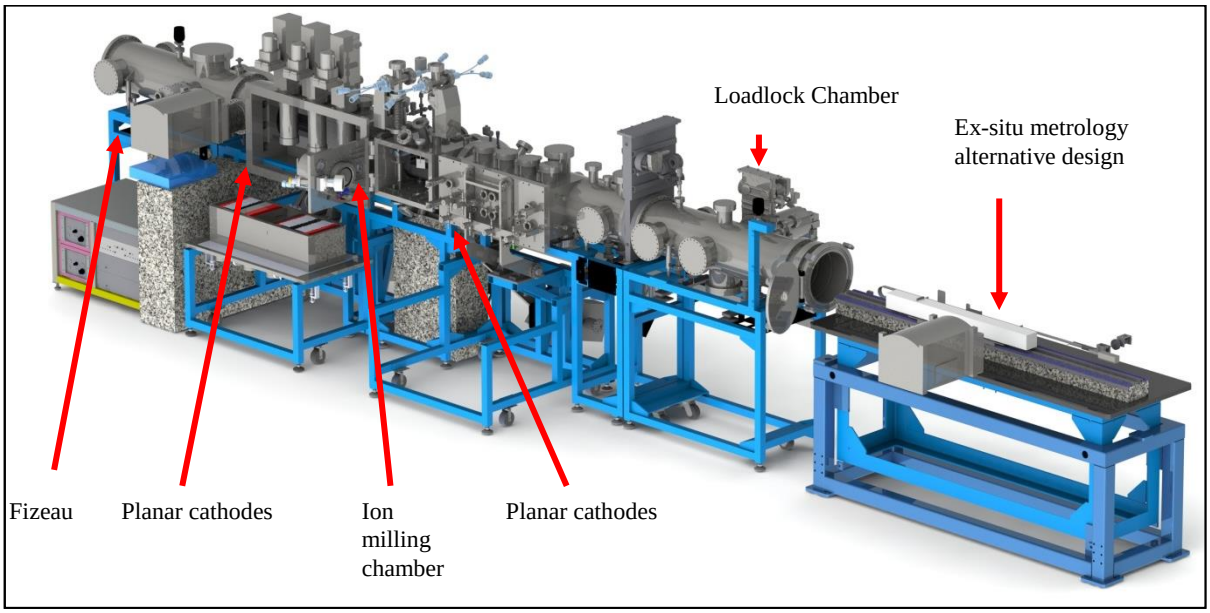

Figure 2.14: Model of the Modular Deposition System. Various components that are not part of the initial scope are included in the illustration.

The MDS has three distinct processing sections. The first section contains four round cathodes and is primarily used for single layer coatings, simple metallization, investigation of new materials, process development, or MLL deposition. The middle section shown in Figure 2.15 is designed around two ion mills; one with a 6mm focal size and another with a vertical "mail-slot" beam profile. The small mill will mount on a vertical translation stage while the larger mill will be stationary. These devices are mounted on a hinged door for easy maintenance access. The third chamber section houses three vertically-oriented planar cathodes approximately 250mm in length. Adjacent to this (left-most chamber section in Figure 2.14) is the landing chamber. The landing chamber provides clearance for the substrate translator to scan the entire length of a large (up to 1.5m) substrate past the planar cathodes On the landing chamber also resides a port for the addition of a 100mm interferometer intended to be used for stitching measurements of large, flat mirrors. Design details of the complete in-situ stitching apparatus are not yet mature, and the performance of in-situ measurements relative to ex-situ measurements is somewhat unknown. Because of the large investment in the MDS, an alternative method for measurement has been designed that utilizes an automated load/unload step to allow the mirrors to be measured outside of the chamber, at atmosphere. The linear translation table for this "backup plan" can be seen on the right-hand side of Figure 2.14.

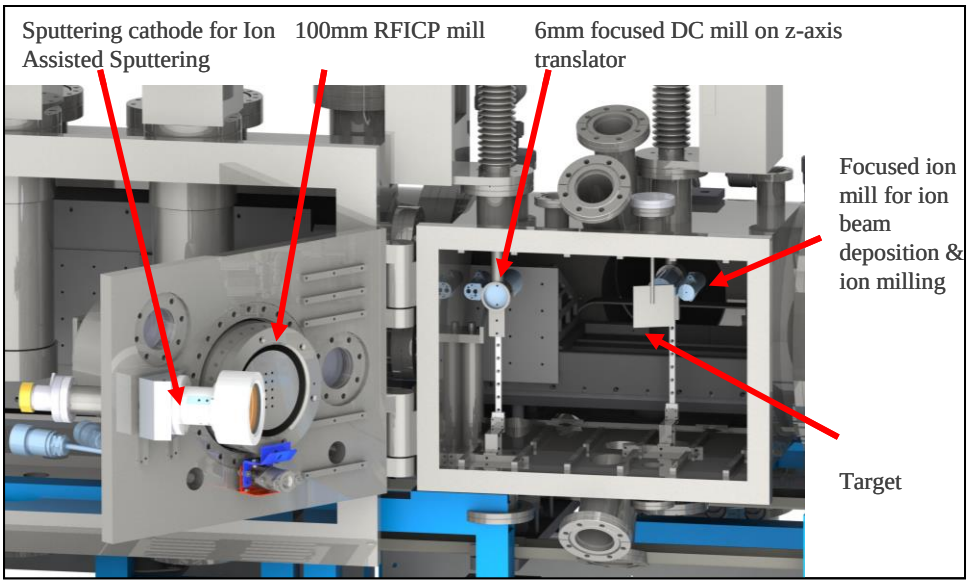

Figure 2.15: Model of the ion milling chamber. Ports to utilize specialized deposition techniques such as ion assisted sputtering are available with the machine.

Individual mass flow controllers (MFC) inject gas directly behind the dark space shield for the cathodes. Each MFC is fed from a selection of mixed gases. Process gas pressure is controlled through any combination of automatic or fixed set points between the variable position gate valves in front of each of the four CT8 cryo-pumps. All the cathodes connect to a high-power relay bank for power distribution. As it is currently, the machine can accept up to 4 different sputtering power supplies. A photograph of the instrument shortly after assembly is seen in Figure 2.16 below.

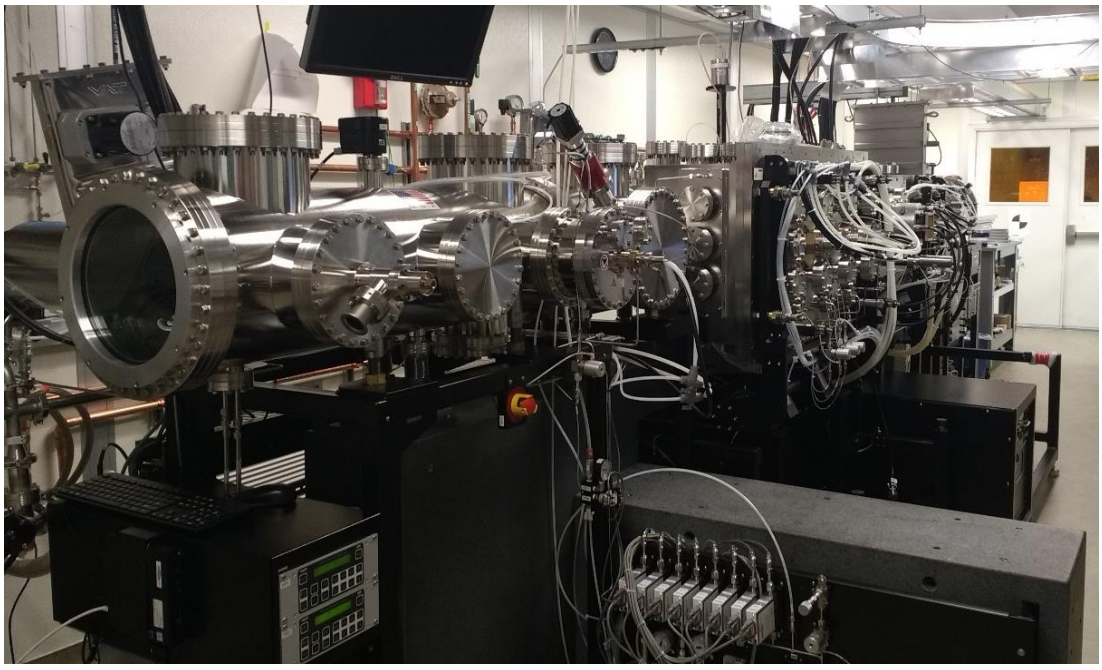

Figure 2.16: The APS Modular Deposition System.

The surface figure shape and precision of optics directly impacts their performance. Synchrotrons, high-energy density laser systems, EUV lithography equipment, and astronomy instrumentation are all limited in some way by the quality of available optics. State of the art mirror figuring techniques include ion-beam figuring, elastic-emission machining, deterministic polishing, and magnetorheological finishing. All of these systems operate in an iterative fashion whereby mirrors are measured off-line in order to generate a correction map, then the figures are corrected with the preferred technique. This process is repeated multiple times until the mirror shape is within the required error budget.

While the figuring technique can be fast, throughput is universally limited by the steps involved with transferring between the processing setup and the measurement setup. Furthermore, most industrial applications physically separate their "open-air" metrology stations from the surface figuring instruments. In particular for ion-beam figuring, significant dwell time is needed for the processed optic to adjust to new ambient conditions when switching between processing and metrology. Figuring performance can also be affected by switching between two separate processing and metrology stations because registration errors between the two steps can accumulate; this is even more prolific when fiducial markings cannot be used and the mirror edges are ambiguous.

In a typical Fizeau interferometry application, a transmission flat (TF) serves as the reference flat. A spherical or flat wave-front passes through this transmission flat in order to reflect off of the surface under test (SUT). This reflected wave-front is collected by the interferometer and processed in order to produce a surface map that is used for figure correction. This is called a two-surface cavity measurement. Insertion of extra optical surfaces into the measurement system, such as a vacuum window, will create aberrations, especially if an off-axis interferometer is used. Furthermore, the reference flat requires precision tip and tilt adjustment and must be rotated in order to perform the most rigorous reference flat error subtraction, called a "three-surface test". Another issue that has been found in certain cases to cause measurement instability is ambient humidity. The hydrophylic nature of antireflection coatings on transmission flats creates surface film stress that fluctuates with humidity, adding curvature to the flat.

These issues are potentially avoided by utilizing a first transmission flat as the vacuum window in order to eliminate refractive index variations within the optical path, and then placing the real transmission flat remotely, in the vacuum system. A new UHV optical gimbal has been designed and built that provides the requisite tip, tilt, and rotation in order to adjust the flat remotely while still accommodating the three surface test. An on-axis interferometer with a tunable cavity length is used so that vacuum pressure on the first flat does not impose aberrations in the wave-front. Barometric pressure changes due to weather conditions can be eliminated or minimized through deployment of an interferometer and window enclosure that maintains a slight overpressure relative to ambient.

The experiments presented here study the effect of a vacuum chamber window (VCW) and were carried out in the APS metrology laboratory. The VCW was intentionally chosen for its particularly curved surface. For these experiments, the 100 mm aperture FizCam 2000 is used to measure the surface of a 100x20x20 mm^3 Si mirror as the SUT. The simulated VCW is a second transmission flat. Two types of measurements are performed. The first is a baseline system repeatability test during conventional use. The second gauges the effect of tilting the VCW

relative to the mirror surface in order to simulate the impact of adding an extra optical component into the measurement path.

A set of 5 stationary measurements were taken in 1 minute increments for 2 scenarios: setup with VCW and setup without VCW as illustrated in Figure 2.17. For each measurement, a single line profile was extracted from the surface plot along the center of the SUT. Difference subtractions of this series of line profiles in Figure 2.17 shows basically the same magnitude of system drift between both configurations.

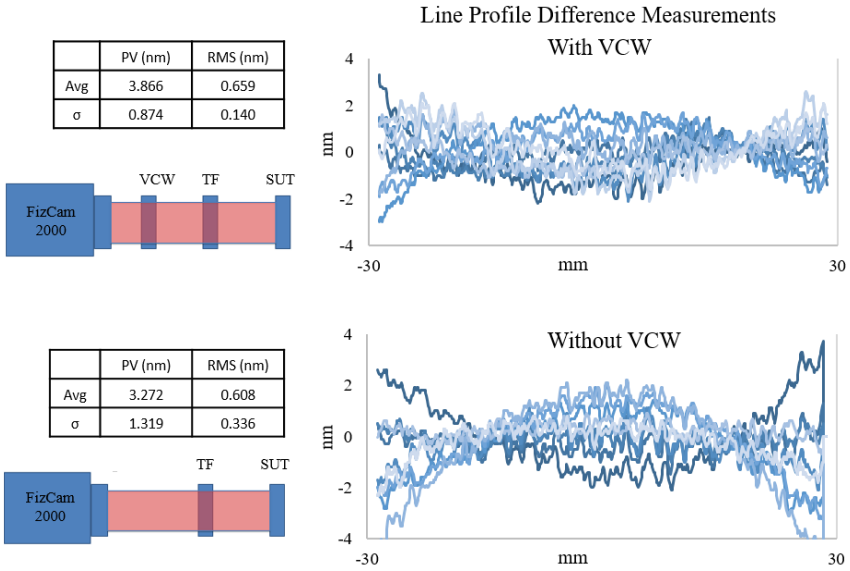

Figure 2.17: Schematic of stationary setup with and without VCW inserted in the optical path. A series of 5 static measurements were taken at 1 minute intervals. 10 difference subtractions of each series are plotted. Overall magnitude of the measurements was very similar. Variation is likely dominated by environmental turbulence such as thermal drift.

The front face of the VCW is flat to less than 20 nm P-V, while the specification for the rear face is about a factor of 4 worse. In order to estimate the effect of tilting or warping of the VCW when inserted in the optical path, a series of measurements were taken with the VCW facing both forward and backward while rotating the VCW from 0° to 1.81° with a step size of 0.36°. A schematic of the configuration along with the difference subtractions of the line profiles are in Figure 2.18.

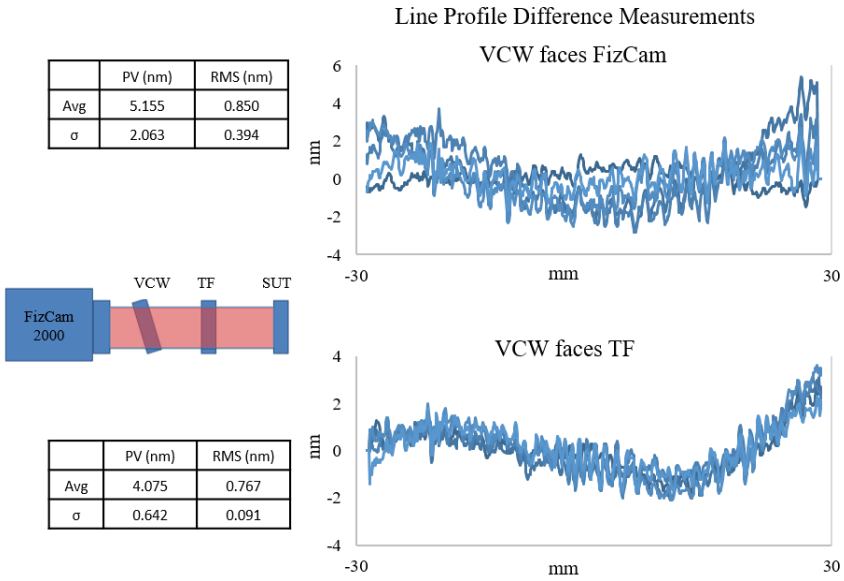

Figure 2.18: Axis of rotation schematic and test result. Difference subtraction measurements were taken when the VCW is facing the FizCam and also facing the TF.

While an obvious shape can be discerned by eye in the tilt subtractions, their magnitude of statistical error is quite similar to the stationary measurements. This indicates that tilting the VCW does not induce measurable difference that is above the stability level or noise floor for the instrument or environmental conditions. This preliminary finding suggests that measurement through a VCW with an on-axis, short coherence interferometer is possible.

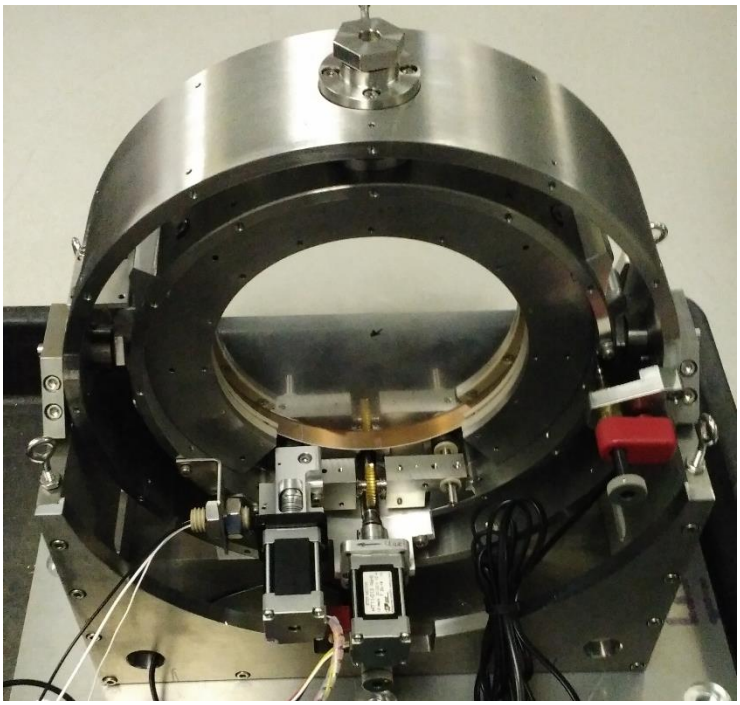

Figure 2.19: UHV Gimbal for *in-situ* interferometry measurements.

In order to implement in-situ metrology, a UHV gimbal shown above in Figure 2.19 was designed and fabricated. This gimbal suspends the TF within the vacuum system. The gimbal has motorized tip/tilt, and a lift-rotate function. The motorized tip/tilt is currently implemented with UHV picomotors and Renishaw absolute encoders providing 1 nm of resolution. This resolution translates to ~10 nanorad angular resolution, however actual angular stability of the system will be a factor of many things including motor step size, system temperature gradients due to localized heat generation, and mechanical stiffness. The TF is normally suspended by a flexible steel band within the inner yoke. The purpose of this band is to evenly distribute weight and avoid distortion due to point forces. When the TF needs to be rotated for reference subtraction, a set of axles brings a pair of wheels together horizontally, which lifts up the TF on the wheels. A third encoder that is adhered to the perimeter of the TF provides angle information.

2.2.4 Multilayer fabrication from 175 eV to 80 keV

The techniques and equipment described in this dissertation can be utilized to produce high quality optical coatings that can be used for a broad range across the optical spectrum. Hard x-rays interact very weakly with matter. This means that absorption is very low and a large number of bilayers can contribute to a reflection. However, the angle of incidence is proportionately decreased as wavelength decreases resulting in physically large reflecting mirrors. In order to reduce the size of the mirror, small d-spacings are required. While multilayer d-spacing can be reduced, the width of the interface between each layer can be considered to be roughly constant. This means that interface imperfections and roughness make up an increasing percentage of the entire stack as the bilayer thickness drops, contributing to performance degradation. Multilayer material systems for hard x-rays are typically chosen based on optical density contrast and their propensity to produce small interfacial widths. Common materials systems combine a very dense metal with a spacer, such as W/B_4C, W/Si, and so on. An example of a typical multilayer used for hard x-ray monochromatization is discussed in Experiment 1 of this chapter. On the other end of the spectrum, soft x-rays interact with matter much more strongly than shorter wavelengths. One challenge in the design of multilayers for these energies is to identify material systems that provide both high contrast and low absorption. The majority of the most appropriate material systems contain materials that are reactive to varying degrees. This greater reactivity poses more challenges in order to maintain sufficiently low layer inter-diffusion and roughness. Many material systems identified for soft x-ray applications are based on lanthanides (or materials chemically similar to them), such as Cr/Sc, La/B_4C, Mo/Y, Mo/La and so on.

Optics for three different applications are presented here. The first set of multilayers target the energy range from 175-400 eV and are intended for high energy density plasma imaging. The next application is intended for beam steering diagnostics at 510 eV. The third multilayer, for focusing at 80 keV, features a precision thickness gradient that was produced by velocity profiling.

2.2.4.1 Multilayers for High Energy Density Plasma Imaging

Most light sources around the world accommodate experimentation utilizing soft x-ray wavelengths (from perhaps 100 eV to a several keV). A wide variety of instrumentation has been implemented in the solar astrophysics community based around these wavelengths for examination of coronal activity. Another application for multilayers in the soft x-ray regime lies in petawatt-class laser research[89]. There are many unanswered questions as to how the laser target (specifically, fuel pellets) disintegrate at the instant after energy injection. Soft x-ray multilayers tuned to particular energies can provide a snapshot of the target at well-defined times (or, more precisely, temperatures) immediately following a laser shot.

Multilayers for use within a range of energies from approximately 175 to 400 eV were produced as part of a collaboration for high energy-density laser studies. These studies (the details of which are outside the scope of this dissertation) aim to understand the physics of fusion fuel pellets in the short time scales directly after the point of ignition. As the pellet is irradiated with laser energy, the temperature increase corresponds with a proportional increase in x-ray emission energy. Chromatic optics allow imaging of the corresponding x-ray emission only at

well-defined wavelengths due to their narrow bandwidth, which results in the ability to image the source at specific points in time following ignition. The material systems Cr/Sc and VSi_2/C were identified for testing based on simulation results. Multilayers utilizing these elements were also deposited in the BNL deposition system; x-ray reflectance measurements at 8 keV are shown below. Figure 2.20 shows a measurement of the commonly used Cr/Sc material system. Estimates from simulation indicate reflectivity in the 8%-12% range at 175 eV, depending on interfacial roughness. Figure 2.21 introduces a new material system comprised of VSi_2/C. Reflectivity estimations at 175 eV are similar to Cr/Sc.

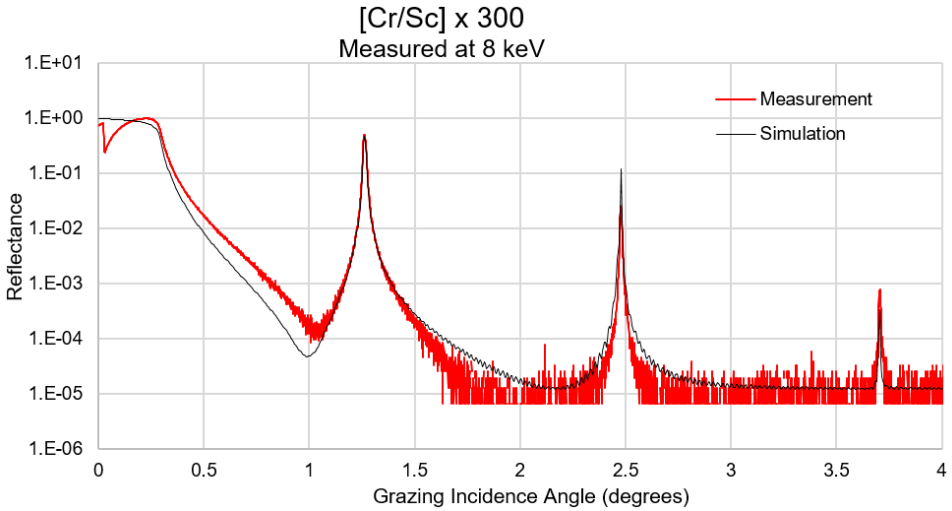

Figure 2.20: Cr/Sc, d=3.59 nm x 300 bilayers, a commonly used material system. Estimated to reflect abut 8-12% at 175 eV, depending on various expected interfacial roughness situations.

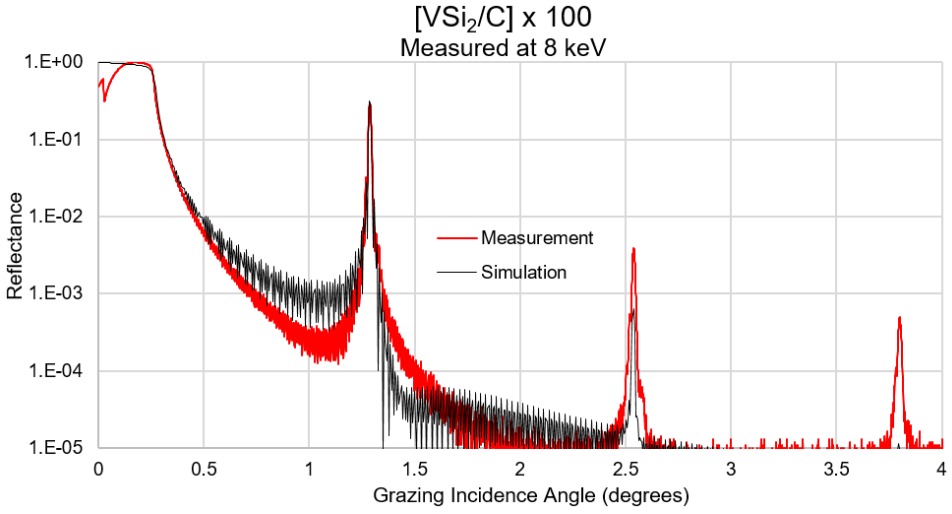

Figure 2.21: 100 bilayer VSi_2/C multilayer reflectivity measurement at 8 keV. With R=30%, simulation indicates interfacial roughness of 0.4 nm. This material system was measured at 150-300 eV, with normal conditions (roughness 0.3 nm) estimated to provide high reflectance in this range.

A series of multilayers with both of these material systems were produced to reflect in the energy range from roughly 170-394 eV, and at either near-normal incidence or at 45 degrees. Measurements performed by collaborators at beamline X24 at the NSLS on a subset of these multilayers are shown in Figure 2.22. Although some of the optics were designed for use above 300 eV, only measurements in the range shown were obtained. Cr/Sc indeed performs satisfactorily, however VSi_2/C universally exhibited poor performance. This poor performance is primarily attributed to high interfacial roughness due to non-optimized deposition conditions.

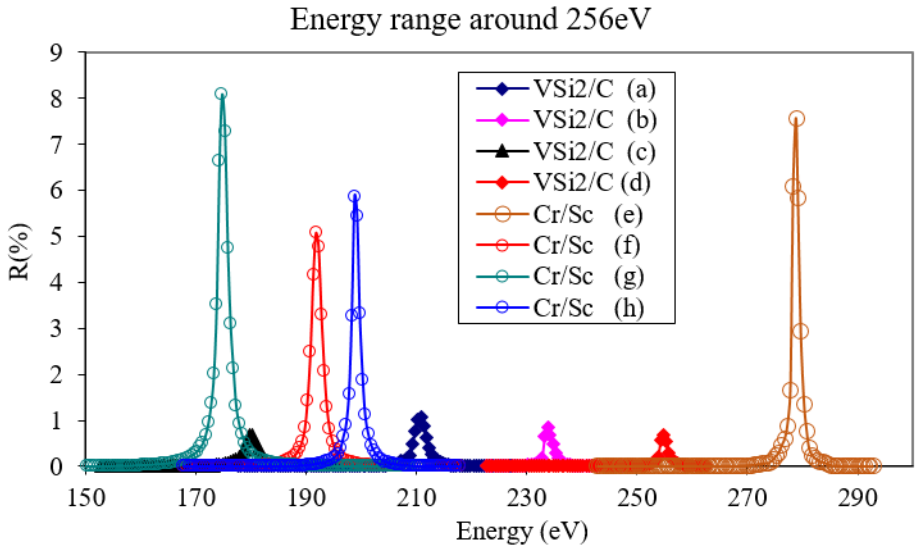

Figure 2.22: Beamline reflectivity measurements at 150-300 eV. The VSi_2/C ML "C" should theoretically have reflectivity of around 3-4% @ 180 eV/85° and 256 eV/45° when extrapolated from the 8 keV measurement and simulation concerning interfacial roughness of 0.5 nm. The combination of the rather large roughness in the hard x-ray measurement and the 3x factor reduction in the soft x-ray measurement indicates that even though the deposition parameters may not have been optimized this is still not a good material system choice for this energy range.

2.2.4.2 Multilayers for Storage-Ring Beam Diagnostics

The next application presented here came about due to a need for beam diagnostics at 510 eV. The NSLS-II storage ring is ideally suited for soft to medium x-ray energies, with world-class brightness up to about 10 keV. In order to commission and align beamlines and optics easily, a multilayer version of a device for beamline characterization[90] was proposed for several of the NSLS-II beamlines. This is a very simple apparatus consisting of a multilayer Bragg reflector which is inserted in the direct beam in order to reflect radiation out of the vacuum system and onto a simple imaging detector. Multilayers tuned to 510 eV for this effort were produced using the V/B_4C and Co/V material systems. These multilayers presented a challenging d-spacing due to the need to reflect this rather short wavelength at an incidence angle of 45 degrees. A V/B_4C multilayer measurement at 8 keV is shown in Figure 2.23.

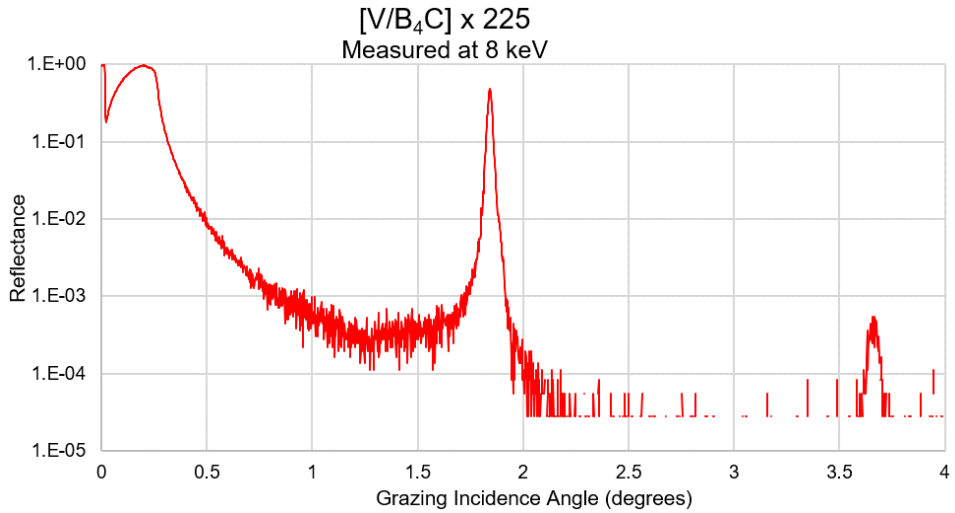

Figure 2.23: V/B_4C x 225 multilayer measurement at 8 keV. D-spacing=2.4 nm. The 1st order Bragg reflection is 47.6%. This extrapolates to roughly 10-20%reflectance at 510 eV at 30.5 deg. angle of incidence.

A second material system, Co/V, was also identified for 510 eV. After growth rate calibration, multilayers were deposited onto flat silicon blanks using both pure Ar and also with a 5% N_2 / 95% Ar mixture. These multilayers were measured using a Cu-tube x-ray system. The Co/V multilayers exhibited higher reflectivity when deposited with a mixture of Ar and N_2 gas, as opposed to Ar only, as shown below in Figure 2.24.

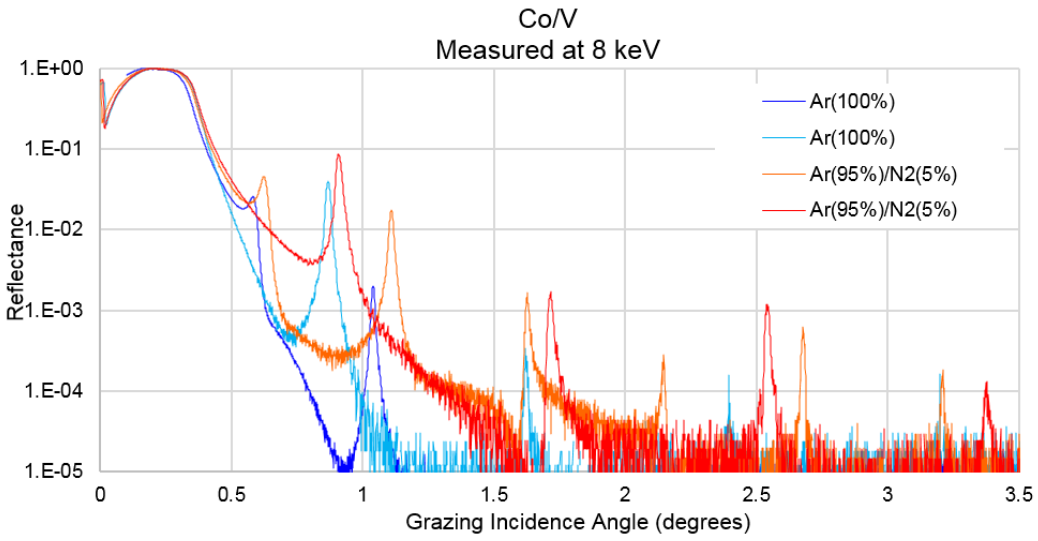

Figure 2.24: Co/V multilayers measured at 8 keV. Addition of 5% N_2 to the process gas mixture resulted in higher reflectance.

The reflectivity for these material systems at 510 eV and 30.5 ° are 12% for V/B_4C and 16% for Co/V. A series of measurements at 510 eV are shown below in Figure 2.25 (taken by colleagues

at NSLS) for a V/B_4C multilayer deposited in a following run with slightly larger d-spacing. The measurements show a significant peak in reflectance at 512 eV, which is exactly where it should be based on absorption edges. The second measurement taken at 512 eV shows a gain of ~800 in reflectance. Further results (not shown, by colleagues at the Advanced Light Source) reported 14% reflectivity for a V/B_4C multilayer deposited in a following run with slightly larger d-spacing at 510 eV. The measurements of the V/B_4C multilayer reveal that this material system performs well at 512 eV.

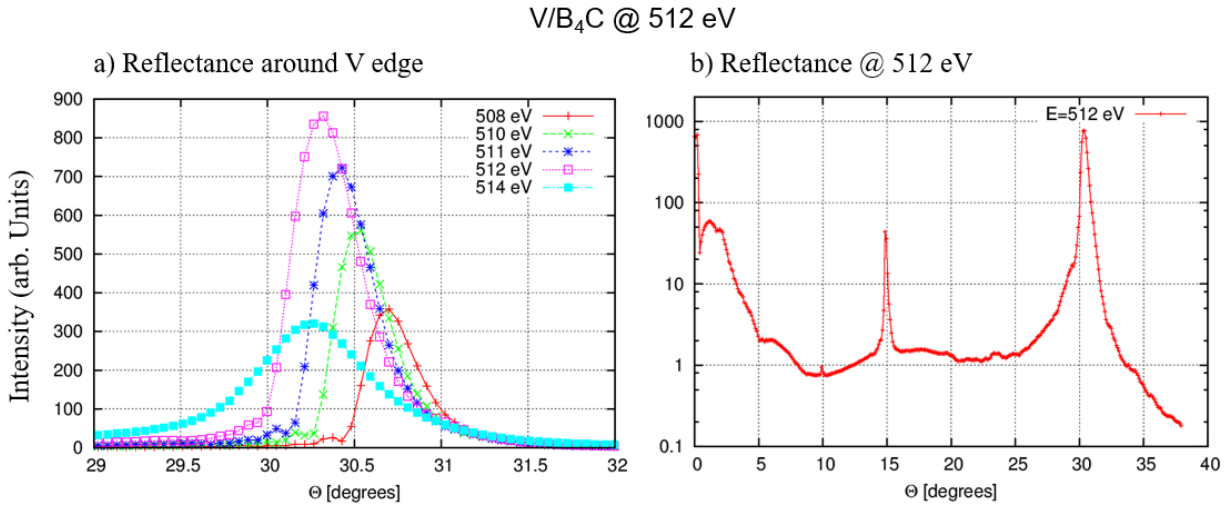

Figure 2.25: V/B_4C measured around the vanadium edge. (a) Reveals a peak in reflectivity at 512 eV, with a factor of 2x reduction in peak reflectance just 2 eV away. Reflectance vs. angle of incidence taken at U4B at the NSLS is shown in (b).

2.2.4.3 Multilayers for High-Energy Focusing

The third multilayer, intended for focusing at 80 keV, features a precision thickness gradient that was produced by velocity profiling. These types of laterally-graded multilayers are able to combine both micro-focusing and high flux density with very hard x-rays (40 keV and above). Particularly for powder diffraction, these sorts of optical elements have not been explored. The x-ray powder diffraction beamline (XPD) at NSLS-II is designed as a tunable beamline for applications requiring 40 keV to 80 keV. This beamline will play host to a variety of scientific applications, such as energy storage, high-pressure studies, and materials processing. In order to increase flux within a well-defined spot or match the beam size to the feature size of the sample under examination, some level of focusing may be required. A common way to achieve focusing for hard x-ray powder diffraction is to utilize the KB geometry, consisting of a bendable substrate and a single metal coating. At very short wavelengths, the incidence angle is exceedingly small; so small that for a sizeable portion of the incoming beam to be reflected the mirror must be very long. The XPD beamline at NSLS-II, for example, has designed into their B hutch a mirror that is over 1 meter in length. In order to greatly reduce the mirror size, a multilayer can be used in order to increase the incidence angle. This multilayer, however, must be tuned to a particular energy, or a combination of a depth gradient and a lateral gradient must be designed that can accept some bandwidth without altering the optical geometry of the mirrors or sample location.

For this experiment, a laterally graded W/B_4C multilayer was deposited on a 200 mm long trapezoid figured silicon substrate. The multilayer was designed for hard x-ray focusing at 80 keV. The BNL deposition system controls were enhanced to accommodate velocity profiling (with a much higher precision than more conventional x-ray multilayer deposition systems can achieve), and software to calculate appropriate velocity profiles based on a desired lateral thickness gradient was written.. Multilayers comprised of W/B_4C were deposited on the substrates, where the tungsten is kept at a constant thickness over the length of the mirrors and the B_4C thickness is varied to match the varying angles of reflection required. The d-spacing calculation accounted for the change in refraction through the varying multilayer thicknesses. The stage velocity profile (Figure 2.26 (a), solid line/right axis) is inversely proportional to the local variation in d-spacing. This d-spacing gradient from 1.7 nm up to 2.2 nm was measured across the length of the 200 mm long substrate using the lab x-ray source (Figure 2.26 (a), marked line/left axis). The d-spacing error was found to be +/- 3 pm, or +/-0.15% over the central 80% of the mirror as plotted in Figure 2.26 (b). The large errors on the edges are attributed to several effects. The first is insufficient allowance of length in order to accelerate and decelerate. The second is that for this mirror, the impact of the source shape and size is ignored.

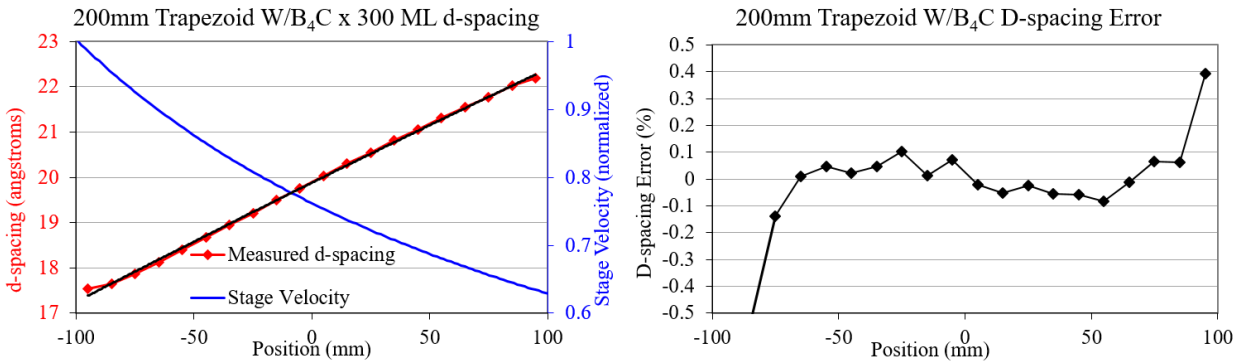

Figure 2.26: Laterally-graded W/B_4C multilayer d-spacing. The gradient along the length of a 200 mm long substrate is shown in (a) along with the design requirement (solid line). The corresponding stage velocity varies by ~40%, proportional to the variation in B_4C. Error is only +/-0.15% over the central 80% of the mirror.

An example of one set of Θ-2Θ reflectivity measurements along a single location of the mirror is shown in Figure 2.27. Here, the measurement at 8 keV exhibits quite sharp, feature-free Bragg reflection with only minor broadening on the 2nd and 3rd order reflection due to a combination of slightly incorrect deposition rate decay compensation due to target erosion as well as a spatial spread in d-spacing due to the footprint size of the measurement beam.

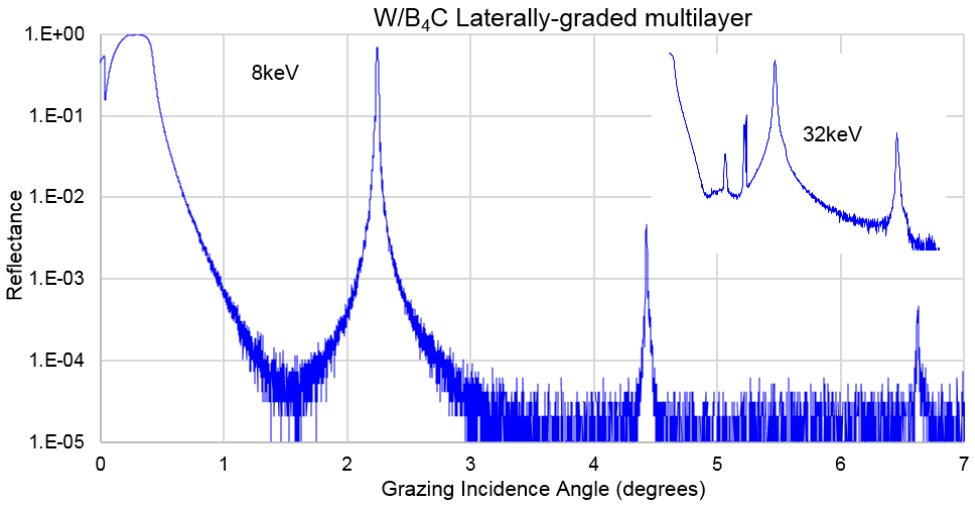

Figure 2.27: θ-2θ measurements at 8 keV and 32 keV of laterally-graded W/B_4C multilayer. The sharp, featureless Bragg reflections at 8 keV indicate proper layer periodicity. Measurements at 32 keV include beamline impurities, nonetheless, reflectance is over 50%.

2.3 Discussion and Future Work

Detailed conceptual designs for a planetary upgrade to the rotary deposition system was presented. The use of an essentially cog-free roller pinion gear system is a path towards precision angular velocity profiling for engineered gradients. This upgrade to the rotary deposition system will provide the APS with new capability for moderate volume production of periodic and depth-graded multilayers having high lateral film thickness uniformity on substrates up to 150mm diameter. The Modular Deposition System will be a world leading instrument providing leading edge capability for production of all types of multilayer-based x-ray optics on substrates up to 1.5 meters in length. This machine has been designed to be as flexible as possible in order to accommodate new film deposition techniques and instrumentation as the technology evolves. The inclusion of ion milling and interferometry will allow the APS to correct the figure of a large variety of existing mirrors. A profile coating deposition system, that was designed and constructed at the APS, has been commissioned. Initial results based on a three stripe double multilayer monochromator indicate that the machine is operating correctly.

No results are available for the new modification to the rotary deposition system; only a detailed conceptual design was completed. Specifications have been devised; namely, that the substrates shall rotate at roughly 200 RPM with a user-controllable speed, and active electrical bias can be applied to substrates. This upgrade is hoped for in the future. Significant progress has been made to commission the MDS, including deposition of the first sets of test multilayers

The modular Deposition is rapidly coming online for production of high quality multilayers for x-ray optical applications. However, much more work is required to debug the control system and fine tune process conditions. The instrument will also be used to explore options for in-situ surface metrology and surface figure correction with ion-beam figuring. Interferometric surface figure measurement through a vacuum window has been demonstrated through a series of simple comparison measurements that suggest that variations in the optical

path contributed by the VCW has negligible effect on the measurement. Any minimal contribution to the measurements could be coming from various environmental factors such as air turbulence or temperature. A UHV gimbal has been designed and constructed. The instrument will be deployed after testing.

The inclusion of reactive gas species during sputtering is known to increase optical performance (reflectance) of several material systems. The source of the change in performance could be due to two physical phenomenon, either a reduction in interface width, or a bulk change in optical properties. For hard x-ray optics, interface width reduction is widely reported as the dominating factor. For the new soft x-ray material systems, it is most likely that the increase in performance for these is due to smaller interfacial mixing and roughness. However, it is also possible that the incorporation of N_2 into the material has also slightly altered the optical properties. Precise measurement of optical constants for reactively sputtered materials can be challenging and can even be somewhat deposition system dependent, so the results here are best taken only at face value as a way to identify which material systems are most promising for at-wavelength measurements. Future investigation of optical properties of as-deposited materials is required.

A multilayer pair for focusing at 80 keV was fabricated. The d-spacing gradient along the length of one of these was presented; both have similar high accuracy and appear to show sufficient performance at 8 keV. Measurements done at NSLS at 32 keV on one of these show reflectance above 50%, however higher energy harmonics and Bragg peak broadening due to beamline effects or measurement setup problems were present.

The optics were not rigorously tested for actual efficiency and focusing performance at 80 keV. This work remains to be fulfilled based on future needs.

Chapter 3: Profile Coating

3.1 Motivation and current status

Beamlines around the world require ever increasing spatial resolution to probe small volumes. A worldwide effort is currently underway to improve x-ray micro-focusing, primarily through the use of Fresnel zone plates, Compound Refractive Lens (CRL), and Kirkpatrick-Baez (KB) mirrors. Compared to zone plates and CRLs, KB mirrors have three intrinsic advantages: greater distance from the optics to the sample, nondispersive (broad bandpass) and achromatic focusing, and high efficiency. A KB mirror pair is comprised of two concave mirrors oriented at glancing angles to the x-ray beam and arranged orthogonally with respect to each other in order to successively focus radiation in the vertical and horizontal directions. As the basic optical configuration of a beamline consists of a first point source of light that must be focused into a second point, the geometry is elliptical. The use of spherical mirrors for what should be an elliptical form will introduce aberrations.

One common method to produce elliptical mirrors is by bending flat substrates. Sophisticated bending techniques have been developed to bend initially flat silicon mirrors into an elliptical shape suitable for micro-focusing. A simple, trapezoidal mirror substrate shape with a single-point force on one end is often sufficient, and has been used to achieve sub μm focusing. Later, it was found that a deviation from a simple trapezoidal shape is required to produce a higher quality elliptical Figure. Free-form machining of silicon to the required tolerances necessitated the use of wire electrical-discharge machining. Heavily doped silicon substrates are used for these optics because EDM requires a conductive cutting material. Adaptive optics such as "BiMorph" mirrors employ directly-bonded piezoelectric bilayers to shape and tweak a substrate into an elliptical form. Adaptive optics at synchrotrons are commercially available for many shapes, such as elliptical, parabolic, or flat. The flat mirror is then then adaptively deformed to remove aberrations accumulated somewhere along the optical path[9,91]. Bendable KB mirrors offer flexibility because focal length can be adjusted to some degree, but the benders are bulky and can be unstable with regard to maintaining a fixed focal position. Monolithic KB mirrors are much easier to use if the required elliptical surface profile can be fabricated.

Several techniques are available to fabricate monolithic elliptical mirrors. One is to directly polish the Si mirror surface to an elliptical profile, which is generally very hard to do by using standard large-pad chemical-mechanical polishing techniques because of the demanding requirements of small figure errors and surface roughness. For x-ray focusing, state of the art elliptical mirrors are approaching 0.1 μrad figure perfection with less than 3 Å (RMS) surface roughness. One method available exclusively from a Japanese company[92] uses elastic emission machining and highly specialized metrology, comes with significant cost and lead time. Other vendors using sub-aperture chemical-mechanical polishing have historically produced equal performance[51], but for unknown reasons their products have not enjoyed any significant use at synchrotron facilities. Sub-aperture ion-beam figuring (IBF) to deterministically correct asphere optics is also used, in particular for fabrication of optics for EUV lithography.

Additive methods involve starting with a flat, spherical, or cylindrical mirror as the base substrate and modifying that flat, sphere, or cylinder into an elliptical Figure The techniques for polishing flat or spherical figures in particular is mature, and such mirrors can be processed in

large quantities. Two additive methods for modifying the figure, both based on sputter deposition, are differential deposition and profile coating. The differential deposition technique uses a small slit in front of the mirror while varying a coating parameter to achieve a film thickness change as the mirror raster scans across the slit. Differential deposition is directly analogous to sub-aperture subtractive processes, but with a (usually) additive material that is different from the mirror bulk substrate. Methods that vary source power were attempted first[10], probably due to the complexities involved with precise mechanical motion in a vacuum environment. Limitations include operating the power supply only within a small linear range, delay in ramp times, the source footprint may change with power, and sputtering energetics will vary. Another limiting factor with any sub-aperture process is the large number of iterations between measurement and figuring step.

Another additive method is the profile-coating technique, which was borne as a way to produce elliptical KB mirrors on either cylindrical, spherical, or flat silicon substrates, with Au as the coating and final shaping material. The profile-coating technique began in the deposition lab at the Advanced Photon Source (APS) and was first attempted on the cable-drive linear deposition system. This machine consists of four large vacuum chambers, each 40 cm in diameter and 1.67 meters in length. Three CT-8 cryo-pumps combined with an Alcatel ADP 81 dry pump achieve a base pressure of ~10^{-8} Torr. Samples are loaded face-down on a carrier, which translates between chambers driven by a simple stepper motor. The entire machine is automated through a text-based scripting language on a control system written in Visual Basic. Four 75 mm dia. MAK brand magnetron sputtering sources are installed facing upwards in the deposition chamber. Masking and linear substrate motion is used to control film thickness in the direction orthogonal to translation. The mask is placed physically within a few mm of the substrate plane on a shroud that encases the sputtering source and collects stray deposition flux. This mask is fabricated with a precisely figured aperture, where the shape of the aperture is dictated by convolution of the source deposition flux footprint with the required film thickness distribution.

3.1.1 Source shape

In order to calculate the given mask shape for a required thickness profile, knowledge is required of how the sputtered flux emanating from the source is distributed on the region of the substrate plane. Film-thickness distribution in magnetron sputtering has been extensively studied in the past few decades[93,94] As indicated in the reference[95], the film thickness, **t**, deposited from a ring source onto a flat stationary substrate aligned and centered is expressed as:

$$t = m_x h^2 (h^2 + r^2 + a^2)/[\rho/[\rho^2 + r^2 + a^2 + 2ar)^{1.5}(h^2 + r^2 + a^2 - 2ar)^{1.5}] \quad \text{(Eq. 3.1)}$$

Where $\mathbf{m_x}$ is the atomic or molecular mass of the ring source emission, $\boldsymbol{\rho}$ is the density of target material, **h** is the distance from the source to the substrate, **r** is the ring radius, and **a** the position on the substrate, or the distance laterally away from the center on the substrate plane. The relative thickness at the substrate distance is then $\mathbf{t/t_0}$, where $\mathbf{t_0}$ is the thickness at **a=0**. The value $\mathbf{m_x}$ is calculated from a measured erosion depth profile and is proportional to the erosion depth at the ring radius **x**. When calculated only as a normalized film thickness distribution for $\mathbf{t/t_0}$, $\mathbf{m_x}$ cancels out, and both **h** and **r** are physical measurements taken inside the deposition

system and of a known erosion profile. This radially-symmetric model is shown below in Figure 3.1 (a) for a source with a distance of 75 mm from the substrate and a ring radius of 23 mm.

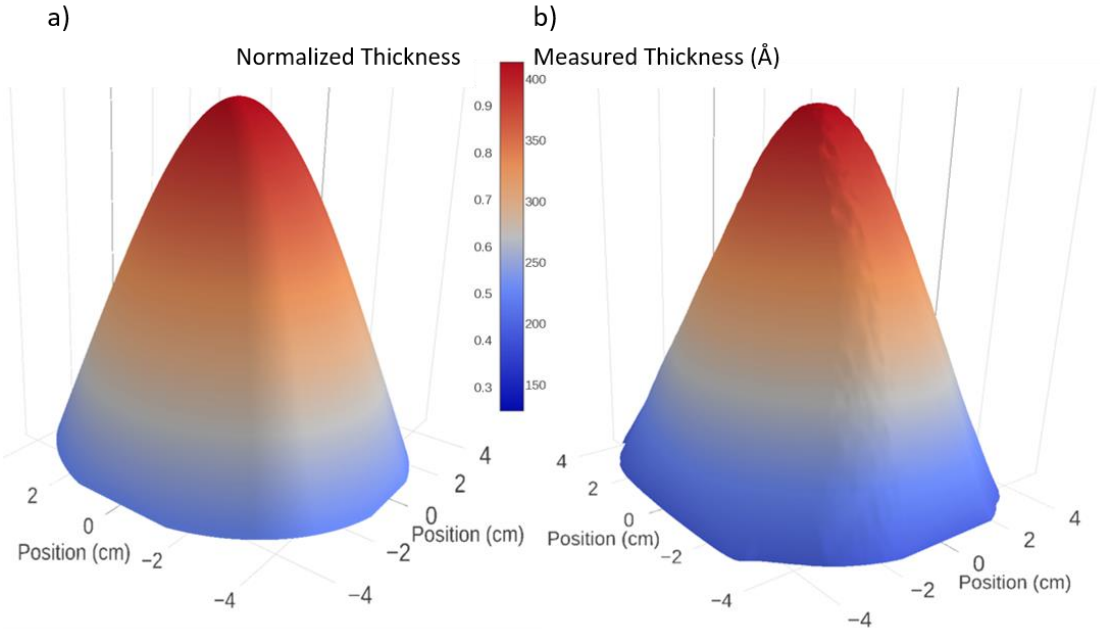

Figure 3.1: Film thickness distribution. Part (a) is an ideal ring source with a radius of 23 mm and a substrate distance of 75 mm, and (b) is an ellipsometric measurement of Au sputtered from a magnetron source with an erosion ring radius of 23 mm radius at a source distance of 75 mm. Even with the factor of 3x change in film thickness, the model fits remarkably well with the measurement. Features evident in the measurement that impact achievable limits include tilt, roll, radial magnet field strength asymmetry, and geometric shape dissimilarities.

The radially-symmetric ideal model is contrasted with a film thickness measurement in Figure 3.1 (b) of a coating with the same parameters. The coating was performed by fixing a 100 mm diameter silicon wafer at the substrate plane level within the machine, and energizing the deposition source for approximately 10 seconds. The film thickness at the center is roughly 40nm. The film thickness measurement was obtained by using an M-44 spectroscopic ellipsometer equipped with a motorized X-Y stage. Over the region of measurement, the film thickness varies from 40 nm at the center down to 15 nm near the edges. Even with this factor of 3x difference in thickness, the model and the measurement show considerable similarity. Observed deviations from the ideal model include tilt and roll, caused by mounting the source out of plane with respect to the substrate plane. Tilt and roll can be observed in Figure 3.2, below. The sources often show some level of radial asymmetry, likely caused by manufacturing and assembly variations in the individual magnets. Lastly, the overall shape can deviate slightly from the ideal model. This could be due to a number of factors, including reflection or re-sputtering of the deposition flux or contribution from the target sidewalls. The inset in Figure 3.2 Suggests that the ideal model can be utilized for coatings with tolerances in the 1-2% range, but that an actual thickness measurement needs to be used to produce coatings with tighter requirements.

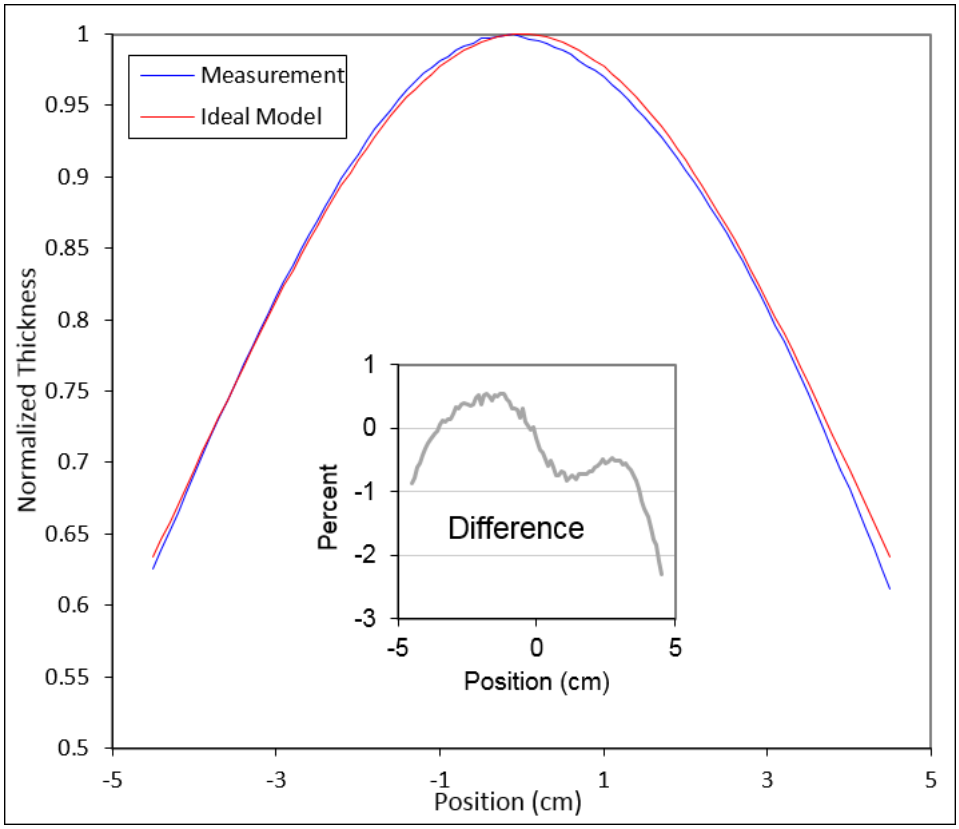

Figure 3.2: Comparison of one section of the ideal model with an ellipsometric measurement. Tilt from mis-mounting the source can be a major source of error. With an accuracy of +/-1.5% the ideal model is useful for most applications, or when the deposition material is difficult to map accurately with a real measurement.

3.1.2 Mask calculation and fabrication

The deposition thickness maps illustrated in Figure 3.1 above are used to obtain the deposition weighting for any location at the substrate plane. When the substrate is scanning back and forth in front of the source, the film thickness is proportional to the size of the aperture along the scanning axis. By equating the summation of relative weighting to the required relative thickness at a given location, the length of the aperture (or mask) at that given location can be determined. By repeating the same calculation for the whole length of the required profile, a contour can be obtained for a required thickness profile or mirror correction. The simplest example to consider is for a uniform coating. To simplify matters, symmetry is used in the calculations and should be ensured in the experimental setup. Figure 3.3 (a) shows a mask for a uniform Au coating on top of a deposition shroud. The Au target can be seen below the mask. Figure 3.3 (b) shows the result of an ellipsometry measurement. Uniformity better than +/-1% is easily achievable without much calibration. When the actual thickness map is used along with careful mechanical alignment, accuracy of up to +/-0.15% has been reported[12].

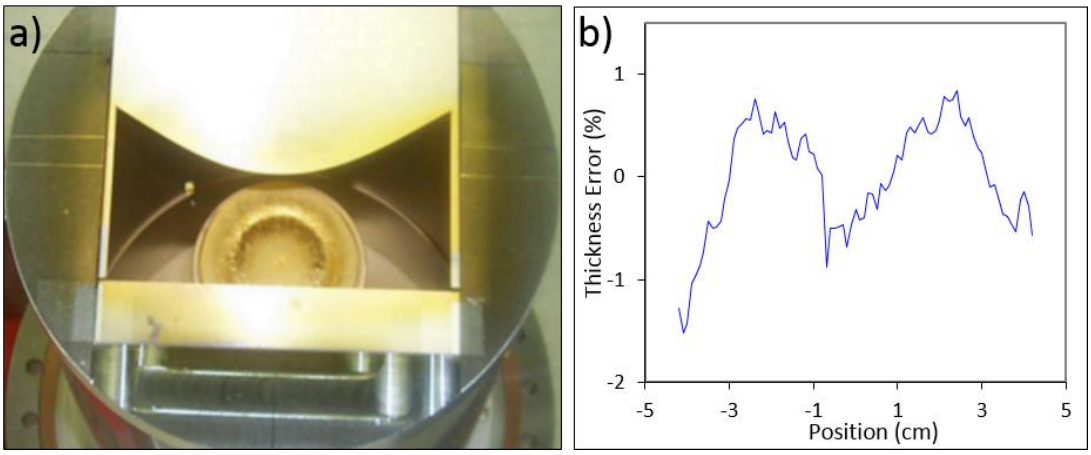

Figure 3.3: Uniform thickness profile-coating mask and measurement. Part (a) shows the partially eroded Au target located behind the mask. In this orientation, substrates scan from top to bottom. An ellipsometry measurement of a silicon wafer coated with Au indicates uniformity slightly better than +/-1% as seen in part (b). If more calibration and the real thickness distribution map is used in the calculation, uniformity better than +/-0.15% has been reported. [12]

3.1.3 Mirror fabrication

In order to employ this process for mirror figure modification, there are a few issues or limitations to consider. First, the profile coating process is merely a method to achieve film thickness variations across some area of a substrate that is scanned back and forth across the aperture. The variation in film is imposed only on the axis orthogonal to translation; the process only concerns two dimensions. This means that shape changes on mirrors can only be achieved on the axis perpendicular to translation. Shape changes or figure errors along the translation axis are not affected and simply "print through" during the coating. The scanning can assume any geometry. Radially-graded multilayers have been produced with this technique. However, for the experiments discussed here, all substrates scan in a linear fashion. Second, the material used for deposition needs to be considered for both optical and physical properties. The material needs to deposit very thick without delaminating or introducing surface roughness. The top surface needs to be optically reflecting. For x-ray wavelengths, this limits the selections to very dense materials such as the precious metals. The deposition material also needs to be able to withstand long-term use in a synchrotron beamline. Other materials will be discussed in later experiments. The third issue to consider is mirror surface figure measurement and registration between the metrology instrument and the profile-coating system, however metrology for profile-coating is outside the scope of this dissertation and will not be detailed.

Fabrication of a KB mirror typically requires the following steps. The first mask is fabricated based on an ideal substrate figure and the required elliptical form. Using an estimation of the mirror surface is typically sufficient for a first coating iteration because coating tolerances overpower any possible gains that may be possible to obtain using actual metrology data. After the mask is installed in the machine, a test strip, which is usually a diced strip from a silicon wafer 12.5 mm wide by 100 mm long (or less, depending on the final mirror length) is loaded for

a test coating. A test coating with a maximum thickness of perhaps 30 nm is deposited. An ellipsometric measurement of this test coating is properly normalized and fit to the required final coating thickness. In the case of depositing an elliptical form onto a flat substrate, the film thickness on the edges of the mirror can approach 10 µm for a 100 mm long mirror, given typical beamline geometries. The ellipsometry fit produces the proper scaling factor for the actual mirror coating. After the first mirror coating, the surface figure of the mirror is measured in order to produce the next iteration coating profile. An example 2nd coating profile is shown in Figure 3.4 below. The process continues until the mirror specifications are achieved.

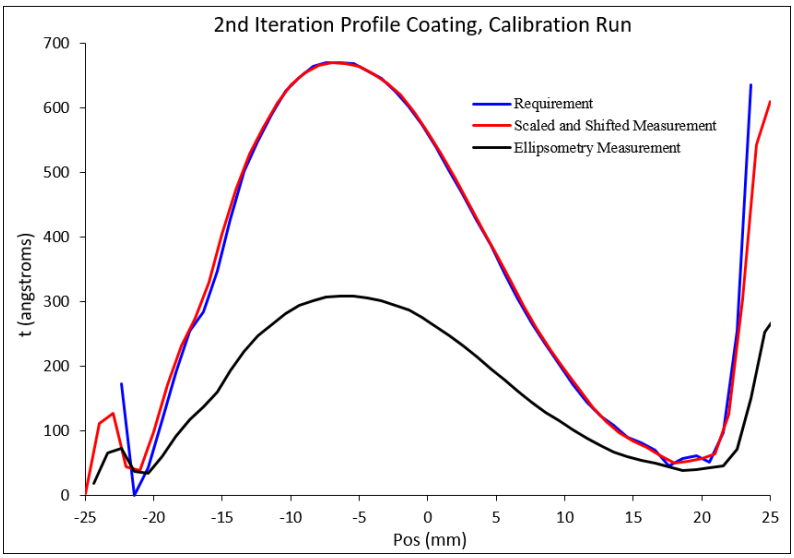

Figure 3.4: Example of a 2nd iteration profile and the associated test-run measurement. The ellipsometry measurement (black) provides two crucial pieces of information: exactly how to laterally offset the mirror to mate with the coating, and by how much to scale the measured deposition thickness to match the requirement (blue). In this case, by offsetting the mirror by 0.6 mm and increasing deposition time (by slowing substrate speed) by a factor of 2.3, the expected coating profile (red) matches well.

Due to machine geometry constraints, mirror lengths of up to 90 mm were able to be accommodated. An example early generation Au profile coated mirror pair fabricated for beamline 34-ID at the APS was produced with spherically polished mirror blanks that were 90 mm long, with a final slope error of 1.66 µrad. Focal spot sizes below 1 µm are standard[11-14]. In one special case, another set of mirrors fabricated for the same beamline achieved a horizontal focus of approximately 70 nm at 15 keV, while the white beam focus under the same conditions was about 80 nm[51].

The exceptional focusing performance shows the capabilities of the profile coating technique, however there are still issues to be solved. A number of users have reported short lifetimes with Au-coated focusing mirrors. In all cases, degraded focal sizes and efficiencies were observed to coincide with clear beam footprints on the mirror surfaces. It is unknown what the root cause of these footprints are, but the high mobility of Au immediately comes into question. Experiment 1 describes the limitations of Au, and the use of Pt for profile coating. Experiment 2 provides the technical reasoning and results of yet another material system: Ti/Rh. Experiment 3 details a new purpose-built profile coating deposition system.

3.2 Experimental Topics

3.2.1 Profile-coating with Pt

Profile coatings several μm thick are required to turn a flat substrate into an elliptical cylinder. High-purity Au was selected because it met several criteria: high deposition rate, no discernable roughness contribution, and acceptable x-ray reflectivity. Mirrors with sub μm focusing capabilities were fabricated, as referenced in Chapter 1. After extensive use of profile-coated mirrors (utilizing Au), it was found that the focal performance would change slightly over time[96,97]. The curvature of the mirrors appeared to drift slightly to a more concave figure, especially when the mirror substrate is rather long compared to its thickness. As the deposition of profile-coated mirrors takes place in an environment of 2.3 milliTorr, the film is under compressive stress. It has been reported[98] that this change in curvature may be the result of plastic deformation of the mirrors. This plastic deformation could possibly be related to stress relaxation. Physical behavior of deposited thin-films due to the complex microstructure and variations in film formation conditions can be vastly different from bulk material. Film stress within a film can be permanently reduced at relatively low temperatures[99], in some cases just a couple hundred degrees C. One example 70 mm long mirror with film thickness up to 6 μm that was beamline deployed was found to have an increase in total height of around 140 nm. A minor relaxation of the built-in compressive stress would explain this change. A similar mirror was also annealed at 350° C for 15 minutes and found to exhibit similar response, in this case a change of 175 nm. It has been reported that this long term irradiation of mirrors would also in rare instances lead to a slight increase in roughness. A spare Au profile-coated mirror fabricated for a beamline at ESRF with an initial surface roughness of ~0.3 nm (as measured with a microscope interferometer) was placed in a vacuum furnace at 350° C for 2 hours. Measurements shown in Figure 3.5 after the heat treatment showed a clear correlation between roughness and film thickness.

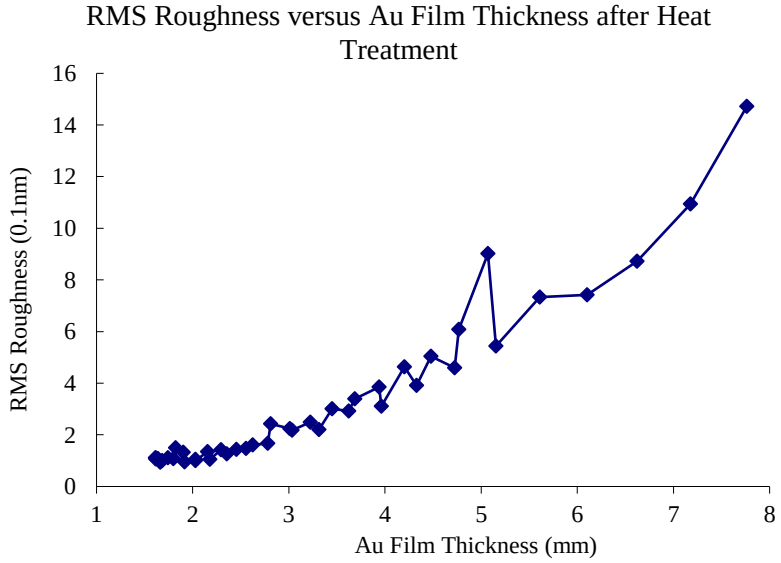

Figure 3.5: Au film surface roughness vs. thickness after 350° C bake for 2 hours. Roughness is heavily dependent on film thickness.

Due to the well-known high-mobility of Au and the requirement that profile-coated mirror figures are as stable as possible, a switch from using Au to Pt was initiated. The advantages of utilizing Pt in place of Au are that it appears more resistant to radiation and heat-induced damage, the right growth conditions produce extremely smooth surfaces (0.23 nm RMS roughness after 6 µm of film growth) and is preferred by most synchrotron users over Au (as are most of the Pt-group metals) for higher reflectance at higher energies. This is illustrated below in Figure 3.6.

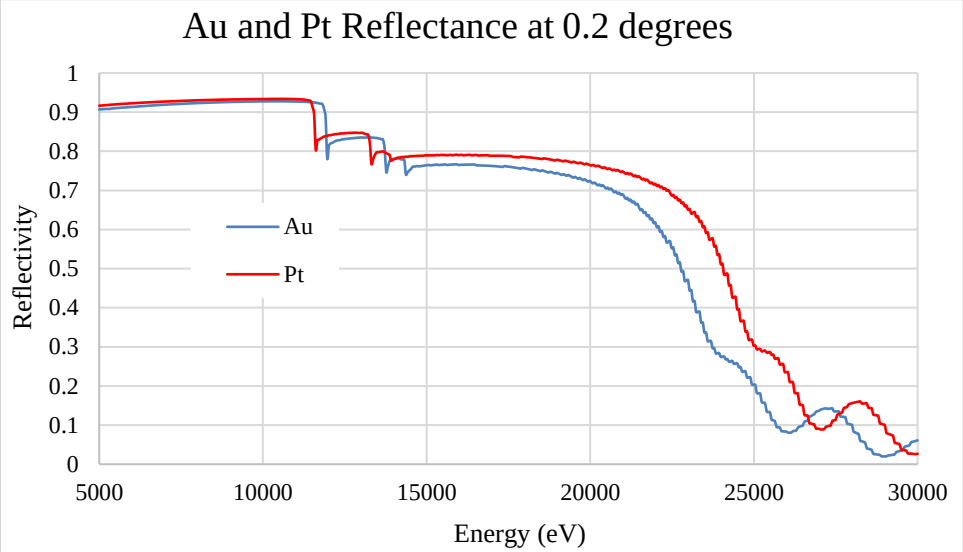

Figure 3.6: Reflectance of Pt and Au at 0.2 degrees angle of incidence. Pt is preferred by synchrotron users due to the higher critical energy of Pt.

The possible disadvantages of using Pt as a replacement for Au are that the growth rate is about 1/6 slower, it has a higher film stress, and has different chemical reactivity characteristics. However, after dissecting these one by one, it becomes evident these aren't a problem, at least when compared to Au. First, the slower growth rate of the film is not a large component in the overall production cycle. Pre-coating metrology, mask design, mask fabrication, and post-coating metrology can take over a week. The deposition system is typically left to pump overnight in order to obtain a decent base pressure because too high of a base pressure leads to gaseous impurities in the system. If the Au deposition process time for Au of 4 hours went to 16 hours for Pt, this is an increase in cycle time of only at most one day. Process times that large have only very rarely approached these scales in the past. The second and third issues, film stress and chemical reactivity, are related in that both will contribute to or result in reduced lifetime of the mirror during use. The potentially higher film stress has not led to increased delamination events. Au is slightly more reactive than Pt, and the 1/3rd higher melting temperature of Pt leads to decreased mobility in the film.

In the following sections, the deposition process, coating precisions, and mirror performance are discussed in the context of an example Pt profile-coated mirror that has no outstanding geometry parameters. For this mirror, the correction ellipsometry data is compared to the required profile in Figure 3.7, below. The accuracy of the profile coating is striking. The middle hidden hump can be identified, albeit in a washed out form. Some, or perhaps at least in

this case, all of this loss of definition might be due to the ellipsometer beam size of around 3mm. The feature size of the short peaks is roughly the same. The mask cutout as an inset illustrates the influence of the bullet-shaped deposition flux distribution. This is evident by comparing the relative heights of the peak triplets. In the actual data, the two outer peaks are at the same height. The outer peak in the mask cutout is taller than the inner peak to compensate for the proportionately less flux density available farther away from the bullet-shaped deposition flux source.

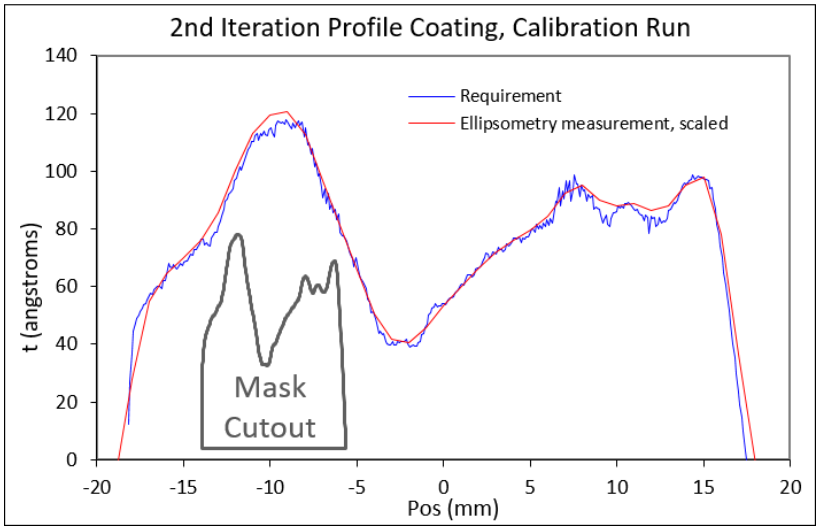

Figure 3.7: Example of a 2nd iteration profile and the associated test-run measurement. Deposition thickness is scaled by a factor of 0.72. The inset diagram of the corresponding mask cutout highlights the asymmetric weighting of the profile due to the flux distribution. This can be seen by comparing the relative heights of the peaks in the data on the right-hand side.

The example 40 mm long elliptically-figured Pt mirror with a maximum coating thickness of almost 4 μm was found to exhibit a surface roughness of less than 0.3 nm with an RMS figure error of less than 1nm, as shown below in Figure 3.8. A focal size simulation with this mirror profile yields a 43 nm FWHM focus, which is very close to the diffraction limit. The simulation of the intensity across the focal plane is shown in Figure 3.9. The focus of both an ideal ellipse and that of the measured surface are included. The main differences appear to be only in the sidelobes.

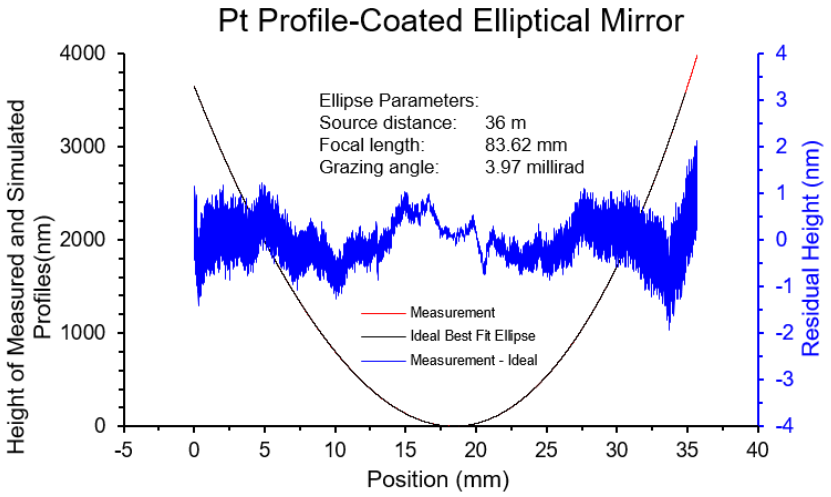

Figure 3.8: Pt-KB height profile. This 40 mm long mirror started out as a spherically polished substrate. The total sag of the mirror is almost 4 µm. The RMS residual height error is 0.5 nm.

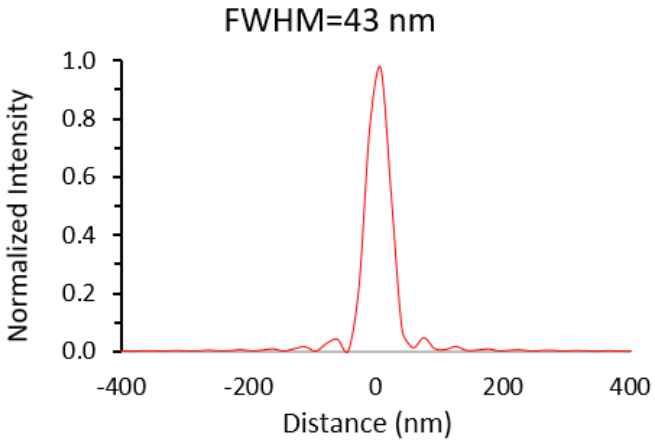

Figure 3.9: Focus simulation of the 40 mm long mirror. The FWHM of 40nm is extremely close to diffraction limit. The quality of this mirror in terms of figure accuracy is as high as any of the best aspherically-figured optics manufacturers can obtain. Profile coated mirrors have consistently been fabricated with similar height tolerances.

A spare Pt-coated mirror with similar dimensions was vacuum annealed under similar conditions as listed above for the Au mirror. It is reported by the same manuscript that after 15 minutes at 350° C the deflection is only about half for Pt as compared to Au. Users of both Au and Pt profile coated mirrors have reported significantly higher lifetimes with Pt mirrors. Profile-coated mirrors consisting of a pre-figured silicon base substrate and a platinum profile layer of up to several µm in thickness have been under steady production for the last 5 years. The conclusion is that Pt is an excellent successor to Au for profile-coated synchrotron focusing mirrors. It is known that the other precious metals have higher film stress, and so it is increasingly unlikely that Pt will be replaced by any of these, especially when starting from a flat substrate.

3.2.2 Commission new Profile-Coating Deposition System

The first trial experiments for profile coating were done in the APS large deposition system. This machine[100] suffers from severe mechanical instability that is incompatible with profile coating, and so work was shifted to an older small machine that was originally developed for multilayer coating[49]. This small system, seen in Figure 3.10 below, was assembled partly from available components by APS staff. The vacuum system horizontally translates substrates that are suspended to face downwards to the ground. The drive motor and feedthrough can be seen on the left of the vacuum chamber. A substrate platen is loaded from the right hand side. Two 75 mm diameter MAK sputtering sources point upwards. The utility cabling to these cathodes is visible below the chamber. One mass flow controller injects 100 % Ar gas. Gas pressure is held at a constant (usually 2.3 milliTorr) via feedback from a Baratron capacitance manometer. The machine featured a relatively rigid substrate platen that was ball-screw driven. Control was via a simple LabView interface through a Macintosh computer.

Figure 3.10: The original profile-coating machine. All the essential components, including two sources, a gas feedback system, and a stable drive mechanism enabled years of profile-coating development and mirror production. Over time, the requirements for profile coating exceeded the capability for this system, and hardware was failing.

In order to meet future expected needs for profile-coated mirrors, a new profile-coating machine has been designed and constructed by a team of scientists and engineers at the APS. This new machine utilizes two 75 mm dia. Round MSI-PE cathodes that sputter horizontally through a mask shroud, towards the substrate translation stage. The machine and some components are illustrated schematically in Figure 3.11. Substrates up to 200 mm in length and 120 mm in height can be accommodated in the machine. The cryo-pumped machine utilizes four PNeucleus mass flow controllers to mix Ar with N_2 and then deliver this mix individually into each cathode body as required

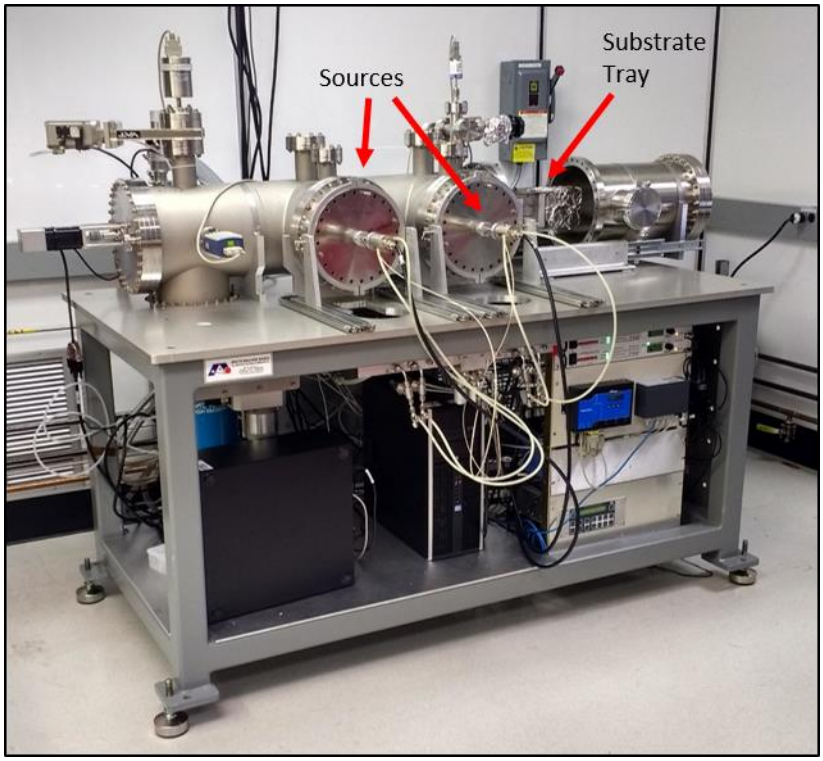

Figure 3.11: Photograph of the new profile-coating machine. Cabling feeding the sources can be seen on the left side of the machine. Supporting instrumentation and electronics are mounted below.

The substrate translation stage is a commercially available UHV stage which uses a recirculating ball screw that is driven through a ferro-fluidic feedthrough by a servo motor. The Aerotech supplied motion system includes the stage, a servo motor drive, and the controller/amplifier. The motion system is capable of arbitrary velocity gradients for production of mirrors using differential deposition or laterally graded multilayers. The example velocity profile in Figure 3.12 (a) suggests that the machine is ready for these sorts of tests, however more integration of this motion capability into the control software is required before testing can begin. Figure 3.12 (b) shows that stage position error during the move is never more than 1 μm during the velocity profile. For more information, see the graded multilayer section in Chapter 2 where this technique was used for a pair of focusing multilayer optics in the BNL MLL deposition system.

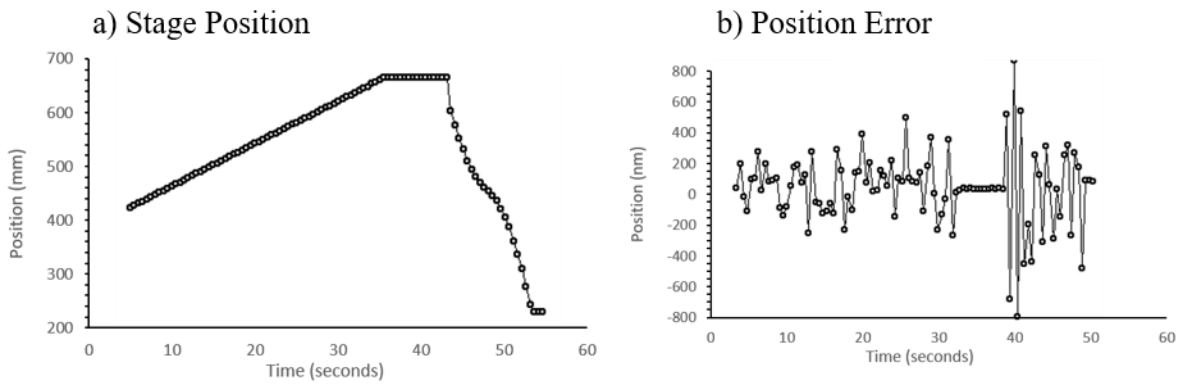

Figure 3.12: Example of velocity profiling in the new profile-coating system. The stage first travels at a constant velocity to 700 mm, pauses, and then follows a variable velocity map back. The variable velocity map consists of time and velocity points that are smoothed with (at a minimum) a third order polynomial. The stage position error is below 1 μm at all locations during the move. Although the position error during a profile move appears somewhat larger than a constant move (As seen in part b), this error is roughly 0.002%. This is well below the required thickness variation required for reflective multilayers. This is also well below the likely measurement accuracy achievable with the available ellipsometry equipment.

All hardware interfaces initially to an EPICS input/output controller (IOC). This low-level interface provides the hardware communication link to a Python-based control system that is described elsewhere[75,101]. The photograph in Figure 3.11 shows the utility cabling attached to the horizontally mounted cathodes and some of the supporting instrumentation mounted below. A Baratron 50 milliTorr capacitance manometer provides process gas pressure measurement. Serial-based hardware interfaces with an Ethernet-based serial port multiplexer. Measurement Computing 1608 multifunction data acquisition are used for all relay and analog interfacing. Two ION1500 power supplies drive the cathodes. Each power supply is independently controlled. Masks are manually installed from the mirror loading opening in the chamber. A mirror installed for coating is seen in Figure 3.13 (a), and a uniform coating mask is visible behind the cathode in Figure 3.13 (b).

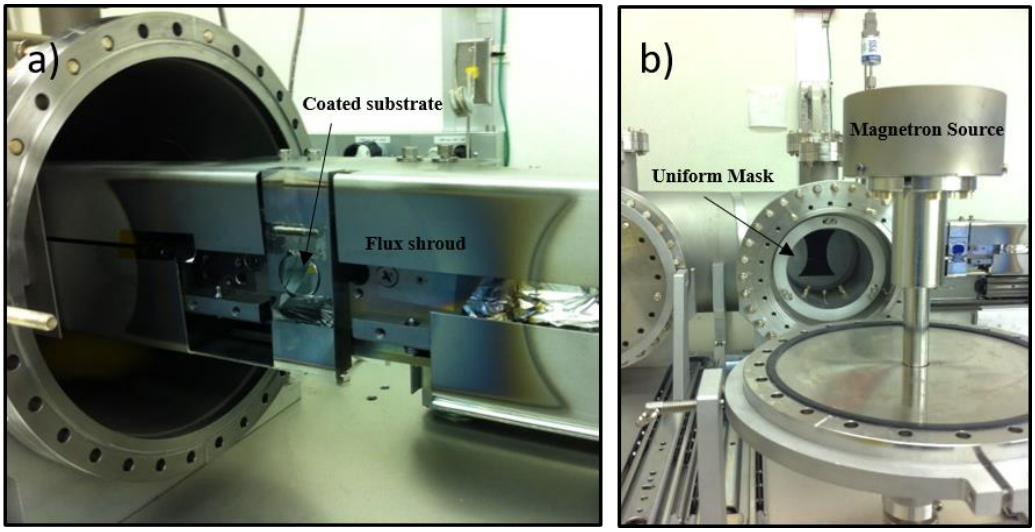

Figure 3.13: Close-up images of the machine. Part (a) shows a small round coated optic mounted in the machine. The deposition flux shields show the mask shadowing clearly. In part (b), the cathode sits removed from the machine, facing upwards for maintenance. The uniform coating mask is seen in the background.

With any new machine, the commissioning period is used to fix problems, assess performance, and calibrate the equipment. Any transient issues with equipment such as power supply fluctuations, gas flow instrumentation, and motion hardware that are likely to surface with a new machine need to be found and corrected before real optics are processed.

Several issues with this machine were identified and solved during commissioning:

- Modification of several of the mechanical mounts and fixtures for the masks and substrate tray due to unforeseen clearance issues.
- The original design for the machine used conflat gaskets for the cathode mounts. This was a problem because the cathodes need to be removed frequently for servicing or target changes. The two flanges were mated with an o-ring conversion to make serviceability easier.
- Film quality, as well as deposition rate, are highly dependent on process gas pressure. A gas influx burst was found to occur during coating on rare occasion. Log file review identified that the gas influx was due to Ar inlet pressure variations caused by sudden use from a neighboring machine. This short gas influx is shown below in Figure 3.14. The issue was solved by separating the machines with different gas source bottles.

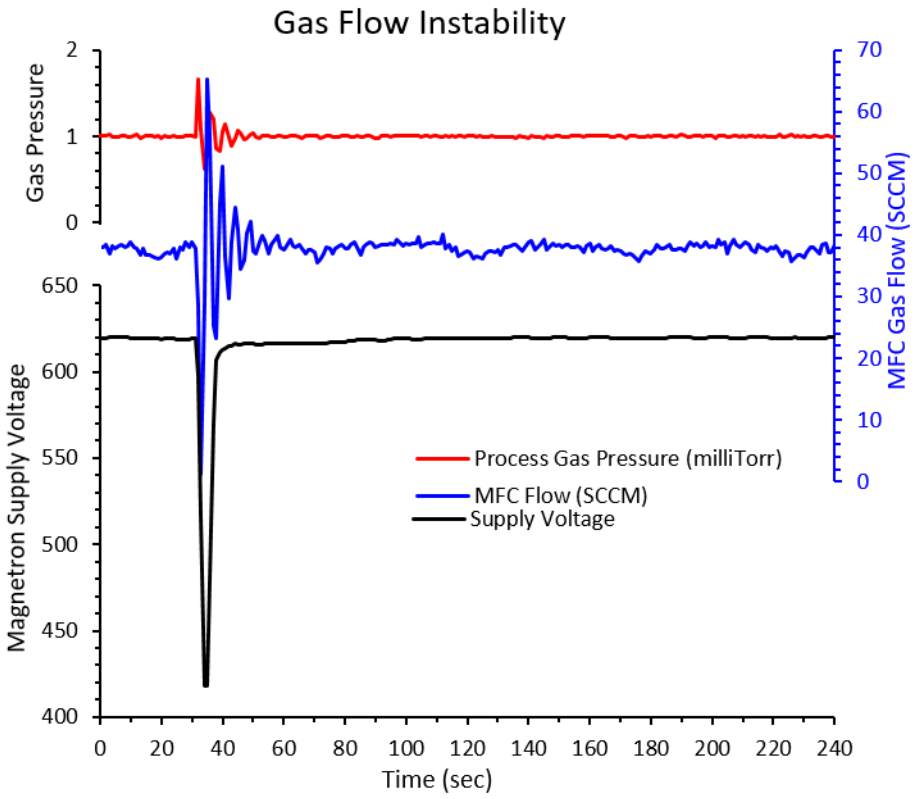

Figure 3.14: Process gas pressure instability due to injection gas pressure variations. Gas pressure in the machine is maintained at a constant value by automatic flow control of mass flow controllers (MFC). Fast, large variations in MFC inlet pressure caused the pressure in the chamber to fluctuate. This causes supply voltage swings.

This machine is primarily intended for fabrication of figured KB mirrors using the profile-coating technique. The machine can also be used to fabricate multilayers. Analysis of multilayer deposition is a good indicator of system performance. X-ray reflectivity measurements provide sensitivity to determine interfacial roughness and layer by layer deposition repeatability. The machine was designed with a precision gas mixing system for reactive sputtering capability, which means a material system can be chosen that might benefit from this feature. Also, because the deposition rate and optical performance of materials that can react is highly sensitive to process parameters, experimentation with a reactive material system is a good way to exercise the equipment and start to examine deposition equipment stability. For this, the WSi_2/Si material system was selected. The sources were first calibrated by measurement of a multilayer pair with one material thickness doubled (as discussed elsewhere in this dissertation). The diffraction measurement at 8.048 keV in Figure 3.15 shows a narrow peak width. Generally, bandpass starts to noticeably degrade when random layer thickness error reaches a value approaching the bandpass, or in this case around 0.5%. This indicates that repeatability and stability of all of the instrumentation (gauges, supplies, gas systems) is sufficient for multilayer deposition, and certainly for profile coating as well. The first order reflectivity is about half what should be expected, indicating that the interlayer roughness is high. This is likely due to non-optimized deposition parameters such as source distance or power, as well as the rather high concentration of N_2 gas used.

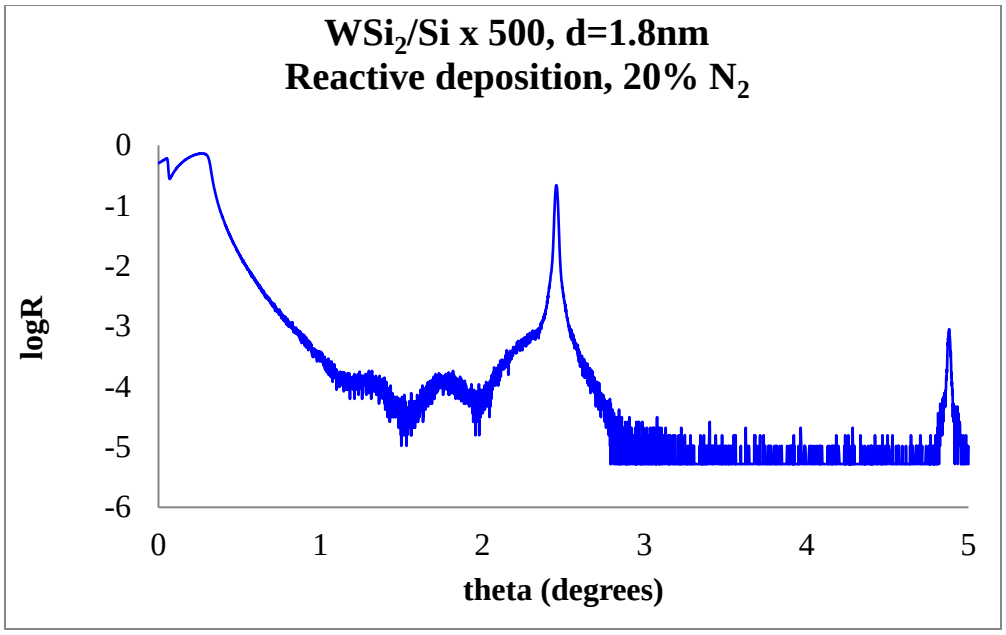

Figure 3.15: Periodic high-resolution multilayer. The narrow first order peak width indicates good performance of the deposition system.

At the time of its commissioning this machine was the best performing system for multilayer fabrication at the APS. So, the first deliverable from this machine was a three-stripe double multilayer monochromator for 7BM at the APS. The substrates were 90x90 mm. The substrates before installation in the beamline are shown in Figure 3.16. Each 10 mm wide stripe was deposited on both substrates during the same deposition run to ensure that the stripes match. All three multilayers were comprised of 100 bilayers of W/B_4C, with d-spacings of 2.1 nm, 3.0 nm, and 4 nm. The coatings were executed at 1.0 milliTorr utilizing a 10% N_2 /90% Ar gas mixture. Reflectivity measurements of the largest and smallest d-spacing stripes taken with an 8 keV laboratory source are also shown in Figure 3.16. While the higher order Bragg reflections of the 4.0 nm d-spacing multilayer show some minor broadening due to slightly incorrect erosion compensation, the first order reflections provide sufficient reflectivity.

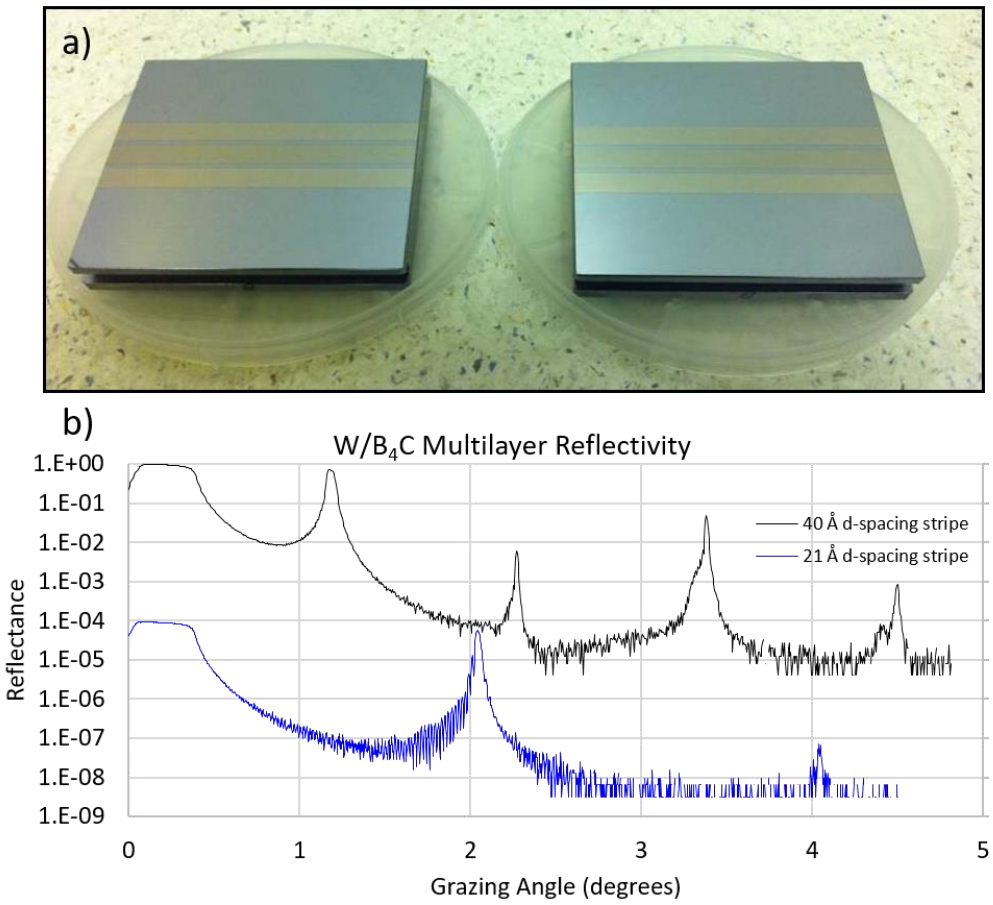

Figure 3.16: The finished DMM. Photograph (a) of the double multilayer monochromator pair with matching three-stripe multilayer coatings. Reflectance of the 21 Å and 40 Å multilayers at 8 keV in part (b) indicate sufficient performance, however some peak broadening is evident due to incorrect target erosion compensation.

A second double multilayer monochromator pair has been made for 2-ID at the APS with this machine, and both pairs are currently under regular user operations deployment. With relatively robust hardware and reliable control software, the machine has been highly productive. Over 100 coating runs per year have been completed with the system. During the last two years, the system was used to produce new binary pseudorandom multilayers[102,103], and several KB mirror pairs. One of these KB pairs is discussed in the next section of this chapter.

3.2.3 Ti/Rh profile-coated mirrors

Profile coated mirrors are used at a handful of beamlines at the APS, with new users appearing about twice per year. One new application requested two sets of KB mirrors, one with maximized flux at energies below 18 keV using Rh, and the other maximized for higher energies using Pt. This is very common for regular beamline mirrors: the same KB bender or flat harmonic rejection mirror will often have multiple stripes. Use of both materials allows complete avoidance of the absorption edges seen in Pt. Reflectance versus energy for Rh and Pt is shown in Figure 3.17 below.

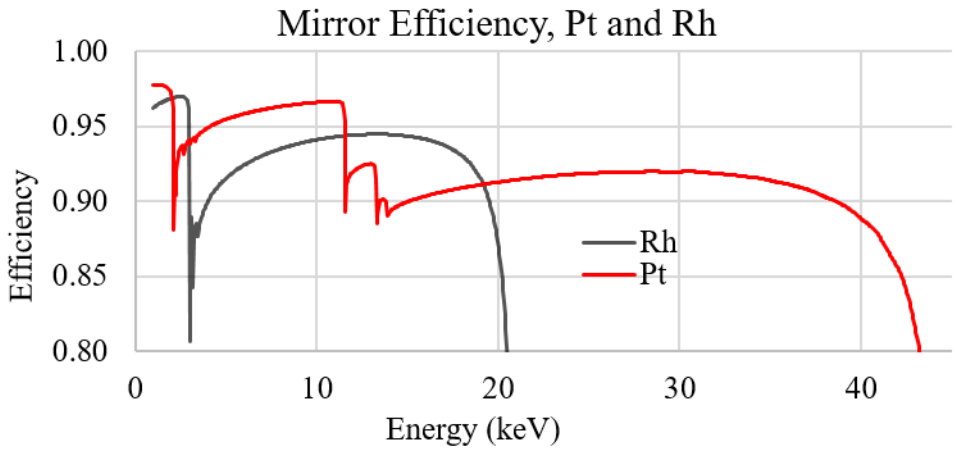

Figure 3.17: Reflectivity vs energy for Pt (Theta=1.9 mrad) and Rh (Theta=3.2 mrad)

Fabricating a profile coated mirror with anything other than Au or Pt as a top metal has never attempted. One may either deposit the Rh over a Pt/Cr profile-coated mirror, or simply use Rh for the profile coating. The main considerations are the ability to deposit Rh to the required film thickness while maintaining low roughness, adhesion, and film stress. Some of the precious metals are known to have higher deposited stress than Pt, in particular Ir, however Ir has been coated quite thick (several μm) as an absorber.

For this experiment, a "case study" is presented where a beamline has requested two sets of KB mirrors. Both sets of KB mirrors will have the same focal lengths, but with different intended energy ranges and angles of incidence. Since the KB sets share some identical parameters, it is possible there are some cost savings can be realized by procuring identical substrates, however some design compromises along with their possible benefits and drawbacks need to be discussed first.

A primary consideration that is coupled with whether or not to use Rh for the profiling is the choice of substrate geometries, which is dictated primarily by the focal length, angle of incidence, and desired aperture. The mirror parameters are summarized in Table 3.1.

Mirror	Length (mm)	F1 (m)	F2 (mm)	Angle (mrad)	Coating
Below 18 keV Horizontal	60	55	90	3.2	Rh
Above 18 keV Horizontal	60	55	90	1.9	Pt
Below 18 keV Vertical	100	55	213	3.2	Rh
Above 18 keVVertical	100	55	213	1.9	Pt

Table 3.1: Mirror parameters for two sets of KB mirrors.

The substrates are procured from an outside vendor and are fabricated using relatively common processes. Both flat and spherically figured substrates can be considered. Both are roughly similar in expense and performance, so the decision is generally made for one of two other reasons. First, if the lifetime of the mirror is expected to be short due to harsh environment or heavy synchrotron use, then depositing on a flat may be desired because new flat substrates are always the same shape (flat) and new blanks can be quickly recoated with the same first

mask set. This is more difficult to do with spherically polished substrates if the vendor is not able to perfectly match the required radius from different polishing batches. The main advantage to using spherically polished substrates is that the total coating thickness is greatly reduced because the profile coating is only correcting the deviation of the best-fit sphere into the ellipse, instead of building up the entire elliptical profile from a flat origin. The elliptical shape of all four mirrors is shown below in Figure 3.18. If the mirrors were to be coated on a flat substrate, these plots indicate that the total film thickness would range from roughly 5 µm up to about 9 µm.

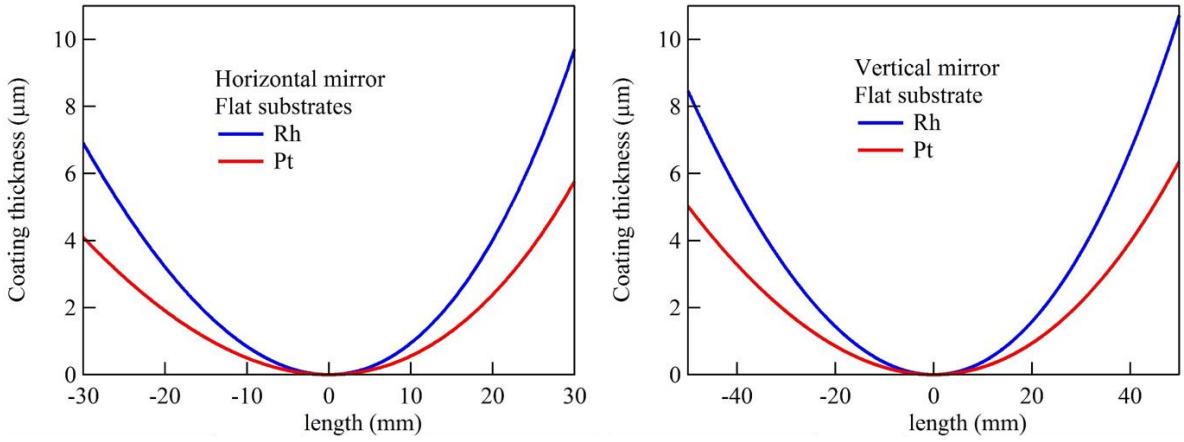

Figure 3.18: Elliptical shells for four KB mirror sets. Total sag ranges from roughly 5 µm to 9 µm.

Both mirror sets are to be elliptically profiled from spherically polished substrates. Typically, the radius of the spherical substrate is optimized to require as thin as possible of a profile correction. However, because these are a pair operating merely at different glancing angles, we can select one spherical radius for both coatings in order to save time and money, at the cost of requiring slightly thicker profile coating. Figure 3.19 shows coating profiles for this set of four mirrors where the initial substrate curvature is optimized for each mirror (resulting in 4 substrates) as well as the coating profile if a single substrate radius is selected that is a compromise between both angles of incidence. This data indicates that using a single, spherically polished substrate brings the coating thickness down by a factor of at least 2x for the horizontal, and almost a factor of 4x for the vertical. Similar gains again are achieved if individual substrates are used for each mirror.

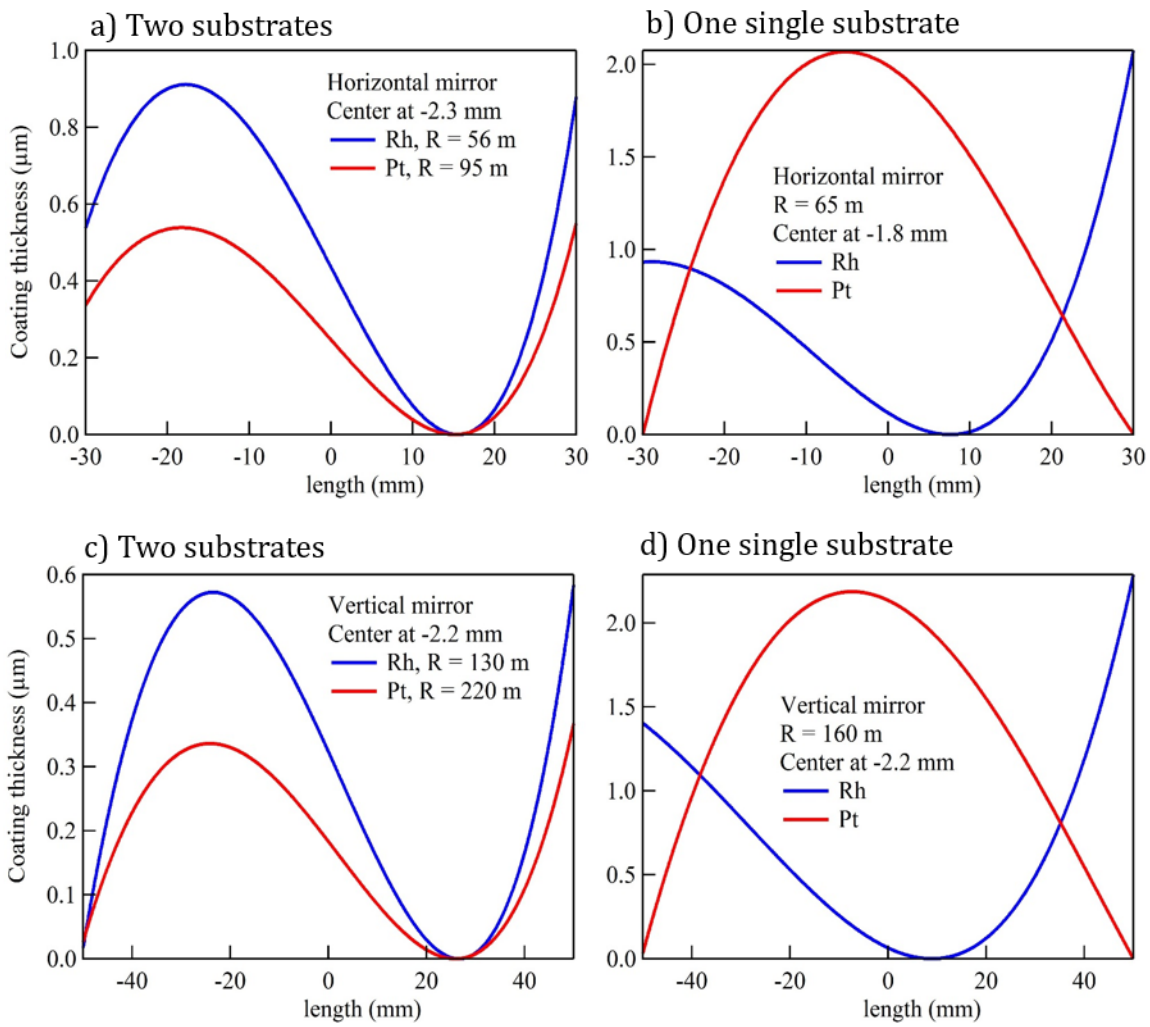

Figure 3.19: Required coating profiles for (a) two substrates versus one substrate (b). The coating profile in (c) and (d) is for two versus one substrate, respectively, for the vertically focusing mirror. Coating thickness will be reduced by a factor of 2 for the horizontal mirror and almost four for the vertical mirror by using dedicated substrates.

Another advantage to using spheres matched to individual mirrors is that the first mask for both has a matching shape, with the only difference between the coatings is total thickness. This means that if the target profiles are sufficiently similar, the same mask can be used for both first coatings. In the end, it was decided to work with individually matched spheres since Rh profile-coating is untested and keeping the film thickness to a minimum is best.

A first coating profile generally following the shape shown in Figure 3.19 (a) that corrects the central 50 mm of the mirror was generated. After initial calibration the first correction coating was deposited on the spherically polished substrate. After measurement, it was found that significantly more coating was required as shown below in Figure 3.20.

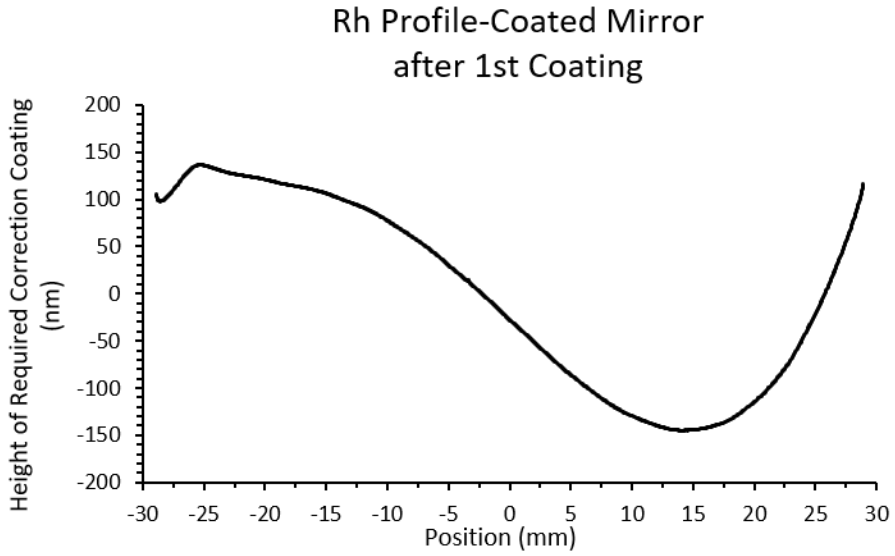

Figure 3.20: The Rh profile-coated mirror after the 1st coating. The lip on the left is due to incorrectly truncating the edge of the mask to 80 mm.

The first correction profile was based on an ideal cylinder with a radius of curvature determined by best fit from an instrument that is new to the metrology lab. This interferometer was mis-calibrated by over 15%. Also, because the mask covers only the central 50 mm of the mirror, a kink was built at roughly the -25 mm position. A second correction was applied through the same mask, resulting in a new correction profile shown below in Figure 3.21.

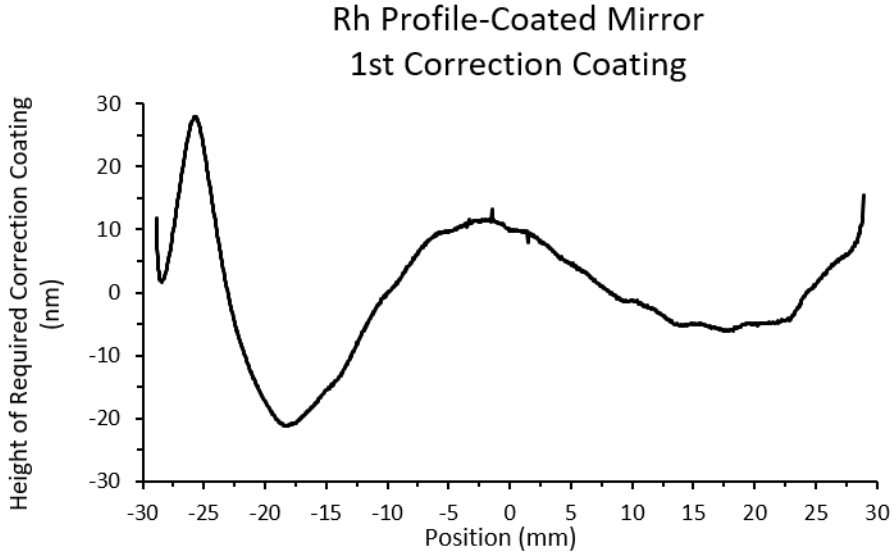

Figure 3.21: 1st correction coating for the Ti/Rh profile-coated KB mirror. The sharp peak and valley at -25 mm are a side effect due to terminating the mask to a size shorter than the length of the mirror. The minor undulations of roughly 5 mm periodicity which are clear on the right side of the data are artifacts due to metrology errors[104].

Surface roughness of deposited films is dependent on a wide variety of factors, however two that are the most impactful are material composition and sputtering process gas pressure. There is no guarantee that the surface roughness of any film will be sufficiently smooth, however some materials have a high affinity for smooth surface deposition. Au and Pt are two of these. Generally, these films will deposit free of any added contributions to surface roughness. As discussed in more detail in Chapter 4, sputtering gas pressure should be kept below the range where clusters start to aggregate in the gas phase. Also, the total thickness of a film can have some impact on surface roughness. It has long been reported that Cr, which is widely used as an adhesion layer for many thin film applications, stays satisfactorily smooth for the first 10-20 nm or so. Once the Cr thickness becomes much thicker than 30 nm, it usually starts to develop surface roughness. Rh is commonly deposited as a reflective surface for synchrotron optics, but is usually deposited with Cr as an adhesion layer, not Ti, and also not to the same thicknesses as required for these profile coatings. In order to evaluate any possible contribution to surface roughness by the coating, roughness before and after coating of a super-polished Si blank is shown below in Table 3.2.

Process Step	Magnification: 5x FOV: 1.68 mm^2		Magnification: 20x FOV: 0.42 mm^2	
	RMS (Å)	PV (Å)	RMS (Å)	PV (Å)
Bare surface, before coating	1.08	10.88	0.78	8.17
Rh surface, After coating	1.13	11.33	0.64	6.43

Table 3.2: Substrate roughness before and after primary coating. The results listed here are the average of 7 optical surface measurements with a microscope interferometer. No observed difference in roughness is apparent at the spatial frequencies sampled by this microscope.

The optical surface measurements shown in Table 3.2 and Figure 3.22 below are taken with a microscope roughness interferometer. This instrument is commonly found among synchrotron facilities for measurement of optical surface roughness as well as surface figure[104]. More information on the impact of surface roughness at x-ray wavelengths is available elsewhere[83]. In Figure 3.22, the top two images are of the surface before coating, and the bottom are after coating. The left-hand column (a) and (c) have a pixel size of 1.64 µm, while pixel size for part (b) and (d) is 0.42 µm. The images are suggestive of a typical super-polished silicon substrate, except for the random appearance of many small craters in Figure 3.22 (b). The craters were observed at all 7 other locations before coating, while their numbers appear greatly reduced after coating. Visual estimation of crater density before coating of about 5000/mm^2 drops to between 50/mm^2 to 100/mm^2 after coating.

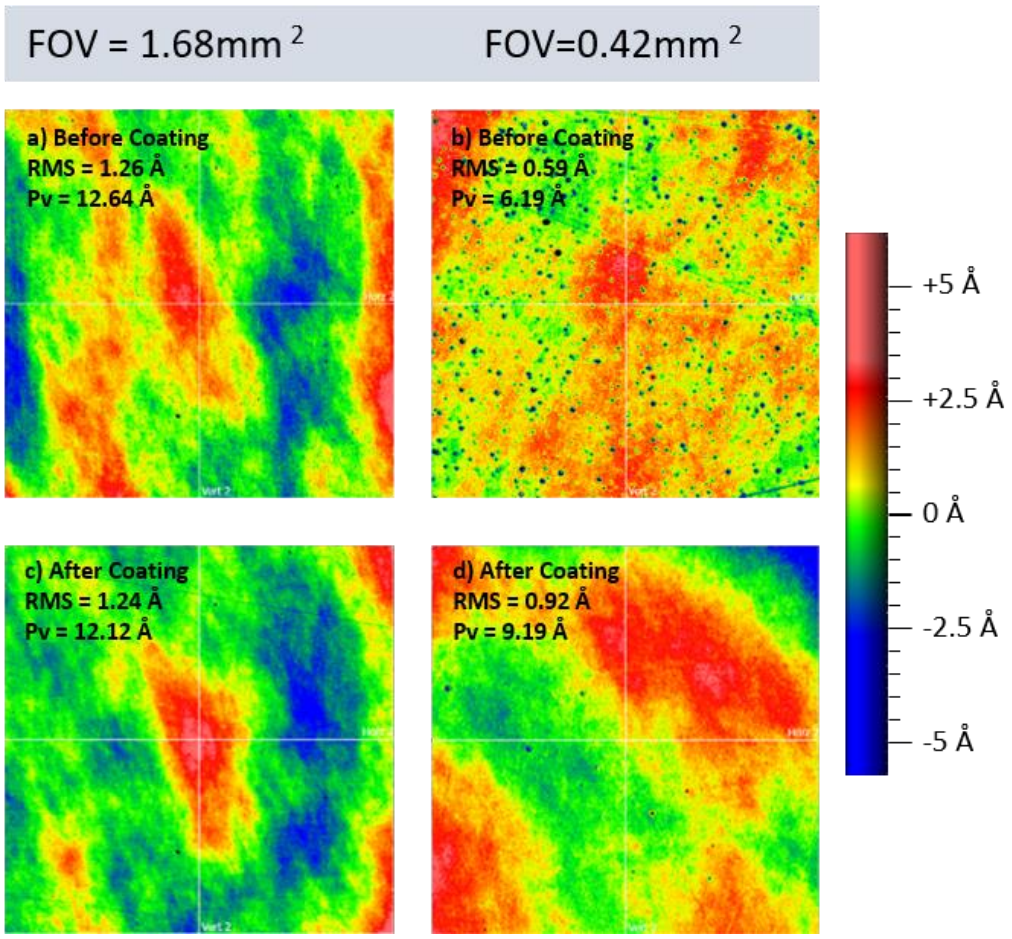

Figure 3.22: Mirror surface before coating (a-b) and after coating (c-d). The images shown here were taken at approximately the same location. Measurements at seven locations were averaged for the results in Table 2. The images on the left, (a-c), have pixel resolution of 1.64 µm, while pixel size for (b-d) is 0.41 µm. The images are normal for a super-polished silicon substrate and indicate that, with the deposition parameters used and thickness coated so far, Ti/Rh can be used for profile-coated x-ray mirrors. The small craters in mostly (b) but also in (d) are addressed in the text.

The results at the time of this writing suggest that Ti/Rh appears appropriate to use for profile-coated x-ray KB mirrors. A spherically polished substrate was profile-coated into a general elliptical shape (albeit with significant height errors) without any apparent delamination, adhesion, or film stress issues. Rh has long been used as a surface coating on x-ray mirrors for certain energy ranges, in particular where other materials have absorption edges. However, the total thickness required to reflect is usually only 30 nm or so. Profile-coating requires film thicknesses two orders of magnitude thicker than is commonly used for total external reflection mirrors because the material is used not only as a reflector but also to shape the surface, so it was unknown how well the material would perform for x-ray applications with this significantly added thickness. Initial roughness measurements indicate the mirror will reflect sufficiently.

3.3 Discussion and Future Work

Profile coating is a method whereby a precisely shaped mask is used to partially block deposition flux in order to selectively deposit a film thickness gradient or profile on a substrate in one dimension. Profile coating is a viable alternative to sub-aperture methods for surface figure modification. The main advantage to profile coating compared to sub-aperture methods is time and efficiency. In order to deposit multilayers with either a uniform or a thickness gradient, a shaped mask is universally used, along with (occasionally) velocity profiling. Profile coating is a computationally correct method for producing thickness profiles in thin films. Ion milling with a profiled mask[105] has also been demonstrated by others. Aspherically figured mirrors have been produced that provide near diffraction-limited performance at x-ray wavelengths. Profile coated mirrors have been built into several beamlines at the APS, and have also been used at other synchrotrons, such as the ESRF. A new dedicated profile coating deposition system was designed, built, and commissioned at the APS. This machine has produced several sets of multilayers and KB profile-coated mirrors. Profile coating was developed by staff at the APS using Au as the deposition material. Cr/Pt has replaced Cr/Au because Cr/Pt provides significantly longer mirror lifetime. Ti/Rh appears to be a promising alternative to Cr/Pt and expands the usefulness of profile-coated mirrors to a wider range of wavelengths.

From a manufacturability viewpoint, it would be beneficial to the profile coating process to explore alternative means to fabricate the masks. Currently, masks are produced with an expensive EDM process. Simple CNC machining may be a cheaper alternative, at least for a subset of applications. Exploring methods alternative to standard machining processes may lead to a creative way to produce masks such as some sort of printing and etching method.

Both Au and Pt were found to exhibit sufficient performance regarding surface roughness, adhesion, and film stress. Through long term testing and beamline usage, Pt was found to last much longer. Ti/Rh profile coatings have also been initiated as a way to extend the useful wavelength range of profile coating. The Ti/Rh mirror pair has not yet been tested at wavelength. No issues are expected since Rh has been used for years on x-ray mirrors, albeit at significantly less film thickness. It is likely that Rh will perform similar to Pt, but time will be needed in order to draw any conclusions. In any case, it will be useful to have data on longevity of this mirror set.

Although Ti/Rh has been explored for spherical substrates, Cr/Pt is still used almost exclusively. It is anticipated that damage thresholds and lifetime for both of these material systems will be similar: this is certainly the case with conventional uniform reflection coatings used currently. Roughly similar numbers of both Pt and Rh coated mirrors are stripped and recoated every shutdown cycle at the APS. It is likely the case, however, that the source of the performance reduction for simple metal-coated mirrors and profile coated mirrors is different. While the fabrication of these mirrors is relatively inexpensive, beamline scientists still report that the mirrors undergo some sort of changes over time, both in a loss of efficiency as well as spot size. Although the root cause of these changes has not yet been determined, two hypotheses are: (1) the thick platinum layer is slowly crystallizing during intensive irradiation, causing both a figure change due to stress relaxation and beam loss due to diffuse scattering and (2) the chromium adhesion layer is diffusing into either the platinum or the native oxide on the substrate (or both) and is causing a loss of adhesion, eventually leading to complete failure of the mirror.

Even though Pt profile coatings last much longer than Au, it is likely that there is always going to be some instability (or at least some manifestation of lifetime limitation) in the mirror figure when this class of metals is used as a structural filler. Instead of exploring how to stabilize platinum, new materials (beyond the precious metals) involving ceramics and alternative adhesion layers should be investigated for feasibility as a figuring medium. The last, thin coating for reflection will still need to be a precious metal due to optical constraints.

Future work will involve examination of other material systems to replace the precious metals as the filler. Wsi_2 and Al-Si have been deposited to extremely thick levels, but as a component in a bilayer for MLL as detailed in Chapter 4. For example, Aluminum with 5% silicon maintains less than 2.5 Å roughness after even 100 µm of multilayer deposition. One of these materials may possibly be a candidate for profile coated mirrors. There are other refractory materials that may also be good candidates to test. Solutions for depositing a thin reflecting layer as a final step on top of a thick profiling material should not be terribly difficult to explore. Profile coated mirrors will likely be useful for many years to come due to the relatively fast production systems put in place at the APS. However, it is possible that there may always be some level of degradation when a mirror utilizes a thick coating. Deterministic ion-beam figuring, widely used in industry, is also being explored at synchrotron facilities but is not yet at the level of optics production. Both the BNL deposition system and the APS modular deposition system installed a large ion mill with a long slit style source for figuring.

Before new materials can be discussed, it is worthwhile to mention the various properties that come into play when considering a new profile-coating material. The material must have very high adhesion to either the base substrate material or an intermediate glue layer. Most metals have high adhesion to chromium, for example. The material must be relatively low stress. High film stress can warp the substrate, contributing to figure error, or can become a source of instability in the mirror figure over time as the stress relaxes. The material must be radiation resistant and temporally stable. A good example of a poor material choice is Au. Au is known over time to diffuse on the microscopic scale. This diffusion causes figure changes over time. A method to deposit the new material must exist whereby the surface of the material is still sufficiently smooth even after many µm of deposition. However, other materials, such as chromium, are extremely difficult to keep below 5 Å roughness even after several 10s of nm of deposition. Lastly, some solution must exist for which an appropriate top-layer reflective material can be deposited. This may imply yet another intermediate adhesion layer. These experiments are discussed in the next section.

One obvious limitation with profile coating is due to the geometry of the process. The mirror must be translated with the long axis perpendicular to the coating direction. This means that the deposition system, cathodes, and masking sizes must match the length of the mirror. With some synchrotron mirrors over 1 meter in length, profile coating becomes impractical. Also, each individual coating and target requires a unique mask for use. The accuracy of this mask degrades as the target profile changes over time.

The complimentary technique, velocity profiling, eliminates many of these constraints. With velocity profiling, a fixed mask is matched to a lateral profile and sputtering target while the long axis of the mirror is oriented in parallel to the translation axis. The velocity of the mirror is accurately modulated in order to raster-scan the mirror across this deposition flux. To a first order approximation, the velocity at any point on the mirror is inversely proportional to the

amount of film deposited at this point. This technique has the potential to produce very accurate, long mirrors with an arbitrary figure (as long as the profile is a continuous function). The process was first attempted for synchrotron optics over a decade ago at the APS[10], and has more recently been demonstrated by others[106].

Velocity profiling mechanics have been tested with two different systems. The servo-based profile coating system at APS has demonstrated a velocity error of below 4 μm/second RMS. Laterally graded multilayers for 80 keV focusing were produced using velocity profiling on the BNL MLL Deposition System. The APS Modular Deposition System has similar capability. However, at the present time, no attempt has been made to use this capability for figure correction. The APS Modular Deposition System is being outfitted with equipment that will enable in-situ surface metrology of mirrors for velocity profiled (deterministic) ion-beam figuring for figure correction.

Chapter 4. Multilayer Laue Lens

4.1 Motivation and current status

Over the last few decades, the x-ray microscopy community has seen tremendous technical advances in nano-focusing optics for hard x-rays. These advances are driven by scientific interest in nondestructive measurement methods that can be used to investigate the internal properties of matter. Hard x-rays provide excellent structural and elemental sensitivity while offering fantastic penetrating power. These properties nicely complement certain in-situ investigations where electron microscopy is not appropriate. Multilayer Laue Lens (MLL) is a relatively new class of x-ray optics that deliver a clear path towards realizing nanometer-level spatial-resolution in the hard x-ray wavelength range. The various types of hard x-ray nano-focusing optics in use today are discussed in Chapter 1. Fabricating an MLL via thin-film deposition provides a method to achieve a linear Fresnel-zone plate structure with zone widths below 1 nm, while retaining a virtually limitless aspect-ratio. Despite its similarity to the Fresnel-zone plate, MLL exhibits categorically distinctive focusing properties and their fabrication comes with a wide array of challenges. This chapter provides a more comprehensive introduction of MLLs, a short introduction to theoretical modeling, discussion on fabrication challenges, their current capabilities, and notable results from x-ray focusing experiments.

Several key properties or capabilities must be realized in order to fabricate MLLs capable of focusing at the nanometer level: growth of MLL films with large total thickness and accurate layer deposition, relatively low interfacial roughness throughout the entire multilayer stack, materials with appropriate optical properties, and defect-free post-deposition processing methods leading to usable x-ray lenses. The associated diffraction theory and x-ray microscopy instruments able to manipulate MLLs have been developed by collaborators and are topics which are outside the scope of this work.

While MLL fabrication has come a long way in the last decade, the effort is still very much in a development mode. Usable optics that satisfy minimum beamline requirements are just now starting to be deployed. It is necessary to outline the various types of MLL, as well as what the state of the art in MLL fabrication is today.

4.1.1 MLL Classification

MLLs are classified into four different types based on their optical illumination geometry and the presence or absence of layer thickness gradients, as shown in Figure 4.1[59]. A flat MLL is functionally identical to a linear FZP; wherein the zones are laterally uniform and parallel to each other, focusing normal-incidence x-rays. A tilted MLL is structurally identical to a flat MLL. However, the lens is tilted with respect to the incident beam which enhances focusing performance and efficiency. In a tilted MLL, all layers have the same tilting angle. In a wedged MLL, each zone is tilted at a different angle with respect to its central optical axis. This angle increases from the center to the outermost zone. In a curved MLL, all layers are curved to form concentric ellipsoids with a common focus. These four different types of MLLs exhibit characteristically different focusing properties due to their different degrees of dynamical effects [59]. As a linear focusing optic, an MLL focuses x-rays only in one direction, regardless of the type. To produce a 2D focused x-ray beam, a pair of MLL optics with different focal lengths

must be aligned; this arrangement is similar to that which is used with K-B mirrors. To reduce the complexity of alignment and eliminate other optical components such as a central beam stop, MLLs with only a partial structure are typically used in practical applications.

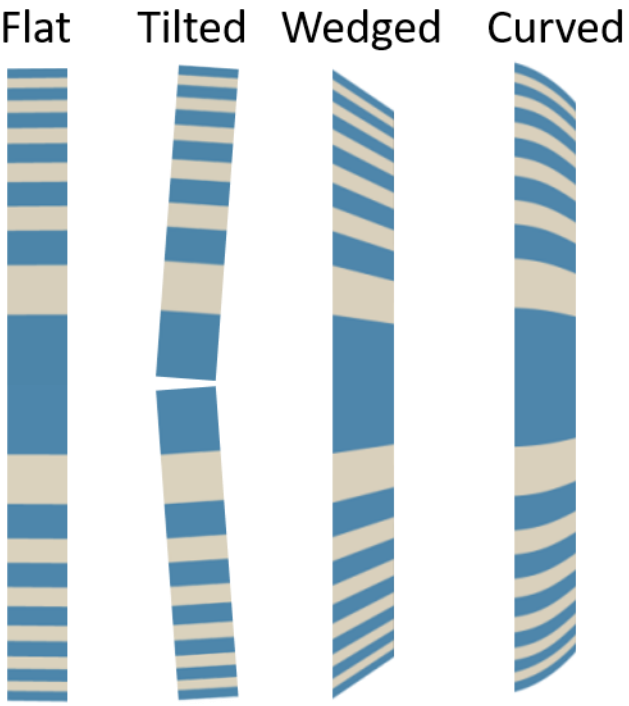

Figure 4.1: Schematic of the different types of multilayer Laue lens.

4.1.2 Theoretical overview of MLL

An MLL may be classified as a type of one-dimensional Fresnel zone plate. For a regular Fresnel zone plate, the structure must abide by the zone-plate law,

$$r_j^2 = j\lambda f + j^2\lambda^2/4 \qquad \text{(Eq. 4.1)}$$

where **j** is the zone index, $\mathbf{r_j}$ is the position of the $\mathbf{j^{th}}$ interface, **f** is the focal length, and **λ** is the wavelength. The performance of a FZP can be described with geometrical-optical theory [15,107] that results in a maximum efficiency of $\mathbf{4/\pi^2}$ for a zone plate where there exists a change in phase of **π**; or more generally, an odd integer **π** between two neighboring zones when absorption is ignored. For a structure with no absorption and only a pure phase change, an optimum structure thickness $\mathbf{t_{opt}}$ satisfying (eq. 4.2) produces the highest possible efficiency. This phenomenon is outlined more rigorously elsewhere[108]

$$\sin(kt_{opt}\Delta\delta) = 0 \qquad \text{(Eq. 4.2)}$$

Where:

$$k = 2\pi/\lambda \text{ and } \Delta\delta = \delta_A - \delta_B \qquad \text{(Eq. 4.3)}$$

When absorption is accounted for, the phase change for two neighboring zones is less than π at the optimum thickness[16]. As wavelength decreases, the thickness of the structure must correspondingly increase in order to maintain the highest possible efficiency. If gold zone plates are considered, an optimum lens thickness of about 2 μm is required for 10 keV x-rays. Due to fabrication challenges with lithographically produced zone plates, significant effort has been expended to develop stacked zone-plate sets[109] which when compounded produce a higher total thickness for increased efficiency.

The focal performance of an FZP is proportional to the width of the outermost zone. For first order focusing, the Rayleigh criterion states that the focus size **s** is related to the outermost zone width $\mathbf{\Delta r_{min}}$ as:[107],

$$s = 1.22\Delta r_{min} \qquad \text{(Eq. 4.3)}$$

It is clear that in order to produce both a small focus and high efficiency in the hard x-ray regime, transmission focusing optics must have extremely high aspect-ratios. To produce a 20-nm focus at 8 keV, the optimal aspect ratio, $\mathbf{t/\Delta r_{min}}$, is about 80. However, the highest reported lithographically produced aspect-ratio is about 28 for 20-nm zone widths [22], roughly only 1/3rd of the optimal aspect ratio and leading to low efficiency. While interesting methods have been introduced and developed in order to create gains in aspect ratios, the intrinsic limitations still remain[18,19,22-25,110].

The multilayer Laue lens was proposed to overcome these limitations on aspect-ratio[111]. Because the lens is fabricated by a thin-film deposition method, zone widths down to 1 nm and even below can be accurately produced. The thickness of the lens is dependent on the physical sectioning of the large deposited MLL substrate. Consequently, an arbitrarily large aspect-ratio can be achieved which leaves MLL essentially limitless in their applicability to focusing hard x-ray and boundless in energy range.

4.1.3 MLL Fabrication Challenges

Conceptualizing an ideal MLL with an aperture competitive to lithographically produced zone plates and an arbitrary section width is straightforward. Actually producing one is not. The technical challenges lie in meeting two requirements—total thickness and placement accuracy. Since beamline monochromaticity requirements are related to 1/N, with N being the number of layers in a stack, structures with several thousand layers equating to many tens of μm worth of aperture can be used today at most x-ray nanoprobes without a specialized high-resolution monochromator. This extreme film thickness, however, is far larger than any other multilayer thin-film applications that have ever been explored, aside from perhaps off-axis cut multilayer gratings [112]. On the other side of the coin, zone placement accuracy and interfacial roughness must be better than a fraction of the smallest zone width over the entire structure in order to achieve diffraction-limited focusing. For a 40% partial-aperture MLL with a 62 μm aperture (i.e. the full aperture would be 155 μm) and 4 nm outermost zone-width targeting a 10 nm diffraction-limited focus, the required zone placement accuracy is 1.3 nm over 62 μm, which corresponds to a thickness accuracy of 20 parts per million. The multilayer material system must exhibit sufficient interfacial properties and relatively low film stress. Furthermore, an appropriate deposition technique must be optimized to guarantee not only precise layer thickness at the nanometer level but also high stability in deposition rate over the entire deposition process,

which could take a few days or even longer. Indeed, the longest deposition run successfully attempted with the NSLS-II MLL deposition system was roughly 170 hours, or just over 1 week of continuous deposition.

4.1.3.1 Post Processing

Post-deposition processing is an essential step in MLL fabrication with its own slew of issues. The optimized lens thickness for WSi_2/Si MLLs targeting 10 keV radiation is 4 μm for a titled MLL [62]. Sectioning as-deposited MLL films down to a thickness of a few μm without introducing structural defects is not an easy task, in particular for MLLs with large apertures around 100 μm. Sectioning and polishing must produce a smooth surface finish without damaging the multilayer structure. This thin, wide structure is highly susceptible to bending or wrinkling, and the resulting curvature produces considerable aberrations in the x-ray focus. The 105 μm structure discussed below was first bonded to a diamond plate for rigid support in order to reduce bending during polishing. To date, mechanical polishing[45], deep reactive-ion-etching[46] and FIB have been used as post-deposition processing methods for circular MZPs and MLLs, although detailed discussion of post-deposition processing is outside the scope of this dissertation.

4.1.3.2 Zone Placement Error

It is commonly accepted that zone-placement error must be smaller than one-third of the outermost zone's width to assure its effect is negligible. This is an extremely stringent requirement. As an example, for an MLL with 50 μm aperture (half structure) and outermost zone width of 5 nm, the absolute error in zone position-placement must be smaller than 1.7 nm across the entire aperture of the lens. In practice, zone placement error is not truly random and usually follows some functional form due to an incorrect calibration or slow drift of the deposition rate. Such imperfection has little effect on the efficiency but induces significant phase-aberration, which results in a distorted, broadened focus. This kind of imperfection has been theoretically evaluated and accounted for in the context of dynamical diffraction theory[73]. Figure 4.2 shows the calculated change in the focus profile due to a zone placement error of ±5 nm across a wedged MLL with 5-nm outermost zone width and 50 μm aperture size. The overall aberration in phase is slightly more than π across the entire lens (for the same zone displacement error, the equivalent phase aberration is much smaller for inner zones). This simulation shows that this small (slightly more than $\boldsymbol{\pi}$) phase aberration reduces the central peak's intensity and enhances the side lobe's intensity. Reducing the phase aberration significantly below π is required to achieve diffraction-limited focusing performance.

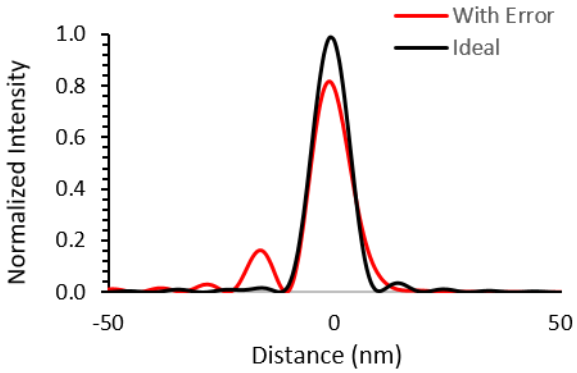

Figure 4.2: wMLL focus simulations, with and without layer placement error[81]. Simulated zone placement error of ± 5 nm in an MLL with 50 μm aperture and 5 nm-wide outermost zones is shown. This result in raised side lobes and also slightly increased focal size.

Intrinsic material attributes and problems in the growth environment dictate film stress, interface quality, and optical properties. The accuracy of layer placement depends on the deposition technique, instrument stability, and overall system repeatability. Physical vapor-deposition techniques, such as PLD[67] or sputtering[113-116] have been the most widely used due to their high rates of growth and excellent repeatability. This dissertation focuses on the considerations and challenges associated with using sputtering for fabricating MLLs as this is the most widely used technique for x-ray multilayer deposition[117].

As mentioned previously, initial MLL fabrication resulted in an aperture of 13 μm Deposited with WSi_2/Si in 100% Ar atmosphere. The MLL work produced for this dissertation yielded: near diffraction-limited MLLs due to the use of marker layers for deposition feedback (experiment 1); new material systems enabling both larger deposition thicknesses for increased aperture and wider sections for increased mechanical rigidity (experiment 2); MLLs with an aperture of 105 μm produced with WSi_2 and an aluminum-silicon matrix (experiment 3); and wedged MLLs for the ultimate in focusing and optical efficiency (experiment 4). Various MLLs produced for this dissertation have been examined by groups at synchrotrons around the globe. Huang et. al. demonstrated an 11 nm line focus[118] at 12 keV by reconstructing the far-field diffraction pattern from an MLL with 43 μm aperture.

By aligning a pair of MLLs, Yan et. al. reported a 2D x-ray focus down to a spot of 25 nm × 27 nm with 2% efficiency at 12 keV, and a spot of 25 × 40 nm with 17% efficiency at 19.5 keV[119]; this achieved focusing capability has been used for scientific investigations[120,121]. While outside the scope of this dissertation, it is worth noting that the instrument requirements for aligning a pair of MLLs to produce a 2D focus is far more complex than that of a FZP. To meet the stringent positioning requirements of MLLs and to obtain accurate scanning x-ray microscopy measurements, specialized MLL scanning x-ray microscopes were developed and are used for x-ray experiments[119,122-124].

4.2 Experimental Topics

4.2.1 Marker Layers

Of the many types of imperfections that can be found in an MLL, optical focusing performance is most affected by zone placement error because this error determines the phase aberration of the pupil function. Ideally, this error is required to be smaller than one third of the smallest zone width to ensure a negligible phase error. We take an MLL with 4 nm outermost zone width as an example. For such an MLL, no zone should deviate from their ideally calculated positions along the lens by greater than ~1.3 nm. One shall note this absolute position error is the summation of the accumulated error throughout the entire deposition, which means that for this example the growth accuracy has to be better than 0.01% for a total 13 μm deposition thickness. Such a stringent requirement gives rise to three challenges in fabrication: a deposition method that is highly reproducible, a metrology method that has sufficient spatial resolution to measure a small error accurately, and a way to incorporate the subsequent metrology data into the deposition to correct the growth error.

The growth accuracy requirement for an MLL is structure-dependent. That is, a thicker MLL with a smaller outermost zone width has a higher accuracy requirement. While the aforementioned MLL requires overall growth accuracy of 0.01%, a diffraction-limited, 100 μm half-aperture flat MLL for 5nm spatial resolution (2.5 nm thick zones) would require 12.5 times greater growth accuracy.

Just as reflective x-ray mirrors contain a complete spectrum of surface figure errors from the nanoscale to the macroscopic scale, MLL can also contain a complete spectrum of layer placement error. Layer placement error exists in MLL because there is always a deviation of the intended deposition rate. Spatial-frequency errors in the nanometer range (one layer to several layers) are considered here as high-frequency errors. High frequency accuracy in layer placement is easily measured by examining x-ray reflectivity measurements of relatively thin, periodic reflective-multilayers[82]. High-frequency error due to process instabilities can come from diverse sources such as fluctuations in the sputtering power supply, pressure transducers, or process gas flow. For example, the rates of reactively sputtered deposition are highly dependent on the ratio of gas species[125]. Minor fluctuations in this ratio can have a significant impact on deposition rate stability. Detailed discussion on high-frequency deposition errors due to process instabilities can be found in the chapter on reflective multilayers. A second source of high-frequency error unique to MLL (or other large-thickness depositions) is caused by plasma perturbations. During a long deposition such as is required for MLL fabrication, accumulated film built-up on the chamber's walls or the shields may flake off and cause a momentary short between the target and ground. This usually results in losing the plasma and produces an error in layer thickness or a skipped layer. Fortunately, these high-frequency errors in growth rate are correlated with easily measured parameters during deposition such as power supply output and process gas flow rate. If these parameters are stable, there is little need for post-deposition metrology (usually done with SEM imaging) to investigate every layer for high-frequency errors, and only low-frequency errors or gradual drifts require mitigation.

Since sputter deposition utilizes a fixed, solid source that is consumed over time, the deposition rates change throughout growth. Source consumption is the main source of low-

frequency layer placement error. The plasma bombardment continuously removes the target material and alters its shape non-uniformly. As the target erodes, the distribution of plasma density over the target changes due to surface and magnet geometry. This erosion also gradually increases the distance from the target to the substrate, resulting in further deposition rate decay. When considering deposition of a few hundred layers, such as when a reflective multilayer is fabricated, a clear solution is to use physically larger magnetrons. If the magnetron source and target are sufficiently large, the change in growth rate due to target erosion is usually low enough that it may be ignored for deposition of just a few hundred layers. As discussed in Chapter 2, the 75mm diameter target size common in most of the older APS deposition systems and the NSLS-II MLL deposition system all require some level of layer-by-layer deposition rate compensation for most reflective multilayers due to their relatively small size. Other machines designed specifically for reflective multilayers such as the equipment at the ESRF or the APS modular deposition system do not. Unfortunately, even the largest commercially available planar cathodes will still suffer from deposition rate decay due to erosion during the long deposition times required for MLL fabrication. Consequently, only a finite thickness of material can be deposited from a fixed target while maintaining good control of the accuracy of the layer thickness. Another method that can potentially mitigate target erosion is to employ cathodes with rotating magnet arrays rather than fixed ones[126]. The magnet pathway is designed to optimize sputtering evenly across the target's entire surface, greatly increasing target utilization which results in a much slower rate of decrease of the deposition rate. Another related method is to rotate a cylindrical target around a fixed magnetic field[127]. Sources with moving parts (whether this be magnets or the target) would provide significantly decreased long-term growth rate decay with the technical cost being both decreased reliability and (potentially) deposition rate fluctuations over short time scales. This would be manifested as something akin to "intra-layer noise". Even with these types of sources, some level of growth rate change during MLL deposition would be expected. When the deposition technique causes an intrinsic change in growth rate over time, some way to compensate for it must be included in the system. With fixed sources, the growth rate decline is slow during the initial stages of deposition. Although the magnitude of erosion is roughly proportional to target consumption (i.e. deposited film thickness), the growth rate decline for a thick MLL progressively accelerates and follows a complicated profile that is related to the change in target erosion geometry and is dependent on the magnetic field distribution of the magnetron source.

4.2.1.1 Deposition Geometry

Another factor affecting the growth rate stability is the deposition geometry. Four different deposition geometries are feasible. All of these different geometries are fairly simple to execute for the deposition of MLL because their small physical size makes mounting and fixturing an easy task to undertake. Each deposition geometry features different strengths and weaknesses. The very first MLLs were produced in the APS Large Deposition System which employed a linear translator and upwards-facing cathodes. This geometry offered straightforward mask design but suffered from target shorts due to flaking during long deposition runs. The mechanical substrate translator in this machine cannot provide repeatable, stable velocity which means that individual layer thickness error is quite high. The second geometry has fixed sources aimed horizontally towards a rotating drum. Substrates are mounted vertically, on the drum's round portion. Multilayer fabrication is accomplished by rotating the drum back and forth sequentially across the deposition sources[72]. Chapter 1 explains details and presents figures on

the MLL rotary deposition system at the APS. With this rotating geometry, the deposition of the substrates follows a circular path. Substrates must pass back and forth across a fixed aperture, with the radial distance or mask width opening defining the angular translation distance of the substrate. As the number of sources increases, the required angular motion rises proportionately. Mask fabrication for this geometry is complex because the masks must not only be cut to provide the requisite vertical film thickness profile, but also bent or curved in order to follow the radial motion of the substrates if good transfer of the film thickness profile is required. The first wedged MLLs (discussed later in Chapter 4) were produced[38] with the rotary deposition system shown in Chapter 1. Another very common rotational geometry has cathodes aiming upwards, and the substrates are fixed to the base of the drum; here, the substrates follow a flat path for deposition. Rastering the substrates through the deposition flux while they are spinning produces multilayers with high intrinsic lateral uniformity; this can be a satisfactory technique for depositing MLLs with flat zones. This technique is heavily used for deposition of precision optical coatings that are physically small with relatively thin coatings (such as single layers or some simple visible-wavelength optical coatings), however, just as with the APS Large Deposition System, target shorts due to flaking during the long deposition times required for MLL would limit total deposition thickness. Often, individual deposition systems can be reconfigured to operate with either geometry[128]. The last geometry utilizes a linear translation of the substrate past fixed sources mounted horizontally. This geometry was employed for fabricating coatings for synchrotron x-ray optics[129], and was adopted in the advanced MLL deposition system at the NSLS-II[75] as well as with the APS Modular Deposition System. Substrates are loaded vertically onto a linear-translation stage or cart that moves one-dimensionally on a stationary base and rail assembly within the vacuum system. The substrate translation system provides high-precision scanning while maintaining vertical planarity, or "trajectory of motion". Since fixed targets have a limited total lifetime due to the removal of material, a simple mitigating solution is to increase the number of cathodes used. The NSLS-II system has nine cathodes which can be activated sequentially, for depositing layer by layer, thus dispersing the effect of target erosion across several sources. Since this method reduces the consumption of individual cathodes, the probability of encountering plasma perturbation effects due to flaking is proportionally decreased. One source is sufficient to deposit a thickness up to 25 μm. Four cathodes are used to fabricate an MLL with a 100 μm aperture. When the overall deposition thickness breaks this thickness limit, more cathodes can be employed as required. These modern machines do not have any performance issues related to mechanical systems that can impose layer thickness error due to precision in-vacuum motion systems. More details on the design and performance of these machines can be found in Chapter 1.

The various deposition geometries impact growth stability and efficiency, and provide different levels of film deposition flexibility. It has been found that horizontal deposition geometries such as those found in the APS rotary system, the NSLS-II Multilayer Laue Lens deposition system, and the APS Modular Deposition System provide the highest level of immunity from flaking events. Efficiency is (in part) related to the amount of deposition flux that reaches the substrate compared to what deposits on the shielding or surrounding components. Wedged MLL masking (discussed later) is intrinsically less efficient in this regard compared to flat MLL masking.

4.2.1.2 Growth monitoring limitations

The growth rate of thin films can be characterized in any number of ways. A large number of in-situ methods for monitoring growth rate or deposition thickness are available[50], however none of the currently available instruments are particularly suited to the demands of fabricating MLLs. Quartz crystal monitors (QCM), the most common instrument for in-situ rate monitoring, provide an accuracy of at best 0.5% of the total thickness, and are highly dependent on crystal temperature stability and geometry. Another issue is the total accumulated growth. Over time, the deposition accumulates on the crystal which eventually causes it to fail. Utilizing a shutter to impose a partial duty cycle on the monitor proportionally reduces the accuracy. Direct optical thickness measurements such as distance-measuring interferometry would need to find solutions to the problems of substrate and carrier thermal expansion, mechanical instability, and many partial reflections through the topmost layers. Obviously, techniques for monitoring the deposition of a single atomic layer are unsatisfactorily slow and mostly appropriate only for crystalline growth. Although computational algorithms for multilayer thickness fitting with ellipsometry exist, accuracy is highly dependent on good prior knowledge of film optical constants. A promising in-situ tool for monitoring real-time deposition rate would be a stable and accurate atomic absorption flux monitoring system[130]. The operating principle for an atomic absorption flux monitor is quite simple. A UV light beam, matched to the absorption energy of the species of interest, passes through the flux coming from the source. The resultant attenuation from resonant atomic absorption by free atoms (or molecules) in the vapor phase is measured. This attenuation is proportional to the atomic number density within the illuminated volume, which in turn corresponds to the deposition rate. By simultaneously monitoring multiple species, film composition can be tightly controlled. Unfortunately, existing commercial solutions deploying this technique suffer from long term deposition rate measurement instability due to lamp luminescence variations. An SBIR topic for advanced in-situ thin film growth rate monitors drafted specifically to assist with MLLs fabricated using techniques developed by Conley, et. al., produced multiple winning Phase 1 awardees for Fiscal year 2015 and two winning Phase 2 awardees for Fiscal year 2016, with the express intent being development of an in-situ growth monitoring technique sufficient for MLL fabrication. The details and results of this project are outside the scope of the dissertation however it is expected that the technical outcome will be utilized in the near future for MLL deposition at both the APS and NSLS-II.

Ex-situ methods must be considered, despite the obvious disadvantage of not giving an instant feedback, and requiring a deposition process featuring adequate reproducibility to iteratively correct for growth decay. Among the techniques available, x-ray reflectivity (XRR) is widely used for gaining information on multilayer performance and for evaluating deposition rate. In addition, XRR is extremely sensitive to interfacial roughness or intermixing. When a material system and deposition technique are considered for multilayer deposition for MLL, simple periodic multilayers must be grown before the deposition for obtaining reflectivity measurements to determine the growth rate and quality of the interfaces. However, XRR has not been reported to be directly applicable to evaluating final MLL structures due to its limited penetration.

4.2.1.3 SEM metrology methods for sectioned MLL

Since, as mentioned, conventional rate monitoring is unsatisfactory, an ex-situ metrology approach based around scanning electron microscope (SEM) imaging was developed. All MLL metrology ends up with quantifiable data based on images, so the data within the images needs to be digitized for subsequent calculation. The first generation of metrology investigated individual layer thickness. In order to extract quantifiable data from an image, metrics must be employed that assign a physical size to individual layers in the stack. A matrix constructed with x, y, and z values for pixel location and brightness forms the basis for image processing. Standard image processing techniques employ a square or rectangular aperture for nearest-neighbor based relationships. However, due to the inherently vertical nature of the MLL images, a "cross" aperture is used, where last-in-first-out (LIFO) scrolling buffers are constructed both horizontally and vertically about each side of the pixel in question in order to determine the average intensity. Comparing the average intensity of the horizontal buffer versus the vertical buffer for each pixel then allows for a binary image to be constructed, where 0 (black) represents material A and 1 (white) represents material B. A numerical comparison between the vertical average with the horizontal average selects which material to assign to the pixel in focus.

Average layer widths are calculated with the data from the previously obtained binary image. Iterating over each row, a state variable is set to the first found layer type - i.e., it is initialized to the first pixel in the row. When the opposite color is found, the pixel width of the layer is recorded, and the state variable is toggled. Due to poorly selected image regions by the user or imperfections in the original SEM images, the number of layers detected per row might differ. In this case, the mode (or most often observed) layer count is used, and rows that differ from this number are discarded. After averaging all of the valid layer widths, the data of interest has now been obtained. Error in the measurement is reduced by selecting as large as possible of a region to process. A simple conversion factor for assigning physical widths to pixel quantities is performed by measuring the scale width found in the SEM image overlay.

An additional problem associated with SEM image metrology for the purposes of image digitization is small amounts of inadvertent rotation. Image acquisition through visual alignment has been found to be accurate to about 2 degrees. This rotation is manually corrected in the software with simple rotation transforms. Final binary conversion and image tilt are illustrated in Figure 4.3, below.

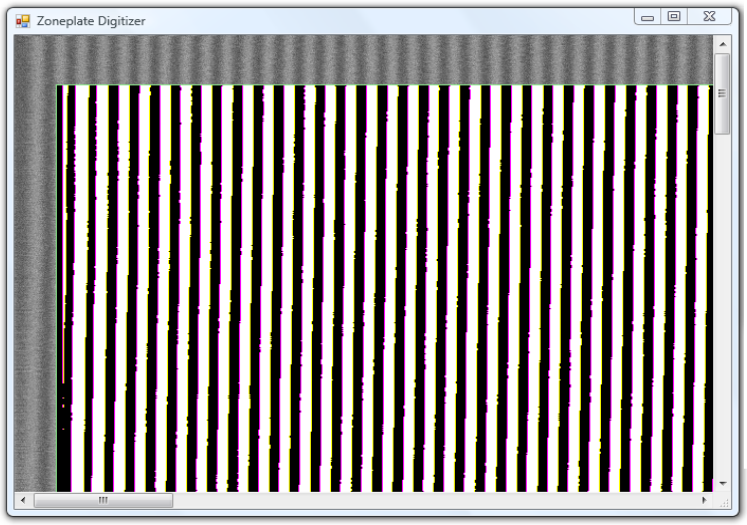

Figure 4.3: MLL image digitizer illustrating binary material selection. Also evident is the tilt which must be corrected for.

Individual data sets are combined and a final plot of the inverse of d-spacing versus layer position provides quick visualization of layer errors, as seen in Figure 4.4, below. Layer thickness noise, seen as high-frequency variations in the data, are found to be an artifact of this metrology method because multiple SEM images of a single location produce a similar line form, but with significant variation in the noise. A linear fit with the data is used to develop deposition rate correction factor which is used for the next deposition iteration.

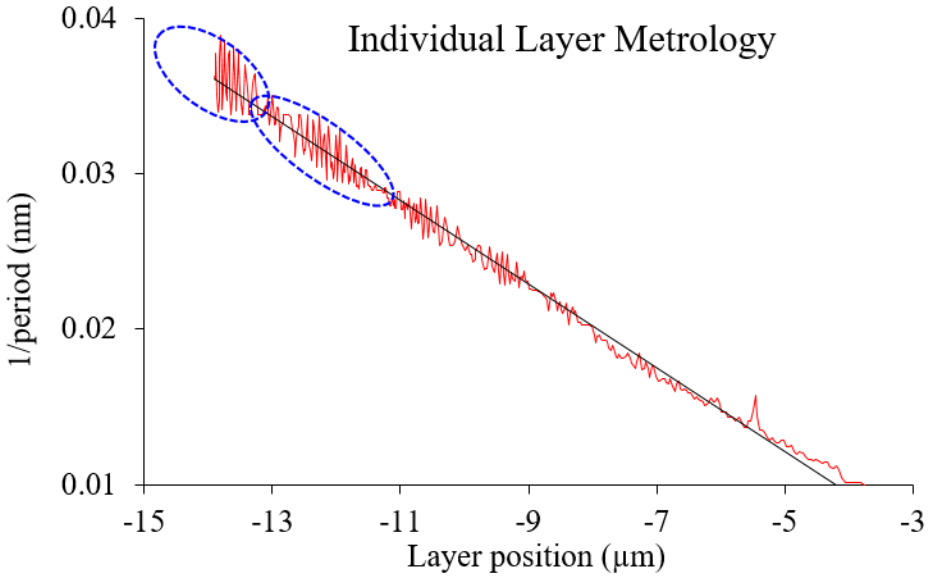

Figure 4.4: Line profile plot of processed SEM data for an early bonded MLL. An ideal MLL plot would be perfectly linear. Noise in the data (circled) increases as the layer width decreases.

4.2.1.4 Marker layer details

As MLL's fabrication matured to an outermost zone width approaching the resolution limit of standard SEM instruments, and a total deposition thickness over 40 μm for a higher NA and larger acceptance aperture, relying on individual layer thickness identification becomes unsuitable in two aspects. First, the limited spatial resolution causes a measurement uncertainty that prevents an accurate determination of d-spacing value. This can manifest as noise in the data, or as skipped or mis-counted layer numbering when layer widths approach the single pixel level. Second, the limited field-of-view requires many images to be stitched together without any error. Due to significant imaging aberrations inherent in the data, image-based stitching is insufficient. The alternative, which is to stitch 2-dimensional line data, must rely on SEM stage position feedback for proper alignment. This often leads to discontinuity in the overlap regions. The effect of this is highlighted below in Figure 4.6 of a 68 μm thick MLL.

In order to address these two challenges, we utilize marker layers for MLL characterization. Marker layers are zones with triple (or greater) nominal width inserted into the MLL during the growth in an aperiodic manner. The aperiodicity is gained naturally by inserting marker layers at regular layer number intervals. Since layer thickness slowly increases as an MLL is deposited, the spacing between each subsequent marker layer increases. This provides a unique spacing between each and every marker layer allowing exact identification without any data from neighboring images. Because the width is tripled, the mark layer provides sufficient contrast in order to ease identification and imaging in SEM and allows a fitting algorithm to be used to obtain sub-pixel accuracy of its position. The aperiodicity between marker layers ensures correct stitching of overlapped images without ambiguity as well as freedom from having to rely on image positioning for stitching. Using this method, we are able to measure the deviation of zone position of an entire lens with no aperture limitations down to ~ 2 nm.

Marker layers have been implemented within the MLL growth whereby the positions normally occupied by an individual layer, or grouping of layers, are intentionally "consumed" by one material. After the marker layer is grown, normal MLL deposition continues unaffected. As the goal of the marker layer is to provide an artificially thick layer within the stack without disturbing the normal position of subsequent layers, the marker layer thickness is the summation of an odd number of layers, as shown in Figure 4.5. By imaging only these marker layers within the MLL, the sub-aperture stitching overlap error is eliminated as the gap between marker layers can be several hundred nanometers or more, which is far greater than the stage uncertainty in any modern SEM. As the marker layer thickness will be a multiple of the nearby layer thickness, lower magnifications can be used to image the MLL.

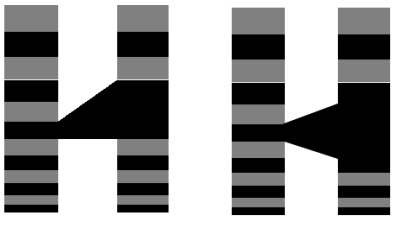

Figure 4.5: Two methods of marker layer generation. Generally, conversion of three layers is sufficient. For large total deposition thicknesses combined with small outermost zones, any number of layers may be consumed by the marker layer to aid in identification.

In order to test both the marker layer concept, as well as make progress on the 100 μm thick MLL goal, a 68 μm thick MLL was grown with reactive sputtering for stress minimization (data for which is shown in Figure 4.6) comprised of 8,058 layers with an outermost zone width of 4 nm. This MLL was the first grown using a regular spacing for marker layer insertion. Unfortunately, at the time of the growth, an error of a factor of ten was included in the growth software, and so the intended marker layer spacing of ~4 μm turned out to be ~400 nm. Almost 50 SEM images were required in order to capture every layer for processing as described in the original method. Indeed – the last two SEM images (of the smallest zones) were not of sufficient magnification to reliably extract layer thickness, which is why the plot becomes discontinuous from 0 μm to 3 μm. At the magnification used, individual layer metrology is clearly very noisy, with the noise level approaching 0.01 nm^{-1} for the smallest zones. The periodic, downward impulses are the 175 marker layers that were inserted within the structure, again, due to a software error. Only 17 marker layers were intended for fabrication.

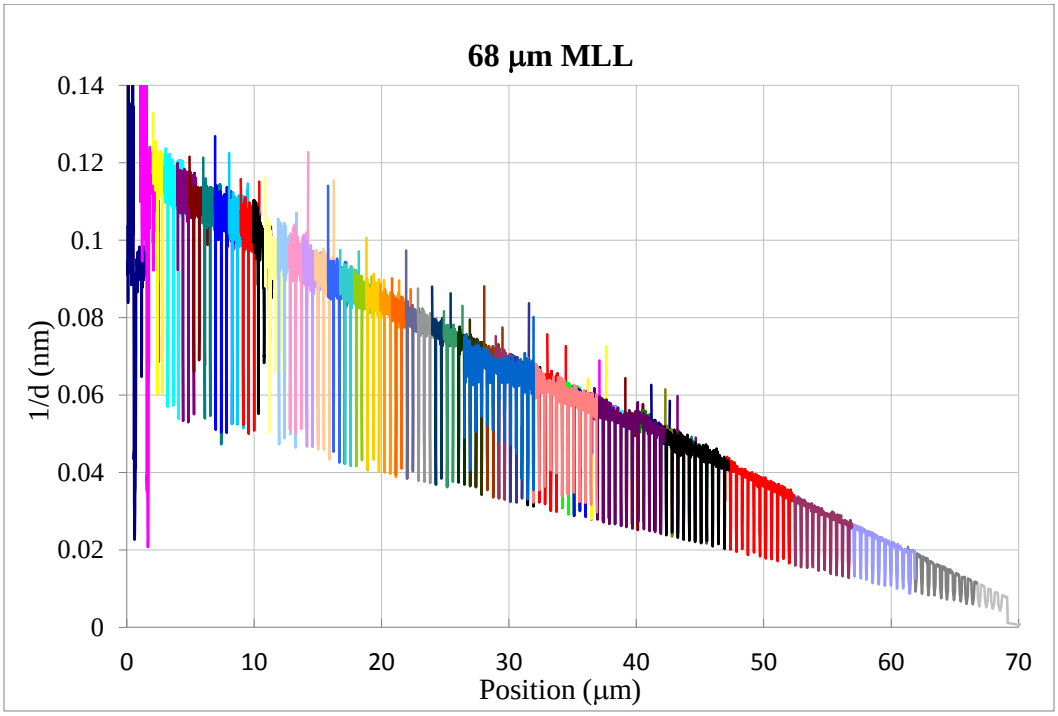

Figure 4.6: Individual layer metrology for 68 μm thick ML grown with marker layers. Data was analyzed with the method first described above. The sub-aperture overlap error and high frequency layer thickness noise in the data introduces significant measurement uncertainty.

Marker layers can be inserted into the MLL stack in many ways, with the general goal to insert markers often enough to capture any deposition rate errors that are expected, with layers sufficiently thick for clear identification, while minimizing the amount of the aperture they displace. A series of 43 μm thick stress-reduced MLLs were grown using four cathodes in the

NSLS-II deposition system. Marker layers were inserted every 512 layers during the growth of 6,510 layers, equating to a total of 12 marker layers. This is shown in Figure 4.7. The marker layer spacing varies with position, from ~2 μm at the bottom, to ~4 μm at the top. A total of 36 layers were consumed by marker layers out of 6,510 total layers, for a total of about 0.5% reduction in total aperture.

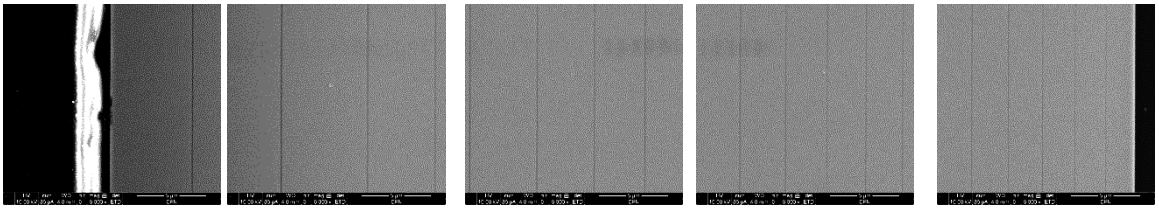

Figure 4.7: SEM image set covering entire 43 μm aperture of the MLL. The 12 marker layers (some imaged more than once for intentional overlap) are seen in the images as dark lines and are used to determine the zone placement error down to the nm level. Because gaps between two reference layers differ, image stitching can be done automatically with no sub-aperture stitching error.

The SEM data for this MLL was analyzed as was done previously where discernable layers are converted to a binary value, and an average pixel distance between layers determines layer spacing. In order to visually remove noise from the plots generated via individual layer position metrology, only the marker layer positions are displayed below in figure 4.8. The inverse d-spacing profile is shown on the left, and a linear fit where position error is visibly clear is shown on the right.

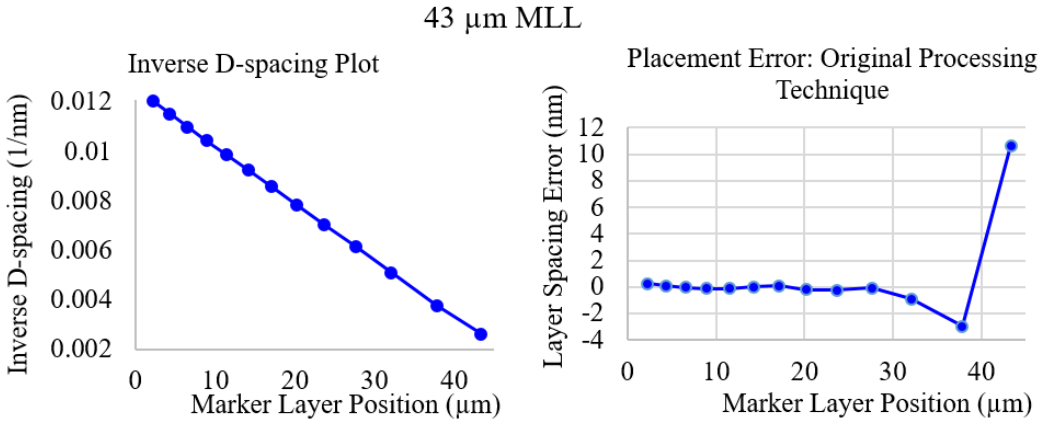

Figure 4.8: MLL layer placement metrology using the old technique. Individual layer noise was removed, and only the marker layers are highlighted for clarity. The data suggests that the MLL is quite linear with only a slight kink for the last few μm of growth.

The same data set when utilized to interrogate only marker layer spacings indicates layer placement error in the +/-100 nm range as seen in figure 4.9 iteration 1. The vastly differing error profiles shown between Figure 4.8 and 4.9 are attributed to accumulated error intrinsic to the original (individual layer) metrology method. Noise within the data means that layers might be missed, or counted multiple times. Binary conversion introduces error including reduction in resolution or lateral shifting. Marker layer metrology was utilized to produce four iterations of

this lens series, with successively lower error in each iteration. Figure 4.9 shows marker layer placement error of these four iterations starting out at about +/-100 nm and ending at +/- 3.5 nm.

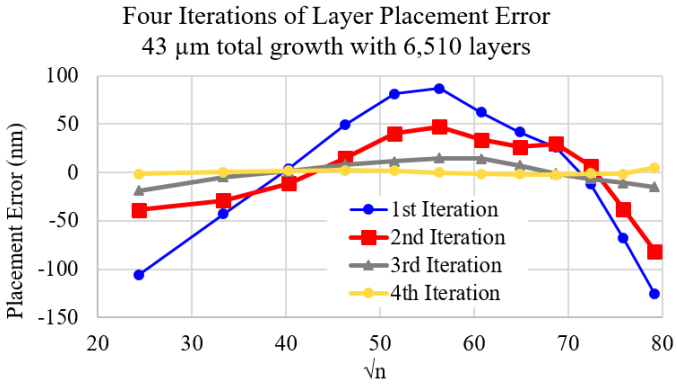

Figure 4.9: Marker layer position error of the 43µm thick MLL. Four iterations of deposition were used to reduce placement error.

One unknown with this method of metrology is how much the absolute layer spacing measurement from scanning electron microscopy can be trusted. The progressively smaller error from Figure 4.9 suggests that the measurements are repeatable, but this does not necessarily indicate any level of absolute measurement accuracy. Conceptually, multiple possibilities exist for the inclusion of measurement error. Slight frame-to-frame variations in magnification may exist. Pincushion effects may be sizeable. Charging from the sample can distort imaging. The electron beam interacts with the sample to a depth of only the top µm or so. Since the MLL sample surface is processed (via polishing or FIB) before imaging, there is also the possibility that the SEM is imaging distortions in the surface that are not present in the bulk. In order to investigate these possibilities, the first iteration 43 µm MLL was also measured with a transmission x-ray microscope (TXM) at the NSLS. The TXM measurement is sensitive to relative absorption and transmission contrast through the entire bulk of the MLL, so any potential errors only on the surface of the optic do not impart error in marker layer measurement. As can be seen in Figure 4.10, the SEM versus TXM measurements are very similar.

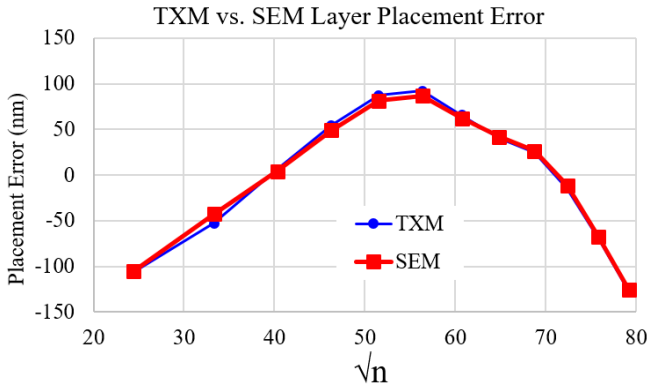

Figure 4.10: Marker layer error measured with both TXM and SEM. Measurements are of the 1st deposition iteration of the 43 µm MLL. Even though both microscopes operate under very different principles, the measurements are quite similar. This result suggests that SEM can be utilized reliably for MLL layer placement metrology.

Figure 4.11a below shows the residual error as a function of sqrt(n) of the fourth (and final) iteration of this lens. The error is within +/-2 nm over the majority of the lens, and has a steep increase in error only across a small region of the thinnest layers. This error is only observed in the last marker layer. This region is deposited first in the multilayer, so this error may be caused by the system initially ramping up to a stable temperature. This level of error was deemed acceptable for synchrotron testing. The small placement error allowed the measurement of a focus of 11 nm as measured with synchrotron radiation using this lens in Figure 4.11(b), very close to its diffraction-limited size of 10 nm[118].

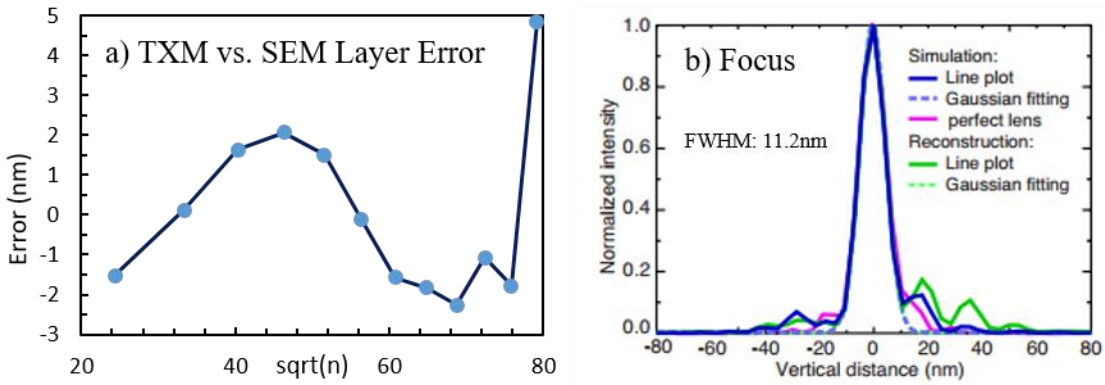

Figure 4.11: 43 μm MLL marker layer error and reconstructed focus. The 43 μm MLL has an outermost zone width of 4 nm, and a 4.2mm focal length at 12 keV. Layer placement error is shown in (a). Phase reconstruction of a beamline measurement revealed a focus of 11.2 nm (b), very close to the diffraction-limited size of 10 nm.

Marker layers have been imaged by SEM and an algorithm for layer detection has been produced. The iterative process of using a previous growth for feedback to subsequent depositions appears to converge. However, these have only been produced with marker layers spaced by 2 to 4 μm which should be sufficient to detect long-term growth rate error. While narrow d-spacing multilayer reflectivity measurements indicate very high layer-to-layer repeatability, these are only measurements of a few hundred bilayers. An MLL growth with variable marker layer spacings is planned in order to determine the threshold between high-frequency layer error and low-frequency layer error. MLL have also been imaged with TXM and this should be analyzed to determine if there is good agreement with SEM data. Marker layers have also only been produced with the spacer material (Si). It is unknown what real effect the inclusion of marker layers will have with both diffraction efficiency and nano-focusing measurements; experiments are planned at multiple beamlines around the world over the next year or so with these MLLs.

4.2.2 Explore new materials to extend the energy range

4.2.2.1 Introduction and motivation

The material systems used so far for MLL fabrication were chosen not primarily because of their optical properties for use in x-ray optics applications, but due to their physical characteristics. The pair of selected materials must exhibit what are sometimes mutually exclusive properties: sufficiently low interfacial roughness, low accumulated stress, high

adhesion to one another, and ability for the material to maintain bulk-like properties during growth[60]. The interfacial roughness and interdiffusion must be small enough to allow the obtainment of an electron density contrast profile through the depth nearly equal to the bulk of both materials. The primary source of multilayer fracture, delamination, and finally complete destruction, film stress, needs to be low enough to withstand not only failure after deposition, but also during the subsequent slicing or sectioning processing. These issues are discussed in further detail in experiment 3 regarding the goal of larger aperture MLLs.

The optical properties at x-ray wavelengths of the materials are often considered next. A few common material systems used for surface diffracting (reflective) multilayer synchrotron applications are W/B_4C [131,132], Mo/Si, and W/Si [133]. The significant optical contrast between these material systems would produce adequate MLL optics. However, each of these systems has different weaknesses. For example, B_4C exhibits high intrinsic compressive stress[134] which means that attempts to produce multilayers with large overall thicknesses may fail due to delamination or crazing. B_4C [135]deposition rates are also very low, so the length of time required for the deposition process makes the growth proportionally more susceptible to outside influences such as ambient temperature fluctuations, instrument instabilities, or even service utility interruptions.

One pair of materials that are found across a large spectrum of multilayers is Mo/Si [2]. While this material system can be grown with extremely thick d-spacings and total overall growth thicknesses (useful for expanding the aperture as discussed in Experiment 3), Mo and Si mix chemically at the interface to form a Mo_xSi_y interdiffusion layer[136]. This interdiffusion layer (and other atomic processes such as back sputtering) is well understood to produce a nonlinear deposition rate response[137] during the deposition of the first couple nm of each new layer in metal/silicon material systems (or any material system that is chemically reactive). This metal-silicide formation must be carefully accounted for or controlled during MLL deposition, particularly for thin layers. Multiple calibration runs with various dwell times can be performed to predict an approximation of growth rate vs. layer thickness, and this is especially useful for fabrication of periodic structures. Accounting for this nonlinear behavior during fabrication of a structure with large thickness variations (such as MLL) would add significant complexity. Indeed, this nonlinear behavior was verified experimentally via MLL fabrication of two identical structures, one with Mo/Si and the other with $MoSi_2$/Si[138].

As was mentioned in Chapter 1, incorporating a metal that is already a silicide was a significant success. Switching to a metal-silicide and silicon material system, such as WSi_2/Si or $MoSi_2$/Si, allowed higher total growth thicknesses[63] and also nearly eliminates the nonlinear growth-rate response caused by chemical intermixing.

Another parasitic side-effect of chemical intermixing at the interface besides the rate calibration complexities involves its impact on optical performance. A large, wide bilayer interface can reduce optical performance if the width becomes a significant proportion of the whole bilayer pair. In an ideal optical structure, the materials would provide an optical contrast perfectly sufficient to produce diffraction but without a default amount of absorption. As the interface widens, the optical contrast between the two materials becomes depressed and as this contrast vanishes the optical characteristics of the bilayer start to behave just as an optical absorber. A widely used method in the reflective (or, rather, surface diffractive) EUV optics community for suppressing inter-diffusion and chemical intermixing is to incorporate a third

material to act as a barrier layer[139]. Although there have been no reports on the fabrication of an MLL including barrier layers, they may possibly play a role in the future.

Much of the work in other parts of this chapter is built upon the multilayer material system of WSi_2/Si. These two materials were chosen because of our initial past success of using them in MLLs and their material properties. From the optical properties viewpoint, this is not the best choice of material system due to the strong absorption found in WSi_2. Tungsten contains L-edges in the 10-12 keV range, which means that careful shielding must be utilized for experiments that are based on x-ray fluorescence. The optical performance of three metal silicide-silicon multilayer material systems based on tungsten, molybdenum, and vanadium will be introduced here. Replacing tungsten with a lighter material such as molybdenum or vanadium reduces the x-ray absorption in the dense layer, and also lowers the fluorescence background for incident x-rays in the 10-20 keV energy range that much of the work here is targeted for. The use of new materials with lower absorption will necessitate far larger section widths (in order to obtain close to π phase shift), which makes sectioning easier and also provides stiffness in the optic (discussed in more detail in experiment 3). V_xSi_x/Si (referred to throughout simplistically here as VSi_2) can produce multilayers with sufficiently low interfacial roughness, and also lacks absorption edges above 5.5 keV. This lack of absorption edges means that any experiment where energy is scanned would benefit from entirely smooth energy response of the optics. Figure 4.12, below, plots the efficiency and ideal section width of an optimized wedged MLL.

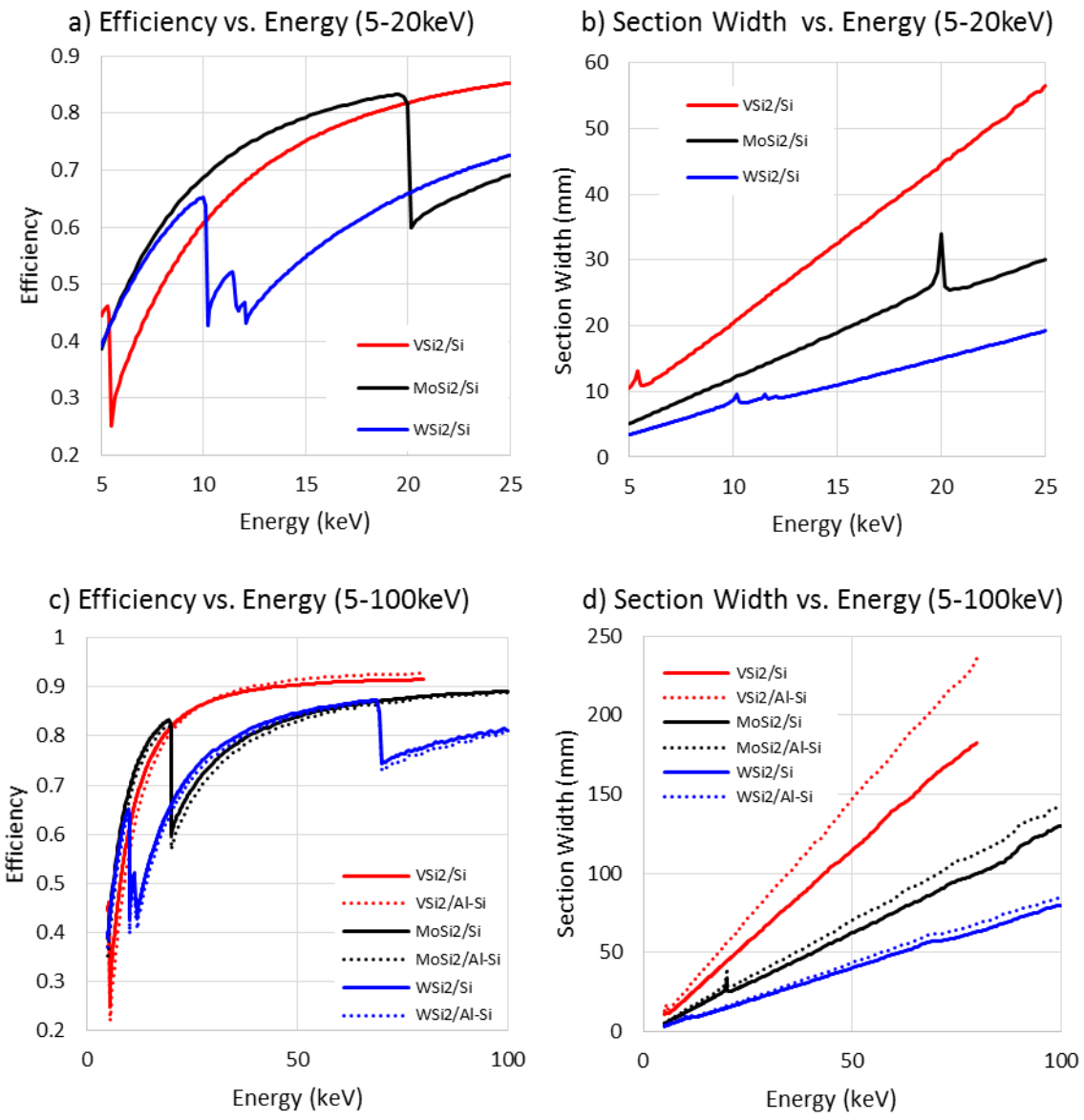

Figure 4.12: Efficiency and section thickness of three material systems. Efficiency and section thickness versus energy from 5-20 keV for three metal-silicide/silicon MLL material systems are shown in part (a) and (b), respectively. The same are shown for 5-100 keV in parts (c) and (d). All calculations are based on an optimized wedged MLL[140]. Of note are the lack of absorption edges for V above 5.5 keV combined with significantly greater section width which helps reduce failure rates during sectioning and adds mechanical stiffness. The roughness in the data is merely due to the calculation method.

W and Mo based MLL offer efficiency gains compared to V-based MLL at energies below 10 keV, although the rather small section widths become increasingly difficult to produce. V based MLL exhibit decent efficiency across the entire range of energies, as well as obvious gains in increased section width and lack of absorption edges. An important distinction also needs to be addressed when considering material system choice for flat or tilted versus wedged MLL. For flat or tilted MLLs, material systems with a low optical contrast require a large section

depth. This large section depth leads to significant dynamical diffraction effects[81]. The smaller section depth intrinsic to WSi_2/Si means that this material system is best suited for flat or tilted MLL, while the lighter metal-silicide based systems outperform for wedged MLL over any energy range.

Part of the experiment involving new material system exploration also involves replacing the silicon with an aluminum-silicon alloy; however this switch is done purely because larger apertures can be obtained with aluminum-silicon than Si alone. A side effect of an aluminum-based MLL is a minor increase in required section width. While the impact on section width and optical performance of multilayers based on Al versus Si is minimal, calculated efficiencies and section widths are provided in Figure 4.12 (c) and (d) above for reference.

4.2.2.2 Multilayer materials selection: Interfacial quality and film stress

Tracking along the periodic table is a reasonable method to optimize the material system and find a balance between estimated bulk physical properties and optical performance. However, switching material systems in practice is no easy task. The material or material systems selected must be rigorously explored for feasibility in a multilayer. The parameter space involved with sputtering includes but is not limited to deposition power, background pressure, gas flow around the cathode, gas combinations and mixture ratios, and substrate to source distance. These need to be explored in order to settle upon a workable environment whereby material deposition doesn't damage the surface being deposited upon, the film has sufficiently low stress, adhesion, near bulk-density, and low surface roughness. Often, these parameters can be somewhat machine dependent.

Deposition experimentation has been focused on the materials VSi_2 and Al-Si. VSi_2 is explored first, and separately, from Al-Si because adopting two new materials can compound potential problems. A familiar material, carbon, was selected as a pair with VSi_2. The process and results from a series of vanadium-silicide and carbon multilayers is reported below.

Vanadium silicide targets were obtained from a commercial manufacturer. Each target was produced by hot pressing mixed powder into a disk, which is then bonded to a Cu backing plate which adds rigidity and mechanical durability to the target. Carbon targets were likewise procured with a copper backing plate. The magnetron sources used for deposition utilize a relatively thin molybdenum cover between the cooling water region and the magnets. Because the cooling water is at a maximum pressure of 1,500 Torr and the opposing face of the molybdenum water jacket shield is under UHV, this plate has a tendency to bow outward slightly. Targets are clamped (with a thermally conductive paste) to the molybdenum water jacket shield. This slight outward bowing can impart enough force to cause brittle targets to fracture. Because of this possibility, it is imperative that brittle targets such as VSi_2 and C are fabricated with a mechanically rigid backing plate such as copper.

The bulk density of vanadium silicide, VSi_2, is listed as 4.42g/cc, but the density of a sputtered thin-film can deviate significantly (usually lower) than the bulk value. Because previously published information on the optical properties of VSi_2, particularly at x-ray wavelengths, does not appear to exist, the density of the sputtered film must first be extracted. A straightforward way to obtain a reasonable estimate of the film density is to measure the specular x-ray reflectance from a thick layer and query the total-external reflection profile. This is done,

below, in Figure 4.13. In order to calibrate the x-ray diffractometer angular position, two reference wafers were measured (GaAs and Si) along with the experimental sample, a 1 μm thick single layer of VSi_2 deposited on a silicon wafer. Instrumental angular alignment error was estimated by fitting both the GaAs and the Si wafers, and using the same error value for the VSi_2 fitting. The VSi_2 x-ray reflectivity measurements indicated that the density falls between 4.06 g/cc and 4.49 g/cc, or between about 8.2% under-dense and 1.5% over-dense compared to bulk. Both values are reasonable, possibly due to less than 100% molecular packing density, and variations in manufactured stoichiometry.

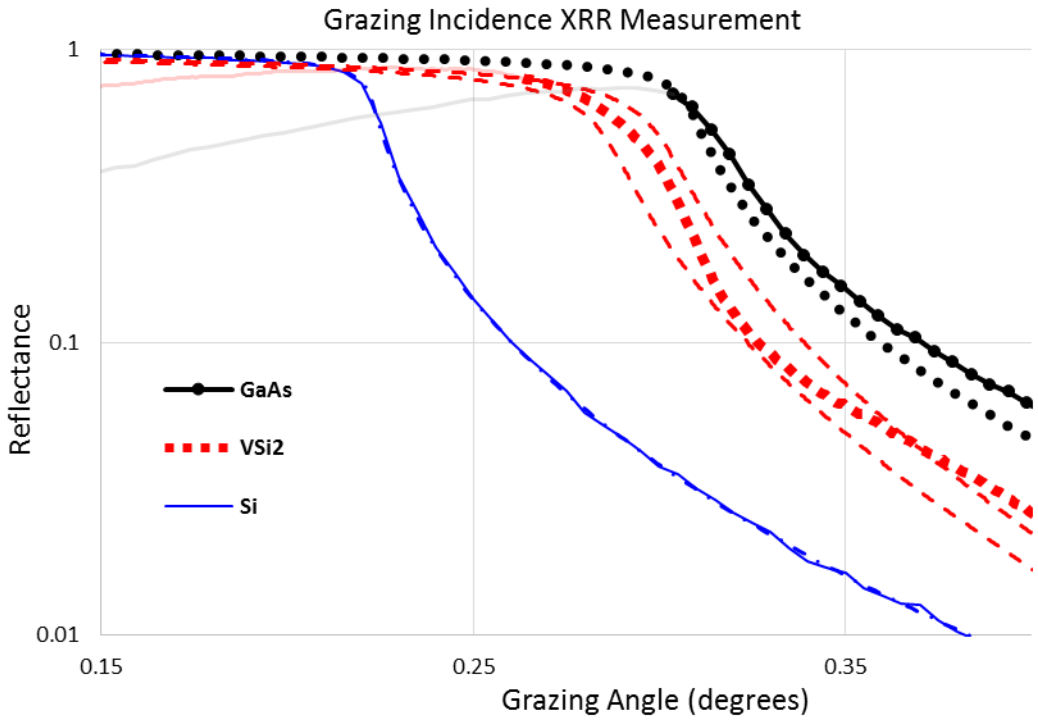

Figure 4.13: Specular reflection from VSi_2, GaAs, and Si wafers. The GaAs and Si wafers were measured to calibrate instrumental angular offset. The sputtered VSi_2 film estimated density is between 4.06 and 4.49 g/cc, which matches reasonably with the published bulk density.

Next, a series of 20 bilayer multilayers were deposited utilizing the standard technique for individual layer growth rate calibration where both multilayers are deposited with the same velocity for the first material, but the second material velocity is doubled. Ignoring layer intermixing or nonlinear deposition rates allows simple reflectivity data fitting to be used to extract the relationship between the d-spacing of the two multilayers to calculate individual deposition rate. For the first set of rate tests, a gas pressure of 2.5 milliTorr is used with 100% **Ar** gas composition. 5 SCCM (standard cubic centimeters of gas per second) of gas is flowed through each cathode and into the deposition chamber. VSi_2 is deposited at 170 watts, and C is deposited at 250 watts. As indicated in Figure 4.14 below, the thickness of VSi_2 is doubled for the 2nd rate sample. X-ray reflectivity data on these two multilayer samples exhibited rather sharp Bragg diffraction peaks, and significant intensity within the Kiessig fringes suggesting that

vanadium silicide deposition is providing good optical contrast, low interfacial roughness, and high layer-to-layer repeatability.

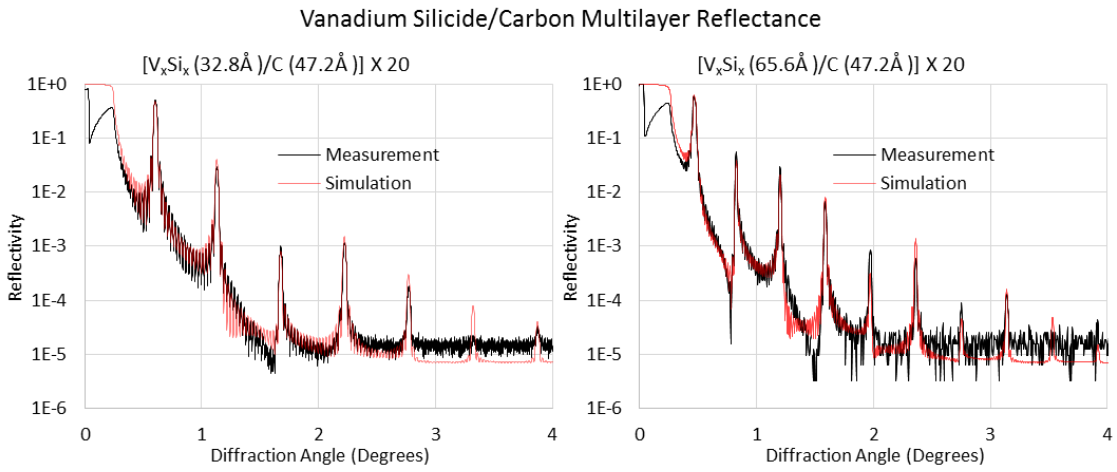

Figure 4.14: X-ray reflectivity measurements at 8 keV of two VSi_2/C multilayers. Each structure contains 20 periods. The structure measured on the right side contains double the vanadium silicide of the structure measured at left. Both structures appear to have narrow interfacial width and high contrast.

For each layer, the substrate is raster scanned back and forth over the shaped aperture with a central opening width of 46 mm at a predefined speed and number of passes. Carbon was deposited with substrate velocity set to 10.7 mm/sec, and VSi_2 was deposited 5.9 seconds at a velocity of 46.7 mm/sec. For the first multilayer, The VSi_2 target was cycled over 3 times (for a total of 6 exposures) and the carbon target was cycled over 5 times (for a total of 10 exposures). For the second multilayer, the VSi_2 target cycle number was doubled. The effective dwell time for carbon was 32.2 seconds per layer. The dwell time for VSi_2 is 5.9 seconds for the first multilayer and 11.8 seconds for the second multilayer. From the given layer thicknesses and deposition dwell times, VSi_2 was deposited at roughly 5.1 times the speed of C. Ignoring the nonlinear effect of applied DC power on deposition rate and all other factors assumed to be equal, the growth rate of VSi_2 appears to be about 7.5 times that of carbon.

Several relatively short d-spacing (below 4 nm) multilayers were then fabricated with a range of power and gas ratios. All VSi_2/C multilayers were deposited on a Cr adhesion layer and measured with the lab x-ray source. A small amount of N_2 was found to slightly increase performance and apparent contrast or sharpness of the fine features within the reflectance measurements. These multilayers show unusually high long-range depth periodicity, as evidenced by the Kiessig fringes in Figure 4.15. The undulating beat pattern with a periodicity of about 1/3 degree corresponds to the approximately 10nm thick chromium under-layer deposited first for substrate adhesion.

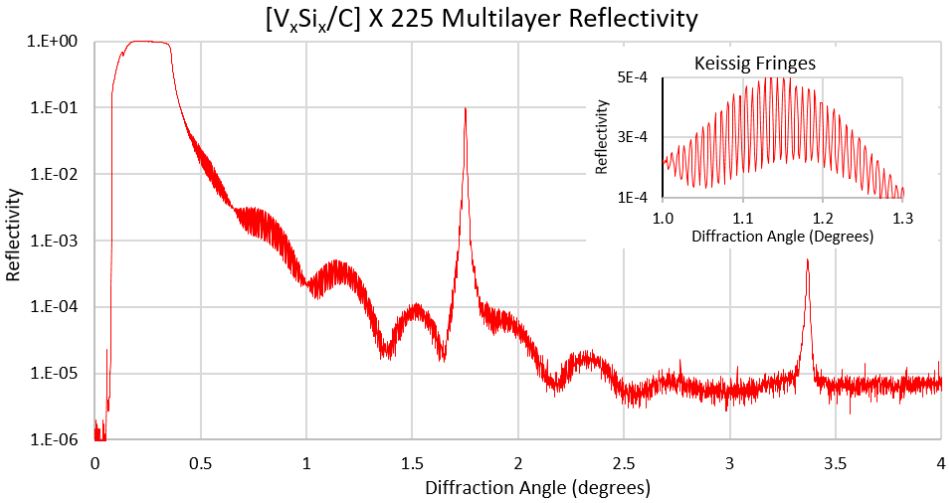

Figure 4.15: [V_xSi_x/C]x225 bilayers, R1=14.75%, BW=0.55% @8 keV.

In conclusion, an exploration of new materials for increased performance when used for MLL fabrication was conducted. Two lower-density metal silicides, $MoSi_2$ and V_xSi_x (simplistically referred to as VSi_2), were examined for optical performance when utilized for wedged MLL (Figure 4.12, by Hanfei Yan and Adam Kubec). The sputtered density of VSi_2 was experimentally estimated to correspond reasonably well with published bulk density vales. Optimized deposition environmental parameters allowing the use of VSi_2 for MLL fabrication were found. Replacing the silicon spacer with an aluminum-silicon alloy will allow the production of much thicker MLL without impacting optical performance. For wedged MLL, VSi_2 provides both higher optical efficiencies as well as significantly greater section widths. Larger section widths are much simpler to fabricate with lower failure rates and also exhibit far greater mechanical stiffness. Tungsten and molybdenum both have absorption edges in the energy range of interest. A side-benefit of employing VSi_2 for wedged MLL the lack of absorption edges from the entire range of 6-25 keV.

4.2.3 100 μm thick MLL

A small aperture MLL for a publication-worthy single-use experiment is difficult to deploy for real beamline use because the short focal length limits usability and the small aperture fails to capture a significant portion of the incident radiation resulting in low overall beamline efficiency and low focused flux. Large aperture MLL optics are required in order to maintain reasonably large focal lengths and subtend a significant portion of the incident beam. The primary source of large aperture MLL failure is film stress. Accumulated film stress can compromise the survival of the multilayer during growth as well as produce bulk defects that adversely affect the MLL's focusing performance. Thin film stress[141] is usually produced independently of the method of deposition, and has been studied in depth[142,143]. It has been reported that lattice mismatch is the main source of strain during epitaxial growth of materials[144]. Thermal stress[145] is induced when a difference in temperature is present within deposited materials that have a difference in thermal expansion coefficients. Intrinsic stress has been observed in all films deposited with environmental parameters that are out of equilibrium. Therefore, stress in films reflects a combination of intrinsic material properties and deposition

processes. As discussed below, the challenge is not only to produce a multilayer with an exceedingly large number of layers and total thickness, but also one where the interfacial width remains sufficiently low to retain high optical performance.

Significant studies around the world[146] have investigated the complicated role and interconnection that materials and deposition processes together share in the formation of interfacial roughness and film stress during growth. Both sputtering and PLD yield a slew of ions, electrons, and energetic neutrals. High-energy impact of particles on a surface contributes high mobility [147] that hopefully ameliorates enough surface reorganization to smoothen deposition. This process, related to "atomic peening", preferentially reorganizes material that is out of equilibrium into a more smooth, dense surface[148]. The source of energy can be either from the deposition flux (more from PLD), a process gas, or a combination of both (for sputtering). While a process gas is often used during PLD, especially during reactive processing, a process gas is most definitely required for sputtering. The energetic bombardment that is intrinsic to the process of PLD led to the conclusion that ZrO_2 displays a frequency-dependent smoothing of its rough surface[149] which results in a Ti/ZrO_2 MLL with very sharp and narrow interfaces. During the sputtering process, typically the process-gas pressure is kept as low as possible while reducing the distance from the source to the substrate, while maintaining a safe distance from the plasma region. The goal is generally to maintain as high an energy transfer as possible at the deposition surface for creating interfaces with minimal interfacial roughness, but typically not also bombard the surface with plasma from the deposition source which can destroy the growing multilayer. This kinetic bombardment also tends to lead to large amounts of film stress[150]. Accumulated film stress within a sputter-deposited multilayer is typically highly compressive when the material is grown at low pressures[63], and gradually decreases to stress-neutral or even tensile with a higher working-gas pressure.

4.2.3.1 Film stress versus pressure

An investigations of film stress outlined below were done with a commercial in-situ laser wafer-curvature monitor. The monitor reflects an array of parallel visible-light laser emission points off the deposited wafer and changes in spacing are used to determine changes in wafer curvature. Changes in the wafer's curvature are associated with a change in accumulated film stress. Figure 4.16 below shows measurements of wafer curvature taken after each deposited layer of a WSi_2/Si multilayer. When deposited at a relatively low pressure, 2.3 milliTorr, Figure 4.16 (a) shows a clear incremental change in wafer curvature (and thus increase in accumulated film stress) after each layer. Figure 4.16 (b) shows measurements of wafer curvature as the Ar pressure is periodically adjusted during deposition. When the process pressure is fixed at 16 milliTorr, the wafer curvature fluctuates around a steady value. This suggests that one material is contributing a tensile stress component while the other material balances this with an equally compressive component, or at least that the overall accumulated stress is not changing.

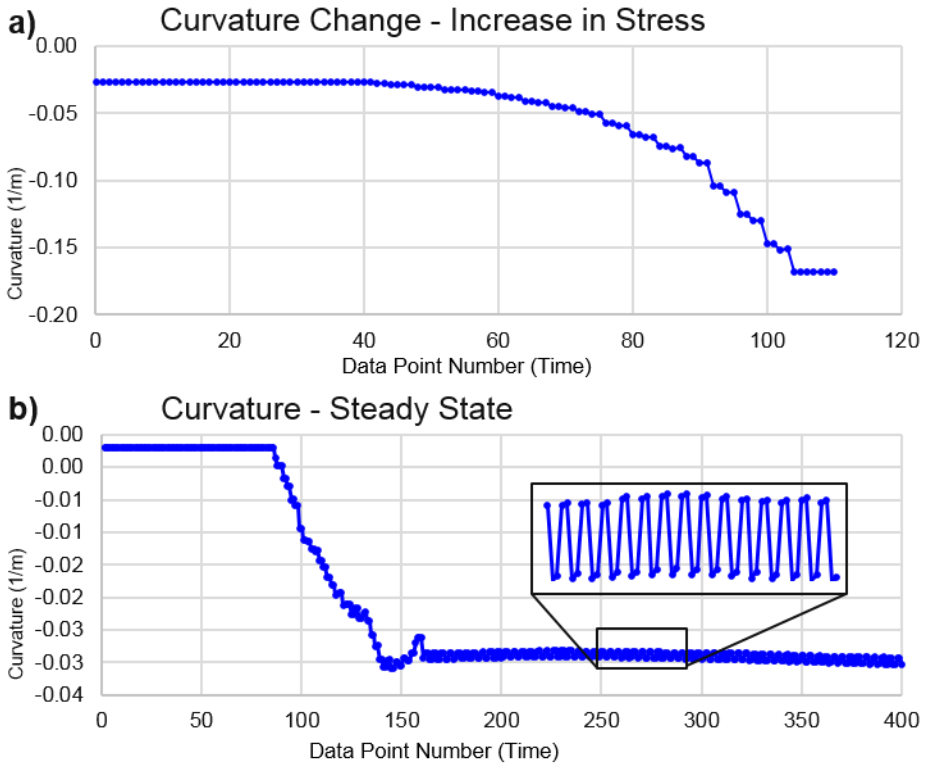

Figure 4.16: Wafer curvature during WSi_2/Si deposition at two pressures. Part a) shows the change in the curvature (and thus change in stress after each layer when deposited at a relatively low sputtering pressure of 2.3 milliTorr. Part b) shows curvature measurements as the Ar pressure is periodically adjusted during deposition, and when the pressure is fixed at a relatively high Ar pressure of 16 milliTorr after data point 170. Overall wafer curvature doesn't change, but rather oscillates around a constant value as the inset illustrates. Two data points per layer were taken.

Following this experiment, an MLL was deposited in the APS rotary deposition system with a monotonically increasing layer thickness at 16 milliTorr, the (roughly) stress-neutral state illustrated above in Figure 4.16 (b). As can be seen in Figure 4.17 (a), the overall radius of curvature of the wafer increases only modestly, suggesting that the corresponding accumulated stress change is relatively minor for a structure with such a large number of layers and total thickness. The individual components of stress from each alternating material clearly contribute significant amounts of alternating tensile and compressive stress. In the experiment, silicon was found to contribute to compressive stress, but the WSi_2 countered this with a significant tensile component. Changes in stress increase with layer thickness as seen in Figure 4.17 (b).

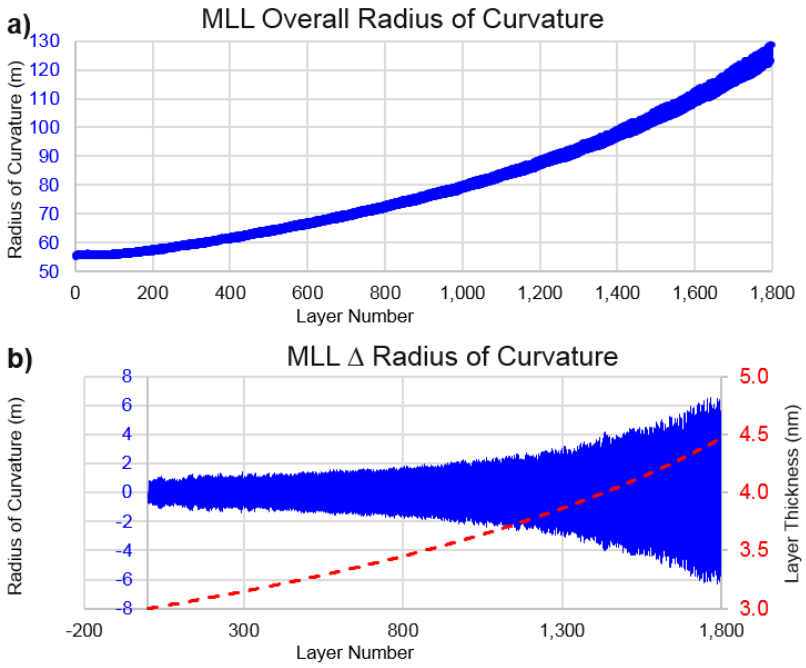

Figure 4.17: Wafer curvature vs. layer number of a WSi_2/Si multilayer Laue lens. Absolute radius of curvature change is modest, seen in (a). The layer-by-layer change in curvature tracks layer thickness (dotted line)

Deposition of thin films at relatively high process gas pressures would allow the fabrication of MLL with exceedingly large apertures, but other quality problems related to high-pressure deposition would ruin the optical performance because higher pressure deposition disturbs (or, more appropriately, reduces) the amount of energy available during deposition leading to very rough interfaces, waviness, and under-dense films. The SEM images in Figure 4.18 of an MLL deposited at low pressure (a) contrast significantly with the waviness and rough interfaces seen in an MLL deposited at 17 milliTorr (b).

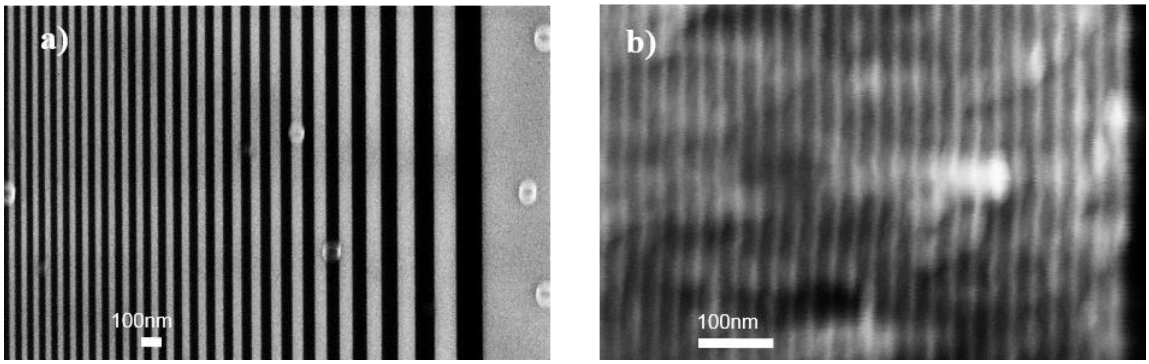

Figure 4.18: Effect of deposition pressure on layer quality. SEM image of partial MLL deposited at low pressure (a) shows sharp interfaces. The image in (b) shows the result of deposition at high pressure (17 milliTorr); significant interfacial roughness and layer waviness.

4.2.3.2 MLL Deposition limit with Ar-only

A thorough study of film stress and pressure with the WSi_2/Si material system [76] reported that a pressure threshold of about 6 milliTorr was found to correspond with a significant increase in interfacial roughness. While an MLL deposited in the above reference at about 12 milliTorr was found to be significantly stress-neutral, interfacial roughness was entirely insufficient. Using typical conditions with an Ar process-gas pressure of 4milliTorr, it becomes progressively more difficult to deposit a layer more than 40 μm in thickness due to the excessive stress. Although the failure rate was very high, several MLL above the 40 μm limit were produced with this process that survived sectioning. Although the marker layer positioning indicated that these should be high-performing optics, at-wavelength testing with synchrotron revealed unusual features in the focused beam which were originating from the bulk within the MLL. This was first seen in farfield images as shown Figure 4.19, below.

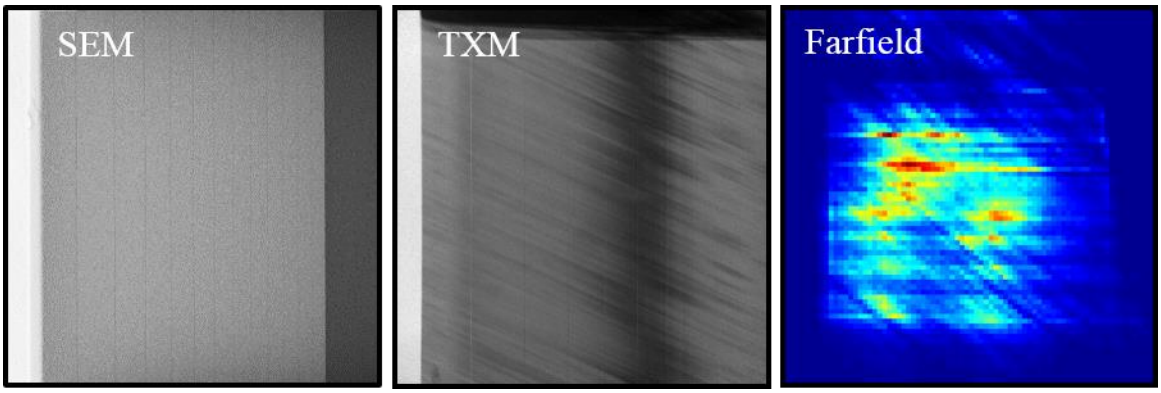

Figure 4.19: Three images[81] which originate from the same MLL. The SEM image reveals no hints that there may possibly be defects within the bulk of the optic. TXM measurements show streaks through the bulk, and these streaks manifest as intensity variation when a farfield image of the MLL focus is taken.

Streaks, which are visible in the farfield, also manifest as intensity striations when the MLL lens is imaged with a TXM. The intensity of the streaks varies with incident angle, suggesting that these streaks are indeed bulk-defects that appear to slightly warp the angular position of a region of multilayer within the lens. This variation in intensity can be seen in Figure 4.20, below. In Figure 4.20, the lens is rocked from the zero-degree position (the lens is parallel with the beam) to the Bragg condition. The excited Bragg condition is the dark band roughly down the center of the lens.

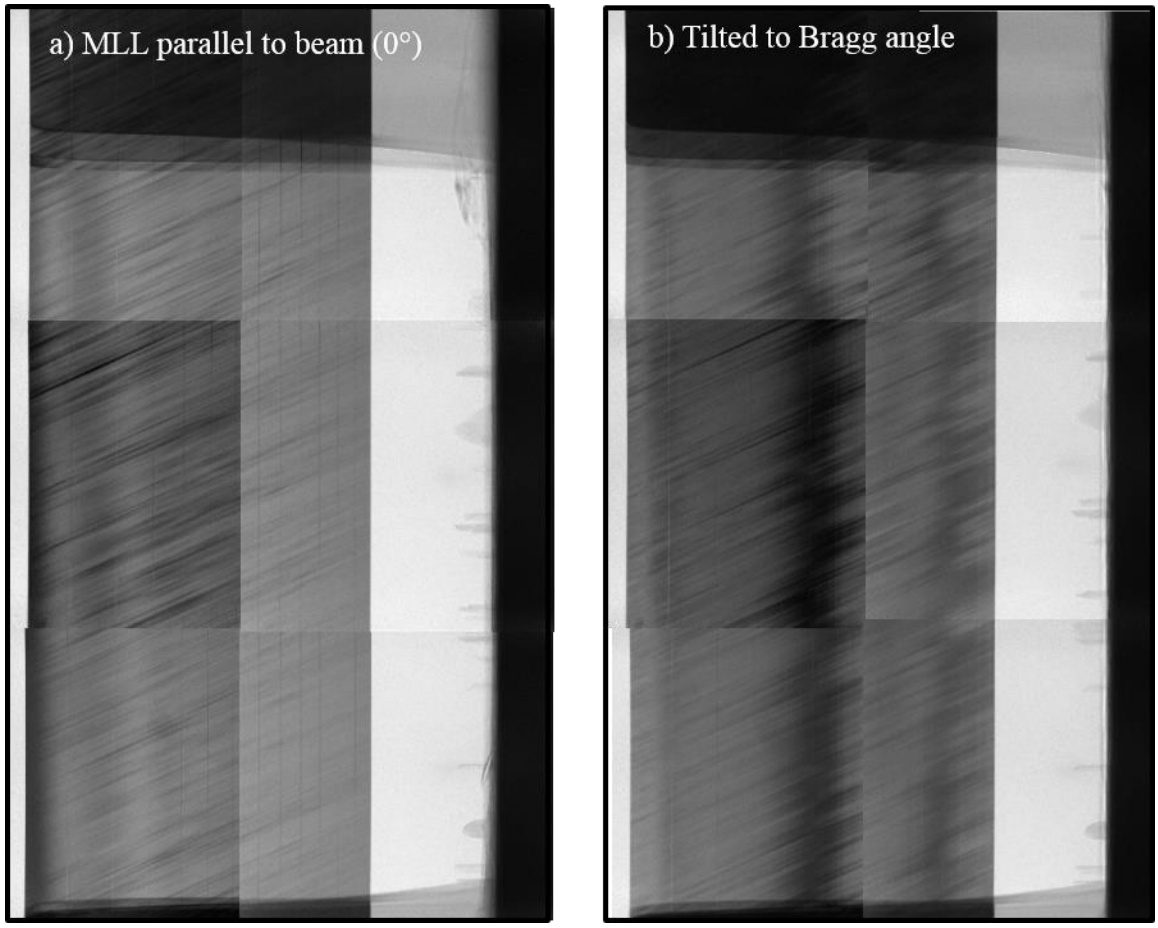

Figure 4.20: TXM measurements show intensity variations from bulk defects. The MLL was deposited with 100% Ar. Measurements were taken by H. Yan at NSLS and APS. The intensity variations shift when the optic is rocked from an angle normal to the incident radiation in (a) to an angle where the Bragg condition is excited roughly in the middle of the optic in (b).

4.2.3.3 Methods to Increase the total deposition thickness

All further attempts to exceed roughly 40 μm in total film thickness with the WSi_2/Si material system deposited with Ar gas resulted in bulk growth defects and multilayer disintegration, thereby leading to a search for new methods to increase the total survivable deposition thickness possible with MLL optics.

4.2.3.3.1 Bonded MLL

A method to achieve this goal which was mentioned in Chapter 1 attempted to bond two halves of an MLL together. The bonding method described below involves attaching MLL halves together which are of the same orientation, meaning that both halves focus in the same plane. Separate bonding efforts have been undertaken by other groups where the end goal is to bond both a horizontal and vertical focusing MLL into a single optical element, which is outside the scope of the work in this dissertation. Since MLL halves are historically fabricated by depositing first the outermost, smallest layers onto a substrate, and continuing this deposition to

the center layers, the inner-most layers of an MLL will be roughly facing one another when deployed. A bonding agent between these two MLL halves would combine both independent MLL halves into one optic. Bonding two halves together would also reduce the number of total optics to align within the beam from four down to two. The top-most layer of two as-deposited MLL chips would be coated with first an adhesion layer and then a prescribed thickness of a bonding (or spacer) material that matched the required spacing between the two halves. For the effort at the Advanced Photon Source, the bonding material[71] chosen was AuSn. An 80% Au / 20% Sn (by weight) eutectic alloy has a melting point of 280^{o} C, which is a survivable temperature for this material system. The two halves are placed in a clamp and heated under vacuum. An SEM image of an after-sectioned bonded MLL is shown in Figure 4.21.

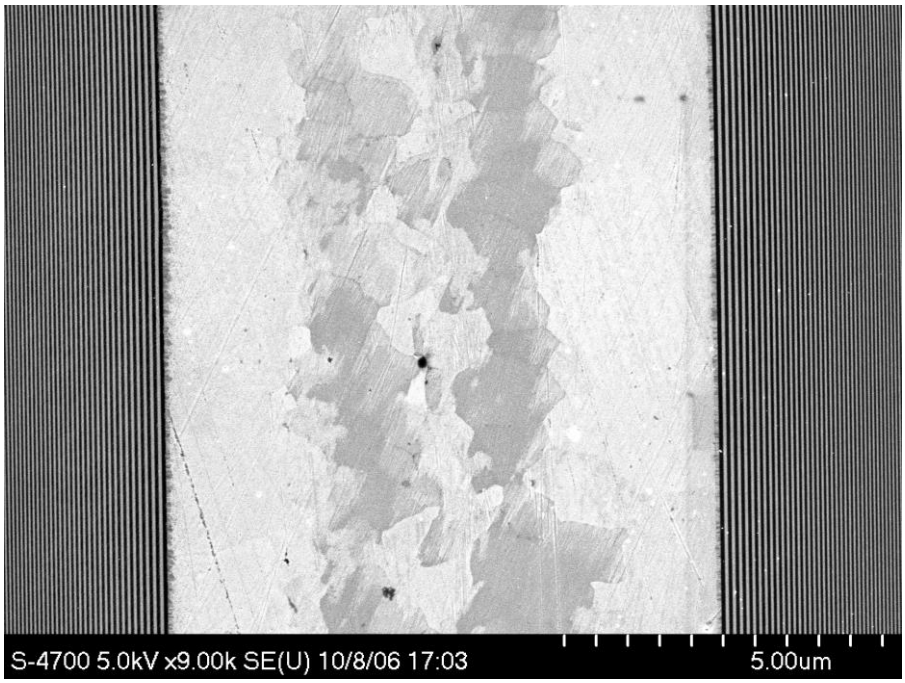

Figure 4.21: Two MLL halves are bonded with AuSn. The AuSn contributes to absorption of the central beam and also rigidly bonds both halves of the MLL into a single optic. Unfortunately, this method does not provide for precise control of the absolute distance between the two halves of the MLL.

Bonding two MLLs of the same orientation in order to increase the total aperture has one main geometric limitation, and one significant fabrication challenge. The geometric limitation for bonding two MLL halves with this method is that the bonded faces of both halves must lie parallel (or at least roughly parallel) to one another. MLL tilting, where both halves of an MLL would be tilted individually in order to partially satisfy the Bragg condition, is not practical with bonding. Bonding two halves of a wedged MLL may be possible if the angular alignment were precisely controlled. The main fabrication issue with bonding MLL using this technique is that the bond thickness cannot be precisely controlled. With diffraction-limited optics, the gap between each matching MLL half must be held to within approximately 1/3 the outermost zone width in order to keep the focus from broadening. We found that a minimum of about 500 nm of AuSn is required to obtain a sufficiently strong bond between two halves, and there is some run-to-run variation in final gap thickness due to variations in clamping pressure,

temperature, time, or even substrate geometry. This large number of variables makes holding a tolerance of below 2 nm (a reasonable value given MLL optics with 5 nm outermost zone width) extremely difficult. The inverse d-spacing plot of bonded MLLs in Figure 4.22 would focus at two points outside the main, broadened focus.

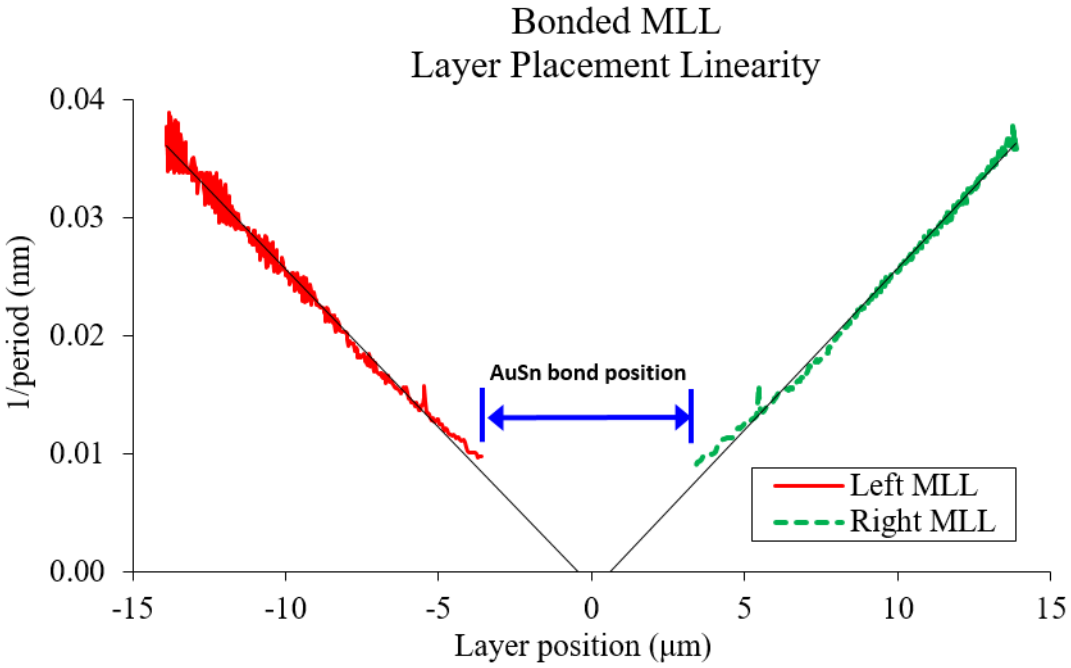

Figure 4.22: Bonded MLL inverse d-spacing plot. The two MLL halves, which were from the same deposition batch, exhibit a slight kink at roughly +/- 7 μm. The bond section width was slightly too large for this optic, such that the individual focal points for each MLL half do not intersect at y=0, which will result in two foci.

Instead of attaching two separate MLL halves into a single optic, an alternative approach is to continuously deposit an entire MLL. This would entail first depositing one side of the MLL starting with the thinnest layers, progressing through the thicker inner layers, depositing the extremely thick central layer, and then progressing through to the other side of the MLL. Significant differences in deposition rate have been observed for layers that are just a few nm thick compared with several hundred nm thick. A single layer of WSi_2 which was targeted for a thickness of 155 nm was deposited under identical conditions as a 3 nm layer. When measured, this layer was found to be only 139.5 nm thick, an error of 9%. One possible reason for this discrepancy is that the target (and substrate) are actually under different conditions when a single, thick layer is continuously deposited compared to a progression of deposition of a series of very thin layers. Before the start of layer deposition, the cathode power is turned on and held for 7 seconds before sample scanning begins. For a layer of just a few nm (and depending on the material), a single layer may require just a few seconds worth of deposition before the layer is complete. Continuous power on the target is applied for only a fraction of a minute for a thin layer. Continuous power is applied on the target for many minutes when a single, thick layer is coated. Two samples were coated with a thick layer of WSi_2 under identical conditions (i.e. identical source power, dwell time, pressure, etc.) but deposition for one sample was duty cycled

by removing applied source power every few nm of coating for 60 seconds, while the other was deposited continuously. The duty cycled sample was 9% thicker than the one deposited at continuous power. Figure 4.23 shows the difference in applied voltage between the two samples. One notes that the average voltage for the duty cycled sample is lower than the continuous power case, and since total power is constant, this means that current follows the opposite trend. We also observe that the surface roughness for the continuous layer is slightly lower than the duty-cycled layer as shown in Table 4.1 and Figure 4.24. One possible physical explanation for these observations is that duty-cycling keeps the target at a nominally lower surface temperature, which affects the deposition rate. The higher voltage also corresponds to slightly higher energy at the deposition surface resulting in a slightly lower roughness.

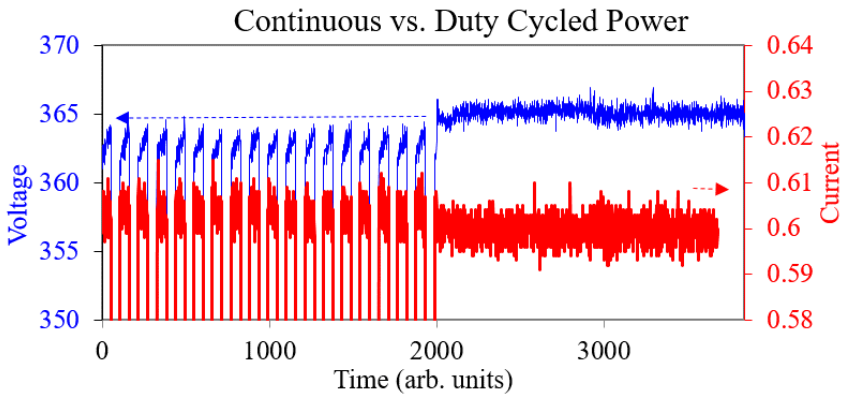

Figure 4.23: Duty cycle vs. continuous power when sputtering. Voltage (left axis, blue) and current (right axis, red) are plotted during WSi_2 deposition on two samples – duty cycled (left half) and continuous power (right half). While the observed difference in voltage and current is less than one percent, this voltage difference when combined with or because of thermal effects may be the source of the difference in observed deposition rate and roughness.

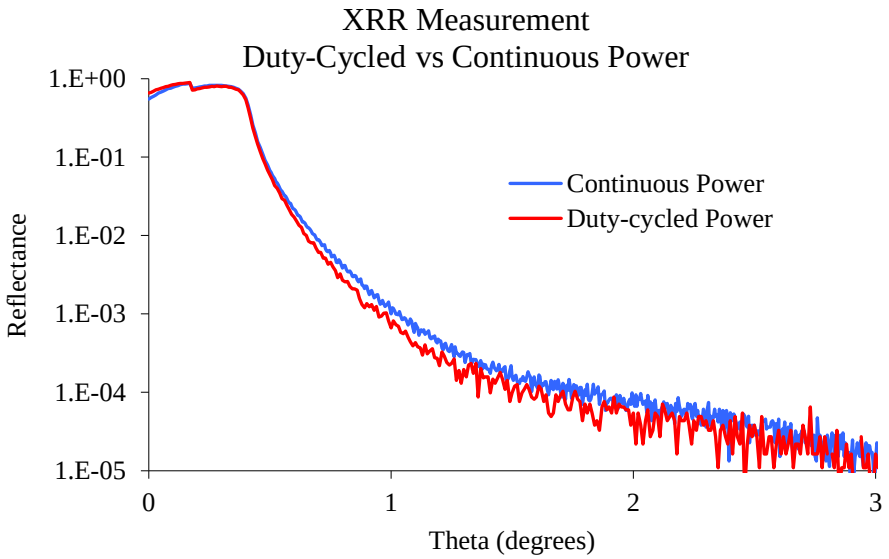

Figure 4.24: X-ray specular reflectance measurement of two WSi_2 samples. One was deposited with power applied to the source continuously for the duration of the layer coating. The second sample was deposited with power duty-cycled to simulate conditions similar to that of MLL layer deposition; many smaller layers are deposited individually. As can be seen in the data, both samples exhibited very similar density, however the sample with power continuously applied exhibited 25% lower roughness. Roughness quantification was done through simulations with parameters listed in Table 1, below.

Power	duty cycled	continuous
Thickness	155 nm	139.5 nm
RMS Roughness[1]	1.26 nm	1.06 nm
x-ray roughness[2]	0.8 nm	0.6 nm
x-ray density	9.7 g/cc	9.7 g/cc
Target density	8.00 g/cc	8.00 g/cc
Published bulk density	9.30 g/cc	9.30 g/cc
Molecular weight	240.01 g/mol	240.01 g/mol

Table 4.1: Measured thickness and roughness for two WSi_2 samples. The sample deposited with power cycling was 9% thicker, but also exhibited slightly higher surface roughness as measured with both (a) visible-light roughness microscope and (b) as simulated with x-ray reflectivity data.

Calibrating an entire MLL deposition to account for the nonlinear response present in the growth rate of thick central layers poses added difficulty in utilizing this technique to increase the deposition aperture. Adding both halves of an MLL into the optical setup also adds complexity in that a central stop must now be used, instead of simply slitting the beam as can be done for a microscope with only two half-MLL. More details on the optical configuration details of a working MLL microscope are available elsewhere[62]. Keep in mind that the two MLL halves must still be positioned with respect to one another with a precision of 1/3 the outermost zone thickness. However, an added degree of freedom upstream and downstream exists[77] within the central layer. Depositing this central layer with a thickness gradient (which is straightforward to do with modern deposition equipment) would produce a through-the-middle MLL chip whereby one location exists within the un-sectioned piece along the direction of the beam that both halves are properly positioned. Finding, and targeting a section at this location would be a required next step. This method may also be applied to wedged MLL.

4.2.3.3.2 Reactive sputtering

An alternative to bonding in order to expand aperture is to reduce accumulated film stress to achieve larger deposition thicknesses. As the contribution to stress from individual material components is unequal, one proposed method of reducing the accumulated stress is to vary the bilayer ratio [151,152]. However, this will degrade optical efficiency which means that a correspondingly larger aperture optic will be required in order to regain total focused flux.

Another method to mitigate the stress issue is to use reactive sputtering. Reactive sputtering with a partial N_2 atmosphere has been reported to reduce film stress in W/B_4C

multilayers[153,154]. Using the precision gas-mixing system that was added to the BNL MLL deposition system, a series of WSi_2/Si bilayer pairs were deposited on a silicon wafer and measured for curvature change. Figure 4.25 shows curvature change for three different N_2 ratios; (9% N_2 / 89% Ar), (4% N_2 / 96% Ar), and (100% Ar).

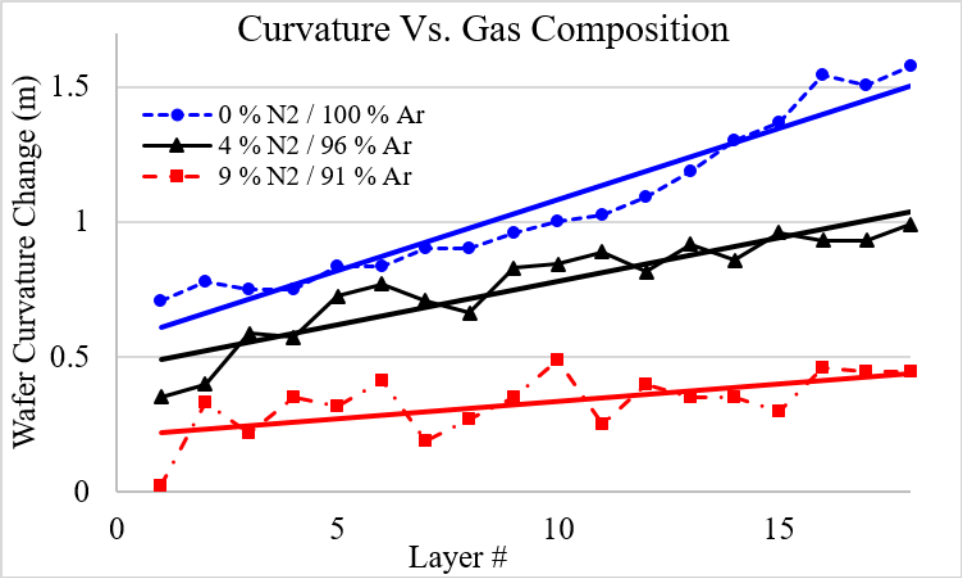

Figure 4.25: Wafer curvature change for three different ratios of Ar/N_2. Noticeable stress reduction is observed with addition of ~9% N_2.

One data point was taken after deposition of each bilayer pair of WSi_2 and Si. Although the data is somewhat noisy, a clear reduction in the rate of curvature change is evident starting when roughly 9% $N_2$is added to the process gas mixture. Further experimentation exploring variations in concentration with stress performance indicated that range of N_2/Ar ratios at roughly 9% / 91% and up to 20% / 80% or more resulted in roughly similar stress reduction advantages. A ratio safely on the lower bounds of this range of (10% N_2/ 90% Ar) is generally chosen based solely on the metric of stress reduction for the remainder of experiments in this work, however other questions about the suitability of this exact choice for the particular equipment in use remain. In order to assess the gas ratio stability requirements for optics fabrication, 11 sets of periodic multilayer pairs were deposited with a variation in N_2 partial concentration from 0% up to 20% in 2% increments. A process gas pressure of 4 milliTorr was used, along with 350 watts of power for both sources. Deposition rates (obtained from x-ray reflectance measurements) versus N_2concentration were obtained for both WSi_2 and Si. The deposition rates at 100% Ar were 19.2 Å/s for WSi_2 and 13.7 Å/s for Si. Figure 4.26 shows the percentage change in deposition rate from this initial starting rate at 100% Ar, as well as the effective global d-spacing change of a structure with equal thicknesses for both materials (Γ=0.5).

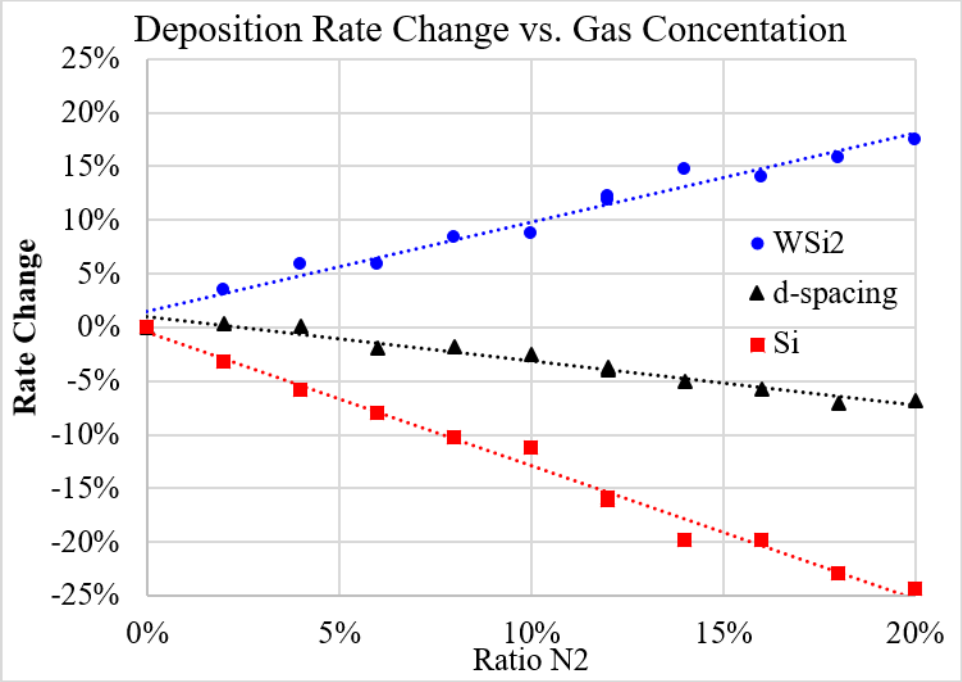

Figure 4.26: Variation in deposition rates versus N_2 concentration. A series of wSi2/Si multilayers were deposited using identical power and dwell times. The initial deposition rates at 0% N2 (100% Ar) were 19.2 Å/s for WSi2 and 13.7 Å/s for Si. The WSi2 rate increases with increasing N_2 concentration. Increasing N_2 decreases the silicon deposition rate. Given a system with equal thicknesses for both materials (Γ=0.5), the average d-spacing would decrease with increasing N_2 concentration.

The significant deposition rate dependence on N_2 composition ratio indicates that accurate deposition requires a stable gas flow and mixing system. Layer thickness repeatability is entirely dependent on stable sputtering parameters and instrumentation since in-situ monitoring and feedback is not currently utilized. The stoichiometry of the material system when fabricated with N_2 is also unknown. While the impact of a stoichiometry change due to the inclusion of N_2 will be minimal for the optical performance of the MLL, it would be useful to verify the presence of N_2 for MLL optical performance optimization. In order to obtain a cursory assessment of the optical performance of WSi_2/Si_xN_x multilayers deposited reactively, two structures were fabricated. Both were 500 bilayers with 1.88 nm d-spacing and 0.885 nm WSi_2, with one si, and the second deposited with N_2. Figure 4.27 plots measurements of both at 8 keV overlaid with simulations.

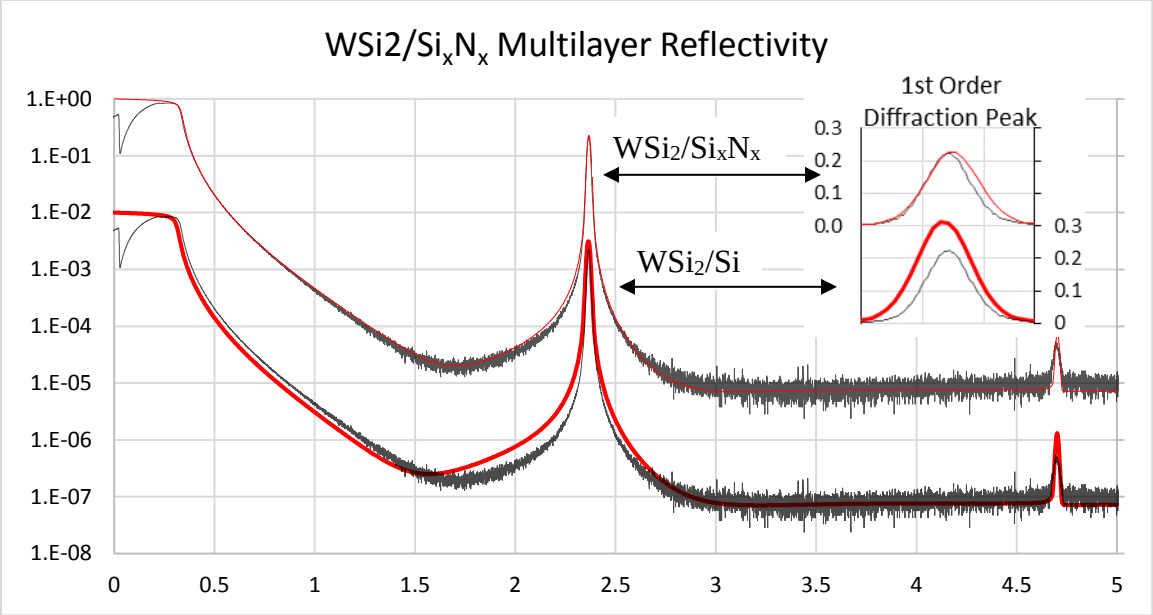

Figure 4.27: X-ray reflectivity of WSi_2/Si_xN_x vs. WSi_2/Si. 500 bilayer, 1.88 nm d-spacing periodic multilayers of two structures deposited with the same target material but, one with Ar/N_2 (top) and Ar only (bottom). Both simulations assumed 0.3 nm interfacial roughness/diffusivity, and 0.9 nm thick silicon dioxide cap layer. The inset shows that higher simulated reflectance can be obtained without N_2.

Simulations suggest that the interfacial roughness and diffusivity is roughly 0.3 nm. Sufficiently matching diffraction peaks are indicative of reliable, stable layer-to-layer deposition rate stability. Both simulations assume 0.3 nm interfacial roughness/diffusivity and an oxide top layer 0.9 nm thick. The inset of Figure 4.27 shows the same measured 1st order diffraction peak alongside both the nitride and silicon-only simulation. Silicon-only exhibits significantly higher reflectance, however the impact of this on MLL performance is a slightly different required section width, as well as a very minor decrease on total efficiency for flat MLL.[81].

Deposition of both tungsten silicide and silicon in a partial N_2 atmosphere results in multilayer structures with reduced film stress while also maintaining sufficiently low interface widths as well as adequate optical performance. The 43 μm thick MLL structure that exhibited streaks due to bulk defects was reproduced with a partial N_2 atmosphere. Just as with the original structure, SEM and TXM data indicated reliable layer placement and no apparent defects. No streaks were observed in far field imagery. Furthermore, structures surpassing 70 μm were deposited without incident.

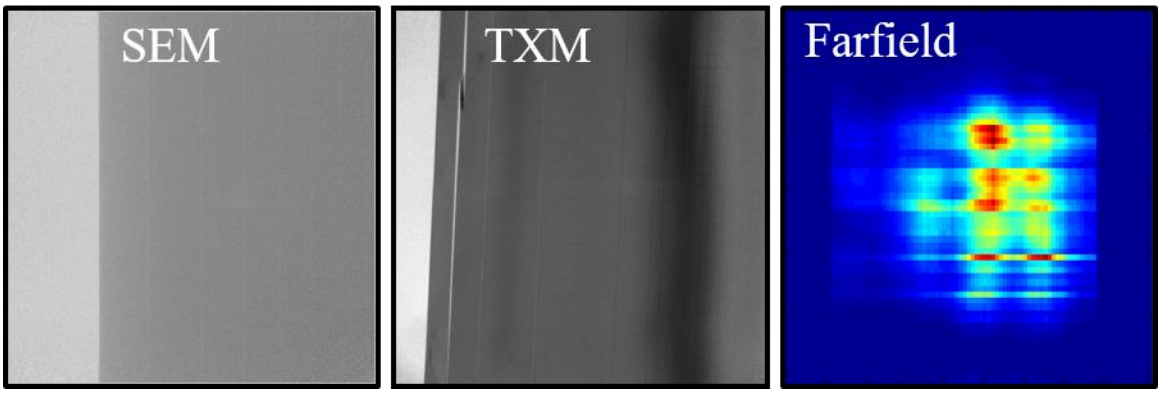

Figure 4.28: SEM, TXM, and farfield of an MLL deposited with N_2/Ar. Streaks that are presumed to be due to bulk defects from film stress are no longer present in either TXM or far field imaging.

N_2 mixing has been reported to assist in the fabrication of other multilayers, and also benefits MLL fabricated with the tungsten silicide-silicon material system. Addition of N_2 appears to result in a silicon nitride layer which has a minor impact on optical performance. In-situ stress measurements are extremely beneficial for process optimization and fast exploration of new materials. A usable MLL must also survive sectioning and be absent of artifacts when imaged with either of the x-ray based techniques (TXM or far-field imaging). Difficulties found in manual polishing, alongside the observed optical artifacts with 40 μm thick MLL deposited in pure Ar were overcome with the addition of N_2, leading to MLL that could now be deposited over 70 μm thick, almost a factor of 2x increase. However, deposition attempts aimed at breaking 80 μm increasingly resulted in disintegration or difficulties during sectioning.

4.2.3.3.3 Aluminum and silicon

In order to break the 100 μm barrier, a new aluminum-silicon based material composition has been selected as a replacement for silicon as the spacer layer. At x-ray wavelengths, aluminum is optically similar to silicon. In order to explore this new material, a 102 μm thick MLL with an outermost zone width of 4 nm and a focal length of 9.6 mm at a photon energy of 12 keV was fabricated. The MLL is comprised of zones 632 – 15,802 of alternating WSi_2 and Al-Si layers. The deposited layers correspond to the outer 80% of a half structure MLL, which will then be used to focus in an off-axis geometry. This thickness is roughly double the thickness reported[118,155] in previous fabrication attempts.

The MLL was deposited in the MLL deposition system at Brookhaven National Laboratory using four out of nine available cathodes[101]. The WSi_2 targets are identical in composition to previous work. The Aluminum targets were mixed with roughly 5% silicon (by weight). The process gas consisted of 90% Ar and 10% N_2 (by volume) with deposition pressure held at 4 milliTorr using the standard upstream control feedback system. Cathode power for all materials was 350 W. Due to the rather large aspect ratios targeted for this lens (total deposition thickness over 100 μm, section width just under 10 μm), it is expected that this lens would warp and bow if left as a free-standing structure, so the sectioning process included bonding the MLL to a diamond plate. After the deposition, the substrate and accompanying multilayer were

sandwiched and diced into 2×2 mm squares. One face was polished using standard methods, and then this face was bonded to a 50 μm thick diamond plate. After bonding, the entire MLL was thinned to a section width of about 8 μm by grinding and polishing the face opposite the diamond plate. The lens remains permanently bonded to the diamond plate during all x-ray experimentation. About 2% of the incident beam will be attenuated by the diamond but no other significant effect on measurements is expected by the diamond plate given its small thickness, low absorption and overall uniformity. SEM images of the sectioned MLL in Figure 4.29 show good layer contrast throughout the entire deposition.

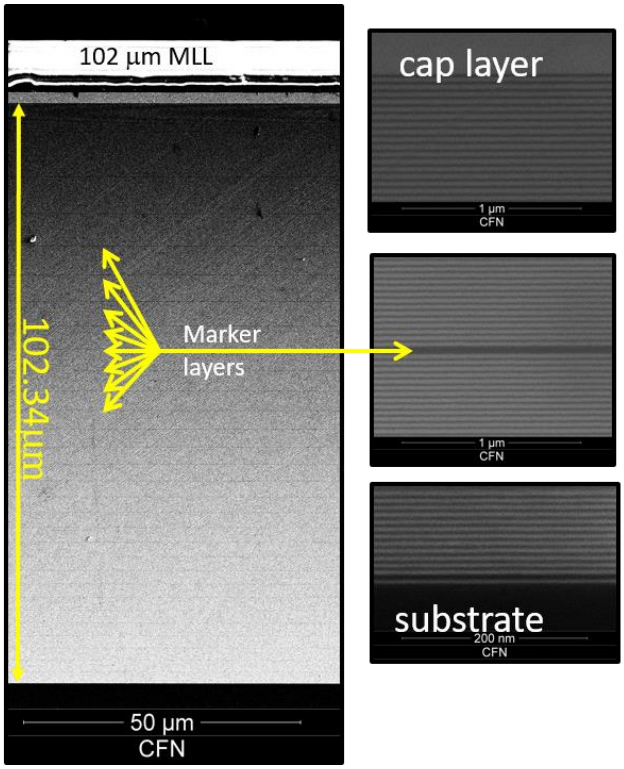

Figure 4.29: SEM images of 102 μm thick WSi_2/Al-Si MLL with 3 μm cap layer. The images reveal high contrast and smooth deposition throughout the entire structure.

The intent for this structure is to explore or verify whether this new material is compatible with significantly thicker multilayer deposition (over 100 μm) while maintaining sufficiently low interfacial roughness, not for focal performance. As such, this structure contained marker layers, but only one initial iteration was executed. The significant layer placement error in the as-deposited MLL (see Figure 4.30, below) would likely require 3 or more iterations in order to reduce layer placement error to below 2 nm RMS.

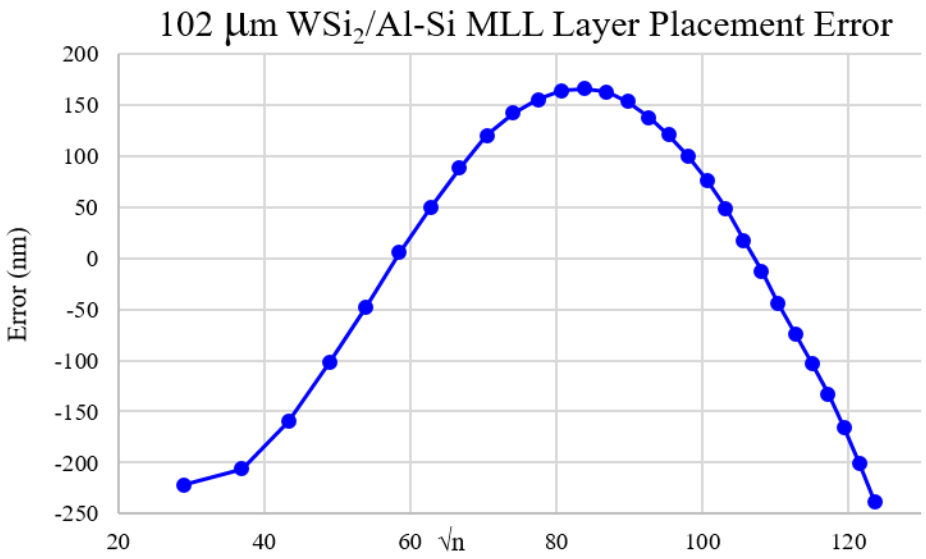

Figure 4.30. Layer placement error of the 102 μm thick WSi_2/Al-Si MLL. Intended only for exploration of large aperture MLL fabrication and not ultimate focusing, only the first iteration of MLL was deposited. Multiple iterations would be required in order to produce a diffraction-limited MLL

Almost universally, a multilayer is required to contain almost entirely amorphous films. Crystalline or nano-crystalline formation commonly leads interlayer roughness and eventually loss of optical contrast. Aluminum-based materials are not commonly found in thin-film based x-ray optics. In order to assess the possibility of crystalline formation or propagation of structure and roughness to the surface, the MLL was measured with two techniques. The top surface of the Al-Si cap layer was measured for roughness with a visible light microscope interferometer. Over a field of view of 180 μm x 130 μm, RMS roughness is 3.2 Å. A false-color height map of the measurement is shown in Figure 4.31 (a). The WSi_2/Al-Si sectioned MLL was also investigated at the NSLS in a simple Θ/2Θ diffraction geometry at 12 keV to scan for diffraction peaks that might indicate crystalline formation. The diffraction measurement is seen in Figure 4.31 (b).

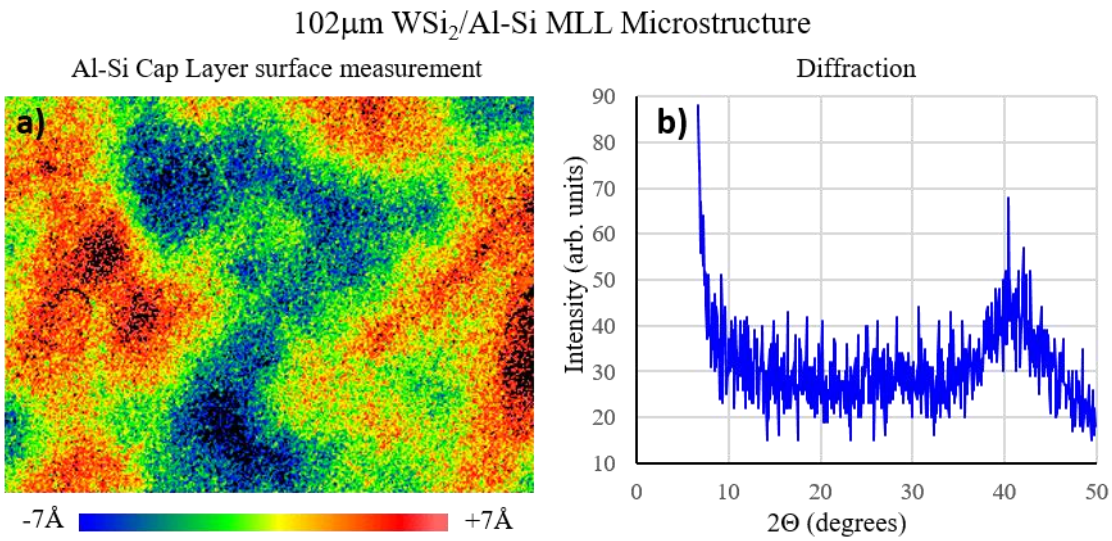

Figure 4.31: Measurement of properties of Al-Si. a) A visible-light interferometric microscopy roughness measurement of the topmost surface of the Al-Si cap layer. RMS roughness is 3.2 Å over a field of view of 180 μm by 130 μm. b) Θ/2Θ diffraction measurement at 12 keV taken at X21 at NSLS of the 102 μm WSi_2/Al-Si MLL structure. No sharp peaks are evident, indicating that the structure is largely amorphous.

Mechanical deformation, such as warping, delamination and kinks in the lens are caused by internal film stresses, the polishing and sectioning process, dicing, and the gluing process. The sectioned lens has a complete length of 2.7 mm. A study of the lens at beamline 1BM at the Advanced Photon Source revealed that the lens has defects along many, but not all regions of this 2.7 mm length. In the experiment[156] by Kubec et. al., monochromatic beam at 12 keV illuminates the MLL which was mounted on the Prototype MLL microscope[122] in horizontal diffraction geometry. Absorbing slits were positioned to cover only the actual structure. The MLL was rocked around a small set of tilt angles while images were collected in the far with imaging detectors. Figure 4.32 below shows a transmission image of the MLL. In the image, the dark outer regions are the slits, and the lighter outer bands are the silicon enclosing the MLL. The darker middle region is the WSi_2/Al-Si MLL, and the whisker-like black structure wandering in the center is the extinction band where the local Bragg condition has been met.

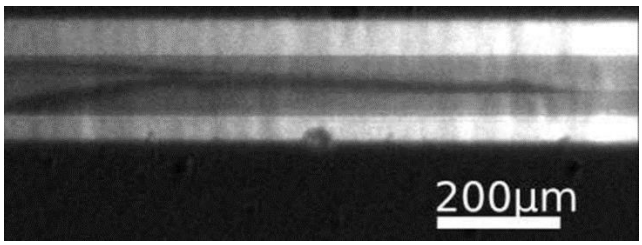

Figure 4.32: A transmission image[156] of an MLL taken at 1BM at APS. In the image, the dark outer regions are the slits, and the lighter outer bands are the silicon enclosing the MLL. The darker middle region is the WSi_2/Al-Si MLL, and the whisker-like black structure wandering in the center is the extinction band where the local Bragg condition has been met.

Next, an orthogonal view of the first focusing and defocusing orders are presented in Figure 4.33. For these views, the horizontal axis represents the angle of the lens with respect to the beam, and the vertical axis represents location along the lens. For these data sets, each image in Figure 4.33 represents the compilation of an entire series of frame grabs from the detector at discrete angles. The results of coupled wave theory calculations[156] for an ideal lens are presented in part a). The calculation shows a smooth progression with tilted angle lacking any discontinuities. Part b) shows a discontinuity in the angle of the lens at about the 74 μm region. This discontinuity may be explained by a kink in the lens that may have resulted from accumulated film stress. The gradual bend in part c) could be due to stresses from sectioning, and is likely compounded by the rather large aspect ratio for this structure. Utilizing a lower density absorber instead of WSi_2 would likely reduce this bending. On the other hand, this bending could also be used as a method to produce a wedged structure from an initially flat or planar MLL deposition.

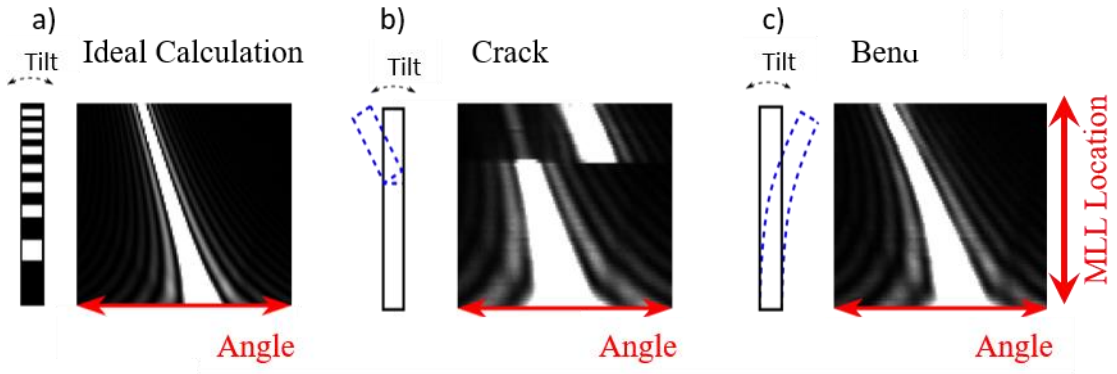

Figure 4.33: Orthogonal views for a) ideal MLL, b) a lens with a kink or discontinuity and c) a gradually bent lens.

Orthogonal view processing (the technical details of which are available in the references) has been used to paint a picture of the topographical features and errors in the MLL. Over the entire length of the 2.7 mm long MLL, it was found that there were two major discontinuities that may be interpreted as a region of layer delamination which allowed the separated regions of the MLL to individually tilt. Slow bending was observed over the majority of the lens. One kink-free region (near the 2.7 mm region of Figure 4.34) was singled out that also had sufficiently low bending to be of interest for future experimentation.

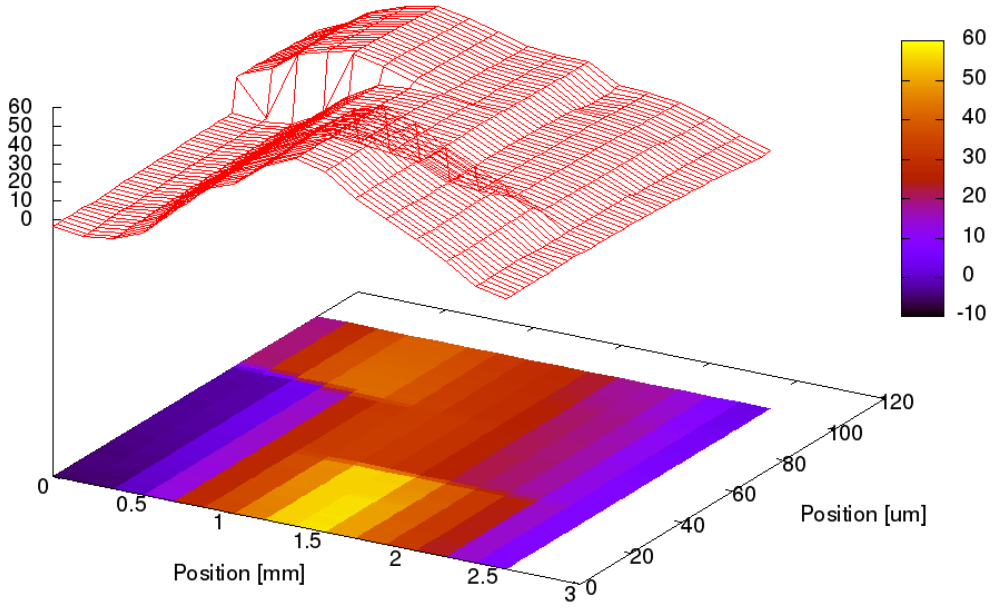

Figure 4.34: Relative bend and discontinuity map of the 102 μm thick MLL. The 2.7 mm long lens showed large kinks across a majority of the lens, but a small section near the right side of the lens appeared defect free and lacking any major bending.

4.2.3.4 Summary

The exploration of MLL bonding, reactive deposition, and new material systems led to an almost factor of 10X increase in total aperture to lenses that exceed 102 μm. The WSi_2/Al-Si material system currently is the largest aperture MLL produced. The replacement of silicon with Al-Si appears to allow MLL to reach new records for MLL aperture. MLL produced with this material system exhibit low interfacial roughness and appear to be defect free when measured at x-ray wavelengths. This limit of 102 μm does not appear to be the upper limit. The upper limit should be explored. Also, this first large area MLL is not ideal in several respects. First, layer placement error was not optimized. The MLL can be measured for ultimate focus which would be useful to verify optical property calculations with experimental data however the use of this particular type of lens structure with flat layers for actual x-ray nano-focusing doesn't satisfy the end goal. In the future, Al-Si needs to be incorporated into a wedged MLL structure with a lower density absorber (such as V_xSi_x, discussed elsewhere in this text) and measured for ultimate efficiency and focal performance.

4.2.4 Wedged MLL

4.2.4.1 Introduction

The majority of global MLL research to date has revolved around using MLLs that consist of flat zones used in a tilted geometry. Work on meeting the challenges for flat MLL such as fabrication of very thin layers with minimal interfacial roughness, good layer placement, and extremely thick deposition have made great progress. However, flat (or tilted) MLLs cannot focus efficiently to spot sizes much below 10 nm due to dynamical diffraction effects[59]. To approach single-nanometer focus size combined with focusing efficiency above 50%, wedged MLLs with progressively tilted zones are required.

The ideal curved MLL geometry for focusing a plane wave is comprised of individual layers forming confocal parabolic zones. These zones satisfy the relation[59]

$$x_n^2 = n\lambda(f_0 - z) + \frac{n^2\lambda^2}{4} \qquad \text{Eq. (4.4)}$$

Where $\mathbf{x_n}$ is the length between the optical axis and the outer edge of the $\mathbf{n^{th}}$ zone, **z** is the distance along the optical axis starting at the upstream face of the MLL, **λ** is the x-ray wavelength, and $\mathbf{f_0}$ is the focal length starting at **z=0**. For the range of MLL apertures and focal lengths relevant to this work, the contribution from the second term is insignificant and can be dropped out. This results in:

$$x_n \approx a(z)\sqrt{n\lambda f_0} \qquad \text{Eq. (4.5)}$$

$$a(z) = \sqrt{1 - z/f_0} \qquad \text{Eq. (4.6)}$$

From this, the positions of every MLL interface (and consequently the thicknesses of every layer) are scaled down as **z** increases by the factor **a(z)**, independent of **n**. A multilayer having the proper internal layer profile can be fabricated by imposing a thickness gradient in the deposition rate (or deposition dwell time) along the **z** direction that is fixed as each zone is deposited.

The depth along the optical axis of an MLL required for high efficiency in the regime of x-ray wavelengths is typically in the μm range, from perhaps 5 μm to 100 μm at the extreme. The focal lengths in question are several mm. Because the section width is much smaller than the focal length, the gradient within the optic is approximately linear and is described as:

$$a(z) \approx \left(1 - \frac{z}{2f_0}\right) \qquad \text{Eq. (4.7)}$$

This equation defines the wedged MLL geometry, where each interface within the structure is flat but lies at an angle with respect to the optical axis proportional to $\mathbf{x_n}$. The extensions of each and every interface in the structure intersect the optical axis at the same point at a distance $\mathbf{z=2f_0}$ as shown in Figure 4.35, below.

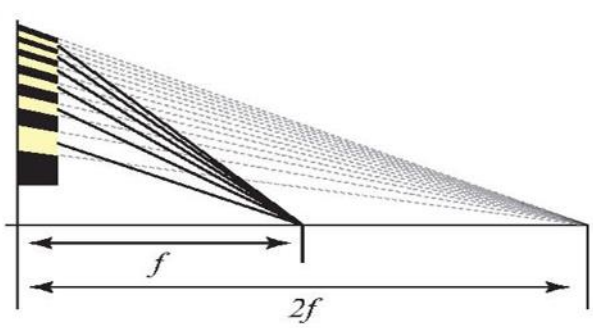

Figure 4.35. Wedged MLL schematic. The MLL section seen on the left has its aperture along the vertical direction. Each interface extends to meet at a point that is defined as twice the focal length ($2f_0$) along the horizontal axis. When the wavelength-dependent optical focal length equals the focal length of the MLL, optimum focusing performance and efficiency are achieved.

The ideal change in the deposition rate gradient (which is $-2f_0^{-1}$) will match the focal length of the layer sequence: $x_n=\sqrt{(n\lambda f_0)}$ at $z=0$. This implies that when designing and subsequently fabricating an MLL the deposition gradient along the optical axis must match the designed focal length of the MLL with precision that keeps the focus well within the depth of focus of the optic. However, because the layer sequence depends on the product of λf_0 (and not only f_0, without regard for λ) any deposition gradient will match for some wavelength λ. So just as with flat or tilted MLL, as long as the layer placement within the wedged MLL is adequate, wavelength can be "tuned" to match the focal length imposed by the in-plane deposition gradient. Thus many wedged MLL sections can be extracted from a large area multilayer produced with a lateral gradient in deposition rate, but the optimum wavelength for each section will necessarily differ depending on the deposition rate gradient along **z**.

4.2.4.2 The first wedged MLL

The first wedged multilayer Laue lens was fabricated in the rotary deposition system at the Advanced Photon Source. The equipment was configured to use side-sputtering circular 75 mm diameter cathodes that aim towards the center of the chamber. As the first machine in the world designed specifically for MLL fabrication, the sources are mounted sideways so that flakes from long deposition accumulation fall down and away from the target, minimizing the possibility of disturbing the deposition process. The sputtering guns are shrouded by an aluminum cylinder upon which a figured mask is mounted. This mask has multiple cut-outs which produce a vertically-oriented deposition rate gradient. The mask profile was designed to accommodate one central uniform coating region and six (6) nominally identical wedged MLL gradient regions, three on either side of the uniform coating region as seen in Figure 4.36. The mask was designed using the profile-coating technique described in Chapter 3. Growth of non-linear gradients (such as parabolic shapes which can be used for sub 1nm focusing optics) can also be achieved by using a different mask.

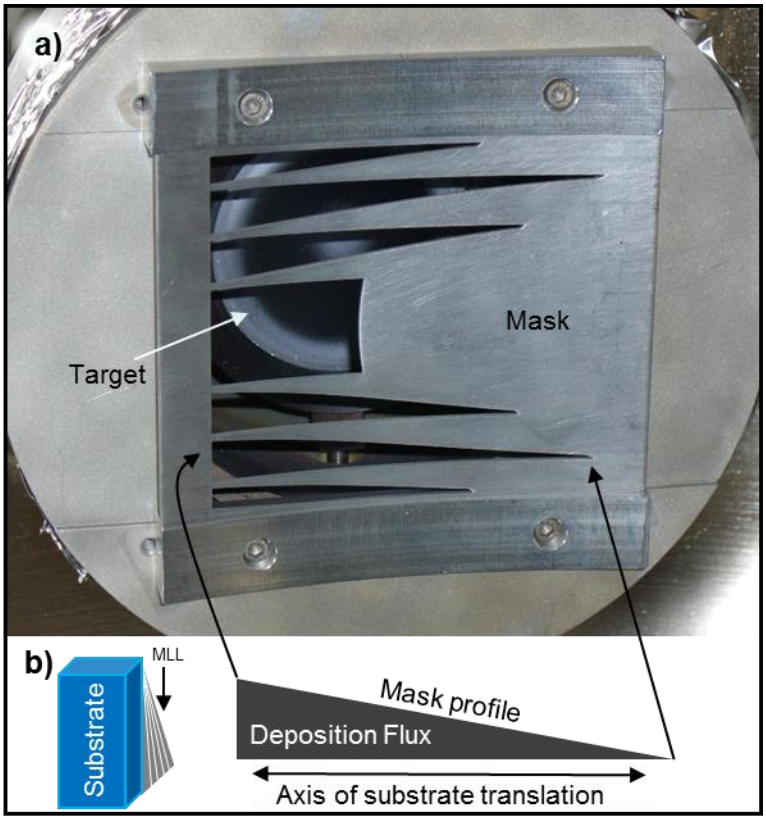

Figure 4.36. Wedged MLL masking installed in the APS Rotary deposition system. The target sits (a), partially obscured, behind a mask with a series of 7 cut-outs. The central cut-out produces a short region of uniform deposition which is used for rate calibration with x-ray reflectivity. The series of six cut-outs with three each above and below the uniform region generate steep thickness gradients. Deposition flux passes through the mask and onto a substrate which is rotating horizontally as shown schematically in (b). The orientation of the wedged MLL growth is visible on the rear face of the substrate.

As described in Chapter 1, the aluminum shroud is lined on the inside with aluminum foil, which flexes slightly with the accumulated film to further reduce flaking. The cryogenically pumped system was backfilled to a constant pressure of 2.3 milliTorr with 100% Ar. This first MLL was produced with the original MLL deposition parameters, meaning there was no N_2 reactive sputtering or new advanced materials besides WSi_2 and Si. Small (12.5 mm x 25 mm x 500 µm thick) Si substrates are mounted in a vertical orientation on one of six facets available on a 200 mm dia. central drum and rotated back and forth in front of each gun for layer growth. The substrate to target distance is 70 mm. The aperture opening in the mask varied from 0 mm up to ~60 mm through the mask shown in Figure 4.36. At areas where the mask opening is 15-mm the Si deposition rate is 1.0 – 1.3 nm/sec, and the WSi_2 deposition rate is 3.0 – 4.0 nm/sec.

While the substrates are positioned outside the mask opening and away from the sputtering flux region, the plasma is ignited. After the plasma has stabilized (typically for 7 seconds for MLL in this dissertation), the substrates are passed back and forth over the sputtering flux in order to build up the layers as has been discussed previously.

This first wedged MLL (wMLL) sample contained 1,588 alternating layers of WSi_2 and Si. The total deposition thickness ranges between 1 μm to 9 μm thick across an 11 mm long span of the substrate, with the thickness at the central linear region (see Figure 4.37 (a), roughly the 21 mm mark) being 6.6 μm. The layer thicknesses at this position increase according to the equations above, starting at 2.5 nm thick at the substrate, and ending at 13 nm on the topmost surface. After growth, the wMLL sample was diced parallel to the lateral gradient direction and edge-polished. An SEM image of the 6.6 μm region of this structure is shown in Figure 4.37 (b). The inset images clearly show the individual layers through the rough polishing scratches on the surface.

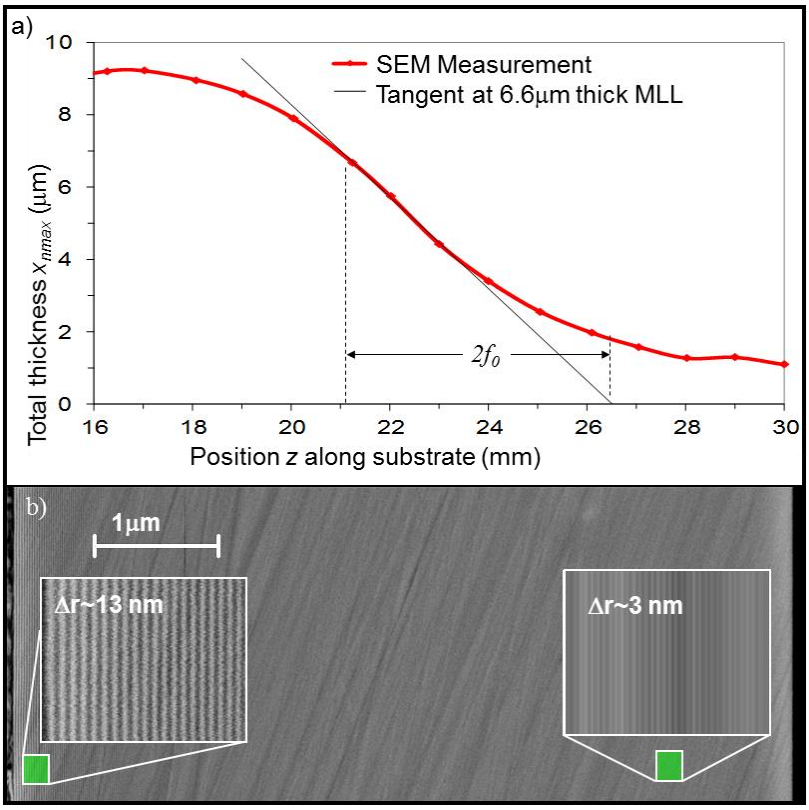

Figure 4.37. SEM data showing wedging, and image of the first wedged MLL. Part (a) shows a variation in thickness from 9 μm thick on the left side down to 1 μm thick on the right hand side. A complete SEM image of the wedged MLL is given in part (b). Although there are significant diagonal striations due to polishing damage, wedged MLL layers are visible. The SEM image in (b) is from the 6.6 μm thick linear region in the center of the structure.

From the measured lateral thickness gradient shown in Figure 4.37 (a), this location of the wMLL has a focal length of 2.6 mm, which is calculated as ½ the distance of the tangent intercept with zero, or $\mathbf{2f_0}$. A linear fit of the layer placement for x-ray parameters[38] indicates that this wMLL is optimized for λ = 0.0151 nm, or a photon energy of 82.1 keV. Using the linear fit shown below in Figure 4.38 (a) and dynamical diffraction theory for MLL structures[59], the calculated intensity contours (isophotes) around the first-order focus are shown in Figure 4.38 (b). An intensity profile through the region of maximum intensity, shown in Figure 4.38 (c),

yields an expected line focus full-width at half-maximum (FWHM) of 5.5 nm[38]. It is important to emphasize that this line focus is calculated from only the partial aperture that this MLL subtends, which is 39% of a complete, symmetric wMLL structure. This aperture is represented by the layers shown in Figure 4.38 (a). An integrated efficiency of 36% has been simulated for this device with a 30 μm section thickness.

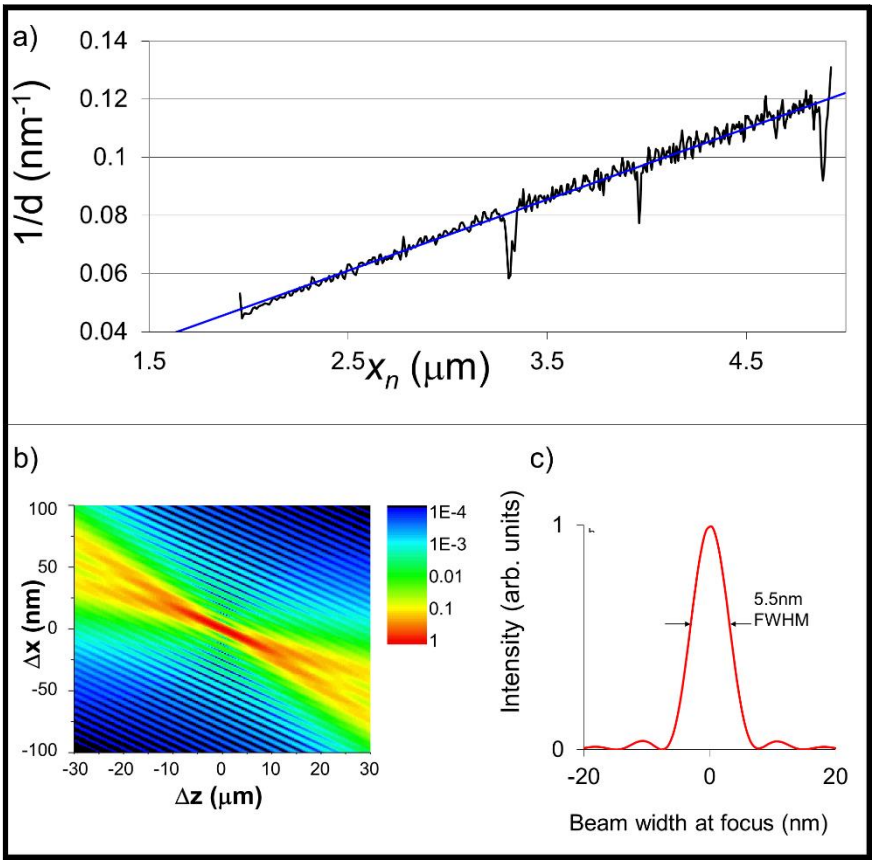

Figure 4.38: Inverse d-spacing plot and calculated focus of the first wedged MLL. taken at the region where the MLL has a linear gradient and is roughly 6.6 μm thick (see previous figure). The calculated intensity contour around the focus is shown in part (b), with an expected line focus (c) of 5.5 nm FWHM. The photon energy is 82.1 keV.

As previously explained, fabrication of a wMLL for a particular X-ray wavelength requires that the multilayer section is extracted from the correct z position so that the in-plane gradient matches the focal length of the layer sequence. Wedged MLL structures have some tolerance to the energy deviation from the optimum value. Within a small energy range, the focusing performance is not degraded significantly according to dynamical diffraction theory[59]. A section of the wMLL extracted at the 6.6 μm position (according to Figure 4.37) with a 30 μm thickness indicate that the focal spot size would be approximately constant[73] within a tolerance of ±10% of the optimum energy (82.1 keV). Lower-energy devices will exhibit a smaller energy bandwidth.

4.2.4.3 Large aperture wedged MLL

The results above demonstrate that wedged MLL can indeed be fabricated with profile coating. Building upon this initial success, a second structure was deposited using the MLL deposition system at Brookhaven National Laboratory[79]. This MLL was deposited with four cathodes, using WSi_2/Si to a thickness of roughly 31 μm. The MLL has an outermost zone-width of 2.8 nm and a focal length of 3.2 mm when operated at 14.6 keV. These lens parameters were chosen so the lens series would be compatible with an MLL microscope for scientific applications[123,157] This lens has been fully characterized by a team of collaborators using scanning electron microscopy (SEM) analysis, rocking curve measurement and ptychography for zone placement error, efficiency and focus wavefield characterization, respectively. Final results and observations about the lens are shown below, while the experimental details are outside the scope of this dissertation and can be found elsewhere[158]. Experimental data show good agreement with calculations, indicating successful fabrication of a wedged MLL. The work cited here is the first linear wedged MLL reported with its performance fully characterized using x-rays.

The extreme lateral gradient for this wedged MLL was again produced using a profiled mask. Figure 4.39 shows a schematic of the mask in use. Part (a) shows five open cut-outs. The cut-out shapes are determined from the distribution of atomic flux density shown as a solid line at the top of the plot and the required deposition thickness profile which is at the bottom of the plot. Details on profile coating are found in Chapter 3. The left and right cut-outs were designed to generate MLLs with flat zones for reference (or reflective multilayers for rate calibration). These two cut-outs have an opening that narrows towards the center because of the non-uniform deposition flux density shown at the top of the plot. The three center cut-outs are used to grow wMLLs on six substrates. Each of the three cut-outs are designed to produce a triangular thickness gradient, where the gradient deposited on neighboring substrates switches sign. The opening is designed in such a way that the amount of material deposited on the substrate is linear in the horizontal direction. The flux density variation along this axis necessitates a slight curvature to the mask profile. Because the maximum flux density is larger at the center, the center cut-out is smaller than its neighbors in order to deposit nominally identical wedged MLLs on all six substrates. Part (b) is a picture of the actual mask used with four magnetron sources. All cut-out profiles are identical for each source.

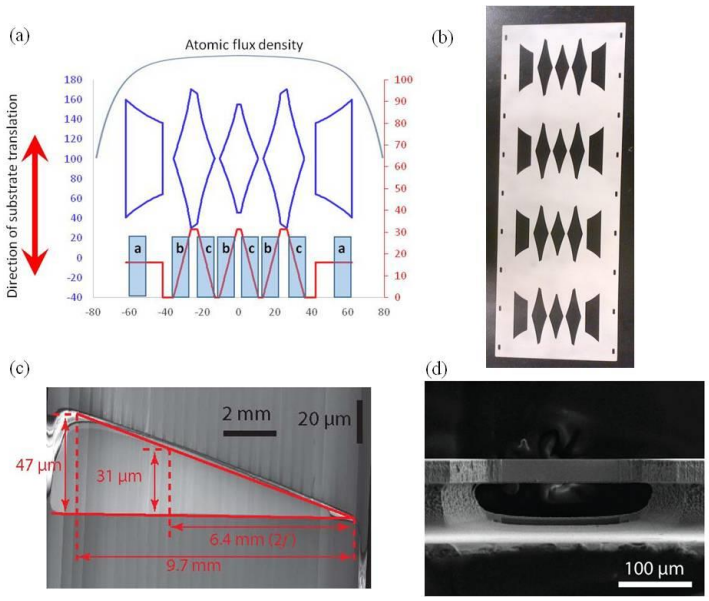

Figure 4.39. Wedged MLL mask and wedged MLL. A profiled mask cut that produces a film gradient which is shown overlaid on a series of substrates labelled "a", "b", and "c". Six sets of substrates labeled "b" and "c" would have identical wedging gradients, although the in the reverse orientation. In order to simplify growth rate calibration with x-ray reflectivity measurements, short uniform thickness sections in the mask were cut to produce a uniform film thickness on substrates labeled "a". The top curve shows the change of the atomic flux density. (b) a picture of the fabricated mask used for four sources. (c) The cross-section of structure. The wedged MLL was sectioned at a place that is 6.6 µm away from the corner. (d) SEM image of the edge view of the sectioned wedged MLL with 31 µm aperture size. Evident in the structure is over-etching during sectioning, which left the MLL

Using this mask and the MLL deposition system[79,101] the wedged multilayer stack was deposited with 7,688 layers of alternating Si and WSi_2, equating to 29% of a full MLL structure. A 2 mm thick Si (100) diced wafer segment is used as the substrate, which is positioned roughly 73 mm away from the magnetron sources. Figure 4.40 (c) is a stitched SEM image showing the deposition thickness variation along the length of the 12 mm substrate, which exhibits a good linearity between 3 mm and 9 mm from the edge of the silicon wafer where the layer thickness approaches zero. The total thickness deposited onto the substrate ranges from 0 to 47 µm. The multilayer stack was then sectioned and smoothed using a combination of reactive ion etching and focused ion beam milling, at a location 6.4 mm away from the right edge. At this location, the lens aperture size is around 31 µm, and the focal length due to wedging is ½ of 6.4 mm, or 3.2 mm. As mentioned for the first wedged MLL, optimum performance is achieved only when the wavelength where the MLL deposited at this location matches a focal length of 3.2 mm. An SEM image of the sectioned MLL window at this location is shown in Figure 4.40 (d). After sectioning, the wedged MLL is about 9.5 µm thick. As can be seen from the image, over-etching of the MLL resulted in an open cavity space directly underneath the MLL.

Marker layers were integrated into this wedged MLL for layer placement metrology. Several of the marker layers are visible in Figure 4.40 (a). A linear fit of marker layer spacing

shows that the optimum energy for this particular section of the wedged MLL is 14.6 keV when the focal length is 3.2 mm. A fit of this data reveals significant phase error as seen in Figure 4.40 (b). Due to the previously stated lack of sufficient in-situ rate monitors, several deposition iterations would be necessary to obtain diffraction-limited zone placement accuracy. This lens was produced without any iterative correction.

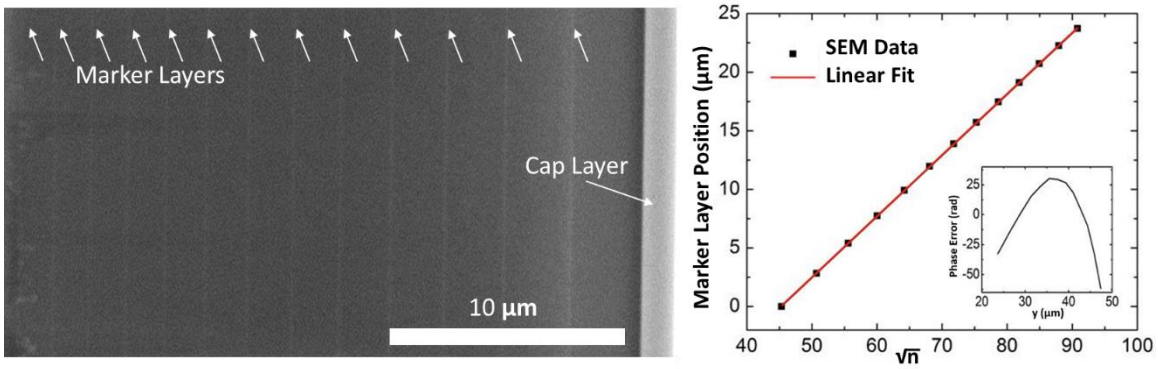

Figure 4.40: 31 µm thick wedged MLL image and linearity. Part (a) reveals a series of marker layers. (b) Shows the marker layer positions vs. √n, where n is the zone index. A linear fit of this data is used to determine the optimum wavelength. The inset shows significant phase error of this very first iteration in what would normally be several iterations to produce a diffraction limited optic.

The performance gains from a wedged MLL versus a flat or tilted MLL is that each layer is placed at the proper angle throughout the entire lens. Characterization of the wedging of this lens was performed at beamline 1-BM at the APS by staff[158] from BNL and ANL. In these experiments, the lens was illuminated at 14.6 keV while an area detector downstream is used to measure the diffraction pattern as the lens is rotated. Efficiency versus rocking angle is calculated by integrating the measured intensity. Data is normalized to the total incident intensity. Figure 4.41 (a) shows calculations for a perfect MLL structure. The wedged MLL focusing (-1^{st}) diffraction order has a sharp peak at 0 degrees, while the diverging ($+1^{st}$) order is broad and low. Also shown for comparison are the calculated efficiencies for a flat MLL that is rocked. Because a flat MLL is symmetric, both the positive and negative orders are symmetric. The experimental data shown in part (b) shows a sharp peak with an efficiency of 32% for the wedged MLL, while the calculated flat MLL would have an efficiency of about 11%. While the calculated perfect lens should have an efficiency around 50%, the reduction in measured efficiency is attributed to imperfect zone placement. This reduction may also be due to bending or warping of the lens, which is mentioned below.

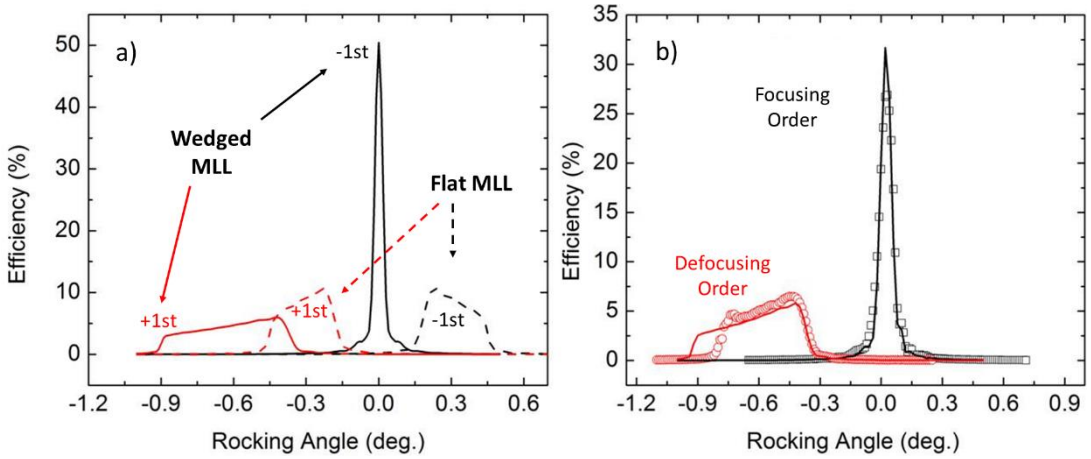

Figure 4.41: Simulated efficiencies of a wedged and flat MLL. The focusing and defocusing orders are shown at 14.6 keV. Both lenses are simulated as perfect structures with identical parameters aside from wedging. The MLL parameters assume a thickness of 10 µm, aperture of 31 µm and outermost zone width of 2.8 nm. For the wedged MLL, focal length is set at 3.2 mm at 14.6 keV. In part (a), the relatively modest efficiency for the flat MLL is contrasted with the intense -1st order and suppressed +1st order peak of the wedged MLL. Part (b) shows the experimental and simulated efficiencies of wedged MLL.

The wavefield around the focus of this lens was also characterized with a ptychography technique at 14.6 keV performed at beamline 34-ID-C, also at APS. Details of this can be found elsewhere[118,159]. The focus reconstructed from this measurement is shown below in Figure 4.42. Also included is the expected focus based on calculation from the phase error shown above in Figure 4.40. The focus profile based on reconstruction from the measurement shows excellent agreement with the profile calculated via marker layer position. Significant side lobes are visible on the right side, instead of a single, strong peak. The center peak has a FWHM of 25.6 nm when fit with a Gaussian profile. The peak as calculated from the marker layer spacing has a FWHM of 26.6 nm. Figure 4.42 (b) shows the same data on a logarithmic scale, with good agreement between reconstruction and simulation. A perfect lens would have a diffraction-limited focus size of 10 nm.

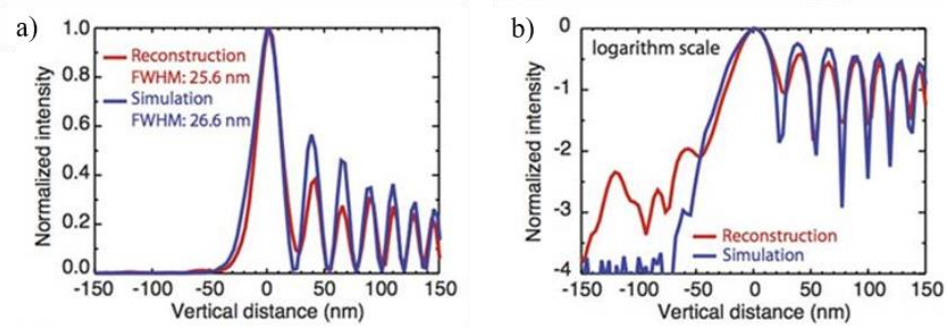

Figure 4.42: Line plot of the focal reconstruction. Data were obtained by simulation incorporating measured placement error from Figure 4.40, alongside the focus obtained from reconstruction via ptychography.The FWHM focal sizes of 25 nm vs 26 nm match closely. Data is plotted in a linear scale in (a) and logarithmic scale in (b).

The slight differences between the measurement and the calculations can be due to a slew of imperfections. Zone placement error is a significant contributor to the error. Also, accumulated film stress during deposition could affect the interfacial characteristics or profile. Sectioning and polishing, which is required for producing a usable MLL optic, could also introduce structural deformation. This wedged MLL was slightly over-etched, resulting in a "membrane" like structure that is supported only on two sides. This is clear in Figure 4.39 (d). This may contribute to bending or twisting of the wMLL layers, which is observed within the transmission x-ray images in Figure 4.43. In the set of three images, the 31 µm aperture of the wedged MLL is along the horizontal plane, and the 200 µm section width is along the vertical plane. As the MLL is rocked along various angles, the dark band is due to extinction at the maximum diffraction efficiency because diffraction removes intensity from the transmitted beam. If the wMLLs were perfect, this band would be parallel and very wide because a large portion of the wMLL would be diffracting all at the same angle. However, in these images, the band is seen to warp or wander through the structure. This suggests that the wedged MLL is somehow warped or bent.

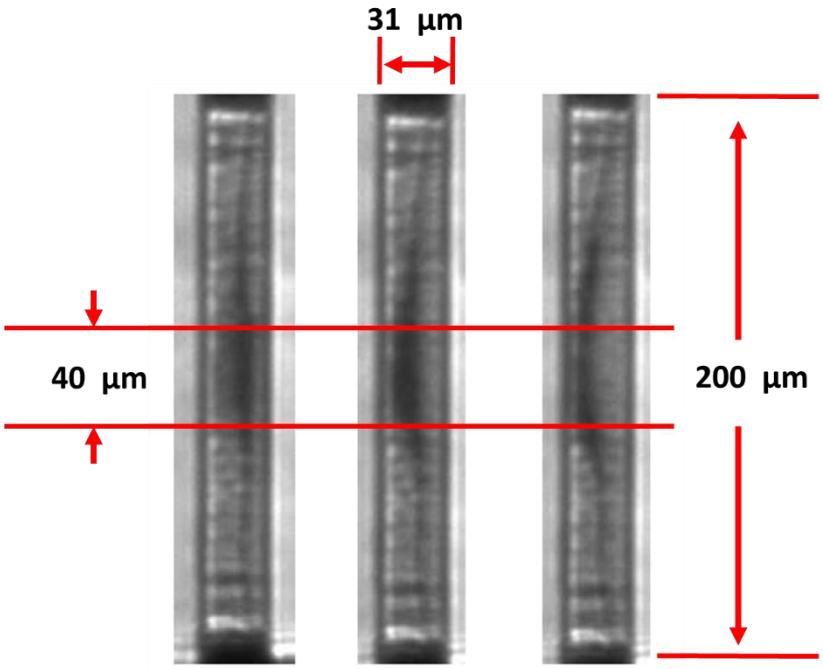

Figure 4.43: x-ray transmission images at 3 rocking angles with 0.02 degree spacing. The dark band down the center is caused by extinction because diffraction removes intensity from the transmitted beam. Near the central 40 µm region, the widening of the band is due to wedging within the wMLL. Warping of the zones outside the center is likely due to physical twisting of the lens. This twisting is caused by stress inside the structure and sectioning damage, and is probably increased because the substrate below the lens was removed during the sectioning process. For all the data in this section, only the central region of the MLL was utilized.

4.3 Discussion and future work

Starting with the first multilayer Laue lens deposition of only a few hundred layers of W and Si, MLL technology has steadily progressed. The MLL work produced for this dissertation yielded solutions for multiple problems. A method to produce near diffraction-limited MLLs by using marker layers for deposition feedback has been developed and tested. By exploring new material systems and deposition processes, larger deposition thicknesses for increased aperture have been realized alongside wider sections for increased mechanical rigidity. WSi_2/Si MLLs that were fabricated with N_2 reactive sputtering have been deployed as regular beamline optics. Because of this work, MLLs with an aperture of 105 μm produced with WSi_2 and an aluminum-silicon matrix have been fabricated. New materials have been identified that will increase optical efficiency. Wedged MLLs, for the ultimate in focusing and optical efficiency, have been fabricated and experimentally verified to work.

Various MLLs produced during this dissertation have been examined by groups at synchrotrons around the globe. By aligning a pair of MLLs, Yan et. al. reported a 2D x-ray focus down to a spot of 25 nm × 27 nm with 2% efficiency at 12 keV, and a spot of 25 × 40 nm with 17% efficiency at 19.5 keV[119]; this achieved focusing capability has been used for scientific investigations[120,121]. Huang et. al. demonstrated an 11 nm line focus at 12 keV by reconstructing the far-field diffraction pattern from an MLL with 43 μm aperture[118]. The first at-wavelength investigation[158] of a wedged MLL resulted in measurement of a focusing efficiency of 27% at 14.6 keV, very close to the theoretical value of 32%. The focal size of 25.6 nm ± 1.2 nm, as determined by ptychography, is in excellent agreement with theory taking into account measured zone placement error. MLL with world-leading aperture sizes over 100 μm have been tested[156,160] at wavelength. The early stages of this work opened a roadmap for powerful new beamlines, with the HXN beamline[161] currently under regular user operations with MLL optics that have an aperture size of 43 μm x 53 μm, producing a focus below 20x20 nm.

Many solutions for the sub-components required for producing larger aperture, higher performing MLL optics have been identified and tested, but these have so far not been tied together into one optic. Vanadium silicide has been identified as a good candidate to replace tungsten silicide however no MLL has been fabricated with this material as of yet. Flat MLL have been produced with WSi_2/Al-Si, and wedged MLL have been produced with the older material system of WSi_2/Si but these have not yet been combined. A wedged MLL needs to be produced from V_xSi_x/Al-Si. Currently wedged MLL aperture lags about 2x or 3x behind flat MLL mainly due to the reduced efficiency in the wedged MLL masking as well as a desire to produce usable wMLL optics and not simply chase aperture size. The wMLL aperture size needs to increase to match flat MLL, but this could happen after or concurrently with material systems changes. Marker layers appear to be a reliable method for layer placement error reduction but require excellent deposition system repeatability. In order to continue realizing gains in real aperture size while maintaining good layer placement, which is currently the limiting factor in large aperture wedged MLL, deposition systems could benefit from larger cathodes as well as some form of in-situ rate monitoring. This in-situ rate monitoring is the topic of two on-going SBIR phase II projects. Another promising instrumentation project initiated at the APS aims to develop a deformable mask which can be adjusted in real time during deposition. This dynamic aperture can be used to define arbitrary film thickness gradients or profiles. A dynamic aperture may be useful to produce a central zone for compensation[77], or for exploration of more exotic

geometries. Equipment that is developed as a result of these projects will need to be integrated into both the APS Modular Deposition System as well as the BNL MLL Deposition System.

Sectioning, mounting, and integration of individual MLL optics has many possible advancements to wade into. This topic is outside the scope of this writing so individual details will be left out however it is important to mention the major issues. The extraction and polishing of individual lens segments continues to be done either exclusively by, or as a combination, of reactive ion etching (RIE), focused ion-beam milling (FIB), and manual polishing techniques. These methods are appropriate because MLL deployment is highly specialized for individual beamlines and significant effort can be spent preparing singular lens elements. If MLL were ever to approach demand requiring more mass production, automated processes will be required. Given modern equipment, however, this might simply manifest itself into a form of batch automated FIB processing. Sectioned lens geometry is also possible to modify into some structurally advantageous form with RIE and/or FIB processing. Currently, monolithically bonded MLL are coming into view. Bonded MLL vastly reduce the motion degrees of freedom required for alignment and might be feasible to use in lab-based x-ray microscopes. More work is needed to craft procedures for extracting the proper MLL segments from a graded structure in order to directly bond two MLL segments with differing focal lengths without astigmatism. Also, as MLL focal sizes decrease, the angular alignment tolerance between the horizontal and vertically focusing MLL gets tighter. With sub 5nm focal sizes, orthogonality must be held to below 0.01 degrees, which is quite a challenge given the small sizes of the lens. While the many circular wire multilayer zone plate efforts have reached limits due to a combination of technical issues, these would be the most convenient optics for use due their ability to directly replace conventional zone plates. Reaching below 10nm focus requires properly tapered zones, so the multilayer zone plate would require a wedged, or curved substrate such as a tapered wire or a section of a sphere. This is a natural progression of the technology and hopefully will become reality in the future.

References

1 Bisset, D. C. & Iball, J. X-Ray Diffraction from Built-up Multilayers Consisting of only a few Monolayers. *Proceedings of the Physical Society. Section A* **67**, 315 (1954).

2 Spiller, E. Reflective multilayer coatings for the far uv region. *Appl. Opt.* **15**, 2333-2338 (1976).

3 Barbee Jr, T. W. & Warburton, W. K. X-ray evanescent- and standing-wave fluorescence studies using a layered synthetic microstructure. *Materials Letters* **3**, 17-23, doi:http://dx.doi.org/10.1016/0167-577X(84)90006-5 (1984).

4 Holland, L. A. CATHODIC SPUTTERING OF METAL AND DIELECTRIC FILMS. United States patent 2,866,502 (1959).

5 Liu, C., Conley, R., Macrander, A. T., Graber, T., Morawe, C., Borel, C. & Dufresne, E. M. Small d-spacing WSi_2/Si narrow bandpass multilayers. *Advances in X-Ray/EUV Optics and Components II*. 154-160.

6 Barrett, R., Baker, R., Cloetens, P., Dabin, Y., Morawe, C., Suhonen, H., . . . Zhang, L. Dynamically-figured mirror system for high-energy nanofocusing at the ESRF. *SPIE Optical Engineering + Applications*. 813904-813904 (International Society for Optics and Photonics).

7 Liu, C., Ice, G. E., Liu, W., Assoufid, L., Qian, J., Shi, B., . . . Tischler, J. Z. Fabrication of nested elliptical KB mirrors using profile coating for synchrotron radiation X-ray focusing. *Applied Surface Science* **258**, 2182-2186, doi:http://dx.doi.org/10.1016/j.apsusc.2011.02.079 (2012).

8 Kirkpatrick, P. & Baez, A. V. Formation of optical images by x-rays. *JOSA* **38**, 766-773 (1948).

9 Mimura, H., Handa, S., Kimura, T., Yumoto, H., Yamakawa, D., Yokoyama, H., . . . Yamauchi, K. Breaking the 10 nm barrier in hard-X-ray focusing. *Nature Physics* **6**, 122-125, doi:http://www.nature.com/nphys/journal/v6/n2/suppinfo/nphys1457_S1.html (2010).

10 Ice, G. E., Chung, J.-S., Tischler, J. Z., Lunt, A. & Assoufid, L. Elliptical x-ray microprobe mirrors by differential deposition. *Review of Scientific Instruments* **71**, 2635-2639 (2000).

11 Liu, C., Assoufid, L., Conley, R., Macrander, A. T., Ice, G. E. & Tischler, J. Z. Profile coating and its application for Kirkpatrick-Baez mirrors. *Optical Engineering* **42**, 3622-3628 (2003).

12 Liu, C., Conley, R., Assoufid, L., Macrander, A. T., Ice, G. E., Tischler, J. Z. & Zhang, K. Profile coatings and their applications. *Journal of Vacuum Science & Technology A: Vacuum, Surfaces, and Films* **21**, 1579-1584 (2003).

13 Liu, C., Conley, R., Assoufid, L., Cai, Z., Qian, J. & Macrander, A. From flat substrate to elliptical KB mirror by profile coating. *AIP Conference Proceedings.* 704.

14 Liu, C., Conley, R. & Macrander, A. Functional profile coatings and film stress. *Journal of Vacuum Science & Technology A: Vacuum, Surfaces, and Films* **22**, 1610-1614 (2004).

15 Attwood, D. T. *Soft X-Rays and Extreme Ultraviolet Radiation: Principles and Applications* (Cambridge University Press, 1999).

16 Kirz, J. Phase zone plates for x rays and the extreme uv. *J. Opt. Soc. Am.* **64**, 301-309 (1974).

17 Wu, S.-R., Hwu, Y. & Margaritondo, G. Hard-X-ray Zone Plates: Recent Progress. *Materials* **5**, 1752-1773 (2012).

18 Chao, W., Harteneck, B. D., Liddle, J. A., Anderson, E. H. & Attwood, D. T. Soft X-ray microscopy at a spatial resolution better than 15 nm. *Nature* **435**, 1210-1213 (2005).

19 Chao, W., Fischer, P., Tyliszczak, T., Rekawa, S., Anderson, E. & Naulleau, P. Real space soft x-ray imaging at 10 nm spatial resolution. *Optics Express* **20**, 7 (2012).

20 Burkhard, K., Pierre, T., Alessandra, G. & Maya, K. Transmission and emission x-ray microscopy: operation modes, contrast mechanisms and applications. *Journal of Physics: Condensed Matter* **23**, 083002 (2011).

21 Tsung-Yu, C., Yu-Tung, C., Cheng-Liang, W., Kempson, I. M., Wah-Keat, L., Chu, Y. S., . . . Margaritondo, G. Full-field microimaging with 8 keV X-rays achieves a spatial resolutions better than 20 nm. *Optics Express* **19**, 19919-19924, doi:10.1364/oe.19.019919 (2011).

22 Vila-Comamala, J., Gorelick, S., Färm, E., Kewish, C. M., Diaz, A., Barrett, R., . . . David, C. Ultra-high resolution zone-doubled diffractive X-ray optics for the multi-keV regime. *Opt. Express* **19**, 175-184 (2011).

23 Vila-Comamala, J., Pan, Y. S., Lombardo, J. J., Harris, W. M., Chiu, W. K. S., David, C. & Wang, Y. X. Zone-doubled Fresnel zone plates for high-resolution hard X-ray full-field transmission microscopy. *Journal of Synchrotron Radiation* **19**, 705-709, doi:10.1107/s0909049512029640 (2012).

24 Maser, J., Lai, B. P., Yun, W., Shastri, S. D., Cai, Z., Rodrigues, W., . . . Trackhtenberg, E. Near-field stacking of zone plates for hard x-ray range *Proceedings of SPIE* **4783**, 74, doi:10.1117/12.451396 (2002).

25 Jefimovs, K., Vila-Comamala, J., Pilvi, T., Raabe, J., Ritala, M. & David, C. Zone-Doubling Technique to Produce Ultrahigh-Resolution X-Ray Optics. *Physical Review Letters* **99**, 264801 (2007).

26 Saitoh, K., Inagawa, K., Kohra, K., Hayashi, C., Iida, A. & Kato, N. Fabrication and Characterization of Multilayer Zone Plate for Hard X-Rays. *Japanese Journal of Applied Physics* **27**, L2131 (1988).

27 Bionta, R. M., Skulina, K. M. & Weinberg, J. Hard x- ray sputtered- sliced phase zone plates. *Applied Physics Letters* **64**, 945-947, doi:http://dx.doi.org/10.1063/1.110968 (1994).

28 Kaulich, B. Phase zone plates for hard X-ray microscopy. *Advances in X-Ray/EUV Optics and Components II* **3449**, 108-117, doi:10.1117/12.330336 (1998).

29 Tamura, S., Yasumoto, M., Kamijo, N., Suzuki, Y., Awaji, M., Takeuchi, A., . . . Handa, K. Development of a multilayer Fresnel zone plate for high-energy synchrotron radiation X-rays by DC sputtering deposition. *Journal of Synchrotron Radiation* **9**, 154-159, doi:10.1107/S0909049502003746 (2002).

30 Kamijo, N., Suzuki, Y., Takano, H., Tamura, S., Yasumoto, M., Takeuchi, A. & Awaji, M. Microbeam of 100 keV x ray with a sputtered-sliced Fresnel zone plate. *Review of Scientific Instruments* **74**, 5101-5104, doi:http://dx.doi.org/10.1063/1.1614882 (2003).

31 Koyama, T., Takano, H., Konishi, S., Tsuji, T., Takenaka, H., Ichimaru, S., . . . Kagoshima, Y. Circular multilayer zone plate for high-energy x-ray nano-imaging. *Review of Scientific Instruments* **83**, 013705-013704 (2012).

32 Doring, F., Robisch, A. L., Eberl, C., Osterhoff, M., Ruhlandt, A., Liese, T., . . . Krebs, H. U. Sub-5 nm hard x-ray point focusing by a combined Kirkpatrick-Baez mirror and multilayer zone plate. *Optics Express* **21**, 19311-19323, doi:10.1364/oe.21.019311 (2013).

33 Mayer, M., Keskinbora, K., Grevent, C., Szeghalmi, A., Knez, M., Weigand, M., . . . Schutz, G. Efficient focusing of 8 keV X-rays with multilayer Fresnel zone plates fabricated by atomic layer deposition and focused ion beam milling. *Journal of Synchrotron Radiation* **20**, 433-440, doi:10.1107/s0909049513006602 (2013).

34 Hidekazu, T., Takuya, T., Takuto, H., Takahisa, K., Yoshiyuki, T. & Yasushi, K. Sub-15 nm Hard X-Ray Focusing with a New Total-Reflection Zone Plate. *Applied Physics Express* **3**, 076702 (2010).

35 Li, Y., Yasa, M., Pelletier, O., Safinya, C. R., Caine, E., Hu, E. E. & Fernandez, P. Metal layer Bragg–Fresnel lenses for diffraction focusing of hard x-rays. *Applied Physics Letters* **82**, 2538-2540 (2003).

36 Yan, H. X-ray nanofocusing by kinoform lenses: a comparative study using different modeling approaches. *Physical Review B* **81**, 075402 (2010).

37 Alianelli, L., Sawhney, K. J. S., Barrett, R., Pape, I., Malik, A. & Wilson, M. C. High efficiency nano-focusing kinoform optics for synchrotron radiation. *Opt. Express* **19**, 11120-11127 (2011).

38 Conley, R., Liu, C., Qian, J., Kewish, C. M., Macrander, A. T., Yan, H., . . . Stephenson, G. B. Wedged multilayer Laue lens. *Rev. Sci. Instrum.* **79**, 053104, (2008).

39 Kang, H. C., Stephenson, G. B., Liu, C., Conley, R., Macrander, A. T., Maser, J., . . . Chapman, H. N. High-efficiency diffractive x-ray optics from sectioned multilayers. *Applied Physics Letters* **86**, 151109-151103 (2005).

40 Kang, H. C., Stephenson, G. B., Liu, C., Conley, R., Macrander, A. T., Maser, J., . . . Chapman, H. N. Synchrotron x-ray study of multilayers in Laue geometry. *Proc. SPIE* **5537**, 127-132, doi:10.1117/12.560173 (2004).

41 Kang, H. C., Yan, H., Winarski, R. P., Holt, M. V., Maser, J., Liu, C., . . . Stephenson, G. B. Focusing of hard x-rays to 16 nanometers with a multilayer Laue lens. *Applied Physics Letters* **92**, 221114, doi:10.1063/1.2912503 (2008).

42 Liu, C., Conley, R., Macrander, A., Maser, J., Kang, H. & Stephenson, G. A multilayer nanostructure for linear zone-plate applications. *Thin Solid Films* **515**, 654-657 (2006).

43 Kang, H. C., Maser, J., Stephenson, G. B., Liu, C., Conley, R., Macrander, A. T. & Vogt, S. Nanometer Linear Focusing of Hard X Rays by a Multilayer Laue Lens. *Physical Review Letters* **96**, 127401-127404 (2006).

44 Yan, H., Rose, V., Shu, D., Lima, E., Kang, H. C., Conley, R., . . . Stephenson, G. B. Two dimensional hard x-ray nanofocusing with crossed multilayer Laue lenses. *Optics Express* **19**, 15069-15076 (2011).

45 Kang, H. C., Stephenson, G. B., Liu, C., Conley, R., Khachatryan, R., Wieczorek, M., . . . Koritala, R. Sectioning of multilayers to make a multilayer Laue lens. *Review of Scientific Instruments* **78**, 046103 (2007).

46 Bouet, N., Conley, R., Biancarosa, J., Divan, R. & Macrander, A. WSi2/Si Multilayer Sectioning by Reactive Ion Etching for Multilayer Laue Lens Fabrication. *Society of Photo-Optical Instrumentation Engineers (SPIE) Conference Series.* 780203-780205.

47 Zhou, L., Wang, Y., Zhou, H., Li, M., Headrick, R. L., MacArthur, K., . . . Macrander, A. T. Pressure-dependent transition from atoms to nanoparticles in magnetron sputtering: Effect on WSi_2 film roughness and stress. *Physical Review B* **82**, 075408 (2010).

48 Rack, A., Assoufid, L., Lee, W. K., Shi, B., Liu, C., Morawe, C., . . . Bouet, N. Hard X-ray multilayer mirror round-robin on the wavefront preservation capabilities of W/B_4C coatings. *Radiation Physics and Chemistry* **81**, 1696-1702, doi:https://doi.org/10.1016/j.radphyschem.2012.06.015 (2012).

49 Libera, J. A., Gurney, R. W., Nguyen, S. T., Hupp, J. T., Liu, C., Conley, R. & Bedzyk, M. J. X-ray nanoscale profiling of layer-by-layer assembled metal/organophosphonate films. *Langmuir* **20**, 8022-8029 (2004).

50 Buzea, C. & Robbie, K. State of the art in thin film thickness and deposition rate monitoring sensors. *Reports on Progress in Physics* **68**, 385 (2005).

51 Liu, W., Ice, G. E., Tischler, J. Z., Khounsary, A., Liu, C., Assoufid, L. & Macrander, A. T. Short focal length Kirkpatrick-Baez mirrors for a hard x-ray nanoprobe. *Review of scientific instruments* **76**, 113701-113706 (2005).

52 Kewish, C. M., Assoufid, L., Macrander, A. T. & Qian, J. Wave-optical simulation of hard-x-ray nanofocusing by precisely figured elliptical mirrors. *Applied optics* **46**, 2010-2021 (2007).

53 Maser, J. & Schmahl, G. Coupled wave description of the diffraction by zone plates with high aspect ratios. *Optics communications* **89**, 355-362 (1992).

54 Koike, M. & Suzuki, I. H. Nanofabrication of Multilayer Zone Plates by Helicon Plasma Sputtering. *Japanese Journal of Applied Physics* **34**, 6754 (1995).

55 Koike, M., Suzuki, I. H., Komiya, S. & Amemiya, Y. Ti/Al multilayer zone plate and Bragg-Fresnel lens. *Journal of Synchrotron Radiation* **5**, 794-796, doi:10.1107/S090904959701666X (1998).

56 Kang, H. C., Chapman, H., Liu, C., Conley, R., Bajt, S., Stephenson, G., . . . Maser, J. *Synchrotron x-ray study of multilayers in Laue geometry*. (United States. Department of Energy, 2004).

57 Pfeiffer, F., David, C., van der Veen, J. F. & Bergemann, C. Nanometer focusing properties of Fresnel zone plates described by dynamical diffraction theory. *Physical Review B (Condensed Matter and Materials Physics)* **73**, 245331-245310 (2006).

58 Schroer, C. G. Focusing hard x rays to nanometer dimensions using Fresnel zone plates. *Physical Review B* **74**, 033405 (2006).

59 Yan, H. F., Maser, J., Macrander, A., Shen, Q., Vogt, S., Stephenson, G. B. & Kang, H. C. Takagi-Taupin description of x-ray dynamical diffraction from diffractive optics with large numerical aperture. *Physical Review B* **76**, 115438-115413, doi:115438 10.1103/PhysRevB.76.115438 (2007).

60 Yan, H. F. X-ray dynamical diffraction from multilayer Laue lenses with rough interfaces. *Physical Review B* **79**, 165410, doi:165410 10.1103/PhysRevB.79.165410 (2009).

61 Huang, Q., Zhu, J., Li, H., Wang, Z. & Tang, Y. Theoretical investigation of higher orders optimized Multilayer Laue Lens for hard x-ray nano-focusing. *Optics Communications* **285**, 5496-5499, doi:http://dx.doi.org/10.1016/j.optcom.2012.07.062 (2012).

62 Yan, H. & Chu, Y. S. Optimization of multilayer Laue lenses for a scanning X-ray microscope. *Journal of Synchrotron Radiation* **20**, 89-97, doi:10.1107/S0909049512044883 (2013).

63 Liu, C., Conley, R. & Macrander, A. Film stress studies and the multilayer Laue lens project. *Advances in X-Ray/EUV Optics and Components II.* 63170J.

64 Eberl, C., Liese, T., Schlenkrich, F., Döring, F., Hofsäss, H. & Krebs, H. U. Enhanced resputtering and asymmetric interface mixing in W/Si multilayers. *Appl. Phys. A* **111**, 431 - 437 (2013).

65 Conley, R., Liu, C. & Macrander, A. T. *Multilayer Deposition Control System*, (2007).

66 Koyama, T., Takenaka, H., Ichimaru, S., Ohchi, T., Tsuji, T., Takano, H. & Kagoshima, Y. in *10th International Conference on X-Ray Microscopy* Vol. 1365 *AIP Conference Proceedings* (eds I. McNulty, C. Eyberger, & B. Lai) 24-27 (Amer Inst Physics, 2011).

67 Ruhlandt, A., Liese, T., Radisch, V., Kruger, S. P., Osterhoff, M., Giewekemeyer, K., . . . Salditt, T. A combined Kirkpatrick-Baez mirror and multilayer lens for sub-10 nm x-ray focusing. *AIP Adv.* **2**, 7, doi:10.1063/1.3698119 (2012).

68 Liese, T., Radisch, V., Knorr, I., Reese, M., Groβmann, P., Mann, K. & Krebs, H. U. Development of laser deposited multilayer zone plate structures for soft X-ray radiation. *Applied Surface Science* **257**, 5138 -5141 (2011).

69 Liese, T., Radisch, V. & Krebs, H. U. Fabrication of multilayer Laue lenses by a combination of pulsed laser deposition and focused ion beam. *Review of Scientific Instruments* **81**, 073710, doi:0.1063/1.3462985 (2010).

70 Mayer, M., Grévent, C., Szeghalmi, A., Knez, M., Weigand, M., Rehbein, S., . . . Schütz, G. Multilayer Fresnel zone plate for soft X-ray microscopy resolves sub-39nm structures. *Ultramicroscopy* **111**, 1706-1711 (2011).

71 Liu, C., Conley, R., Qian, J., Kewish, C., Macrander, A., Maser, J., . . . Stephenson, G. Bonded Multilayer Laue Lens for focusing hard X-rays. *Nuclear Instruments and Methods in Physics Research Section A: Accelerators, Spectrometers, Detectors and Associated Equipment* **582**, 123-125 (2007).

72 Conley, R., Liu, C., Kewish, C. M., Macrander, A. T. & Morawe, C. Multilayer growth in the APS rotary deposition system. *Advances in X-Ray/EUV Optics and Components II* **6705**, 670505-670507 (2007).

73 Yan, H., Kang, H. C., Maser, J., Macrander, A. T., Kewish, C. M., Liu, C., . . . Stephenson, G. B. Characterization of a multilayer Laue lens with imperfections. *Nucl. Instrum. Methods Phys. Res. Sect. A-Accel. Spectrom. Dect. Assoc. Equip.* **582**, 126-128 (2007).

74 Jahedi, N., Conley, R., Shi, B., Qian, J., Lauer, K. & Macrander, A. Metrology of multilayer Laue lens structures by means of scanning electron microscope imaging. *Nuclear Instruments and Methods in Physics Research Section A: Accelerators, Spectrometers, Detectors and Associated Equipment* **616**, 89-92 (2010).

75 Conley, R., Bouet, N., Zhou, J., Yan, H., Chu, Y., Lauer, K., . . . Jahedi, N. Advanced multilayer Laue lens fabrication at NSLS-II. *SPIE Optical Engineering + Applications.* 850202-850207 (International Society for Optics and Photonics).

76 MacArthur, K., Shi, B., Conley, R. & Macrander, A. T. Periodic variation of stress in sputter deposited Si/WSi_2 multilayers. *Applied Physics Letters* **99**, 081905-081905-081903 (2011).

77 Conley Jr, R., Liu, C., Macrander, A., Yan, H., Kang, H., Maser, J. & Stephenson, G. B. ZONE COMPENSATED MULTILAYER LAUE LENS AND APPARATUS AND METHOD OF FABRICATING THE SAME. U.S. patent PCT/US2010/060057 (2008).

78 Lauer, K. *Deposition Control System* (Brookhaven National Laboratory, 2010).

79 Conley, R., Bouet, N., Biancarosa, J., Shen, Q., Boas, L., Feraca, J. & Rosenbaum, L. The NSLS-II multilayer laue lens deposition system. *Advances in X-Ray/EUV Optics and Components II.* 74480U-74481.

80 *X-ray Optics for BES Light Source Facilities*, <https://science.energy.gov/~/media/bes/pdf/reports/files/BES_XRay_Optics_rpt_print.pdf> (2013).

81 Yan, H., Conley, R., Bouet, N. & Chu, Y. S. Hard x-ray nanofocusing by multilayer Laue lenses. *Journal of Physics D: Applied Physics* **47**, 263001 (2014).

82 Chu, Y., Liu, C., Mancini, D., De Carlo, F., Macrander, A., Lai, B. & Shu, D. Performance of a double-multilayer monochromator at Beamline 2-BM at the Advanced Photon Source. *Review of Scientific Instruments* **73**, 1485-1487 (2002).

83 Windt, D. L., Waskiewicz, W. & Griffith, J. Surface finish requirements for soft x-ray mirrors. *Applied optics* **33**, 2025-2031 (1994).

84 Idir, M., Kaznatcheev, K., Qian, S. & Conley, R. Current status of the NSLS-II optical metrology laboratory. *Nuclear Instruments and Methods in Physics Research Section A: Accelerators, Spectrometers, Detectors and Associated Equipment* **710**, 17-23, doi:http://dx.doi.org/10.1016/j.nima.2012.10.122 (2013).

85 Macrander, A., Erdmann, M., Kujala, N., Stoupin, S., Marathe, S., Shi, X., . . . Sullivan, J. X-ray Optics Testing Beamline 1-BM at the Advanced Photon Source. *12th International Conference on Synchrotron Radiation Instrumentation (SRI-2015), New York, NY.* 6-10.

86 Windt, D. L. IMD—Software for modeling the optical properties of multilayer films. *Computers in physics* **12**, 360-370 (1998).

87 Ellingham, R. W. Roller-pinion. 860536 (1907).

88 Windt, D. L. & Conley, R. Two-dimensional differential deposition for figure correction of thin-shell mirror substrates for x-ray astronomy. *SPIE Optical Engineering+ Applications.* 96031H-96012 (International Society for Optics and Photonics).

89 Marshall, F. J. & Oertel, J. A. A framed monochromatic x-ray microscope for ICF (invited). *Review of Scientific Instruments* **68**, 735-739, doi:10.1063/1.1147688 (1997).

90 Moreno, T., Otero, E. & Ohresser, P. In situ characterization of undulator magnetic fields. *Journal of Synchrotron Radiation* **19**, 179-184, doi:10.1107/S0909049511052873 (2012).

91 Yamauchi, K., Mimura, H., Kimura, T., Yumoto, H., Handa, S., Matsuyama, S., . . . Ishikawa, T. Single-nanometer focusing of hard x-rays by Kirkpatrick-Baez mirrors. *Journal of Physics: Condensed Matter* **23**, 394206 (2011).

92 Somogyi, A., Kewish, C., Ribbens, M., Moreno, T., Polack, F., Baranton, G., . . . Samama, J. Status of the nanoscopium scanning hard x-ray nanoprobe beamline of Synchrotron Soleil. *Journal of Physics: Conference Series.* 012027 (IOP Publishing).

93 Holland, L. Vacuum deposition of thin films. *London: Chapman & Hall, 1970* **1** (1970).

94 Swann, S. Film thickness distribution in magnetron sputtering. *Vacuum* **38**, 791-794 (1988).

95 Liu, C., Assoufid, L., Macrander, A. T., Ice, G. E. & Tischler, J. Z. Profile coating for KB mirror applications at the Advanced Photon Source. *SPIE Optical Engineering + Applications.* 104-112 (2002).

96 Shi, B., Liu, C., Qian, J., Liu, W., Assoufid, L., Khounsary, A., . . . Macrander, A. T. Platinum Kirkpatrik-Baez mirrors for a hard x-ray microfocusing system made by profile coating. *SPIE Optical Engineering + Applications.* 78020G-78026 (International Society for Optics and Photonics) (2010).

97 Liu, C., Conley, R., Qian, J., Kewish, C., Liu, W., Assoufid, L., . . . Tischler, J. Plastic Deformation in Profile-Coated Elliptical KB Mirrors. *ISRN Optics* **2012** (2012).

98 Liu, C., Conley, R., Qian, J., Kewish, C. M., Liu, W., Assoufid, L., . . . Tischler, J. Z. Plastic Deformation in Profile-Coated Elliptical KB Mirrors. *ISRN Optics*, p. 1-3, doi:http://dx.doi.org/10.5402/2012/151092 (2012).

99 Quinn, D. J., Wardle, B. & Spearing, S. M. Residual stress and microstructure of as-deposited and annealed, sputtered yttria-stabilized zirconia thin films. *Journal of Materials Research* **23**, 609-618, doi:10.1557/JMR.2008.0077 (2008).

100 Liu, C., Erdmann, J., Maj, J. & Macrander, A. Thickness determination of metal thin films with spectroscopic ellipsometry for x-ray mirror and multilayer applications. *Journal of Vacuum Science & Technology A: Vacuum, Surfaces, and Films* **17**, 2741-2748 (1999).

101 Conley, R., Bouet, N., Lauer, K., Carlucci-Dayton, M., Biancarosa, J., Boas, L., . . . Rosenbaum, L. Multilayer Laue Lens Growth at NSLSII. *AIP Conference Proceedings* **1365**, 69 (2011).

102 Yashchuk, V. V., Anderson, E. H., Barber, S. K., Bouet, N., Cambie, R., Conley, R., . . . Voronov, D. L. Calibration of the modulation transfer function of surface profilometers with binary pseudorandom test standards: expanding the application range to Fizeau interferometers and electron microscopes. *Optical Engineering* **50**, 093604-093612 (2011).

103 Yashchuk, V. V., Conley, R., Anderson, E. H., Barber, S. K., Bouet, N., McKinney, W. R., . . . Voronov, D. L. Characterization of electron microscopes with binary pseudo-random multilayer test samples. *Nuclear Instruments and Methods in Physics Research Section A: Accelerators, Spectrometers, Detectors and Associated Equipment* **649**, 150-152 (2011).

104 Assoufid, L., Qian, J., Kewish, C. M., Liu, C., Conley, R., Macrander, A. T., . . . Saxer, C. A microstitching interferometer for evaluating the surface profile of precisely figured X-ray KB mirrors. *Advances in X-Ray/EUV Optics and Components II.* 670460.

105 Liu, C., Qian, J. & Assoufid, L. Profile etching for prefiguring X-ray mirrors. *Journal of synchrotron radiation* **22**, 0-0 (2015).

106 Alcock, S. G. & Cockerton, S. A preferential coating technique for fabricating large, high quality optics. *Nuclear Instruments and Methods in Physics Research Section A: Accelerators, Spectrometers, Detectors and Associated Equipment* **616**, 110-114, doi:http://dx.doi.org/10.1016/j.nima.2009.10.097 (2010).

107 Born, M. & Wolf, E. *Principles of optics*. (Cambridge University Press, 1999).

108 Levashov, V. E. & Vinogradov, A. V. Analytical theory of zone plate efficiency. *Physical Review E* **49**, 5797 (1994).

109 Gleber, S.-C., Wojcik, M., Liu, J., Roehrig, C., Cummings, M., Vila-Comamala, J., . . . Vogt, S. Fresnel zone plate stacking in the intermediate field for high efficiency focusing in the hard X-ray regime. *Optics express* **22**, 28142-28153 (2014).

110 Chao, W., Kim, J., Rekawa, S., Fischer, P. & Anderson, E. H. Demonstration of 12 nm Resolution Fresnel Zone Plate Lens based Soft X-ray Microscopy. *Optics Express* **17**, 17669-17677 (2009).

111 Maser, J., Stephenson, G. B., Vogt, S., Wenbing, Y., Macrander, A., Kang, H. C., . . . Conley, R. Multilayer Laue lenses as high-resolution x-ray optics. *Advances in X-Ray/EUV Optics and Components II* **5539**, 185-194 (2004).

112 Chapman, H. A High-Efficiency Spectral Purity Filter For EUV Lithography. (2005).

113 Braun, S. & Mai, H. in *Metal based thin films for electronics* (eds K. Wetzig & C.M. Schneider) 276 - 292 (Wiley, 2006).

114 Koyama, T., Ichimaru, S., Tsuji, T., Takano, H., Kagoshima, Y., Ohchi, T. & Takenaka, H. Optical Properties of $MoSi_2$/Si Multilayer Laue Lens as Nanometer X-ray Focusing Device. *Applied Physics Express* **1**, 117003 (2008).

115 Qiu-Shi, H., Hao-Chuan, L., Zhu-Qing, S., Jing-Tao, Z., Zhan-Shan, W., Ai-Guo, L., . . . Ming, L. Hard X-ray one dimensional nano-focusing at the SSRF using a WSi2/Si multilayer Laue lens. *Chinese Phys. C* **37**, 028002 (2013).

116 Liu, C., Conley, R., Macrander, A. T., Maser, J., Kang, H. C., Zurbuchen, M. A. & Stephenson, G. B. Depth-graded multilayers for application in transmission geometry as linear zone plates. *Journal of Applied Physics* **98**, 113519-113516 (2005).

117 (74% of the multilayers catalogued in the CXRO (Center of X-ray Optics) database were produced with sputtering)

118 Huang, X., Yan, H., Nazaretski, E., Conley, R., Bouet, N., Zhou, J., . . . Chu, Y. S. 11 nm hard X-ray focus from a large-aperture multilayer Laue lens. *Scientific Reports* **3**, doi:10.1038/srep03562 (2013).

119 Yan, H. F., Rose, V., Shu, D. M., Lima, E., Kang, H. C., Conley, R., . . . Maser, J. Two dimensional hard x-ray nanofocusing with crossed multilayer Laue lenses. *Optics Express* **19**, 15069-15076 (2011).

120 Kang, H. C., Yan, H., Chu, Y. S., Lee, S. Y., Kim, J., Nazaretski, E., . . . Maser, J. Oxidation of PtNi nanoparticles studied by a scanning X-ray fluorescence microscope with multi-layer Laue lenses. *Nanoscale* **5**, 7184-7187, doi:10.1039/c3nr00396e (2013).

121 Yan, H., Chu, Y. S., Maser, J., Nazaretski, E., Kim, J., Kang, H. C., . . . Chiu, W. K. S. Quantitative x-ray phase imaging at the nanoscale by multilayer Laue lenses. *Scientific Reports* **3**, 1307, doi:10.1038/srep01307 (2013).

122 Shu, D., Yan, H. & Maser, J. M. Multidimensional alignment apparatus for hard x-ray focusing with two multilayer laue lenses. U.S. patent 7597475 (2009).

123 Nazaretski, E., Kim, J., Yan, H., Lauer, K., Eom, D., Shu, D., . . . Chu, Y. S. Performance and characterization of the prototype nm-scale spatial resolution scanning multilayer Laue lenses microscope. *Review of Scientific Instruments* **84**, 033701-033707 (2013).

124 Shu, D., Yan, H. & Maser, J. Mechanical design of a multi-dimensional alignment system for an MLL system with nanometerscale 2-D focusing. *Proceedings of SRI-2008.* (to be published in Nucl. Instrum. Methods A).

125 Safi, I. Recent aspects concerning DC reactive magnetron sputtering of thin films: a review. *Surface and Coatings Technology* **127**, 203-218, doi:http://dx.doi.org/10.1016/S0257-8972(00)00566-1 (2000).

126 Anderson, R. L. & Helmer, J. C. Sputtering apparatus with a rotating magnet array having a geometry for specified target erosion profile. US patent (1991).

127 De Gryse, R., Haemers, J., Leroy, W. P. & Depla, D. Thirty years of rotatable magnetrons. *Thin Solid Films* **520**, 5833-5845, doi:http://dx.doi.org/10.1016/j.tsf.2012.04.065 (2012).

128 Windt, D. & Waskiewicz, W. Multilayer facilities required for extreme- ultraviolet lithography. *Journal of Vacuum Science & Technology B: Microelectronics and Nanometer Structures* **12**, 3826-3832 (1994).

129 Morawe, C., Borel, C. & Peffen, J.-C. The new ESRF multilayer deposition facility. *Proc. of SPIE.* 670504.

130 Pinsukanjana, P., Jackson, A., Tofte, J., Maranowski, K., Campbell, S., English, J., . . . Gossard, A. Real-time simultaneous optical-based flux monitoring of Al, Ga, and In using atomic absorption for molecular beam epitaxy. *J. Vac. Sci. Technol. B* **14**, 2147 (1996).

131 Rao, P. N., Rai, S. K., Nayak, M. & Lodha, G. S. Stability and normal incidence reflectivity of W/B4C multilayer mirror near the boron K absorption edge. *Applied Optics* **52**, 6126-6130, doi:10.1364/ao.52.006126 (2013).

132 Rao, P. N., Nayak, M., Modi, M. H., Rai, S. K. & Lodha, G. S. Growth of Multilayer Optics for Synchrotron Radiation Sources *J. Phys., Conf. Ser.* **425**, 052023, doi:10.1088/1742-6596/425/5/052023 (2013).

133 Chu, Y. S., Liu, C., Mancini, D. C., De Carlo, F., Macrander, A. T., Lai, B. & Shu, D. Performance of a double-multilayer monochromator at Beamline 2-BM at the Advanced Photon Source. *Rev. Sci. Instrum.* **73**, 1485-1487, doi:10.1063/1.1423628 (2002).

134 Zhang, Z., Liang, Y., Li, W., Wang, Z. & Chen, H. Stress evolution in B4C and Cr mono-layer and B4C/Cr multilayer films with variable layer thickness for neutron detectors. *Thin Solid Films* **531**, 302-305, doi:http://dx.doi.org/10.1016/j.tsf.2013.01.084 (2013).

135 Bozorg-Grayeli, E., Li, Z., Asheghi, M., Delgado, G., Pokrovsky, A., Panzer, M., . . . Goodson, K. E. Thermal conduction properties of Mo/Si multilayers for extreme ultraviolet optics. *Journal of Applied Physics* **112**, 083504, doi:10.1063/1.4759450 (2012).

136 Rosen, R. S., Vernon, D. S. P., Stearns, G., Viliardos, M. A., Kassner, M. E. & Cheng, Y. Silicide layer growth rates in Mo/Si multilayers. *Applied Optics* **32**, 6975-6980, doi:10.1364/ao.32.006975 (1993).

137 Windt, D. L., Christensen, F. E., Craig, W., Hailey, C., Harrison, F., Jimenez-Garate, M., . . . Mao, P. Growth, structure, and performance of depth-graded W/Si multilayers for hard x-ray optics. *Journal of applied physics* **88**, 460-470 (2000).

138 Takenaka, H., Ichimaru, S., Ohchi, T., Koyama, T., Tsuji, T., Takano, H. & Kagoshima, Y. Mo/Si and MoSi2/Si nanostructures for multilayer Laue lens. *Journal of Physics: Conference Series.* 012074 (IOP Publishing).

139 Braun, S., Mai, H., Moss, M., Scholz, R. & Leson, A. Mo/Si multilayers with different barrier layers for applications as extreme ultraviolet mirrors. *Japanese journal of applied physics* **41**, 4074-4081 (2002).

140 Kubec, A., unpublished simulation.

141 Freund, L. B. & Suresh, S. (Cambridge University Press, Cambridge, England, 2003).

142 Chason, E., Sheldon, B. W., Freund, L. B., Floro, J. A. & Hearne, S. J. Origin of Compressive Residual Stress in Polycrystalline Thin Films. *Physical Review Letters* **88**, 156103 (2002).

143 Floro, J. A., Kotula, P. G., Seel, S. C. & Srolovitz, D. J. Origins of Growth Stresses in Amorphous Semiconductor Thin Films. *Physical Review Letters* **91**, 096101 (2003).

144 Ibach, H. The role of surface stress in reconstruction, epitaxial growth and stabilization of mesoscopic structures. *Surface Science Reports* **29**, 195-263, doi:http://dx.doi.org/10.1016/S0167-5729(97)00010-1 (1997).

145 Kozawa, T., Kachi, T., Kano, H., Nagase, H., Koide, N. & Manabe, K. Thermal stress in GaN epitaxial layers grown on sapphire substrates. *Journal of Applied Physics* **77**, 4389-4392, doi:http://dx.doi.org/10.1063/1.359465 (1995).

146 Barabási, A.-L. *Fractal concepts in surface growth*. (Cambridge university press, 1995).

147 Chrisey, D. B. & Hubler, G. K. *Pulsed Laser Deposition of Thin Films*. Vol. 1 648 (Wiley-Interscience, 2003).

148 Hoffman, D. W. & Thornton, J. A. Internal stresses in Cr, Mo, Ta, and Pt films deposited by sputtering from a planar magnetron source. *Journal of Vacuum Science & Technology* **20**, 355-358, doi:http://dx.doi.org/10.1116/1.571463 (1982).

149 Röder, J. & Krebs, H. U. Frequency dependent smoothing of rough surfaces by laser deposition of ZrO2. *Appl. Phys. A* **90**, 609-613, doi:10.1007/s00339-007-4375-0 (2008).

150 Windischmann, H. Intrinsic stress in sputter-deposited thin films. *Critical Reviews in Solid State and Material Sciences* **17**, 547-596 (1992).

151 Windt, D. L. Stress, microstructure, and stability of Mo/Si, W/Si, and Mo/C multilayer films. *J. Vac. Sci. Technol. A* **18**, 980 - 991 (2000).

152 Shi, B., Macrander, A. T., Maser, J., Conley, R. & Assoufid, L. The effect of unequal bilayer thickness on stress in WSi2/Si multilayers for multilayer Laue Lens structures. 920708-920705.

153 Windt, D. L. X-ray multilayer films and smoothing layers for x-ray optics having improved stress and roughness properties US patent (2008).

154 Windt, D. L. Reduction of stress and roughness by reactive sputtering in W/B4C multilayer films. *Optical Engineering+ Applications.* 66880R-66810 (International Society for Optics and Photonics).

155 Morgan, A. J., Prasciolu, M., Andrejczuk, A., Krzywinski, J., Meents, A., Pennicard, D., . . . Barthelmess, M. High numerical aperture multilayer Laue lenses. *Scientific reports* **5** (2015).

156 Kubec, A., Kujala, N., Conley, R., Bouet, N., Zhou, J., Mooney, T. M., . . . Macrander, A. Diffraction properties of multilayer Laue lenses with an aperture of 102 μm and WSi 2/Al bilayers. *Optics express* **23**, 27990-27997 (2015).

157 Nazaretski, E., Lauer, K., Kalbfleisch, S., Wagner, U., Rau, C., Chu, Y. S., . . . Gofron, K. Pushing the limits: an instrument for hard X-ray imaging below 20 nm. *Journal of Synchrotron Radiation*, in press.

158 Huang, X., Conley, R., Bouet, N., Zhou, J., Macrander, A., Maser, J., . . . Chu, Y. S. Achieving hard X-ray nanofocusing using a wedged multilayer Laue lens. *Optics Express* **23**, 12496-12507, doi:10.1364/OE.23.012496 (2015).

159 Nazaretski, E., Huang, X., Yan, H., Lauer, K., Conley, R., Bouet, N., . . . Chu, Y. S. Design and performance of a scanning ptychography microscope. *Review of Scientific Instruments* **85**, 033707, doi:http://dx.doi.org/10.1063/1.4868968 (2014).

160 Macrander, A. T., Kubec, A., Conley, R., Bouet, N., Zhou, J., Wojcik, M. & Maser, J. Efficiency of a multilayer-Laue-lens with a 102 μm aperture. *Applied Physics Letters* **107**, 081904, doi:http://dx.doi.org/10.1063/1.4929505 (2015).

161 Chu, Y., Yan, H., Nazaretski, E., Kalbfleisch, S., Huang, X., Lauer, K. & Bouet, N. Hard x-ray nanoprobe facility at the National Synchroton Light Source II. *SPIE Newsroom*, doi:10.1117/2.1201508.006068 (2015).